Structural Health Monitoring of Wind Turbine Blades using Guided Wave NDT Technique

Kenneth C. Burnham

A thesis submitted for the degree of
Doctor of Philosophy
At the University of Strathclyde
2014

This thesis is the result of the author's original research. It has been composed by the author and has not been previously submitted for examination which has led to the award of a degree.

Signed:
Date:

Acknowledgements

This thesis has been a long time coming. There are several reasons for this, not least the part played by the banking crisis in 2008 whereupon my hasty acceptance of a job offer resulted in redundancy just four months later by the subsequent recession of 2009. As a consequence, my research was conducted in two halves: 3 years at the University of Strathclyde, and almost 3 years at TWI (Cambridge).

Starting with the University of Strathclyde, my first and overwhelming thanks go to my supervisor, Dr. Gareth Pierce, whose support has ensured that any of this was put down on paper at all. I thank Dr. Pierce for his guidance, the chats on materials and Guided wave propagation, and just generally for keeping me sane. Thanks too to Walter Galbraith whose help and general humanity meant that a smile would appear on my stressed face anytime we met. I'd like also to thank Grant Smillie, Michelle McGuire, Gordon Dobie, Simon Whiteley and Campbell McKee for their support. Thanks too to Prof. Hayward and Prof. Andonovic for their support.

The experiments conducted at Strathclyde University produced only mixed results. I therefore would like to offer my heart-felt thanks to TWI. Working on FP7 renewable energy projects ensured that I was able to conduct appropriate experiments on real wind turbine blade samples. Massive thanks to Alex Haig, Kena Makaya, Hugo Marques, Carmen Castellanos and Ruth Sanderson for their assistance in setting up experiments, equipment and their flexibility regarding schedules. I would also like to thank Peter Mudge for his support and calmness in the face of harsh deadlines. Acknowledgement also to Dr. Paul Jackson and Dr. Chiraz Ennaceur for inviting me to Cambridge in the first place – a move, without which, the realisation of this work would be in significant doubt.

Finally, thank you David, Yvonne, Glen & Charlie for your understanding and unstinting support during challenging times.

Table of Contents

Table of Figures

List of Tables

List of Abbreviations

2DFFT	2-Dimensional Fast Fourier Transform
AE	Acoustic Emission
B	Bulk Modulus
BEM	Boundary Element Method
CFRP	Carbon Fibre Reinforced Plastic
c_{ij}	Stiffness coefficient
DECC	Department for Energy & Climate Change
ξ	Displacement gradient
DSP	Digital Signal Processing
E	Young’s Modulus
EC	European Commission
EMAT	Electro-Magnetic Acoustic Transducer
EMI	Electro-mechanical Interference
fd	Frequency-thickness product
FD	Finite Difference
FEA	Finite Element Analysis
FEM	Finite Element Modelling
FFT	Fast Fourier Transform
FP7	Framework Project 7
FSE	Finite Strip Element
G	Shear Modulus
GFRP	Glass Fibre Reinforced Plastic
Γ	Gruneisen’s coefficient
GWEC	Global Wind Energy Council

IDT	Interdigitated Transducer
ILSS	Inter-Laminar Shear Strength
IR	Infrared
K	Elastic constant
k	Wave number
∇^2	Laplacian operator
LISA	Local Interaction Simulation Approach
MEMs	Micro Electromechanical systems
MFC	Macro-Fibre Composite
MSLM	Mass Spring Lattice Model
MWh	Mega Watt-hour
NDT	Non-Destructive Testing
NDI	Non-Destructive Inspection
NEWS	Non-linear Elastic Wave Spectroscopy
NIR	Near Infra-Red
NRUS	Non-Resonant Ultrasound Spectroscopy
O&M	Operation & Maintenance
OEM	Original Equipment Manufacturer
ρ	Medium density
ς	Permittivity
PVDF	Polyvinylidene Fluoride
PWAS	Piezoelectric Wafer Active Sensor
PZT	Lead (Pb) Zirconate Titanate
r(d)	Cross-correlation function
SAW	Surface Acoustic Waves

VAMT	Vibro-Acoustic Modulation Technology
SE	Spectral Element
SHM	Structural Health Monitoring
SNR	Signal to Noise Ratio
ε	Strain
σ	Stress
UT	Ultrasonic Testing
UD	Unidirectional
U, W	Displacement components
ν	Poisson's ratio
v	Wave velocity
λ	wavelength
WT	Wavelet Transform
Z	Acoustic Impedance

Abstract

Wind energy is an increasingly important contributor of power within the renewable energy sector. In the year to 2012, wind generation within the United Kingdom (UK) increased 40% meeting 6% of the UK's national electricity demand. The UK is committed to providing 15% of its energy from renewable resources by 2020. Currently, the UK has approximately 40% of Europe's entire wind resource with significant potential for development of both on and offshore wind.

In recent years, the number of reports on defective blades contributing towards turbine failure has grown. Blade manufacturers have privately reported a recurring problem with the spar cap - a critical strengthening component - which when weakened by damage, hastens the onset of operational failure. The contents of this thesis consider composite materials used within the blade and the detection techniques appropriate for in-field implementation.

Application of Guided Waves, in particular Lamb waves, suits the typical dimensions of the blade composite structure. Experiments were conducted to understand the characteristics of Lamb wave modes within glass fibre reinforced plastic (GFRP) to assess attenuation levels; modal propagation; and dispersion with respect to fibre orientation. Finite Element Analysis (FEA) was used to observe material characteristics and discern possible modes of wave propagation. To exploit the directional qualities of GFRP, directional Macro Fibre Composite (MFC) sensors were applied to a wind turbine blade providing low-profile, light-weight, durability and conformability with sufficient sensitivity to detect elastic disturbance over large areas.

Parametric monitoring of GFRP samples under loading identified tensile stress from defect onset. Cross correlation and sliding-window correlation signal processing techniques on recorded data from the applied sparse array identified the onset of fibre damage using Guided wave modes. This technique was able to identify modal changes to specific defects providing the prospect for *in-situ* blade monitoring.

1 An Overview of Structural Health Monitoring

1.1 Thesis Background

Structural damage can occur in any engineered asset: infrastructure, transport, heavy equipment. If ignored, damage can spread, eventually causing operational failure, at which point maintenance costs and costs due to loss of service may well be prohibitive.

When catastrophic failure arises in transportation vehicles, human loss is often the outcome. The National Institute for Occupational Safety & Health (NIOSH) recorded 386 fatal commuter aircraft crashes in the U.S. between 1990 and 2007, [1]. A significant proportion of these crashes resulted from structural failure. The likelihood of failure increases with age. The Eschede train crash in Germany 1998 is to date the most serious high-speed train crash due to defect onset. 101 people were killed when a damaged wheel disintegrated just as the train passed over a switch-track (causing cars to derail and impact the bridge supports). Subsequently, major engineering changes and safety improvements were implemented, [2]. To prevent loss, whether it is human, service, financial or a combination thereof, a monitoring technique is required to overcome the need for site specific experience and provide an early warning system.

Structural Health Monitoring (SHM) is an instrumented, *in situ* technique to overcome the need for regular site specific analysis providing an early warning of developing problems so that assets can be better managed. An integrated sensing system permits autonomous monitoring of loading conditions and the onset of damage which can then be recorded, analysed, ideally localised and predicted in such a way that non-destructive testing becomes an integral part of the structure, [3].

SHM has been applied to structures (bridges, buildings), aerospace (fuselage, wings), and ground transport (military vehicles, high-speed rail). In each instance, information on structural behaviour and performance, loads, design principles, maintenance, and Systems for structural assessment is required.

The ready availability of structures can be improved, with greater cost efficiency and reliability and no compromise of safety, by making sensors an integral part of the structure. Implemented into a structure at the manufacturing stage, SHM can be conducted on operational loads to provide a prognosis on the components most likely to suffer structural damage. Successfully installed SHM systems can supplant general visual inspections and detailed inspections.

The wind energy sector is such a sector which may benefit from implementation of SHM systems. End users are currently researching methods that extend the life-cycle of wind turbine components as utility companies constantly strive to reduce the operational and maintenance (O&M) costs of wind farms.

Some components within a wind turbine are heavily monitored. For example the gearbox and generator are turbine components which are monitored using mature sensing systems. Comprising a temperature controllable oil reservoir and variable speed pump, oil analysis at the bearings is a standard technique where ferrous and non-ferrous particulates are measured. Their presence creates a change in the inductance of a transducer coil causing frequency shift from which the particulates can subsequently be determined ferrous or non-ferrous. Signal amplitude indicates the particle size and quantity. Information relating to the size of the debris gives an indication as to the fault source, [4,5].

The use of optical fibre based sensors for measurement of strain and damage is a relatively well-established technique and is often installed on wind-turbine blades to provide edgewise and flap-wise bending moment data and micro-strain values. A sensor interrogation unit is installed in the rotor hub to interface with the turbine's programmable logic controller which utilises data from the blade sensors in conjunction with turbine data as part of the inter-process communication system to optimise turbine operation, [6].

However, there remains considerable scope for further monitoring of the wind turbine blade. Whilst optical sensors are effective for detecting defects in large structures, they are relatively insensitive to undersized damage or the evolution of structural deterioration without the implementation of a very dense array of sensors, [7]. The integrity of blade load-bearing components is critical to equip optimum turbine operation and provide the desired energy conversion. Condition monitoring techniques can be used to analyse composite components which provide support to the blade.

SHM is a process of monitoring component integrity during operation and often incorporates different non-destructive testing (NDT) techniques. Conceptually, there is a difference between the two: typically, NDT is limited to the detection of a flaw and its geometry; flaw assessment and impact on component lifecycle are the remit of SHM given the NDT data, [8].

This Chapter will provide an overview of SHM using NDT.

1.2 Structural Health Monitoring (SHM)

Structural health monitoring (SHM) is a developed technology which aims to provide near real-time information concerning structural integrity to help reduce the number of unnecessary inspections and lower instances of maintenance. The integration of SHM within a system is particularly important where the structure is under severe operational conditions and decisions need to be taken rapidly to avoid catastrophic failure.

As an initial step, it is necessary to ascertain the critical issues regarding a structure, and how they may be addressed. Table 1.1 identifies the main initiation processes of damage.

Table 1.1 Issues leading to the onset of damage

Issue	*Solution*	*Comment*
Accident	Visual and/or Non-Destructive Inspection (NDI)	Barely visible damage regularly reported
Loads	Design spectrum; NDI	Subjective judgement
Fatigue & Fracture	Damage tolerance design; Major structural testing; NDI; Inspection interval	Time consuming & labour intensive
Corrosion	Design; Corrosion protection plan; NDI; Inspection interval	
Multi-site Damage	NDI; inspection interval	
Repair	Quality Assurance; NDI; Inspection interval	

Most offline non-destructive testing methods (NDT) are localised, external to the structure and are typically ‘non-persistent’. Components requiring regular inspection may be located in inaccessible areas or involve complicated disassembly prior to assessment. The process is often time consuming and expensive due to the required operational down-time. As a result, there is increasing pressure for longer intervals between maintenance. The prerequisite for SHM is to reduce O&M costs, and extend the lifecycle of the structure by sustaining the integrity of the comprising components.

A heuristic approach to provide SHM typically comprises: a monitoring principle in terms of the physics; sensors appropriate for the application; hardware to instigate and provide data collection; signal processing to interpret any change in data; and experience to optimise a holistic approach.

In addition, a number of functions are required: data acquisition and storage, data management, data transmission, data interpretation and visualisation as well as likely system prognosis – whereby a risk assessment can be conducted based on evidence of the structural hazard.

1.2.1 Monitoring Process

Figure 1.1 demonstrates the monitoring process required to remotely identify and locate the presence of damage within a structure, assess the severity of the defect and provide a prognosis of damage development.

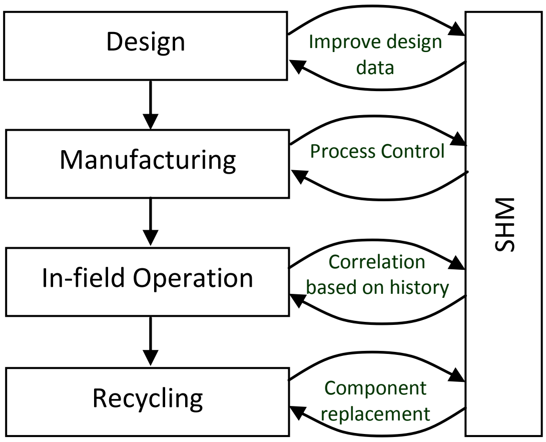

Figure 1.1: Monitoring process based on decision making

For a successful SHM system to be implemented, it is first necessary to define the phases leading to structural damage, [9]:

- A *defect* is an imperfection within the material present at the micro-structural level. It is within the defined limits of manufacture and thus not considered to be a non-conformance.
- *Damage* is a change in the material's structure such that it causes the component to perform below a required level. Whilst the component may still operate correctly, the loading conditions have changed such as to further weaken the material.
- A *fault* occurs when the damage is so extensive that the component no longer serves the function required of it. This may now undermine the whole structure and have safety implications.

The full monitoring process system includes sensor technology, data analysis and handling, network and communication systems, electronics, and material science, reproduced in Figure 1.2.

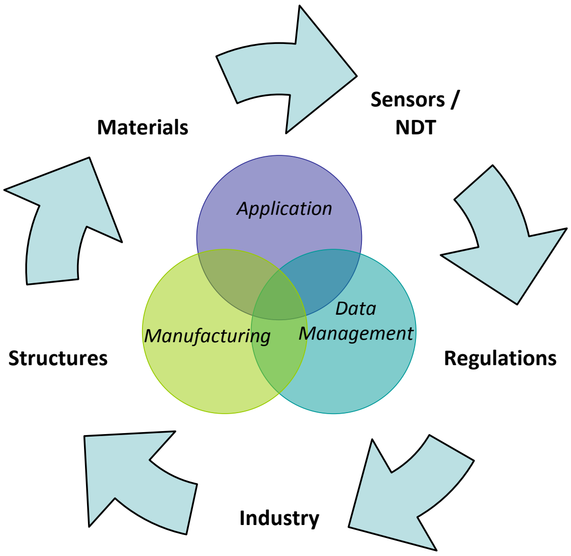

Figure 1.2: SHM platform, [10]

The SHM cycle is configured to acquire data and distinguish signal content during the feature extraction process. Embedded algorithms are typically used to discriminate real damage from environmental or cyclic effects. As part of the signal conditioning stage, digital signal processing (DSP) techniques such as filtering and averaging are used to improve the signal-to-noise ratio (SNR), whilst baseline subtraction is used to identify ‘new’ contributing components to the complex signal. Such damage-detection algorithms are based on the assumption that, when the response for an undamaged component is compared with a damaged component, a difference of signal will emerge at a specific point in time. The signal processing faculty of an SHM system combines with a continually developing knowledge-based expert system able to identify damage and determine the size and location of a flaw. The dedicated software provides anomaly detection between previously unrecorded patterns and recognised patterns to provide information on the severity of the damage, determination of damage growth, customised visualisation of the structurally compromised area. In addition, the SHM system typically includes a ‘go/no-go’ alert regarding ensuing action to assist maintenance support operations - contributing towards a system for high-level management.

1.2.2 Composite Materials

The main benefit of composite materials is the strength to weight ratio – or stiffness to weight ratio. It is this feature which has acted as the driver for its use in many applications. Figure 1.3 provides a timeline of the materials used in composites for both fibre and matrix showing the increased confidence level. It is the aerospace and automotive industries which are driving the increasing use of composite materials within structural designs.

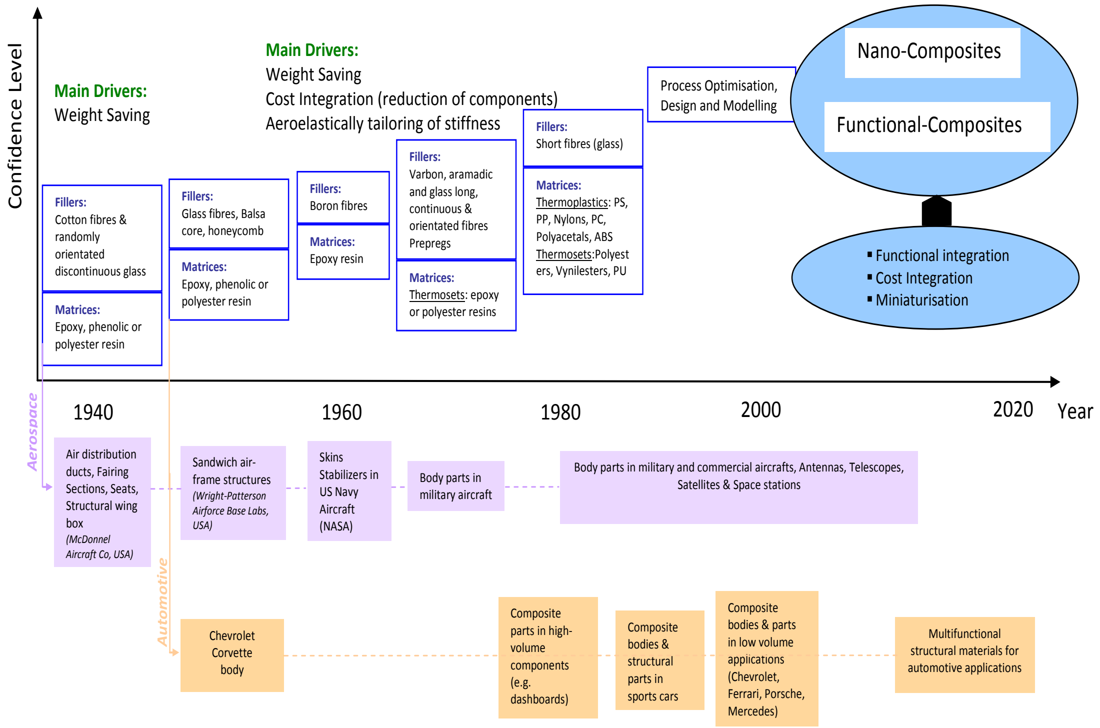

Figure 1.3: Development & use of composite materials, [11]

Within the renewable sector in the UK, composite materials have been used as part of the turbine structure since 1991 when the first wind-turbine farm was connected to the Grid in Delabole, Cornwall, [12]. The occurrence of damage within a composite component decreases its strength, and consequently its ability to withstand typical loading conditions, with ensuing inefficiency often leading to an unsound structure.

Detection of compromised structural integrity allows appropriate and timely intervention, preventing component failure. Damage within composite materials accumulates via a variety of mechanisms: fibre breakage; matrix cracking; disbond and delamination. For example, fatigue loading of a structure can lead to a delaminated component which subsequently leads to further redistribution of the load, further increasing the area of delamination.

Non-destructive testing (an integral part of an SHM system) permits management of risk: it detects structural problems; it assesses damage growth; and it provides safety and insurance.

1.2.3 Non-Destructive Testing (NDT)

The British Institute of Non-Destructive Testing defines NDT as “the branch of engineering concerned with all methods of detecting and evaluating flaws in materials”. The flaws may be cracks or inclusions in welds and castings, or variations in structural properties which can lead to loss of strength or failure in service, [13]. An essential feature of NDT is that it leaves the material intact and undamaged.

In practice, NDT is a series of tests to detect defects arising from changes in structural properties from which SHM will extract key features to provide a prognosis of the health of the structure. In addition to providing in-service damage inspection and extending product life, NDT provides the added attraction of satisfying quality assurance and legal and regulatory requirements. It also offers component assurance for safety critical applications.

Recent years have seen a significant progress in NDT techniques and there are now a range of methods available for in-service testing of composite structures. Table 1.2 lists a number of NDT methods commenting on their strengths and weaknesses, [14].

Table 1.2: NDT Techniques

Method	*Strengths*	*Limitations*	*SHM Potential*
Strain Gauge	Embeddable Simple procedure Low data rates	High sensor density required Does not directly detect damage	Low power Localised results
Optical Fibres	Embeddable Simple results Conformable	Sensor density/coverage high Intrusive technique	Localised results Robust
Eddy Current	Surface mountable Most sensitive	Material under test must be conductive Limited Bandwidth Poor device sensitivity	Localised results Damage differentiation
Acoustic Emission	Inexpensive Surface mountable Good coverage	Broadband complex results Sensitive to other ultrasonic sources Event driven	Structure-borne activity Triangulation for source location Impact detection
Vibration/Modal Analysis	Inexpensive Surface mountable Good coverage	Complex results High sensor density for analysis	Low power Complex structures Multiple sensor types
Lamb Waves	Inexpensive Surface mountable Good coverage	Complex results High data rates	Triangulation for defect location Damage differentiation
Thermography	Non-contact & remote inspection	High energy required Poor penetration Not a continuous monitoring technique	Location & sizing capability

The selection of the NDT method will depend upon a number of factors including access, regularly developing defect type, component thickness, surface condition, and material quality. The type of defect and its likely location is a particularly influential factor when deciding upon a testing methodology. A number of NDT procedures have been standardised and consequently are accompanied with proprietary software. An effective SHM system should identify the presence of damage at its earlier stages. Therefore, the appropriate application point of NDT within an SHM system is indicated in Figure 1.4.

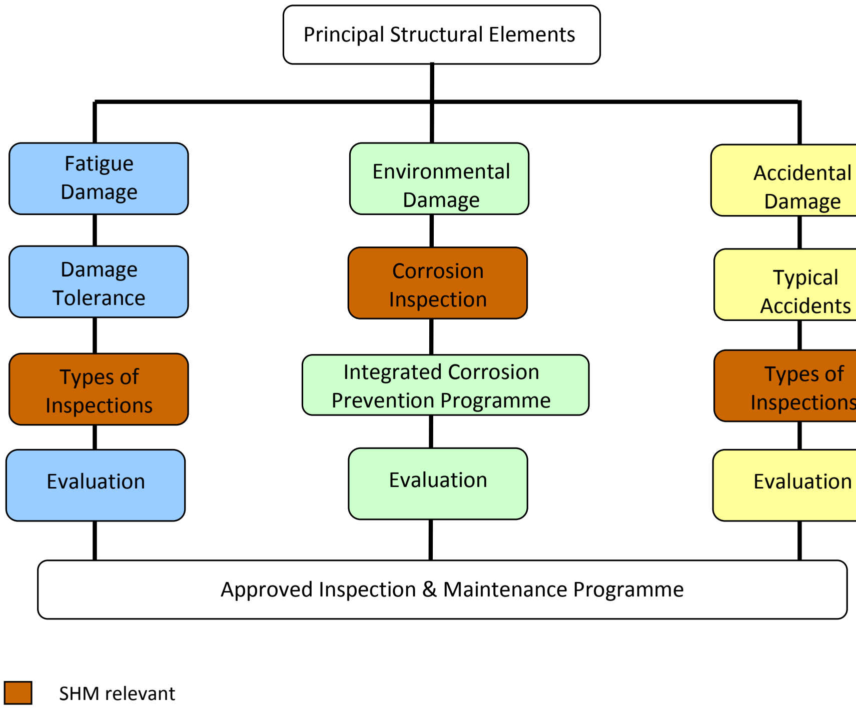

Figure 1.4: Positioning of SHM within the maintenance process, [3].

The process illustrated in Figure 1.4 is known as Maintenance Service Group-3 (MSG-3) and is a system widely used by commercial airplane manufacturers, [15]. Commencing before an aircraft enters service, the process continues throughout the life-cycle of a particular model. The MSG-3 processes include tasks such as lubrication, visual inspections, operational or functional checks, restoration and discard (removal and replacement of life-limited parts). MSG-3 stresses a top-down approach to analysis; starting at the highest manageable level and examines the consequences of that failure. Should analysis reveal that a certain functional failure threatens operational safety, and is not addressed within the hierarchy of standard tasks, redesign of the component in question is then deemed mandatory. Although the effects of failure are considerably more serious within the aviation industry, such an approach can be utilised for other industry sectors with few changes (if any).

There may be considered to be four main techniques within the NDT canon: Acoustic Emission (AE), fibre optics, vibration analysis and ultrasonic Guided waves.

1.2.3.1 Static Parameter-Based

The presence of damage causes changes in displacement and strain distribution when compared with baseline measurements. They are sensitive to local defects. However, it is an NDT solution requiring a high density of distribution on large components. Furthermore, strain measurement is relatively insensitive to undersized damage or continuous deterioration. Fibre optic strain sensing exhibits: superior data capacity, better noise immunity, and better multiplexing solutions than electrical strain gauge sensing, [16]. Fibre optical sensors have been used for strain monitoring for many years, but their application within the wind industry is relatively recent. Although a robust technology, introduction of any new technique raises concerns over reliability. Optical sensors provide high levels of accuracy and can easily be embedded during the production phase of turbine construction, [17]. Immune to electromagnetic interference, optical sensors can be an expensive NDT solution.

1.2.3.2 Vibration Analysis

Vibration measurements are most commonly measured using accelerometers. They are usually piezoelectric and permit determination of a structure’s acceleration on condition that the natural frequency of the accelerometer is greater than the highest frequency component of interest. Since the sensor is physically attached to the structure to be monitored, the mass of an accelerometer - which can vary from 0.5 g to 500 g – is a crucial parameter for adjustment during results analysis, [18].

1.2.3.3 Acoustic Emission (AE)

Acoustic Emission (AE) analysis is a powerful technology that can be widely applied as an NDT technique across a variety of sectors. AE is defined as the stress wave resulting from the rapid release of strain energy when micro-structural changes occur in a material. The propagating elastic wave is typically detected using piezoelectric sensors which convert the energy into an electrical signal, [19]. AE monitoring is both a passive and a broadband technique. Calibration of AE sensors using HSU-Neilson sources on the surface of the structure to be monitored maximises sensitivity for the detection of mechanical transient waves. Attenuation and wave velocity measurements characterise the acoustic properties of the material under test and enables two-dimension localisation of AE events.

1.2.3.4 Ultrasonic Guided Waves

Ultrasonic Guided Wave inspection is dependent upon the material and the geometry of the waveguide. These characteristics will determine which wave modes propagate when the material is elastically excited. Typically an external ultrasonic signal source is used to excite the structure which is subsequently used for inspection. Information on the presence of damage can be found in changes of amplitude, change of mode arrival time, and mode conversion. The changes to these Guided Wave parameters may be slight for incipient damage and consequently require extensive signal processing to deliberate on the integrity of a particular structure. An effective approach, able to inspect large areas within a relatively short period of time, it is also fast and repeatable, [20].

1.2.3.5 Eddy Currents

Eddy-current testing is an NDT technique that uses time-varying magnetic fields to induce eddy currents in a conducting material. A time-varying current in a drive coil, at a prescribed frequency or time-dependent signal characteristics, creates a time-varying magnetic field which induces an eddy current in the material with a pattern dependent upon the drive coil geometry. The sensor response is dependent upon electrical conductivity, magnetic permeability, material thickness and the proximity of the sensors to the surface, [21]. This method of NDT is not suitable for non-conducting materials such as glass fibre reinforced plastic (GFRP).

1.2.3.6 Thermal Imaging

Mechanical phenomena exhibits thermo-mechanical coupling such that the analysis of structural surface temperature with respect to space distribution and time evolution can lead to an evaluation of the structural health. There are several methods of measuring temperature: infra-red radiometry, [21]; thermoelectric effect (thermocouples), thermoresistive effect, [22]; thermochromic liquid crystals, [23,24]; thermocolor or heat-sensitive paints, [25]; and fluorescence, [26].

1.3 Thesis Objectives

The main objective of this thesis is to contribute to the development of the characteristics and analysis of composite materials, specifically GFRP typically used within wind turbine rotor blades. The identified NDT approach may then contribute towards the overall SHM of a turbine suitable for implementation by the Wind Energy industry.

This work involves:

- A review of the energy sector, the natural resource and related costs

- A review of the structural challenges facing the wind energy sector
- A review of the current monitoring techniques used within the NDT industry
- An evaluation of the components comprising a wind-turbine best suited for the application of appropriate NDT
- Analysis of GFRP composites and its material effects on propagating ultrasonic Guided Waves
- Analysis of the applicability of various sensor types for use on composite materials
- Investigation using FE modelling to predict sensor outputs
- Investigation of material effects on propagating Guided Waves within a static wind turbine blade using an appropriate sensor arrangement
- Application of suitable signal processing techniques
- Investigation of material effects on propagating Guided Waves within a wind turbine blade undergoing dynamic loading

1.4 Thesis Outline

The chapter order within this thesis provides a top-down approach concerning: the drive for greater efficiency of energy production; the sectors favoured due to national and supranational directives; issues facing wind energy utility companies and the failing components impacting on O&M costs; and the NDT possibilities to enhance the overall SHM of wind turbines.

The research is broadly split between analysis of the geometrical effects of GFRP composite materials typically used within wind turbines, and the application of suitably configured sensors on a real turbine blade to ascertain the efficacy of the selected NDT techniques. Throughout the investigation, various signal processing techniques are applied and a comparison is drawn between the acquired experimental data and the subsequent generated finite FE model for the purposes of validation. Each chapter has an overview and a conclusion. Where additional background information is necessary, appropriate appendices are located at the end of the thesis.

Chapter 2 provides a review of wind-turbine technology including the state of the energy industry and the consumption from both renewable and traditional sources. A discussion of planned installed wind energy capacity is presented within the context of the UK. The economies of scale that have provided ever greater energy yield with respect to structural investment may now be approaching a limit, given the current design methodology. The increasing drive for efficiency means that there is an increasing demand for life-cycle design to be implemented from the design stage through to the commissioning stage, in-use stage and finally end-of-life stage. A description of the various turbine drive-chain components is provided with the purpose of identifying a component structure on which NDT would offer significantly enhanced turbine operation.

Chapter 3 reviews the structural concerns of the wind turbine rotor blade from the design together with the composite material used. The weaker components identified, a review of NDT candidate techniques is presented with their suitability for application. To ascertain the appropriate sensor, the discussion progresses to regularly occurring defect types and the generated physical properties. With Guided waves distinguished as being particularly suited to the most commonly emerging defects, a variety of sensors are considered. To facilitate an optimal array configuration for both coverage and sensor density, the chapter concludes with a recommended outcome to determine sensor distribution and achieve appropriate sensitivity for defect identification.

Chapter 4 describes the wave propagation properties of ultrasonic waves within isotropic materials and considers the relationship between stress and strain leading to Hooke's law. Having identified the composite material for structural monitoring as exhibiting transversely isotropic characteristics, the transformation properties affecting the acoustic field are analysed to ascertain the transformed stiffness coefficient relating the strain to the stress. The chapter concludes with the excitation arising from the proposed sensor for selection and how the stress amplitude may be assessed.

Chapter 5 develops a detailed experimental study of fundamental wave mode (A_0; S_0) interaction with a variety of GFRP samples featuring different lamina lay-ups. Fibre orientation impacts on wave mode characteristics such as amplitude, arrival time and presence of dispersion. Different methods for both excitation and reception are analysed to identify the preferred sensor design for optimum detection of change within the mechanical properties of a GFRP material. An analysis of the effect of matching directional sensors with the inherent directionality of the material upon which they are placed to sense is subsequently performed. The chapter compares experimental results with finite element models created within the PZFlex and ABAQUS modelling environments.

Chapter 6 takes the ideas developed in Chapter 5 and applies them to a real wind-turbine blade to identify the relevant issues surrounding structural lay-up. Different sections of the blade were configured with an array of directional sensors to establish: the distance travelled by a propagating Guided wave; the sensitivity of the wave to a change in boundary conditions; and the variation of array sensitivity with respect to blade location. The effects of loading were considered on GFRP samples to establish whether such conditions can be differentiated from defect onset.

Chapter 7 considers the response of a sparse array to blade component characteristics upon application of defect onset. Application of signal processing techniques are applied to recorded data including cross correlation analysis and sliding window cross correlation analysis used to establish the measurability of varying levels defect severity: surface defect; fibre-breakage; and thorough localised component discontinuity.

Chapter 8 provides a summary of the work conducted and the potential contribution to the wind energy sector, particularly blade manufacturers and end-users. The chapter concludes with a discussion on further work for consideration to enhance the proposed NDT capability with respect to wind turbine rotor blades.

1.5 Contribution to Knowledge

The research contained within this thesis provides a method for monitoring the structural integrity of a wind turbine blade by careful means of positioning low-profile directional sensors responsive to in-plane particle displacement ensuing from an elastic disturbance. This has been achieved on a decommissioned full-size wind turbine rotor blade, featuring a strengthening member, upon which a sparse array of sensors was affixed. The array, configured for partial-matrix data capture, detects altered Guided wave data upon application of a defect. Subsequent processed data is able to identify defect incidents and the component area of the blade in which they occurred using a design-specific aligned array in order to maintain operational efficiency for the end-user. Loading effects were readily distinguishable from blade component defect onset. Finally, the investigation showed the potential for an SHM system to optimise this novel technique to monitor a specific mode known to be sensitive to a particular recurring blade defect.

1.6 Publications

During the period of research summarised within this document, a number of publications have arisen out of this work. These include the following papers:-

'*Acoustic Techniques for Wind Turbine Blade Monitoring*', Burnham, K., Pierce, S.G., pp639-644, DAMAS 2007.

'*Structural Assessment of Turbine Blades using Guided Waves*', Makaya, K., Burnham, K., NDT 2010 Conference, Cardiff.

'*Simulation of Ultrasonic Lamb Wave Generation, Propagation and Detection for a Reconfigurable Air Coupled Scanner*', Dobie, G., Spencer, A., Burnham, K., Pierce, S.G., Worden, K., Galbraith, W., Hayward, G., Ultrasonics. 2011 Apr; 51(3):258-69.

'*Assessment of Turbine Blade Defects using Guided Waves*', Makaya, K., Burnham, K., ESIA11, Engineering Structural Integrity Assessment: Design, Fabrication, Operation and Disposal, Manchester 24-25 May 2011

'*Investigations of the guided wave data analysis capabilities in structural health monitoring of composite objects*', Mažeika, L., Samaitis, V., Burnham, K., Makaya, K., ISSN 1392-2114 ULTRAGARSAS (ULTRASOUND), Vol. 66 No. 3, 2011.

2 Review of Turbine Technology

2.1 Overview

This chapter discusses wind-turbine technology and the part it plays within the United Kingdom’s energy sector. Efficiency is an ever-constant issue of wind-turbines. Downtime to investigate maintenance issues remains a concern and mitigation by offering a viable solution, for both blade manufacturers and end-users, is necessary to identify the problematic turbine components. Thus, the effect of installing a defect detection system on the overall maintenance programme can be assessed and subsequently optimised by negotiating reliability, cost and loss-of-service impact. In addition, it is necessary to have an awareness of the readily installed defect detection techniques available on the market in order to appreciate the extent of any added premium.

2.2 Wind Turbines – State of the Industry

The United Kingdom (UK) Government is committed to reducing carbon emissions to 80% below 1990 levels by 2050, [28]. The UK is legally bound to deliver 15% of its energy demand from renewable sources by 2020 thereby attaining energy security and decarbonisation objectives, [29]. In 2012, the breakdown of energy consumption within the UK was: 32.1% natural gas; 45.4% petroleum products, 18.4% electricity, and 4% renewable energy [30]. In 2011, the UK imported a net

53% of its coal supply; 47% of gas supply; and imported more oil than it produced. Import reliance will increase over the coming years as output from the UK declines.

The Global Wind Energy Council (GWEC), a member based organisation representing the global wind energy sector in over 70 countries, reported a total wind capacity of 10.5 GW over 557 wind farms at the end of 2013, [31]. The UK has approximately 40% of Europe's entire wind resource with significant potential for further onshore (Figure 2.1) and offshore (Figure 2.2) wind development, [32]. According to the latest report by RenewableUK, a further 5 GW of offshore-wind capacity is expected to be installed by next year, [33].

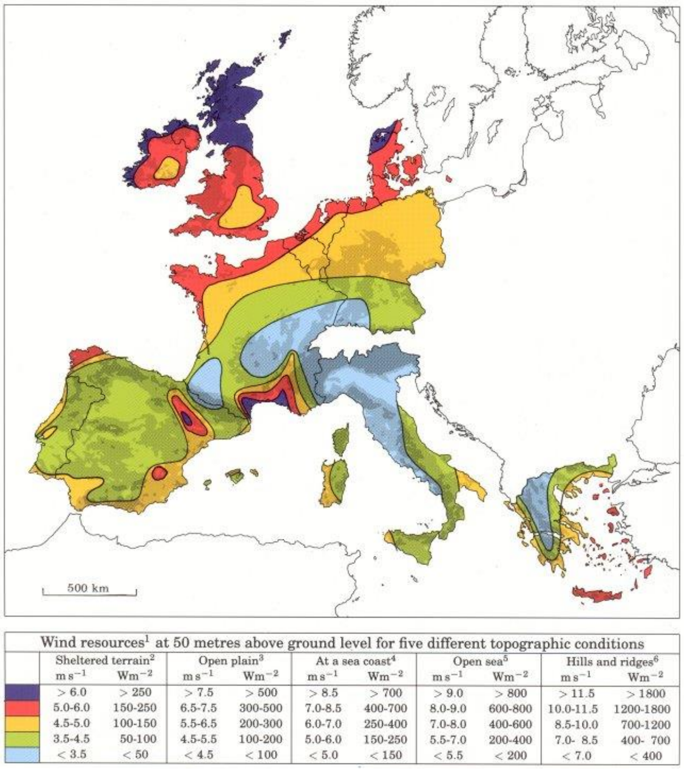

Wind resources[1] at 50 metres above ground level for five different topographic conditions

	Sheltered terrain[2]		Open plain[3]		At a sea coast[4]		Open sea[5]		Hills and ridges[6]	
	$m\,s^{-1}$	Wm^{-2}	$m\,s^{-1}$	Wm^{-2}	$m\,s^{-1}$	Wm^{-2}	$m\,s^{-1}$	Wm^{-2}	$m\,s^{-1}$	Wm^{-2}
🟪	> 6.0	> 250	> 7.5	> 500	> 8.5	> 700	> 9.0	> 800	> 11.5	> 1800
🟥	5.0-6.0	150-250	6.5-7.5	300-500	7.0-8.5	400-700	8.0-9.0	600-800	10.0-11.5	1200-1800
🟨	4.5-5.0	100-150	5.5-6.5	200-300	6.0-7.0	250-400	7.0-8.0	400-600	8.5-10.0	700-1200
🟩	3.5-4.5	50-100	4.5-5.5	100-200	5.0-6.0	150-250	5.5-7.0	200-400	7.0- 8.5	400- 700
🟦	< 3.5	< 50	< 4.5	< 100	< 5.0	< 150	< 5.5	< 200	< 7.0	< 400

Figure 2.1: Wind map of Europe: onshore, [34].

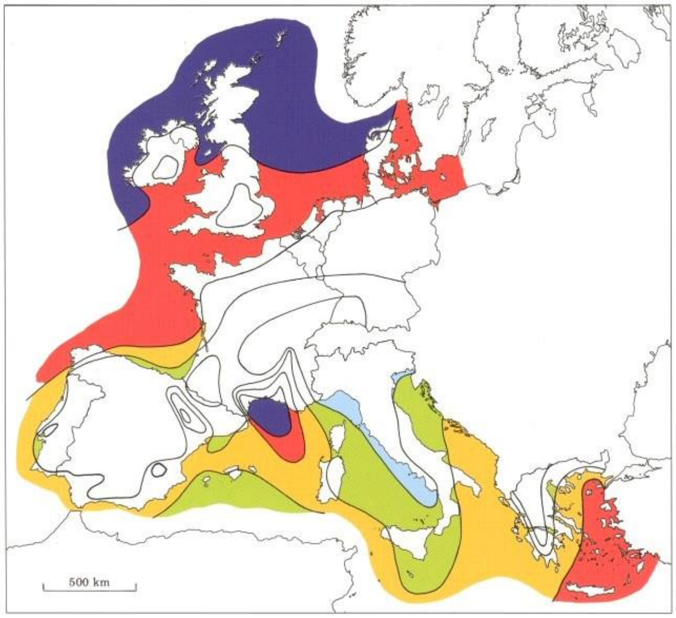

Wind resources over open sea (more than 10 km offshore) for five standard heights

	10 m		25 m		50 m		100 m		200 m	
	$m\,s^{-1}$	Wm^{-2}	$m\,s^{-1}$	Wm^{-2}	$m\,s^{-1}$	Wm^{-2}	$m\,s^{-1}$	Wm^{-2}	$m\,s^{-1}$	Wm^{-2}
🟪	> 8.0	> 600	> 8.5	> 700	> 9.0	> 800	> 10.0	> 1100	> 11.0	> 1500
🟥	7.0-8.0	350-600	7.5-8.5	450-700	8.0-9.0	600-800	8.5-10.0	650-1100	9.5-11.0	900-1500
🟨	6.0-7.0	250-300	6.5-7.5	300-450	7.0-8.0	400-600	7.5- 8.5	450- 650	8.0- 9.5	600- 900
🟩	4.5-6.0	100-250	5.0-6.5	150-300	5.5-7.0	200-400	6.0- 7.5	250- 450	6.5- 8.0	300- 600
🟦	< 4.5	< 100	< 5.0	< 150	< 5.5	< 200	< 6.0	< 250	< 6.5	< 300

Figure 2.2: Wind map of Europe: offshore, [34].

Due to the strength of potential for further development of both onshore and offshore wind, the UK government has put in place a range of measures and is committed to additional growth of wind generation. In April 2002, the Renewables Obligation came into effect, requiring electricity suppliers to source a specific and annually increasing proportion of electricity from eligible renewable sources or pay a penalty, [29].

Wind energy continued to be the leading individual technology for the generation of electricity from renewable sources during 2011 with 45% of renewable generation coming from this source. The contribution from wind is set to increase further over the next few years. In July 2011, the Renewable Energy Roadmap was published, setting out the path to achieving the UK’s renewable energy targets, [29]. Top-level predictions indicate that offshore wind could contribute up to 18 GW, and onshore wind up to 13 GW of installed capacity by 2020, [31].

Cost analysis of power generation is often uncertain. Much depends upon the scope of a project (e.g. technology and scale, numbers ordered, suppliers selected, bundled warranties), the ruling market conditions (commodity prices, supply chain bottlenecks), and the ability of the developer to manage costs. This is particularly true of immature technologies such as offshore wind where a ‘first-of-a-kind’ premium exists - largely dependent upon the responsiveness of the supply chains, [35].

In the UK, the maximum wind energy installation costs reported in 2009 were 1,600 €/kW for onshore installations rising to 2,375 €/kW for offshore installations, [36]. Additional costs for offshore installation include electrical connection to the shore and inter-turbine cabling. It is evident from the additional cabling alone that O&M costs for offshore installations will exceed those for onshore. However, O&M costs such as service, consumables, repair, and insurance for new large turbines are rarely reported. Comparison of technology cost generating electricity, for energy projects commissioned in 2009, reveals that onshore wind energy is competitively placed with regards to carbon fuels and nuclear energy, Figure 2.3.

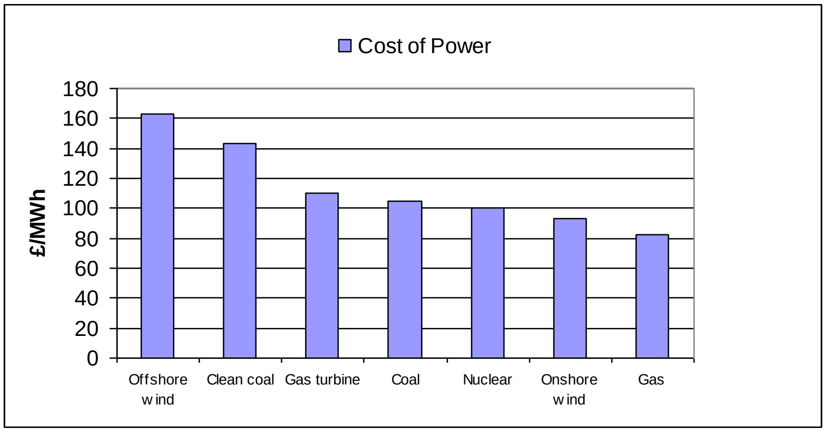

Figure 2.3: The cost of power, electricity prices by technology, [37].

Figure 2.3 refers to energy projects commissioned in 2009. As time progresses, costs may be expected to drop. For example, the government estimates that offshore wind energy can reach £100/MWh by 2020.

One report by L.W.M.M. Rademakers et al., disclosed 60% of turbine lifecycle cost comprised component parts, [38]. These figures provide no more than an indication of the O&M costs but are sufficiently considerable to provide a motivation for cost reduction.

Considerable attention is devoted to the siting of wind farms in order to keep turbulence to a minimum and guarantee maximum operational efficiency (turbulence hinders wind speed resulting in lower efficiency). Many countries have reported a shrinking supply of good wind sites near load centres – one reason for the increased interest in offshore developments. A particular advantage of offshore wind farm installations is turbulence effects are considerably lower due to a combination of lower temperatures between the sea surface and the air, smaller variations in temperature between the different altitudes in the atmosphere, and fewer objects at sea, [32]. As a consequence, the life-cycle of off-shore installations is greater than that for onshore turbines. In addition, since wind-speed does not change significantly with hub height at sea, the supporting towers are generally smaller (0.75 times rotor-blade diameter) than required for their onshore counterparts (where parity between the two is usual). It is these aspects of offshore wind-farms, combined with local political impact issues that utility companies find particularly appealing to offset the extra installation issues encountered offshore.

2.3 Wind Turbine Operation and Components

Wind turbines operate by harnessing the local wind kinetic energy and converting it into electricity via an induction generator. The power in the wind is extracted when the rotor blades interact with a wind field. A percentage of that power is converted into torque on the rotor. Rotation of the rotor blades rotates the low-speed shaft so spinning the high-speed shaft connected to a generator which produces electricity. The amount of power transferred is dependent upon the wind speed, the swept area and the density of the air. As the wind turbine extracts energy from the air flow, the air slows down causing it to spread out and divert around the wind turbine. German physicist, Albert Betz, determined that at most a wind turbine can extract 59% of the energy that might otherwise flow through the cross-section of the turbine, regardless of its design, [39]. Power varies with the cube of the wind speed: so twice the wind-speed equates to eight times the power, [34]. Conversely, strong gusts provide extremely high levels of power but it is not economically viable to build turbines to harness energy at the power peaks since their capacity would be redundant for large periods of time. The ideal site, therefore, is one with steady winds where a turbine is able to make the most of the lighter winds whilst surviving the strongest gusts.

Figure 2.4 illustrates each component location within an integrated turbine system, [40].

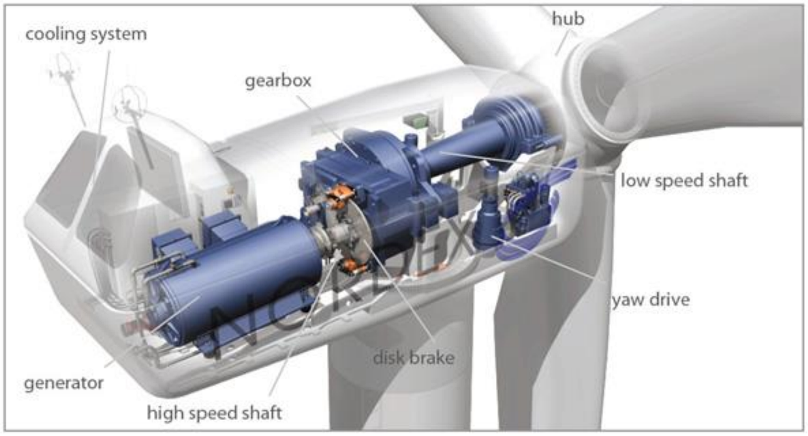

Figure 2.4: Wind turbine main components, [41]

Table 2.1 provides details on the components comprising the turbine and their cost contribution to the overall turbine cost.

Table 2.1: Turbine components & relative cost - based on a REpower MM92 turbine with 45.3 m blade length and a 100 m tower, [42]

Component	***Purpose***	***Contribution to overall turbine cost***
Tower	Made from rolled steel sections or lattice structure. Height varies from 40 m to >100 m	26.3%
Main Frame	Supports the Nacelle containing the full drive train	2.8%
Rotor Blades	Lift & rotate as wind blows across them. Varies in length up to 60 m. Manufactured using designed moulds from composite materials	22.2%
Rotor hub	Made from cast iron. Holds the blades in place as they turn.	1.4%
Main shaft	Transfers the rotational force of the rotor to the gearbox	1.9%
High speed shaft	Drives the generator at speeds of 1200 rpm to 1500 rpm	
Gearbox	Increases the low rotational speed of the rotor to the high rotational speed (in several stages) required by the generator	12.9%
Generator	Converts mechanical energy into electrical energy	3.4%
Yaw	Rotates the nacelle to face the changing wind direction	1.25%
Pitch	Adjust the angle of the blades in accordance with prevailing wind	2.7%
Power Converter	Converts DC from the generator to AC for the grid network	5%
Transformer	Steps up electricity from turbine suitable for grid network.	3.6%
Brake system	Disc brakes halts system when required	1.3%
Nacelle	Lightweight box to house drive train	1.3%

The turbine is the largest single cost component of the total installed cost of a wind farm. Figure 2.5 shows the cost of wind turbines from 2004 to 2012. Wind turbine prices have declined since 2009 in both Europe and the US, reflecting increased competition among manufacturers and lower commodity prices.

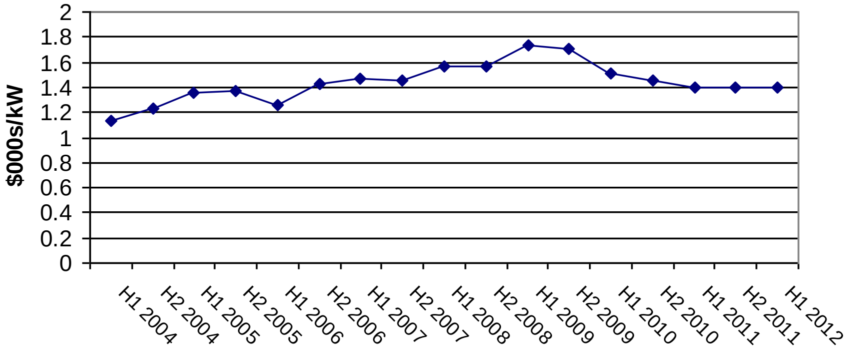

Figure 2.5: Wind turbine cost per kilowatt from 2004 to 2012, [42]

The wind industry designs wind turbines with regard to their aerodynamic load and response. The nature of the loading and the inherent dynamic response calls for design methods that are able to accommodate environmental loads and their interaction with various components.

Considering potential health monitoring strategies, virtually all of the components listed in Table 2.1 are suitable for fault detection. However, there are a number of factors which require consideration as regards monitoring prior to component selection:

- What is the percentage contribution of a component's failure rate to that for the whole turbine?
- What 'added value' does sensing a particular component contribute to the overall health of the turbine?
- Which component, when failing, is the most prohibitively expensive to replace?
- Which component preserves most the integrity of the turbine upon early detection of a fault?

- Which component, upon failure, expends the greatest ‘down-time’?

The wind turbine industry has yet to fully document the areas in which defects regularly occur. Figure 2.6 provides a breakdown of failure costs. In terms of identifiable parts, the gearbox fails most often.

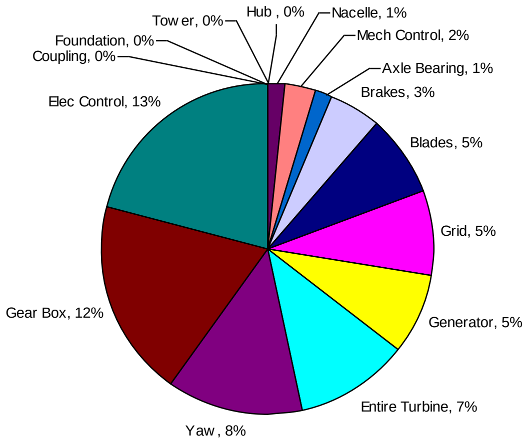

Figure 2.6: Component failure breakdown, [43]

Combining the component cost (Table 2.1) with typical component failure rate (Figure 2.6) provides normalised information with respect to frequency of failure against product cost, Figure 2.7.

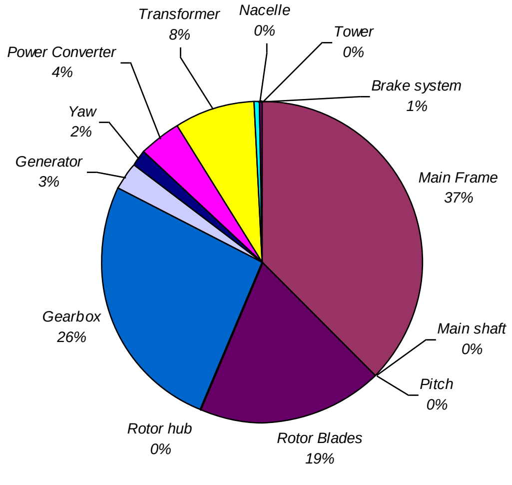

Figure 2.7: Normalised frequency of failure with turbine cost component contribution

The cost of a component and its propensity for failure represents only one part of the problem. Some components are easier to replace than others. Components such as generators may well be off-the-shelf resulting in a swift turnaround upon failure. However, blades are less likely to be off-the shelf components. In addition to the complicated logistics of replacement, blade suppliers are likely to be located at some considerable distance from the wind farm site, having implications in terms of downtime. Figure 2.8 illustrates rotor blades contributing towards the greatest loss of revenue for a single component fail. Thus, the components with potentially the greatest effect on operational costs are the generator, gearbox and rotor blades.

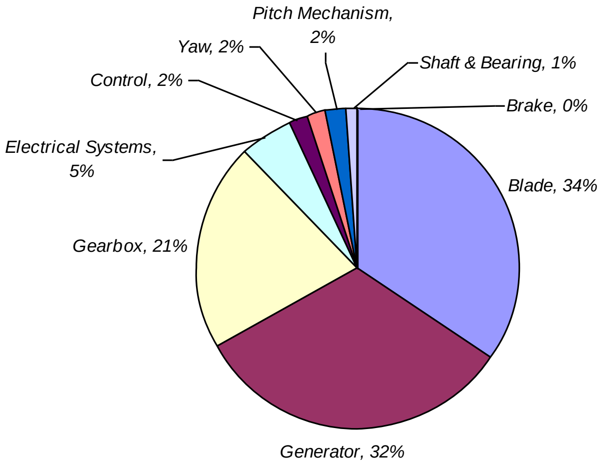

Figure 2.8: Downtime due to component failure, [38]

A study of 1500 250 MW wind turbines over a period of 15 years was conducted by Hahn *et al,* [44]. The component annual failure frequency was considered against downtime, Figure 2.9. Whilst the Electrical System is observed to have a high annual failure frequency, the downtime is just over a day. Conversely, the statistics for the Generator reveal a typically high downtime of 7 days but is accompanied by a comparatively small failure rate. Rotor blades, by contrast, have a significant annual failure rate of approximately 0.2 with a typical downtime of 4 days.

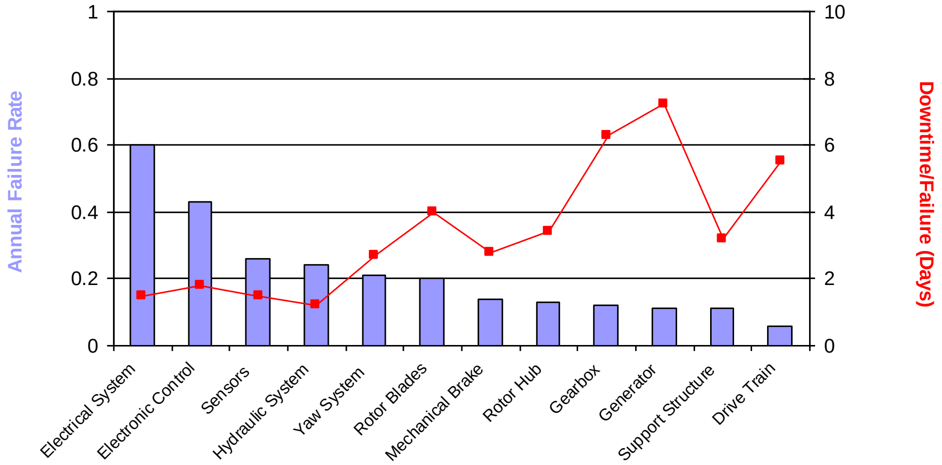

Figure 2.9: Turbine component reliability - 1500, 250 MW wind turbines over a period of 15 years, [44]

In 2010, CP-Max reported on an assessment of 2000 turbine blades, Figure 2.10. Statistically evaluated into 5 different damage categories, it revealed the presence of structural damage in more than one third of the tested blades.

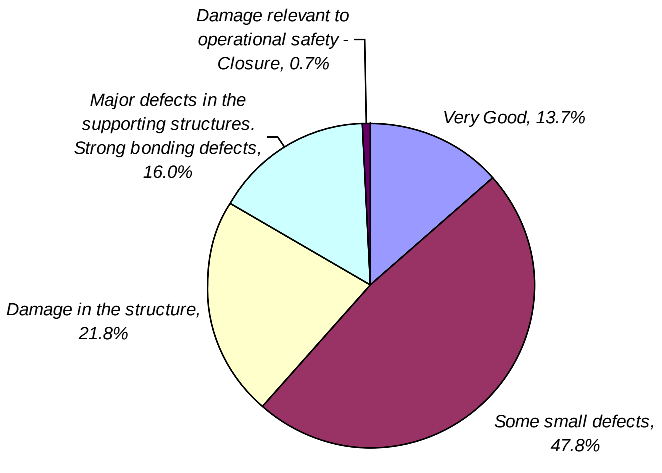

Figure 2.10: Assessment of 2000 blades categorised in terms of level of damage, [45]

Predictably, offshore structures experience extreme environmental conditions. The aerodynamic load and response create a complex dynamic system exposed to two different, yet correlated, environmental loads: aerodynamic (rotor/nacelle, tower) and hydrodynamic (substructure and support). To ensure a suitable level of robustness, the industry has created a deterministic set of conditions to simulate the behaviour of the turbine under extreme conditions. Ideally, the design should be based on the long term distribution of extreme response values with a return period of 50 years - known as the '50-year gust', [46]. To weather such extreme conditions, additional materials are utilised within the turbine structure that is unnecessary for the majority of its life-cycle. Thus, the wind turbine requires large generators and strong gearboxes which are typically under utilised during normal conditions. Much of the turbine's capacity is therefore idle during its lifetime ensuring electrical infrastructure costs of offshore wind farms are greater than that of similarly productive fossil fuel power-plants (which may be recovered over time since associated O&M costs for wind farms are lower). Figure 2.11 provides a comparison of cost breakdown for typical onshore and offshore wind turbines.

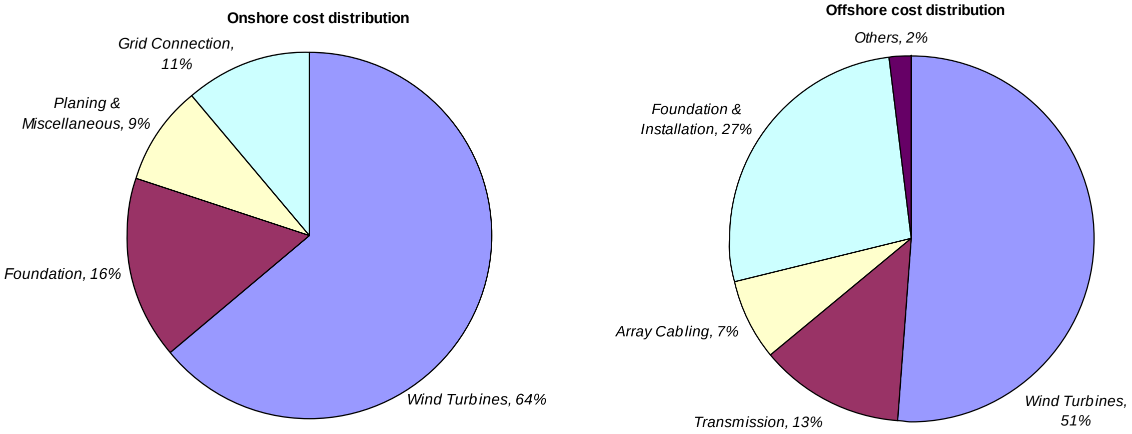

Figure 2.11: Capital cost breakdown for typical onshore and offshore wind turbines, [42]

The cost of foundation and installation is shown to be approximately two thirds greater for offshore applications. Site parameters such as water depth, wave heights and soil conditions have a significant influence on the support structure which requires site specific designs.

Designed to operate autonomously with control and safety systems, wind turbine failure compromises economic projection. Failure may require subsea diving in high tide sites where operations are severely restricted resulting in long periods of downtime which will incur considerable costs to the utility company.

2.4 Identified Turbine Component for SHM

The preceding section reported three turbine components which regularly fail: gearbox, generator, and rotor blades. Component analysis involving either the generator or the gearbox would logically entail monitoring of bearings. Bearings eventually become unserviceable due to defects such as flaking, peeling, spalling, smearing, stepped wear, speckles and discolouration, indentations, chipping, cracking, rust & corrosion, seizing, fretting, electrical pitting, rolling path skewing, retainer damage, creeping and false brinnelling, [47]. Each of these defects produces unique acoustic features.

Furthermore, blade failure can arise due to a faulty brake mechanism or gearbox. The brake mechanism is designed to stop the turbine turning when the wind is at a level such that the turbine has to shut down for safety reasons. The gearbox is used to develop useful electricity from the turbine as it turns at relatively low revolutions. If either fails, the turbine revolves at speeds greater than normal, imposing loads on the blades well in excess of design. However, gearboxes and generators are already widely monitored using vibration sensors and strain gauges.

In addition to the gearbox and generator, OEMs have identified the rotor blade as a key area of interest. Data on rotor blade loss or failure is documented in Appendix A. Generally robust, there nonetheless exist identified key areas of weakness. Section 2.3 identified the rotor blade as:

- Having significant failure rate
- A major failure mode when factoring in contribution to cost of a turbine
- Incurring significant downtime period when identified as the failure source
- Exhibiting significant annual failure frequency with downtime implications

Rotor blades are primarily designed to withstand inherently complex operating load vibrations consisting of both stochastic and deterministic sources including aerodynamic forces, multi-axis wind shear, random turbulence, gravity load and gyroscopic forces, [48]. Early awareness of blade structure degradation and defect onset will lead to improved management and maintenance of wind turbines, minimising routine operational costs and mitigating against sudden failure. The costs of sudden failure exceed the cost of replacing a blade as additional damage may occur in the gear box and generator as well as in turbines which may be physically damaged by loose blades.

Consequently, structural health monitoring of rotor blades is the focus of the work reported within the thesis.

2.5 Benefit to Industry

The purpose of an installed NDT system for turbine blades is to reduce long-term O&M costs for utility companies by minimising downtime precipitated by the onset of defects. Currently, a standard condition monitoring technique satisfactory to OEMs to perform routine autonomous inspection and provide details of blade integrity is unavailable. The present technique for supplying the end-user with information - visual inspection – is relatively slow and expensive. Currently, the industry deploys hands-on-action as deemed necessary – usually long before a critical failure occurs. The aim is to confine repairs to straight-forward up-tower repairs to prevent costly down-tower serious repairs that may require extended shutdowns accompanied with costly crane-callouts involving outlays of $50,000- $400,000 or more, [49].

There are a variety of reasons for the delay in standard implementation of a condition monitoring system, for example: the complicated nature of wind turbines; the remoteness of their installations; and the random nature of the industry's early years. However, the remote locations of wind farm sites provide a strong argument for structural monitoring.

There are two ways in which condition monitoring systems can be brought to the market:-

- As a factory-installed system controlled by the OEM
  - Downside is that it permits the OEM to control the data and hide flawed equipment
  - Negotiation process required on behalf of the buyer at the contractual stage
- Retro-fitting the system onto ageing turbines
  - May not be possible whilst the turbine is under warranty
  - Upon full end-user ownership of turbine operation, considerable scope for mass implementation

Statistics indicate that large numbers of wind turbines will come out of warranty within the next couple of years, [49]. Costs will then automatically transfer to the owners (i.e. utility companies). The suggestion being when the burden of repair costs becomes apparent to end-users, mass implementation of condition monitoring will to take place.

With progressively deteriorating operational efficiency implied within the advanced stages of a turbine’s natural life-cycle, proponents of NDT technology may be well-placed to exploit the approaching cycle of maturity set to occur within the wind industry.

Caution must be applied when considering the perceived viability of retro-fit NDT systems: typically locked into a 20-year balance sheet derived from an up front power purchase agreement, return on investment may not be so easy to prove. Consequently, it is difficult to warrant retrofit of existing installations unless an identified turbine platform exhibits specific and serious problems. From an executive standpoint, a £5000 system that detects 50% of all defects in the field may prove to be a more attractive proposition than a £20,000 system which detects 80% of all failures. The cost of detection has to be traded against failure detection yield. Typically, there is a tipping-point beyond which failure detection costs become prohibitive. Such a point may be identified by an Acceptance Criteria which can determine the defect types leading to structural failure. Defined within these criteria are flaw types, size and typical location.

However, postulating the cost-benefits of condition monitoring systems to end-users carries a risk: a detected failing component resulting in the replacement of a turbine blade ultimately saved no money - the blade still had to be replaced.

2.6 Conclusions

This chapter has discussed how renewable energy is contributing to the changing nature of the UK energy sector. According to statistics by the DECC, the total installed capacity for both onshore and offshore wind energy has increased significantly. With 40% of Europe’s entire wind resource, there remains considerable potential for further onshore and offshore wind development.

The cost of wind power generation is difficult to accurately ascertain. Currently, offshore wind energy is a more expensive enterprise than on-shore wind energy. With the increase in turbine size and number, comes an increase in O&M costs. As a result, there is a drive to lower O&M costs - achieved by identifying component cost which is dependent upon implications of turbine downtime arising from component failure. Such analysis revealed that monitoring of the turbine rotor blade may significantly reduce operational costs for the industry. The cost associated with sudden failure usually extends beyond blade damage since additional damage may be incurred elsewhere in the drive train.

3 Blade Mechanics, Failure & Candidate Inspection Techniques

3.1 Overview

This Chapter reviews the structural aspects of wind turbine rotor blade design. Consideration is given to the composite materials used and associated lay-up. Compromised structural integrity can arise at the design, manufacture or component integrating stages. Geometric areas where regular structural problems have been reported by OEMs and utility companies are described together with the accompanying defect type.

Once the weaker areas of the blade have been ascertained, techniques for monitoring blade integrity are considered whereupon a suitable method for defect detection is identified. An overview is provided of the NDT methods available and their likely efficacy for the blade component and its environment.

Once an appropriate method for defect detection has been selected, the transduction technique best suited to couple stress data from blade component materials is discussed. Configuration of the selected transduction technique is considered together with issues concerning satisfactory data acquisition.

3.2 Wind Turbine Rotor Blade

The turbine rotor blade is typically a composite structure. The properties of composites can be tailored to allow for efficient structural design. A typically layered composite will comprise several fibre layers (lamina) of different fibre orientation, known as a laminate. Each lamina comprises a strong fibrous material (e.g. glass fibre reinforced plastic – GFRP) suspended in a stabilising thermoplastic matrix (e.g. epoxy, acrylic or phenolic), Figure 3.1. The layered laminate can then be used to surround a lightweight core material (e.g. balsa wood; foam) making a sandwich structure. The composite is then moulded into the desired blade shape via a detailed manufacturing process.

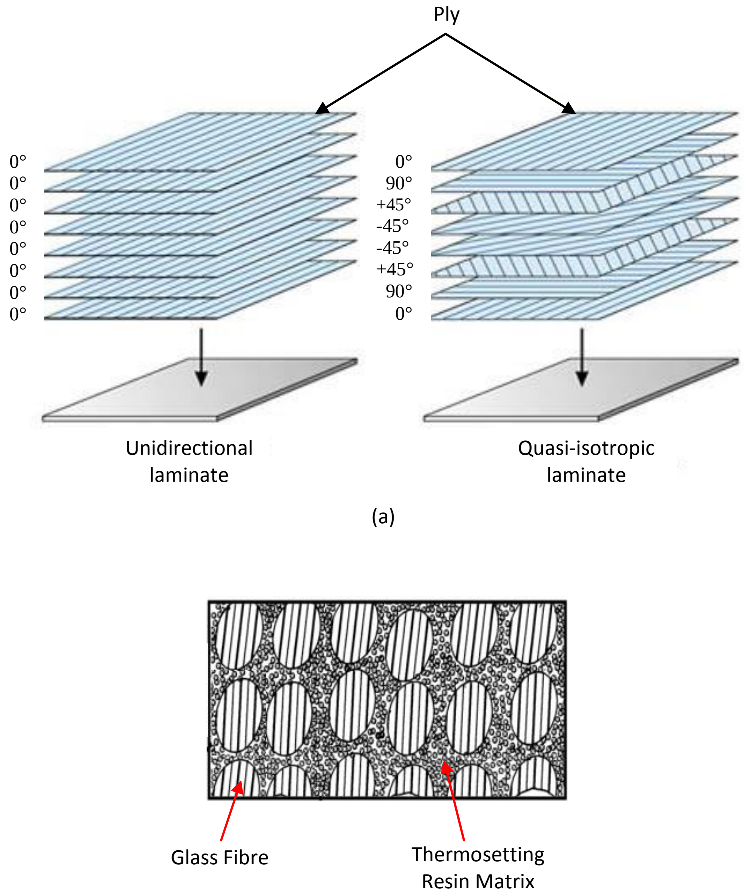

(a)

(b)

Figure 3.1: Layered composite, (a); Glass fibre suspended in resin, (b), [50]

Rotor blades are manufactured to many different specifications. There is no one uniform method of design and manufacture across the industry, suggesting that an optimum blade design has not yet been agreed for a known application (e.g. blade length; tower height above sea-level; distance from shore). Figure 3.2 details considerations for blade production.

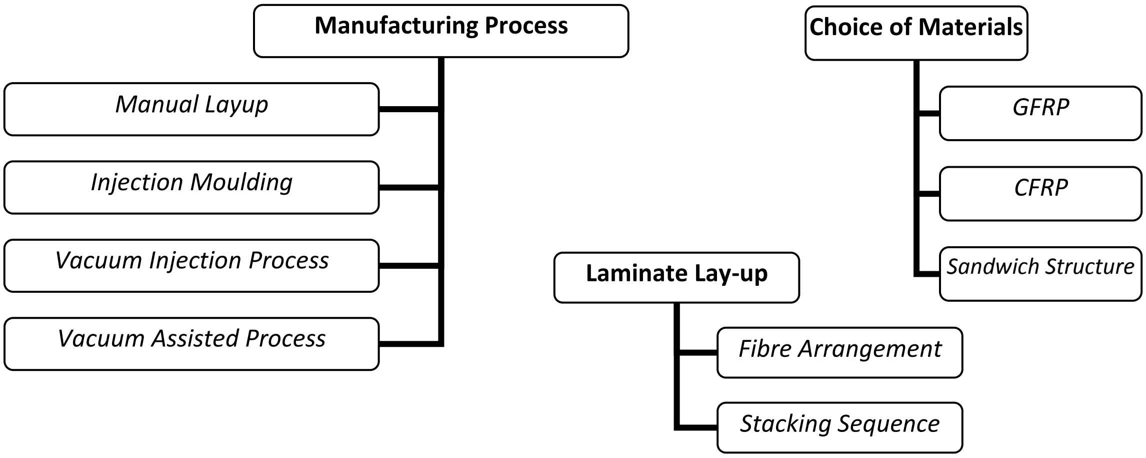

Figure 3.2: Blade production considerations, [51]

The choice of manufacturing process and material selection is often predetermined by the blade specification: blade length; rated power; rated speed; design wind class. The structural characteristics of the blade - mechanical characteristics - are dependent upon the inner blade design. To achieve overall control of the mechanical characteristic, precise management of the manufacturing process of various components comprising the blade is required. Design variables such as layer thickness, lamina orientation and material type can be optimised for structural performance.

3.2.1 Blade Construction

For quality control purposes, large OEMs typically use pre-impregnated glass fibre (pre-preg) – a sheet of glass fibre uniformly impregnated with a resin-catalyst mix which can be activated by heat. The process allows good alignment of the fibres in unidirectional layers. The resultant material is then conformable for lay-up work which can be cured by heat and pressure. Large blade manufacturers can typically construct a 40 m rotor-blade in 16 hours. The blade production steps are detailed in Table 3.1.

Table 3.1: Blade manufacturing – process flow, [52]

Process	**Step**
Preproduction	Pre-preg layers cut to size Adhesive mixing
Prefab production	Root insert Spar cap + Shear web / Spar box Bottom shell Top Shell
Moulding	Surface coat application Preform assembly Vacuum bagging Curing Cooling Demoulding
Dry Finishing	Root drilling Surface finish Painting Balancing

The completed product is shown in Figure 3.3 comprising the root section, the aerodynamic frame and the load bearing spar cap.

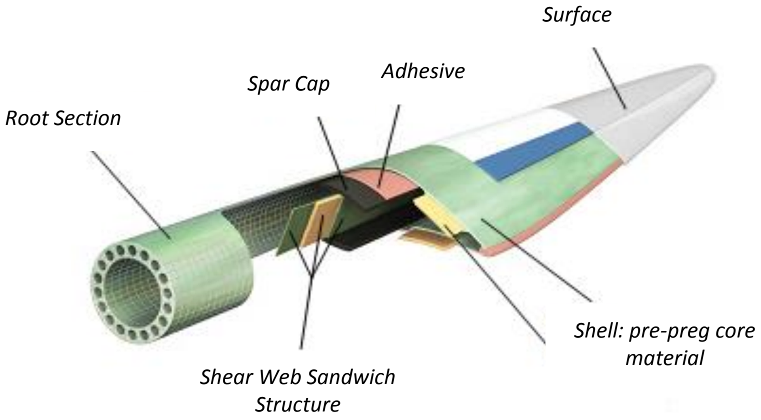

Figure 3.3: Sections of a wind turbine blade, [53]

The internal blade structure may feature one of a number of configurations. Figure 3.4 illustrates blade cross sections with varying design features.

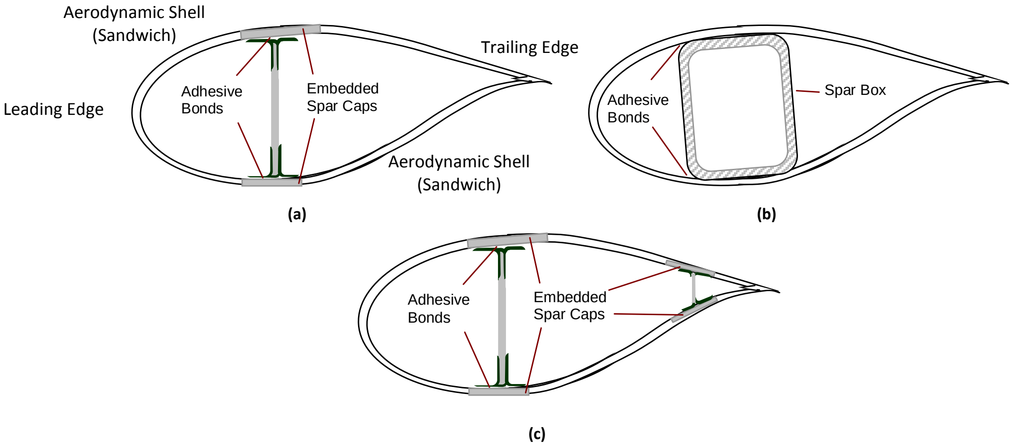

Figure 3.4: Typical Rotor Blade cross-sections: shear web with embedded spar caps (a); spar box (b); double shear-web design (c).

All designs feature a strengthening member for added support spanning near full length of the blade (recessed from the blade root extending towards the blade tip).

Considering the shear web arrangement in Figure 3.4(a), a single vertical stiffener between the two half-shells is attached to spar-caps typically embedded within the inner blade shell.

The spar-cap (placed along the central axis of the blade on both inner shells) acts as the back-bone of the blade. Its thickness varies over the blade length to balance the flap-wise torque, Figure 3.5.

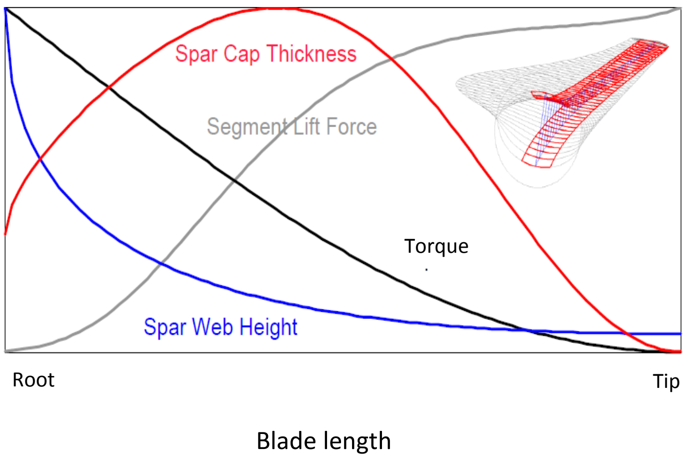

Figure 3.5: Change in spar thickness along length of blade, [54]

3.2.2 Blade Failure Modes

Deficiencies in the blade design may lead to on-site failure. Control over the manufacturing process will result in fewer outages and greater cost efficiency for the end-user.

The causes of on-site turbine blade failure can be attributed to any one or a combination of the factors, Figure 3.6.

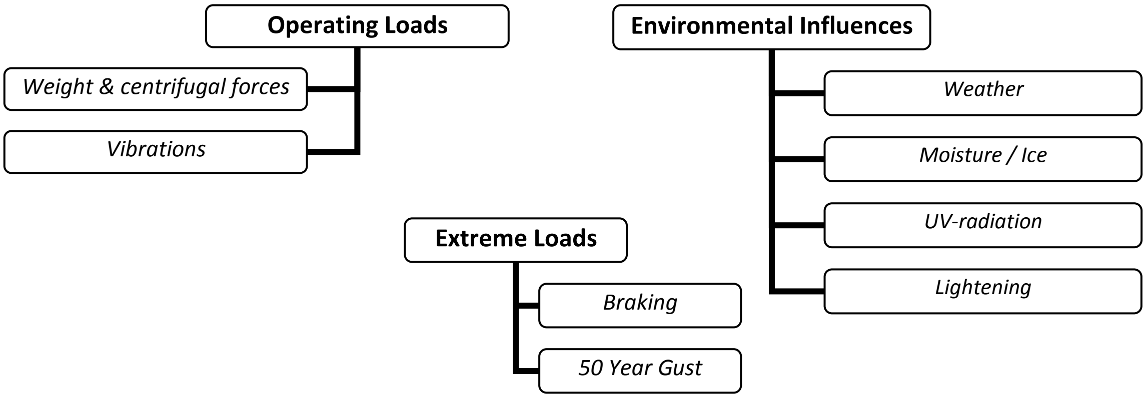

Figure 3.6: Causes of on-site turbine blade failure

The cost of repair (occasionally factored in as part of the commissioning schedule) is significantly higher on-site due to potential equipment hire and additional labour costs to cover travel and accommodation (costs are appreciably more for off-shore wind farms). Furthermore, where a contractual commitment to deliver power exists, an imposed penalty on the utility company for failure of delivery may potentially be passed onto the turbine manufacturers. It is, therefore, desirable for the blade producer to optimise the manufacturing process where possible and detect defects - when they occur - at a suitably an early stage.

However, even when the manufacturing process has been optimised, defects introduced at the commissioning stage can subsequently compromise the on-site operational performance of the blade.

Damage during transportation is not uncommon, particularly for onshore wind turbine blades where the site of the wind farm is usually remote with limited access. Often, repairs have to be performed on the blade on site prior to mounting of the blade onto the rotor hub. These repairs, conducted in an uncontrolled environment, may not be of the highest quality.

Figure 3.7: Crane support as rotor hub is lifted into position; internal blade damage & repair (right)

Figure 3.7 shows internal repair of a spar box within a 25 m blade during a visit to Tangy Hill wind farm in Kilkenzie. The blade is supported prior to being attached to the rotor hub whereupon a second crane is utilised providing evenly distributed support as the rotor hub is manoeuvred into position on the nacelle. As observed, there is significant scope for further damage to each of the blades during this procedure – damage which may subsequently go unobserved.

In addition, blade performance may be compromised due to the existence of internal defects within any of the components which comprise the blade. For example, one critical area is the large bonding area between the spar cap and shear web flange. Just as critical is the bond between the upper and lower halves of the blade shell at the leading and trailing edges, Figure 3.8.

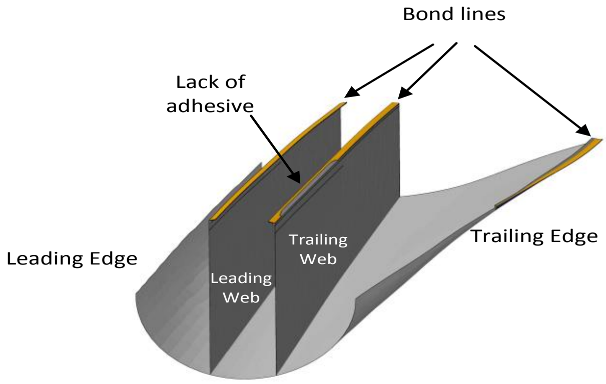

Figure 3.8: Bond lines connecting one half of a blade to the other, [54]

If insufficient adhesive is applied, disbond between blade-components is likely to occur. Conversely, if excessive adhesive is applied at the join, it may squeeze out into the blade interior, solidify, potentially detach where it is then free to cause internal damage. One possible consequence is blockage of the drain-holes at the tip of the blade where retention of excess moisture can lead to corrosion. Adhesive join failure is just one failure mode. Other modes of failure are detailed in Table 3.2

Table 3.2: Typical failure modes, associated damage modes and occurrence within blade, [45]

Structural Failure Mode	***Blade Location***	***Damage Mode***
Adhesive Joint Failure / Disbond	Leading- and trailing edges Main spar joint	Crack in adhesive layer Laminate/adhesive interface cracking
Sandwich face/core delamination	Skins Webs in main spar	Interface cracking
Laminate failure	Skins Main spar	Tensile failure Compressive failure Shear failure Crack (parallel to fibre) Delamination
Gelcoat/skin delamination	Upwind/downwind skins	Interface cracking
Gelcoat cracking	Upwind/downwind skins	Thin film cracking

The damage modes listed in Table 3.2 arise from deficient manufacturing processes. Images of a few defect types are shown in Figure 3.9

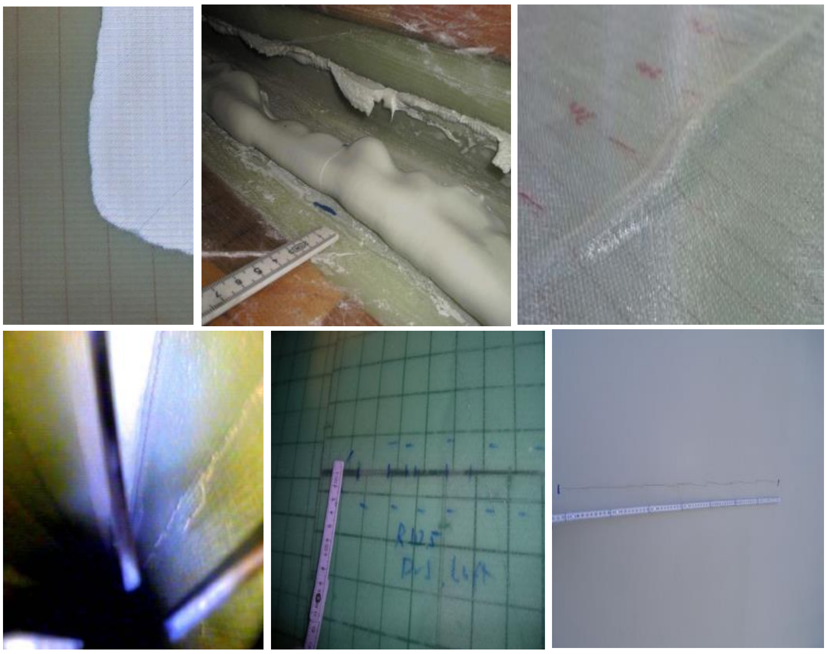

Figure 3.9: Some defects arising from uncontrolled manufacturing processes: void arising from poor infusion (top left); excess bonding resin (top middle); fibre-wrinkling (top right); crack in shear web (bottom left); fibre discontinuity (bottom middle); cracking arising from discontinuity (bottom right), [45]

The basis for the damage modes listed in Table 3.2 (and illustrated in Figure 3.9) is identified as follows, [55, 56, 57, 58]:

- Incompletely cured matrix due to incorrect curing cycle or defective material
- Incorrect fibre volume fraction due to excess or insufficient resin - variations will typically occur but large departures from specifications result from uncontrolled manufacturing processes
- Voids due to improper debulking, volatile resin components or air not properly controlled during cure
- Foreign bodies
- Fibre misalignment, causing local changes in volume fraction by preventing ideal packing of fibres

- Ply misalignment - as a result of mistakes made in lay-up of the component plies altering overall stiffness and strength of the laminate and may cause bending during cure
- ‘Wavy’ fibres, produced by in-plane kinking of the fibres in a ply which can seriously affect laminate strength
- Ply cracking - thermally induced cracks due to differential contraction of the plies after cure; cracks due discontinuity within the design
- Delamination - rare during the manufacture of the basic material but may be produced by contamination during lay-up or by machining
- Fibre defects - present in fibres as supplied; they are always likely to be present and must be considered as one of the basic material properties

These failure modes, upon occurrence, take place within the laminate material, GFRP. A flawless GFRP sandwich composite material - commonly located at the shear web and the aerodynamic shell (Figure 3.3) - provides added strength and stiffness to the structural panel. A high stiffness to weight ratio is created by separating the GFRP laminate to sandwich a light core material, [59]. However, a further failure mode is possible when disbond occurs between the core material and the GFRP laminate at the adhesive join (cracking within the bond-line). Impact of a sandwich structure typically results in delamination of the sandwich packing side of the laminate.

Defect sizes and their frequency of occurrence vary with a particular process cycle. All defect types are known to adversely affect performance in some respect during the lifecycle of the blade. However, to lengthen blade lifecycle (and avoid repairs on insignificant damage), a ‘mark & monitor’ programme is often implemented by utility companies to help lower O&M costs. Such an approach implies a certain level of damage-tolerance which can be considered upon understanding damage modes and their probable development.

However, some defects are more likely to occur than others. In practice, the most common manufacturing defect is the presence of voids. Some of the other defects (previously bulleted) rarely tend to occur or do not occur in isolation, [60]. For example, incorrect fibre volume due to insufficient resin within laminates will usually be accompanied by voids as will incorrectly cured resin. Other defects such as foreign bodies, delaminations and disbonds tend also to be detected together with the presence of voids. Void content influences the inter-laminar shear strength (ILSS) and can be estimated ultrasonically by measurement of attenuation; the reduction in wave amplitude on passing through a specimen. (Since a material with no voids will also suffer attenuation, some care must be taken when testing for the presence of voids).

Composite materials can be degraded in service by a number of mechanisms dependent upon the environment and the robustness of the materials used: impact; fatigue; overheating and creep. Although the mechanisms by which defects are initiated and develop are varied, only a small number of different types of defect result, [58]:

- Fracture or buckling of fibres
- Failure of the interface between the fibres and matrix
- Cracks
- Delaminations
- Bond failures
- Moisture ingress

Delamination due to fatigue or impact is one of the foremost in-service defects detected, [61]. It is possible to detect a high density of cracks as a precursor of delamination growth and this can be done ultrasonically, [62].

The presence of delamination or disbond (due to weakened adhesives) corresponds with a loss of transmitted wave energy.

Discussions with one leading blade manufacturer revealed they perform in-service inspections once every three months for both on- and off-shore turbines. These inspections are maintained because the strain gauges located within the blade have repeatedly failed to detect disbond between two materials. Consequently, the research contained within this thesis focuses upon identifying a non-destructive technique for the detection of defect onset within the spar-cap area of the blade.

3.3 Candidate Techniques for Defect Detection

Having identified the spar cap as the critical failure point, methods of monitoring these large bond areas within the wind turbine blade are considered. The physical change within a material arising from an event (such as loading, fatigue or impact) changes the material's characteristics. Typically, this will be accompanied by a sudden burst of released energy which can then be detected by sensors carefully positioned and sufficiently sensitive to identify structural change within its immediate vicinity.

SHM is defined as the non-destructive and continuous monitoring characteristics using an array of sensors related to the fitness of an engineered component as it operates, so as to diagnose the onset of anomalous structural behaviour. SHM involves measuring and evaluating the state properties and relating these to defined performance parameters, [63]. There are two aspects to SHM: damage diagnosis; and damage prognosis. The former refers to the identification of a particular type of damage (e.g. disbond), the latter refers to an estimation of the component's subsequent useful life, [64].

A number of techniques have been developed for defect detection in structural components. A summary of some of these techniques is presented now.

3.3.1 Modal Analysis

Modal analysis detects the reduction of material stiffness resulting from structural damage upon examining: Eigen-frequencies; mode shape and curvature; strain energy; flexibility; or damping characteristics, [14,65]. Global damage will result in a shift of Eigen-frequency or a change in frequency response function and mode shapes.

The advantages of this technique are that it is relatively simple and low cost, and is particularly effective for the detection of large damage in large structures. Disadvantages are that its global nature makes modal analysis insensitive to small damage or damage growth, is difficult to excite at high frequencies, requires a large number of measurement points, and is sensitive to boundary and environmental changes, [20]. Furthermore, it is not possible to measure modal shapes with the same accuracy as natural frequencies. Test errors in the range of 5–10% are typical, [66].

3.3.2 Electro-mechanical Impedance Analysis

A structure or system exhibits characteristic electro-mechanical impedance. The occurrence of damage or damage growth will typically modify the impedance at high frequencies. Electromechanical impedance (EMI) is a measure of opposition to the mechanical motion of an electrically excited piezoelectric element. Typically piezoelectric wafer active sensors (PWAS) facilitate SHM once affixed to the structure whereupon the electro-mechanical impedance is monitored, [67,68].

Advantages of this technique are the relatively low cost and simple implementation. However, the inability of this technique to detect defects distant from the sensors is a distinct disadvantage and would require a high sensor density to ensure appropriate coverage, [20]. Furthermore, EMI analysis tends to be a more accurate system for detection of large defects.

3.3.3 Static Damage Analysis

Static damage analysis refers to the study of damage models that does not consider growth or retardation of damage, [69]. Parameters for static measurements include strain or displacement within a component structure. The presence of damage produces localised element displacements and monitoring of strain will detect microscopic changes in the length of a component at pre-selected points.

The advantages of static damage analysis are: sensitive to localised defects; simple implementation; and cost effective, [70]. However, analysis of static parameters is relatively insensitive to undersized damage and the growth of defects. It does directly detect damage in a structure but simply monitors the change in displacement from a certain reference point, [20].

3.3.4 Dielectric Analysis

Dielectric analysis is used both for assessment of bonded structures and monitoring the changes that occur within the bond structure occurring due to the aging process, [71]. Two different approaches exist for dielectric analysis: low frequency measurements (0.001 – 60,000 Hz) on bonds where the two surfaces (e.g. blade and shear web) act as electrodes, the epoxy forms the dielectric medium; and high frequency measurements (30,000 – 2 x 10^{10} Hz) where reflection coefficients are evaluated using impedance measurements of the structure. Dielectric analysis can be used to monitor ingress of moisture into a joint structure where the ensuing chemical process produces a distinct dielectric signature. Researchers at the University of Strathclyde have concluded that structural factors dominate the overall dielectric response, [71]. Wave propagation in the adhesive bond is influenced by: thickness of the adhesive bond; the dielectric permittivity of the adhesive; water ingress as a consequence of exposure to atmospheric moisture resulting in the change of the dielectric permittivity; and the width of the joint structure.

3.3.5 Thermography

Thermography is an NDT technique that can highlight changes within a material via observation of temperature differences across a structure. Anomaly detection can be conducted to determine the onset of defects within a particular material. Typically, the test strategy requires an external source of energy to produce heat in the structure with the resulting heat transfer producing thermal energy that is propagated through radiation, producing a thermographic image. For appropriate assessment of composite structures, fibre direction, composite type, material thickness, emissivity/transmission and geometry must all be considered.

3.3.5.1 Infra-Red Thermography

Due to thermo-mechanical coupling, infrared thermography is able to provide a non-destructive, noncontact, and real-time test to monitor the physical processes within a material. Heat images are produced from the invisible radiant energy emitted from the monitored object at a distance without surface contact or influence of the actual surface temperature of the object viewed, [72]. There are two key classical active thermographic techniques:

- Optical – an external excitation by photographic flash (for heat stimulation) or halogen lamps (for periodic heating). Thermal waves propagate by conduction through the material whereupon any discontinuities will reflect thermal energy back toward the surface.

- Mechanical – internal excitation by system phenomena (e.g. loading) or surface-coupled transducer. Propagates energy in all directions and upon occurrence of a defect, dissipates energy as heat travelling to the surface by conduction.

Each technique is based on two excitation modes: lock-in thermography and pulsed thermography, which are optical techniques applied externally; and vibrothermography using pulsed or amplitude modulated ultrasonic waves to excite a material. Details of a material’s thermo-physical properties are visualized using thermal images (thermograms), spatial profiles and thermal contrast curves where any discontinuities due to the onset of defects will be indicated, [73].

3.3.5.2 NIR Imaging

Near Infra-Red (NIR) is a simple imaging technique which recovers reflected or transmitted radiation from a specimen using wavelengths between 700 nm and 900 nm. Photons do not interact with the material molecular structure in this wavelength range and therefore transmission through the material is dependent upon the thickness of the sample and intra specimen particle size. The material under analysis is placed between an energy source and typically a camera which provides greater sensitivity and resolution when compared with photodiodes.

For both IR thermography and NIR imaging, algorithms and statistical techniques are used to quantitatively assess the captured image data and provide information on the integrity of the structure under test.

Work conducted by researchers for the FP7 EC funded project, ComPair; for the promotion of composite materials within the European public transport sector, yielded results showing that NIR was a suitable method of defect detection for GFRP components, whereas IR thermography provided better image detection for defects on CFRP components, [73].

The disadvantage utilising either technique is that whilst in-situ monitoring can be carried out, it is not a continuous monitoring technique as it requires scheduled periods of down-time to be conducted.

3.3.6 Acoustic Techniques

When strain energy is suddenly released within a structure due to microstructural changes, the altered local stress field results in transient waves which produce audible sound. The energy to produce the stress waves originates from stored elastic energy that is redistributed, Figure 3.10.

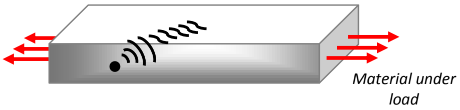

Figure 3.10: Microstructural change within the material resulting in propagating stress waves

No more than a fraction of this released energy is transformed into acoustic emission (AE), [74]. Acoustic NDT techniques can be divided into two subgroups: *Passive* and *Active*.

3.3.6.1 Passive Acoustic Testing

A variety of source mechanisms exist which give rise to localised transient signals. The passive technique detects the subsequent presence of a changed stress field accompanied with the onset of a defect. The structure-borne elastic activity produces an expanding wave-front from which detection of wave modes can be achieved when the released energy is sufficiently large.

3.3.6.2 Active Acoustic Testing

An ultrasonic signal launched into a specimen and subsequently interacts with the material and its geometry is considered an active acoustic approach. Two basic configurations are usually used in elastic-based damage detection: *Pitch-Catch* or *Pulse Echo.*

- Pitch-Catch employs multiple transducers: some are used to transmit a signal; some are only used to receive. The transmitted signal interacts with the material and the characteristics of the ‘convolved’ output, is interpreted accordingly.

- Pulse-Echo ultrasonic techniques are often employed in NDE where transducers are used to transmit a signal and are then switched to receive mode to detect any portion of the incident signal due to material geometry that may be reflected back along the incident path to the original transducer.

Both methods couple acoustic energy into or out of the medium monitored by the attached sensors. The complex signal comprises wave modes which can be identified and impart information regarding any changes that have occurred within the medium.

Acousto-Ultrasonics is an umbrella term covering both AE and Ultrasonics. AE originates from an internal source process within a material in the form of elastic waves detected at frequencies above 20 kHz, [75]. Ultrasonic Testing (UT) refers to the analysis of active or passively generated structural activity for a similar frequency range.

3.3.6.3 Ultrasonic Testing

If the elastic waves within a structure propagate at frequencies above 20 kHz, they can be detected using Ultrasonic Testing (UT). Ultrasound is a commonly used technique in NDE to detect the presence of defects. There are several categories of ultrasonic waves – termed *wave modes* – used in UT each possessing unique characteristics. A wave mode describes how energy propagates through a body of material and is defined typically, by their displacement characteristics (mode shape) at a particular frequency. The mode shape is determined by the particle motion generated by a wave mode and is described in terms of a Cartesian (x,y,z), cylindrical (r,ϑ,z), or spherical ($r,\vartheta,\emptyset$) coordinate system. Different structural geometries will support different wave modes at different frequencies.

All wave modes comprise a linear combination of longitudinal and transverse waves. Longitudinal waves (also known as Bulk or compression waves) describe pressure waves propagating through the material body where the particle displacement is oriented in the same direction as the travelling wave mode. For isotropic materials, the velocity of compression waves (c_l), for a specific material, is described by Equation (3.1).

$$c_l = \sqrt{\frac{E}{\rho}\frac{1-\upsilon}{(1+\upsilon)(1-2\upsilon)}} \tag{3.1}$$

Where, *E* is the Young's Modulus, ν is the Poisson's ratio and *ρ* is the density of the material.

Transverse waves (also known as Shear waves) describe particle displacement perpendicular to the direction of the pressure wave propagating through the material. For a specific material described by Equation (3.2) transverse waves propagate at a velocity (c_t).

$$c_t = \sqrt{\frac{G}{\rho}} \tag{3.2}$$

Where, G is the shear modulus and *ρ* is the density as before.

3.3.6.4 Rayleigh Waves

Rayleigh waves exist when there is a boundary between one medium and another. For a semi-infinite half-space, Rayleigh waves propagate along the boundary surface of a body. The greatest particle displacement exists on the surface with an exponential decay in particle displacement progressively deeper into the material body. Insignificant particle displacement occurs beyond a depth of one wavelength and as a result, the active depth of particle displacement is heavily frequency dependent. In addition to the wave mode velocity being sensitive to material parameters such as elastic wave properties, Poisson’s ratio, Young’s modulus, and density; each parameter is in turn sensitive to environmental conditions such as temperature. For this reason, Surface Acoustic Wave (SAW) sensors are used for a wide range of applications within the electronics and measurement fields.

3.3.6.5 Guided Waves

Guided waves are stress waves where the path of propagation is confined by the material boundaries of a specific structure. For example, the geometry of a plate is such that the two free and parallel surfaces guide the propagating waves in the plane of the plate. The structure of the waveguide will support distinct wave modes exhibiting different shapes, wavelengths, propagation velocities, and frequencies.

3.3.6.6 Acoustic Emission

AE is a condition monitoring NDT method which analyses the transient release of stored elastic energy occurring as a result of rapid localised changes in strain within a material due to a perturbation which is then communicated to the surrounding material by means of an expanding wave-front. The presence or growth of a defect can be evaluated by capturing these damage emitted acoustic waves. The frequency spectrum of interest is 25 kHz to 1 MHz.

Depending upon the material type and its application, potential sources may vary. Nevertheless, AE detects active sources under applied loads and therefore, is able to provide real-time information on flaw occurrence and development, i.e. AE detects active sources such as propagating damage. AE is a passive NDT technique. Unlike other NDT techniques where a generated signal is launched into a material and interrogated at some later point, AE is structure-borne activity. AE signals are not affected by environmental noise.

Other advantages include: greater sensitivity to defect activity; simple indicator as to defect presence; good trending parameters, [75].

However, detection of AE signals requires highly specialised sensors and signal processing techniques. Other disadvantages includes sensitivity to other ultrasonic sources (e.g. turbulence, crushing), insensitivity to minor imbalance or misalignment and the weakness of signal strength when compared with other techniques, [75].

In recent years, there have been significant developments within the AE field. The advanced capability of electronics, software, together with the computational speed of desktop and portable computers have resulted in OC housed AE boards capable of recording and analysing thousands of signals per second for high-speed applications.

AE sensors are piezoelectric transducers which are particularly sensitive to any surface movement of the material caused by the emission of elastic stress waves due to defect growth. Due to their sensitivity and robustness, Piezo-ceramics are most widely used. AE sensors can typically be embedded within the test material or attached to the material surface, however; appropriate mounting techniques must be employed to keep the sensors in place and maintain good acoustic coupling with the monitored materials.

The most common means of detection are described with respect to the method in which the sensor output is processed:

- Time Domain Analysis – faithful detection of the surface displacement at a particular point on the material is necessary.
- Frequency Domain Analysis – application of a Fast Fourier Transform (FFT), the signal can be analysed within the frequency domain. A broadband transducer will be able to detect the range of source dependent frequencies.

- Resonant Detection – narrowband transducers with a high mechanical Q to provide enhanced sensitivity. Outwith this range of frequencies sensitivity is low thus minimising the amplitude of out-of-band signals.

An airborne transducer technique was conducted by researchers at Cardiff University whereby an array of microphones were placed adjacent to a composite panel to detect fibre-failure and matrix cracking. Detection of surface strain measurements were successful validated using Short-Time Fourier Transform, [76].

Research has been conducted using AE as a method for defect detection in composites undergoing cyclic loading. Data analysis of signal amplitude levels and frequency content revealed that AE is capable of detecting barely visible impact damage in composite components under fatigue loading, [77].

There are, however; a number of limitations associated with AE detection. The Kaiser effect determines that material does not emit AE activity until the applied stress exceeds levels previously experienced, [75]. Therefore, if a defect is not being stressed, it will not be detected. AE results in complex signals and does not provide information on defect size, depth or orientation. Structurally insignificant flaws may, also, be detected.

3.3.6.7 Non-Linear Techniques

Non-linear acoustic techniques are used to detect micro-damage within a structure prior to the onset of structural fatigue. The micro-scale (10^{-3} m) would, for example, refer to individual grains within a fibre-reinforced composite laminate. These micro-failures eventually coalesce into macro-scale (10^{0} m) damage - detectable upon application of linear health monitoring techniques. The onset of cracks within a material, for example, will produce high levels of elastic nonlinearity characteristics thereby increasing the dissipation of propagating elastic waves, [78].

Several non-linear techniques have been developed:

- Nonlinear Elastic Wave Spectroscopy (NEWS) used to detect harmonic intermodulation arising from the onset of structural damage, [79]

- Vibro-Acoustic Modulation Technique (VAMT) utilising the changes in interaction between a continuous wave and impact signals and its correlation with crack size, [80]

- Non-Resonant Ultrasound Spectroscopy (NRUS) where the resonant frequency is analysed as a function of the excitation amplitude, [81]

- Slow Dynamics where a low amplitude swept frequency is applied close to the material resonant frequency to measure the resonant frequency deviation, [82]

Non-linear vibro-acoustic wave modulation has been successfully used to detect barely visible impact damage in composite plates instrumented with low-profile piezoceramic transducers for high-frequency ultrasonic excitation. Low-frequency modal excitation was achieved using an electromagnetic shaker. Scanning laser vibrometry was used to acquire data. Optimised results were observed when the ultrasonic excitation frequency corresponded with the damage resonant frequency, [83].

Most non-linear techniques require a low-frequency vibration signal for the purposes of modulation. Whilst the continuous rotation of the wind turbine blades would provide such a signal, the average rotational speed is between 15 - 30 revolutions per minute. The frequency component of such a signal (<1Hz) would require application of high precision signal processing techniques to ensure that the intermodulated components (arising from the onset of a defect) could be isolated from carrier components.

3.3.6.8 Lamb Waves

Lamb waves are a subset of Guided waves where the thickness of the material under analysis is comparable with the wavelength of the propagating elastic wave. Lamb wave modes propagate within plate-like geometries as a series of symmetric and antisymmetric modes. Particle displacement is initiated as bulk waves in the form of longitudinal and transverse waves, Figure 3.11.

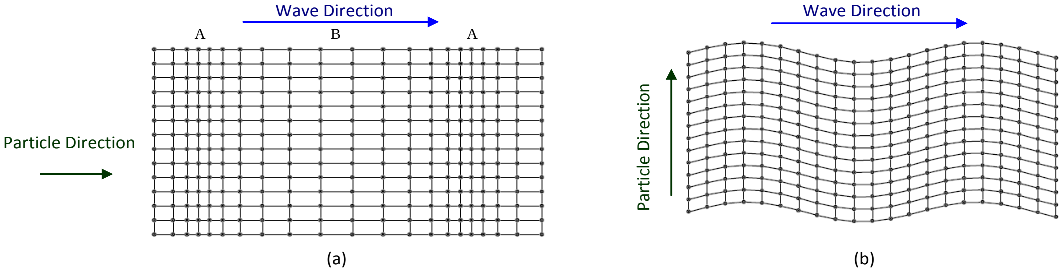

Figure 3.11: Longitudinal (a), and Transverse waves (b)

For longitudinal waves, the motion of particle displacement is in the same direction as the propagating sound wave. In Figure 3.11(a), 'A' denotes regions of compression where the density of the material is slightly larger, and 'B' denotes regions of rarefaction representing areas of decreased density. Figure 3.11 (b) illustrates a transverse or shear wave where particle displacement is perpendicular to the direction of the propagating wave. There are no regions of compression or rarefaction.

The propagation of bulk waves and its interactions with material boundaries induces mode conversion. To illustrate, Figure 3.12 shows simplified propagation between two media boundaries arising from the occurrence of a planar incident wave-front at the boundary between *Medium 1* and *Medium 2*. Below the first critical angle, three new waves are generated at the first boundary (*Medium*

1/Medium 2). A longitudinal wave is reflected back into the air at an equal but opposite angle to the incident wave. Refracted longitudinal and shear waves are generated within the solid and each of these waves in turn generates three more waves at the second boundary (*Medium 2/Medium 1*).

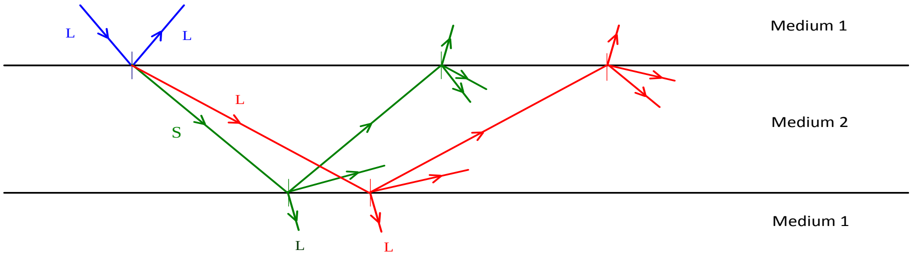

Figure 3.12: Longitudinal and transverse waves and their interaction with the material boundary, [86]

This process is repeated many times where after a particular point the interaction of longitudinal and transverse waves with the material boundaries creates a complex pattern of waves and mode conversion occurs. The resultant wave shapes appear as a series of symmetrical and antisymmetrical modes. Figure 3.13 shows the particle displacement for the fundamental symmetric mode, S_0, where a plane of symmetry is evident through the centre of the plate. Figure 3.14 shows the particle displacement for the fundamental antisymmetric mode, A_0, which features a plane of asymmetry through the centre instead.

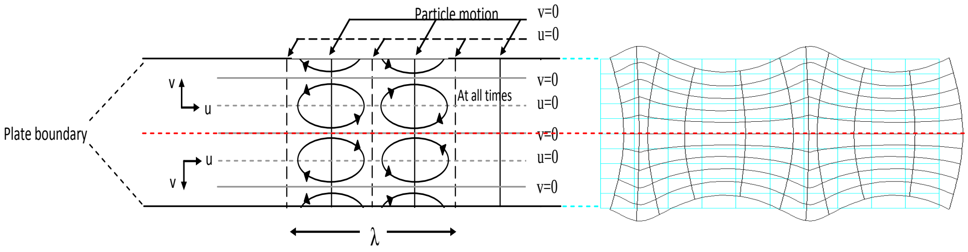

Figure 3.13: Fundamental symmetric Lamb mode, *S_0,* in a plate, showing particle motion through plate thickness, [84]

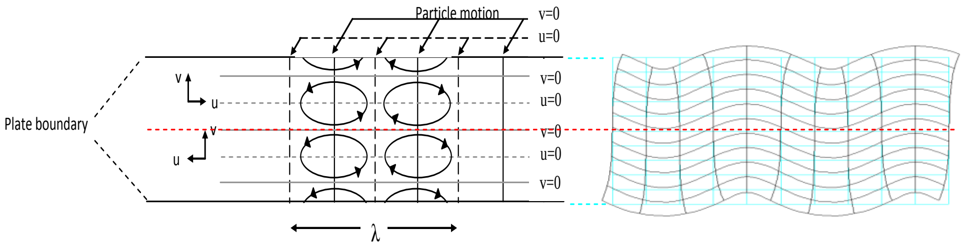

Figure 3.14: Fundamental antisymmetric Lamb mode, A_0, in a plate, showing particle motion through plate thickness, [84]

These waves are termed Lamb Waves and due to the interaction between the upper and lower surfaces of the plate, are forms of Guided waves. The fundamental modes (as highlighted in Figure 3.13 and Figure 3.14) are present for the full frequency bandwidth of a material. Taking aluminium as an example, at low frequency thicknesses there is an in-plane displacement component for the S_0 mode which is almost constant across the thickness of the plate, whilst the out-of-plane remains close to zero, Figure 3.15 (a). However as the frequency thickness increases, the in-plane displacement pattern becomes heavily concentrated at the centre of the plate and the out-of-plate component becomes dominant at the plate surface. For the A_0 mode at low-frequency thicknesses, the in-plane component features some displacement at the surface, whilst the out-of-plane component is almost constant. At higher frequency thickness values, the in-plane component displacement becomes more concentrated at the surface whilst the out-of-plane component displacement increases just below the surface of the material.

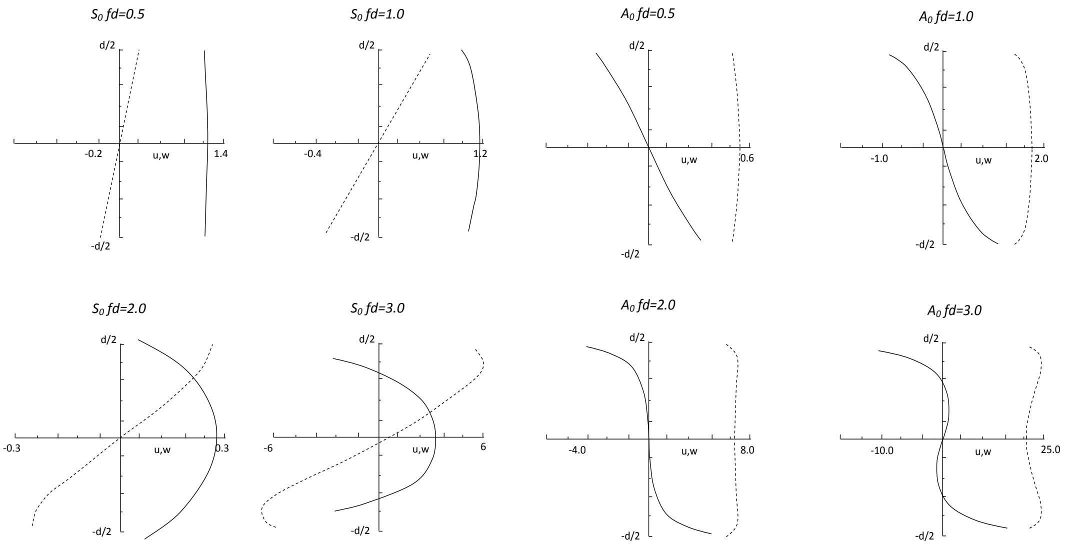

(a) (b)

Figure 3.15: Wave structure in aluminium for various points on: (a), S_0 mode; and (b), A_0 mode, [85]

Furthermore, with increasing frequency and plate thickness, additional modes appear which feature more complex displacement patterns. Because these higher order modes retain the symmetrical or asymmetrical wave characteristic about the central plane of the plate material, they also retain the nomenclature of the fundamental modes and are labelled A_m and S_m accordingly. Their complexity is indicated by their in-plane and out-of-plane displacement patterns. The progression of a wave through a material is known as the *phase velocity* while the envelope of the tone burst is the *group velocity*, Figure 3.16.

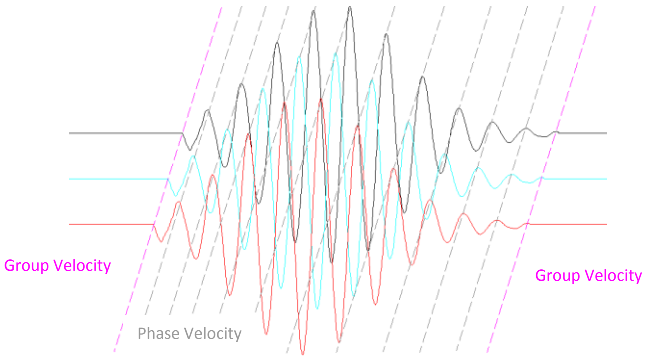

Figure 3.16: Wave phase and group velocity through a material

Waves may differ from one another by their phase and group velocities depending upon the material thickness, *d*, and the frequency, *f*, [75]. The relationship between the two velocities for a material of uniform thickness is presented in Equation (3.3).

$$c_g = \frac{c_p}{1-\left(\frac{f}{c_p}.\frac{dc_p}{df}\right)} \tag{3.3}$$

Where *f* denotes the frequency-thickness product, c_p is the phase velocity and c_g is the group velocity. The phase velocity is dependent upon frequency, an effect known as dispersion, but any particular frequency can propagate at a number of different velocities in one of a number of different modes. It may be observed that when the derivative of c_p with respect to *f* becomes zero, Equation (3.3) is reduced to $c_g = c_p$, indicating that the tone burst remains unaffected by dispersion.

The mode dispersion curves relating phase velocity to a frequency for a specific plate thickness is illustrated in Figure 3.17.

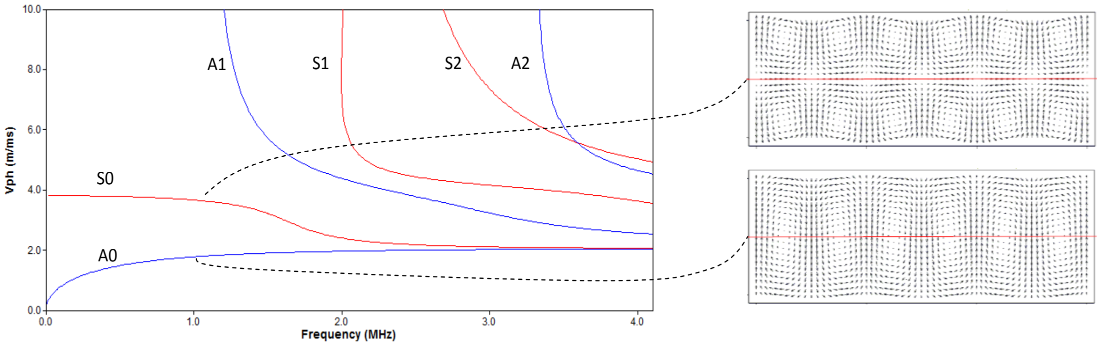

Figure 3.17: Relationship between frequency and phase velocity for symmetrical (S_n) and antisymmetrical (A_n) waves

It may be observed that the wave mode shape can vary as the *fd* product is increased. As the frequency increases for a particular plate thickness, the S_0 and A_0 modes tend towards one another. These two modes are present for the full signal bandwidth of the material. Of the two, it is observed that at low frequency-thickness values, the S_0 mode exhibits significantly less dispersion than the A_0 mode. As previously indicated by Figure 3.15, the symmetric mode comprises primarily in-plane displacement, but also features out-of plane displacement. Similarly, anti-symmetric modes comprise primarily out-of-plane displacements but also feature in-plane displacements, [85]. As a result of the dominant out-of-plane displacement orientation, the A_0 mode suffers higher attenuation than the S_0 mode due to particle energy leaking across the plate boundaries into the surrounding medium. All other modes have a cut-off frequency below which the mode does not propagate.

The dispersion curves plotted in Figure 3.17 are realised by attaining the real solutions of the Rayleigh-Lamb equations, Equation (3.4), [86].

$$\frac{tan\left[\bar{d}\sqrt{1-\zeta^2}\right]}{tan\left[\bar{d}\sqrt{\xi^2-\zeta^2}\right]} \pm \frac{4\zeta^2\sqrt{\xi^2-\zeta^2}\sqrt{1-\zeta^2}}{\left[2\zeta^2-1\right]^2} = 0 \tag{3.4}$$

Where, $\bar{d} = k_t d$, $\zeta = c_t/c$, $\xi = c_t/c_l$, k is the wave number, $c = \omega/k$, d is the plate thickness, ω is the frequency, c_t and c_l are the transverse and longitudinal velocities respectively. The positive and negative roots relate to symmetric and anti-symmetric Lamb wave modes respectively. Equation (3.4) presents the case for a single uniform isotropic plate where the influence of mechanical wave absorption and scattering may be neglected. The Lamb wave equations are analysed at length in Chapter 4.

3.3.6.9 Lamb Waves in Defective Plates

Due to their complex appearance, Lamb waves are typically employed in conjunction with signal processing techniques to establish differences in the wave signature against a baseline signal. A statistical approach is often necessary because Lamb waves are prone to contamination from the environment (ambient noise, temperature fluctuations) as well as structural variations (inhomogeneity, anisotropy).

A Lamb wave experiences two phenomena as it travels through a plate: material response process; and wave interaction process. The material response involves:

- Geometric attenuation due to beam spreading occurring in a plate as a circular wavefront and related to the wave amplitude by $A \propto \frac{1}{\sqrt{r}}$
- Material attenuation due to intrinsic energy absorption into the atomic lattice
- Dispersion due to changes in signal propagation velocity through a plate, subject to wave frequency
- Nonlinearity due to anisotropy

The wave interaction processes involve:

- Configurational attenuation due to the presence of boundaries
- Material scattering due to inhomogeneities and defects
- Doppler effect

The material responses are considered as the baseline characteristics. They are repeatable, predictable and may be considered as the material's signature response to a propagating Lamb wave. The wave interaction responses may be repeatable but are not predictable. Analysis such as baseline subtraction can reveal the presence of defects, their magnitude and location. It has been observed that upon transmission across a 7 mm defect in a composite laminate, 52% of the total energy is dissipated, [87].

To assess the reliability and accuracy of Lamb waves as a structural health monitoring method for the detection of defects within a plate material, knowledge of the signal response upon encountering a defect within a structure is required.

An investigation into Lamb wave sensitivity to different notch sizes within a steel plate was conducted by Alleyne and Cawley, [88]. A wideband ultrasonic immersion transducer was used to generate Lamb waves, captured by a receiving transducer and viewed on an oscilloscope. Results revealed the sensitivity of Lamb waves was dependent upon the frequency-thickness product, the wave mode and the geometry of the notch. Lamb waves were successfully detected for notches where the wavelength to notch depth ratio was of an order of 40. The Lamb waves were found to be insensitive to the notch width since their wavelengths were greater than the notch-width.

Lamb waves were investigated for estimation of wind turbine blade conditions using piezoelectric active sensing to identify incipient damage. The 13 mm piezo patches monitored 15 possible wave propagation paths (ranging in distance of 220 mm to 600 mm). Localised changes in boundary conditions were recorded by the sensor pair closest to the damage. The results demonstrated that whilst Lamb wave techniques were able to detect damage on or near the path of the propagating, for paths longer than 50 cm, the results were less promising due to the high damping properties of composite turbine blades, [89].

Increasingly, industrial applications include composite materials which are replacing metal alloys to lower the overall mass. Composites exhibit other advantages such as improved strength to better withstand stress, greater stiffness to resist material deflection, fatigue resistance to withstand vibration and loading, impact resistance to maintain strength against impact loads, thermal conductivity, and resistance to corrosion such as pitting, [90]. Composites are a structural material comprising two or more components that are combined at the macroscopic level. The composite materials used in wind turbine blades comprise reinforcing fibres of thin diameter embedded within an epoxy matrix. Their inherent anisotropy determines that Lamb wave velocity is dependent upon the direction of wave propagation.

In addition to directional-dependent velocity, beam steering and damping are also key considerations that limit mode selection and usable frequency bands, [91]. Lowe *et al*. investigated complications arising from steering of the propagating signal in an anisotropic plate due to damping and scattering by the fibres. These studies focused on in-plane fibres of the plate. The phase velocity in unidirectional carbon-fibre epoxy plate was found to vary significantly with the azimuth angle (ϕ) to the extent that the phase velocity of the S_0 mode along the fibres was approximately three times that of the phase velocity across the fibres. Consideration was given to the spatial nature of the signal source. PZT discs were aligned at 20° to the fibre and driven by a 50 kHz tone burst, detected by a laser 30, 35 and 40 cm from the source over a range of angles. The received signal amplitude did not correspond with 20° (as might be expected) but with a steering angle of -13°. Thus, it was observed that beam steering tends to steer the wave packet back towards the fibre-direction. In contrast, a point-source excitation generated Lamb waves radially where attenuation along a principal axis in a [0/90/+45/-45] symmetric cross-ply plate varied significantly for different modes and increased with rising frequency. A notable difference was observed between the A_0 mode and the S_0 mode. The fibres were a significant contributor of strain energy in the latter mode whereas strain energy in the former mode was influenced by the composite matrix and experienced viscoelastic damping.

The influence of dispersion on wave propagation within glass fibre reinforced plastic was investigated by Pierce *et al.,* [92]. Laser excitation was used to provide in- and out-of-plane displacement in the upper resin layer of a 3 mm thick plate. Application of a two dimensional fast Fourier transform (2DFFT) was used to resolve the A_0 mode. However, due to the effects of dispersion, the S_0 mode was not clearly resolved from adjacent higher order modes.

Signal processing techniques provide a significant function in resolving propagating wave modes within materials. Two such techniques are 2DFFT and Wavelet Transforms (WT). WT is applied to time-frequency data of transient waves propagating in media. Jeong and Jang analysed results from experiments conducted on quasi-isotropic and unidirectional graphite/epoxy laminates, [93]. It was found that WT using the Gabor wavelet was an effective tool for experimental analysis of composite materials. Numerical agreement was achieved using the Mindlin plate theory, [20].

The basis for calculating the fibre content of a composite plate is either given in term of mass, $M_f = m_f / m_c$, or volume, $V_f = v_f / v_c$. Where v_c and v_f are the volume of the composite and fibre; m_c and m_f are the mass of the composite and fibre. Considering volume, the relative fraction of fibres can significantly influence the propagating Lamb wave. For example, material stiffness, strength and hygrothermal properties of unidirectional lamina are a function of fibre volume fraction, [90]. The presence of voids within the material will also influence the fibre volume fraction.

Zak *et al.*, analysed a 1 m x 1 m x 1 mm unidirectional graphite-epoxy composite panel with free boundary conditions and volume fraction was 0.25, [94]. An excitation force was launched into the sample and the influence of the fibre orientation on the propagation of the in-plane and out-of-plane waves observed. Numerical calculations indicated that the velocities of the in-plane transverse and longitudinal waves were functions of both the volume fraction ratio and the direction of wave propagation.

3.3.7 Summary

Several acoustic testing techniques have thus far been discussed. However, it is the requirement of the proposed structural monitoring technique to offer adequate, cost-effective coverage using as few sensors as possible which at the same time are able to detect: existing defects; growing defects; severity. In addition, sensors must be light-weight. Lamb waves can propagate over long distances in plates; making them suitable for the examination of large cross-sectional areas where multiple wave modes may detect internal damage as well as surface damage. It has been evaluated that the ratio of the inspected plate area to the area of the circular transducer array can be 3000:1, [95]. Quantitative structural evaluation of plate damage can be achieved scrutinizing the scattered wave reflections. Damage classification is possible using modal analysis.

Lamb waves are highly sensitive to damage and appropriate signal processing techniques can be successfully used to locate the source of the defect. As an NDT approach, Lamb waves are cost-effective, fast and repeatable. Their scope for detection is illustrated in Figure 3.18 together against other NDT techniques.

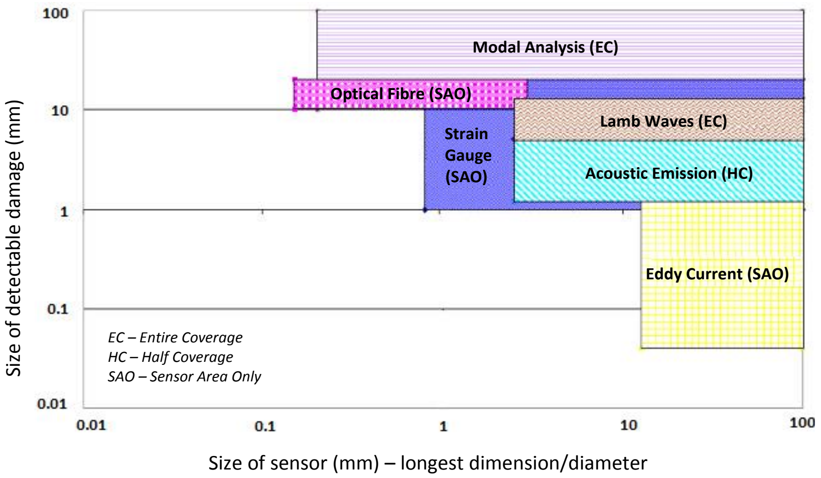

Figure 3.18: Comparison of Lamb wave detection with other methodologies, [20]

All techniques are capable of detecting damage and can be implemented with similar size sensors, however; modal analysis and Lamb wave techniques alone offer full surface coverage for a 1 m^2 plate. Whilst other methods, such as eddy currents, can offer better damage resolution, they are only capable of detecting damage directly below the sensor, increasing sensor volume, [96].

Having identified an appropriate NDT technique with the ability to monitor the structural integrity of large components such as is present within wind turbine rotor blades, a method for sensing the presence of Lamb waves is now considered.

3.4 Transduction

Ultrasonic transducers are used to convert electrical energy into mechanical energy for a transmitter; and to convert mechanical energy into electrical energy for a receiver. Transducers are complex systems and are a function of the manufacturing process. They are responsive to slight changes in construction resulting in different characteristic frequency and amplitude responses. For practical applications, directional sensitivity and bandwidth considerations must be addressed. The range of operational frequencies is also dependent upon application but typically falls between 20 kHz and 300 kHz.

There are number of different solutions for acoustic transduction, however; considerations such as material geometry, accessibility, and local environment will limit the available device options. Several device types are considered within the following sub-sections.

3.4.1 Piezoelectric Transducers

The piezoelectric effect produces a mechanical stress of a crystal structure. When an electric field (or mechanical stress) is applied a mechanical stress (or electric field) is recorded. An oscillating voltage creates an oscillating stress which produces propagating waves. There are few common piezoelectric crystals and typically ceramics such as Lead Zirconate Titanate (PZT) are used for industrial applications. Piezoeceramic transducers (typically disc-shaped) are robust, offer high sensitivity, low attenuation and are physically small in size which combine to produce a resonant response. A broad band response is achieved through application of damping materials to suppress natural resonance. Surface displacement is measured by direct contact of the transducer disc with the material under test. As such, any measurements will be modified to some extent by the mere physical presence of the transducer. This is an additional contributor of wave attenuation, however; due to the significant area of the material to be analysed, this effect is slight.

The stress generated due to piezoelectric excitation, created by an electric field is shown in Equation (3.5).

$$\sigma = K\varepsilon + eE \tag{3.5}$$

Where e is the piezoelectric coefficient, K an elastic constant, ε the deformation strain and E is the electric field. The gradient of the electric field is a source for propagating waves, [110].

For the purposes of frequency control and wave mode selection, transducers require directional sensitivity. A piezoelectric sensor can be configured as an interdigitated design using polyvinylidene fluoride (PVDF) polymer film to excite/detect a narrow bandwidth of frequencies, Figure 3.19. Signal generation/detection within this range of frequencies can produce/sense the desired Lamb wave mode, [97]. The device operates by applying an electrical potential between two parallel electrodes. To excite/detect a Lamb wave efficiently, several digits are placed one after another in an interdigitated pattern. In this way, the separately excited/detected waves reinforce one another giving rise to a suitably large acoustic signal. This is achieved by ensuring that a wave travels the distance between digits in exactly the time required for the signal to repeat itself; i.e. the digit spacing is precisely one wavelength.

Figure 3.19: Interdigitated transducer (IDT)

This arrangement makes the IDT conformable, flexible, able to couple to curved and flat surfaces.

3.4.2 Lasers

Lasers provide an approach for contactless activation and acquisition of Lamb waves, [98]. It is a flexible ultrasonic technique and can be used on complex geometries. In addition, laser sources can be configured for broadband or narrowband sensitivity to suit the required application.

Excitation by configuring the laser beam for the desired wave frequency and applying it to the material under test, results in predominantly in-plane wave propagation. Fabry-Pérot and Michelson interferometers are the devices typically used. The former is sensitive to changes in wavelength, whilst the latter responds to changes in phase.

Hutchens *et al.* have achieved some success performing experiments on the production of Lamb waves to image pseudo defects on plate aluminium sheets by tomography with the aid of a pulsed laser source and an Electromagnetic Acoustic Transducers (EMAT) detector, [99]. Although non-contact detection using laser interferometry is advantageous, it is a complex technique and has poor sensitivity compared with piezoceramics, [75]. Furthermore, laser equipment is typically large and relatively fragile and consequently is not typically a practical field solution for inspection.

3.4.3 Electromagnetic Acoustic Transducer

EMATs induce eddy currents into a conductive material. The eddy current creates a static magnetic field which produces a Lorentz force and results in radiated ultrasonic waves. The arrangement of the coil and the magnetic field can be optimized to provide frequency and wavelength control. Configured as a receiver, the inductive coil is used to detect eddy currents generated on the material surface by mechanical displacement within a magnetic field, [100]. The reciprocal nature of device operation means that EMATs can also be configured for transmission applications. Consequently, EMATS are suitable for the transmission/detection of a particular wave mode.

EMATs can be less sensitive to excitation and reception of ultrasonic activity than other devices. However, they are regularly used within the field and are robust in harsh environments. In addition, EMATs have the distinct advantage of operating without contact to the surface or the need of a liquid couplant. As a result, contamination of the sample is unlikely and the state of the material has less of an impact on the transducer, making it suitable for operation at elevated temperatures. One restriction for EMAT use is the material under test must be conductive. Other disadvantages include limited bandwidth and poor device sensitivity, [101].

3.4.4 Electrostatic Transducers

Analogous to the operation of capacitors, proximally close conductive plates will mechanically contract or expand upon application of a driving signal. Comprising a conducting back-plate and a polymer film (membrane) placed in contact with the back-plate, metalized on the non-contact face; electrostatic transducers operate upon application of a bias voltage which electrostatically draws the membrane against the back-plate. Good acoustic impedance matching with air ensures that when a driving signal is applied, the variation in electrostatic force causes the membrane to vibrate over the air pockets and induce acoustic energy into the air load, [102]. The nature of the applied voltage will determine the frequency of operation. Inverse operation, sensing variation in plate distance will result in an alternating voltage.

Castaings and Hosten wide-band electrostatic transducers were air-coupled to a unidirectional 16-ply glass-fibre plate, [103]. Clear detection of the A_0 mode was achieved and matched numerical analysis. The A_1 mode was detected only when it propagated normal to or parallel to the fibres, whilst the S_0 mode was strongly affected by material anisotropy and was detected only in the dispersive region (when there is considerable out-of-plane displacement).

Electrostatic transducers have a particular application in micro electromechanical systems (MEMs), [104].

3.4.5 Variable Reluctance Transducers

Variable reluctance transducers are magnetic field transducers. Suitably idealised, they are the counterpart to electrostatic transducers. Comprising an electromagnet separated into two parts by a narrow air gap, a magnetic field is created when a current flows through the windings causing an attractive force between the two poles of the magnet. One part of the magnet is attached to a moveable plate in contact with an acoustic medium. The other part is fixed. The magnetic reluctance varies as the moveable part vibrates, [104].

Although good for low frequency applications, the technology experiences increasing signal distortion at higher frequencies.

3.5 Conclusion

In this chapter, the structure of a wind turbine blade and its component parts was discussed. The method of blade manufacture is dependent upon blade length, rated power, rated speed and design wind class. Whilst power varies with the cube of the wind speed, a similar relationship exists between the blade length and blade mass. Composite materials (typically GFRP) are an attractive solution due to their enhanced strength and stiffness (better able to withstand loads) and their light weight which limits blade mass for larger turbines. Blade construction is achieved through a meticulous manufacturing process to achieve optimum design. The internal blade formation can vary to include a central shear web, a double shear web, or a spar-box arrangement – each to strengthen the blade under load conditions. However, OEMs and utility companies have reported regular disbond of the supporting member from the blade inner shell as a particular issue as well as delamination within the spar cap. Consequently, identification of a non-destructive technique for the detection of defect onset within the spar-cap area of the blade is an area for research, as this thesis testifies.

Whilst a number of NDT techniques may be applied for NDT inspection, there are two important requirements: the method of inspection must be continuous to lower the cost of maintenance checks for utility companies; and the sensors must have wide-coverage and be unobtrusive. Detection of emitted acoustic signals using piezoceramic transducers to sense guided Lamb waves satisfies both criteria. Lamb waves can propagate over long distances in plates making them suitable for the examination of large cross-sectional areas where multiple wave modes may detect internal damage as well as surface damage.

Piezoceramic sensors are robust, offer high sensitivity, low attenuation and are physically small in size. The combined fibre and matrix of composites ensures directional material characteristics where Lamb waves will propagate with lower attenuation when the direction of travel is parallel to fibre orientation. To achieve maximum sensitivity to stress waves, sensors should be configured to match the directionality, where possible, of the material being monitored. Interdigitated transducers (IDTs) provide directionality, conformability to non-flat surfaces; and frequency and wavelength control dependent upon spatial distribution of the piezo digits. Other material characteristics for consideration include fibre volume of the composite which influences the propagating wave velocity and the frequency thickness product also influences signal integrity. The two broadband wave modes, A_0 and S_0, have regions of dispersion where mode resolution by a sensor will be more challenging.

Frequency control of the received signal is therefore, an important parameter for coupling Lamb waves from the plate material. Post data-capture; signal processing techniques such as 2DFFT and WT can be applied to resolve the presence of individual propagating wave modes contributing to the acoustic disturbance.

Subsequently, the work reported within this thesis aims to detect the onset of defects at the GFRP spar cap structural support. The work focuses on the use of piezeceramic transducers to couple propagating Lamb waves from the composite component arising from a natural excitation due either to perturbation or structural loading. The acquired data will be processed via numerical analysis or application of a 2DFFT. The outcome will determine sensor distribution and resolution of defect size.

Having established the geometrical structure of the blade component material, the monitoring technique and the transduction process, consideration is now given to the underpinning theory.

4 Theory of Elastic Wave Propagation

4.1 Overview of Chapter

The previous chapter provided an overview of the methods available for non-destructive testing where it was concluded that Lamb wave propagation was an ideal method for structural health monitoring of wind turbine blades. To fully appreciate the characteristics of Lamb waves, it is important to understand the interaction between the forces of elastic deformation and inertia of the solid material to which a force has been applied. Different materials exhibit different characteristics. For example, a material is considered isotropic where the elastic stiffness constants are independent of direction. Alternatively, a material where the elastic stiffness constants vary with direction is considered anisotropic.

This chapter provides an overview of the generalised form of Hooke’s law. The inherent symmetry of anisotropic material (e.g. GFRP) leads to a discussion on the transformation of coordinate axes consistent with its characteristics (different from the symmetry axes of the material) where it is useful to write stress and strain tensors in the new reference frame.

Finally, the chapter concludes with a discussion on methods of excitation and how a change in active region can yield different results.

4.2 Mechanical wave propagation

Infinite solid materials support two fundamental acoustic propagation modes - longitudinal and transverse. With just one boundary, the configuration is considered to be a semi-infinite half-space body bounded by a different medium. In such an environment, Rayleigh waves can exist, Figure 4.1.

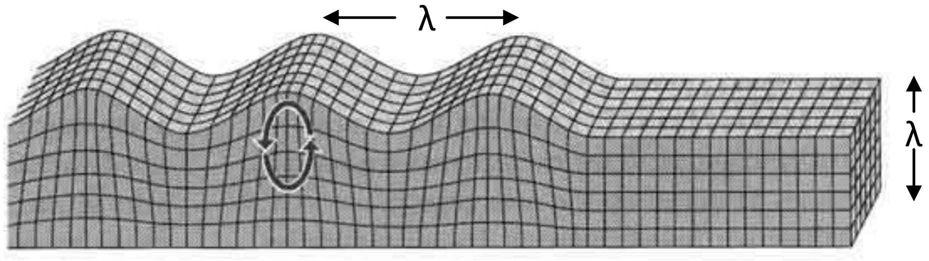

Figure 4.1: Propagating Rayleigh wave in a semi-infinite half space, [105]

Although displacement will occur through the half-space, it may be observed that there is very little particle oscillation at a depth of one wavelength. Introduction of additional boundaries will introduce the presence of other wave mode types. The geometry of the specimen under analysis will determine the number of propagating modes – each with a particular mode-shape and wavelength.

For materials with plate-like geometries (i.e. sample thickness is smaller than the propagating wavelength), the interaction of longitudinal and transverse waves with the boundaries produces mode conversion and energy is transferred into Lamb waves, Figure 4.2.

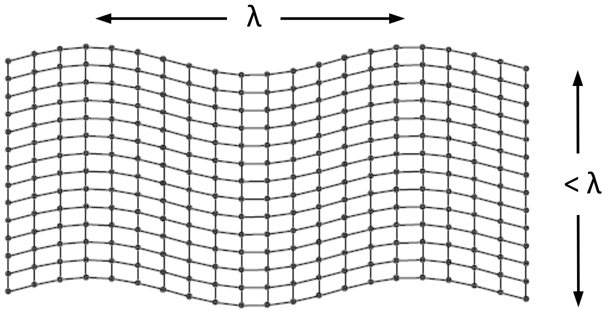

Figure 4.2: Propagating Lamb waves in a medium bounded at each surface by another medium

This chapter provides a review of relevant theory on the propagation of stress waves within plate-like materials as outlined by Viktorov [106], Auld [107], Kolsky [108] and Datta [109].

In a thin isotropic and homogenous plate-structure, Figure 4.3, the propagation of elastic waves is derived from knowledge of the stress-strain relationships and the equations of motion.

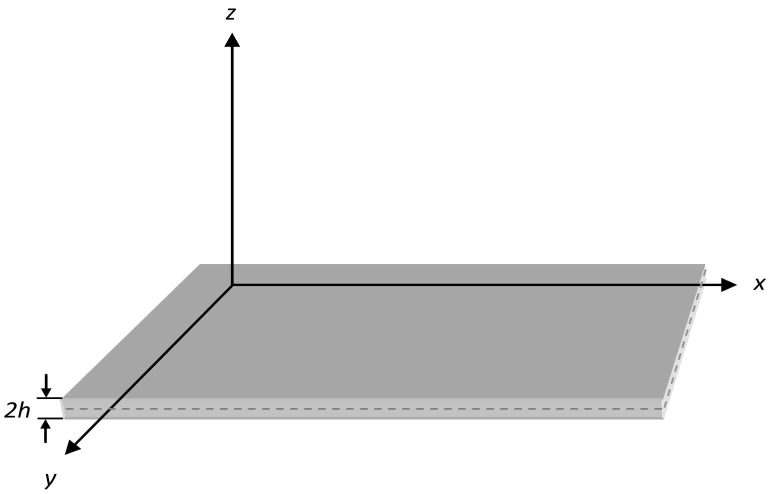

Figure 4.3: Plate material with 2h thickness

If the plate shown in Figure 4.3 is divided into cube elements, then each surface displacement is described by Equation (4.1).

$$\delta u_x = \frac{\partial u_x}{\partial x}\delta x + \frac{\partial u_x}{\partial y}\delta y + \frac{\partial u_x}{\partial z}\delta z$$

$$\delta u_y = \frac{\partial u_y}{\partial x}\delta x + \frac{\partial u_y}{\partial y}\delta y + \frac{\partial u_y}{\partial z}\delta z \quad \Rightarrow \quad \begin{bmatrix}\delta u_x \\ \delta u_y \\ \delta u_z\end{bmatrix} = \begin{bmatrix} \frac{\partial u_x}{\partial x} & \frac{\partial u_x}{\partial y} & \frac{\partial u_x}{\partial z} \\ \frac{\partial u_y}{\partial x} & \frac{\partial u_y}{\partial y} & \frac{\partial u_y}{\partial z} \\ \frac{\partial u_z}{\partial x} & \frac{\partial u_z}{\partial y} & \frac{\partial u_z}{\partial z} \end{bmatrix} \begin{bmatrix}\delta x \\ \delta y \\ \delta z\end{bmatrix} \qquad (4.1)$$

$$\delta u_z = \frac{\partial u_z}{\partial x}\delta x + \frac{\partial u_z}{\partial y}\delta y + \frac{\partial u_z}{\partial z}\delta z$$

The displacement vector, $\vec{q}$ defines the x-, y- and z-displacement components as illustrated in Figure 4.4.

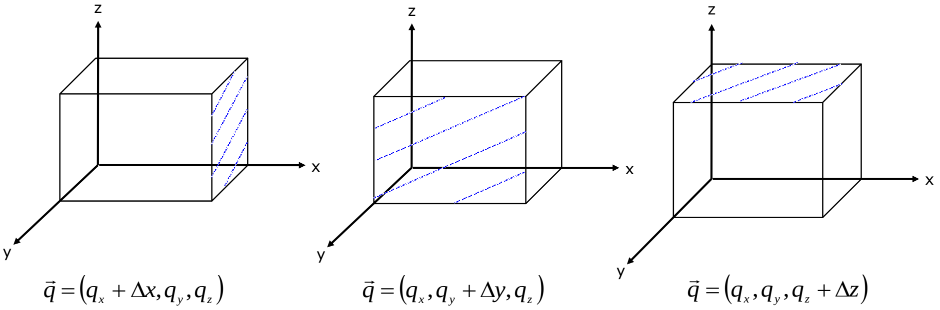

Figure 4.4: Displacement components

Which, in truncated form, is summarized by Equation (4.2)

$$[\delta u_i] = [\xi_{ij}][\delta i] \qquad i, j = x, y, z \qquad (4.2)$$

Where $[\xi_{ij}]$ is the displacement gradient matrix.

The partial derivative of (4.1) can be split into strain components defining longitudinal and shear displacement respectively, Equations (4.3) to (4.5).

$$\varepsilon_{xx} = \frac{\partial u_x}{\partial x} \qquad \varepsilon_{yy} = \frac{\partial u_y}{\partial y} \qquad \varepsilon_{zz} = \frac{\partial u_z}{\partial z}$$

$$\varepsilon_{xy} = \varepsilon_{yx} = \frac{1}{2}\left(\frac{\partial u_y}{\partial x} + \frac{\partial u_x}{\partial y}\right) \tag{4.3}$$

$$\varepsilon_{yz} = \varepsilon_{zy} = \frac{1}{2}\left(\frac{\partial u_z}{\partial y} + \frac{\partial u_y}{\partial z}\right) \tag{4.4}$$

$$\varepsilon_{zx} = \varepsilon_{xz} = \frac{1}{2}\left(\frac{\partial u_y}{\partial z} + \frac{\partial u_z}{\partial x}\right) \tag{4.5}$$

By separating the displacement gradient matrix into its symmetric and anti-symmetric parts, a physically simple relationship is observed between the strain matrix and the displacement gradient matrix, in the linear range, Equation (4.6).

$$[\xi] = \frac{1}{2}\left([\xi] + [\tilde{\xi}]\right) + \frac{1}{2}\left([\xi] - [\tilde{\xi}]\right) \tag{4.6}$$

Where $[\tilde{\xi}]$ represents the transpose of matrix $[\xi]$. For an isotropic plane in the y-axis direction where wave propagation occurs along a normal ($\hat{n}$) at an angle (α) to the x-axis in the x-z plane, its plane will lie along the y-axis, particle motion occurs in the x-z plane, Figure 4.5, [110]. There is no variation in the y-direction.

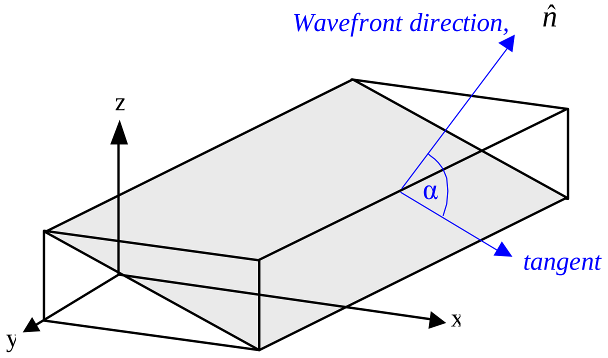

Figure 4.5: Isotropic propagation in the x-z plane

Longitudinal wave motion, described by a scalar potential $\varphi(x,z,t)$, is along the normal; and transverse wave motion, described by the vector potential, $\vec{A}_y(x,z,t)$ is along the tangent. Since there is no variation in the y-direction, components $\vec{A}_x$ and $\vec{A}_z$ are zero. The displacement vector field is then defined as the sum of a gradient and a curl: known as the Helmholtz theorem, Equation (4.7).

$$\vec{q} = \nabla\varphi + \nabla\times\vec{A}_Z \tag{4.7}$$

Hooke's law states that strain (ε) is linearly proportional to stress (σ). Considering an infinitesimal cubic element, the surface stress comprises a normal element and two tangential elements Figure 4.6.

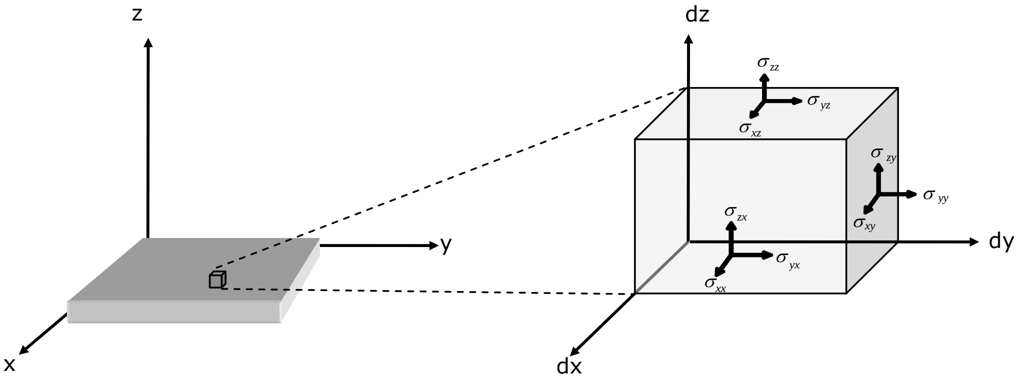

Figure 4.6: Infinitesimal cubic element

There are 9 stress components: $\sigma_{xx}, \sigma_{yx}, \sigma_{zx}, \sigma_{xy}, \sigma_{yy}, \sigma_{zy}, \sigma_{xz}, \sigma_{yz}, \sigma_{zz}$.

Where the first subscript denotes the axis normal to the surface upon which the stress is acting and the second subscript demotes the direction of the stress. If the cubic volume is sufficiently small such that any stress variation across a surface is negligible, the nine stress components can be reduced to six, i.e. $\sigma_{yx} = \sigma_{xy}$, $\sigma_{zy} = \sigma_{yz}$ and $\sigma_{xz} = \sigma_{zx}$.

The generalized form of Hooke's Law states that each of the 6 components of stress is a linear function of the 6 components of strain, thus related by 36 elastic stiffness constants, c_{ij}, Equations (4.8) to (4.13).

$$\sigma_{xx} = c_{11}\varepsilon_{xx} + c_{12}\varepsilon_{yy} + c_{13}\varepsilon_{zz} + c_{14}\varepsilon_{yz} + c_{15}\varepsilon_{zx} + c_{16}\varepsilon_{xy} \tag{4.8}$$

$$\sigma_{yy} = c_{21}\varepsilon_{xx} + c_{22}\varepsilon_{yy} + c_{23}\varepsilon_{zz} + c_{24}\varepsilon_{yz} + c_{25}\varepsilon_{zx} + c_{26}\varepsilon_{xy} \tag{4.9}$$

$$\sigma_{zz} = c_{31}\varepsilon_{xx} + c_{32}\varepsilon_{yy} + c_{33}\varepsilon_{zz} + c_{34}\varepsilon_{yz} + c_{35}\varepsilon_{zx} + c_{36}\varepsilon_{xy} \tag{4.10}$$

$$\sigma_{yz} = c_{41}\varepsilon_{xx} + c_{42}\varepsilon_{yy} + c_{43}\varepsilon_{zz} + c_{44}\varepsilon_{yz} + c_{45}\varepsilon_{zx} + c_{46}\varepsilon_{xy} \tag{4.11}$$

$$\sigma_{zx} = c_{51}\varepsilon_{xx} + c_{52}\varepsilon_{yy} + c_{53}\varepsilon_{zz} + c_{54}\varepsilon_{yz} + c_{55}\varepsilon_{zx} + c_{56}\varepsilon_{xy} \tag{4.12}$$

$$\sigma_{xy} = c_{61}\varepsilon_{xx} + c_{62}\varepsilon_{yy} + c_{63}\varepsilon_{zz} + c_{64}\varepsilon_{yz} + c_{65}\varepsilon_{zx} + c_{66}\varepsilon_{xy} \tag{4.13}$$

The fourth order tensor (c_{ij}) is an abbreviated notation for c_{xyxy} where $i, j = 9 - \left(x + y\right),\ 1 \leq x, y \leq 3$ and $x \neq y$. Symmetrically equivalent directions in a crystal have equivalent elastic properties. Love revealed that if the elastic energy is a single-valued function of the strain, a coefficient $c_{ij} = c_{ji}$, and the 36 elastic constants are reduced to 21 in matrix formation, [111], Equation (4.14).

$$\begin{bmatrix} \sigma_{xx} \\ \sigma_{yy} \\ \sigma_{zz} \\ \sigma_{yz} \\ \sigma_{zx} \\ \sigma_{xy} \end{bmatrix} = \begin{bmatrix} c_{11} + c_{12} + c_{13} + c_{14} + c_{15} + c_{16} \\ \qquad\qquad c_{22} + c_{23} + c_{24} + c_{25} + c_{26} \\ \qquad\qquad\qquad c_{33} + c_{34} + c_{35} + c_{36} \\ \qquad\qquad\qquad\qquad c_{44} + c_{45} + c_{46} \\ \qquad\qquad\qquad\qquad\qquad c_{55} + c_{56} \\ \qquad\qquad\qquad\qquad\qquad\qquad c_{66} \end{bmatrix} \begin{bmatrix} \varepsilon_{xx} \\ \varepsilon_{yy} \\ \varepsilon_{zz} \\ \varepsilon_{yz} \\ \varepsilon_{zx} \\ \varepsilon_{xy} \end{bmatrix} \tag{4.14}$$

However, symmetry systems within particular materials allow for further reduction of elastic constants. A material where the material properties are independent of orientation is considered isotropic. In such a material, only two constants are required to define the elastic properties and the elastic matrix reduces to Equation (4.15).

$$\begin{bmatrix} \sigma_{xx} \\ \sigma_{yy} \\ \sigma_{zz} \\ \sigma_{yz} \\ \sigma_{zx} \\ \sigma_{xy} \end{bmatrix} = \begin{bmatrix} (\lambda+2\mu) & \lambda & \lambda & 0 & 0 & 0 \\ & (\lambda+2\mu) & \lambda & 0 & 0 & 0 \\ & & (\lambda+2\mu) & 0 & 0 & 0 \\ & & & \mu & 0 & 0 \\ & & & & \mu & 0 \\ & & & & & \mu \end{bmatrix} \begin{bmatrix} \varepsilon_{xx} \\ \varepsilon_{yy} \\ \varepsilon_{zz} \\ \varepsilon_{yz} \\ \varepsilon_{zx} \\ \varepsilon_{xy} \end{bmatrix} \tag{4.15}$$

Where λ and μ are the Lamé constants and $(\lambda+2\mu)$ is the longitudinal modulus. Equation (4.15) can be written in shorthand notation, Equations (4.16) and (4.17).

$$\sigma_{ii} = \lambda\Delta + 2\mu\mu_{ii} \tag{4.16}$$

$$\sigma_{ij} = \mu\varepsilon_{ij} \tag{4.17}$$

Where $\Delta = \varepsilon_{xx} + \varepsilon_{yy} + \varepsilon_{zz}$ is the dilation and represents the change of volume over a unit cube. Although λ and μ completely define the elastic behaviour of an isotropic solid, three other constants are often utilized: Poisson's ratio (v) which is the ratio of the lateral contraction to longitudinal extension $\left(\frac{-\varepsilon_{yy}}{\varepsilon_{xx}}\right)$; Young's Modulus (*E*), the ratio between applied stress and resultant strain on a bar specimen; and Bulk Modulus (*B*) which is the ratio between applied pressure and the fractional change in volume when a solid is subjected to a uniform hydrostatic compression $\left(\frac{-\sigma_{xx}}{\Delta}\right)$. These parameters can be defined in terms of λ and μ [108]; Equations (4.18) to (4.20).

$$v = \frac{\lambda}{2(\lambda+\mu)} \tag{4.18}$$

$$E = \frac{\mu(3\lambda+2\mu)}{\lambda+\mu} \tag{4.19}$$

$$B = \lambda + \frac{2\mu}{3} \tag{4.20}$$

The variation of stress across the faces of a small cubic element of material (of any symmetry) is described using the elastic equations of motion, Equations (4.21) to (4.23).

$$\rho \frac{\partial^2 u_x}{\partial t^2} = \frac{\partial \sigma_{xx}}{\partial x} + \frac{\partial \sigma_{xy}}{\partial y} + \frac{\partial \sigma_{xz}}{\partial z} \quad \Rightarrow \quad \rho \frac{\partial^2 u_x}{\partial t^2} = (\lambda + \mu) \frac{\partial \Delta}{\partial x} + \mu \nabla^2 u_x \tag{4.21}$$

$$\rho \frac{\partial^2 u_y}{\partial t^2} = \frac{\partial \sigma_{yx}}{\partial x} + \frac{\partial \sigma_{yy}}{\partial y} + \frac{\partial \sigma_{yz}}{\partial z} \quad \Rightarrow \quad \rho \frac{\partial^2 u_y}{\partial t^2} = (\lambda + \mu) \frac{\partial \Delta}{\partial y} + \mu \nabla^2 u_y \tag{4.22}$$

$$\rho \frac{\partial^2 u_z}{\partial t^2} = \frac{\partial \sigma_{zx}}{\partial x} + \frac{\partial \sigma_{zy}}{\partial y} + \frac{\partial \sigma_{zz}}{\partial z} \quad \Rightarrow \quad \rho \frac{\partial^2 u_z}{\partial t^2} = (\lambda + \mu) \frac{\partial \Delta}{\partial z} + \mu \nabla^2 u_z \tag{4.23}$$

Where ρ is the density of the medium. Equations (4.21) to (4.23) show further simplification for isotropic materials is achieved using $\nabla^2 = \frac{\partial^2}{\partial x^2} + \frac{\partial^2}{\partial y^2} + \frac{\partial^2}{\partial z^2}$, the Laplacian operator. As previously stated, it is assumed that there is no particle motion in the y-axis direction (all cross-sections of the plate parallel to the x-z plane are identical) and therefore, it is necessary only to satisfy the right-hand side of Equations (4.21) and (4.23). The vector potentials Φ and Ψ, which describe the longitudinal and transverse components respectively, satisfy Equations (4.24) and (4.25).

$$\frac{\partial^2 \Phi}{\partial x^2} + \frac{\partial^2 \Phi}{\partial z^2} + k_l^2 \Phi = 0 \tag{4.24}$$

$$\frac{\partial^2 \Psi}{\partial x^2} + \frac{\partial^2 \Psi}{\partial z^2} + k_t^2 \Psi = 0 \tag{4.25}$$

Where $k_l^2 = \frac{\rho}{\lambda + 2\mu}; \;\; k_t^2 = \frac{\rho}{\mu}$. The relationship between the potentials and the displacement components, u_x and u_z along the *x* and *z* axes is given by Equations (4.26) and (4.27).

$$u_X = \frac{\partial \Phi}{\partial x} - \frac{\partial \Psi}{\partial z} \tag{4.26}$$

$$u_Z = \frac{\partial \Phi}{\partial z} + \frac{\partial \Psi}{\partial x} \tag{4.27}$$

Where $\rho \frac{\partial^2 \Phi}{\partial t^2} = (\lambda + 2\mu)\nabla^2 \Phi$ and $\rho \frac{\partial^2 \Psi}{\partial t^2} = \mu \nabla^2 \Psi$. Using Hooke's law, the relationship between Φ and Ψ, and the stress tensor is defined by Equations (4.28) to (4.30).

$$\sigma_{xx} = \lambda\left(\frac{\partial^2 \Phi}{\partial x^2} + \frac{\partial^2 \Phi}{\partial z^2}\right) + 2\mu\left(\frac{\partial^2 \Phi}{\partial x^2} - \frac{\partial^2 \Psi}{\partial x \partial z}\right) \tag{4.28}$$

$$\sigma_{zz} = \lambda\left(\frac{\partial^2 \Phi}{\partial x^2} + \frac{\partial^2 \Phi}{\partial z^2}\right) + 2\mu\left(\frac{\partial^2 \Phi}{\partial z^2} + \frac{\partial^2 \Psi}{\partial x \partial z}\right) \tag{4.29}$$

$$\sigma_{xz} = \mu\left(2\frac{\partial^2 \Phi}{\partial x \partial z} + \frac{\partial^2 \Psi}{\partial x^2} - \frac{\partial^2 \Psi}{\partial z^2}\right) \tag{4.30}$$

Where Φ and Ψ are represented by Equations (4.31) and (4.32).

$$\Phi = A_s e^{ikx} coshqz + B_a e^{ikx} sinhqz \tag{4.31}$$

$$\Psi = D_s e^{ikx} sinhsz + C_a e^{ikx} coshsz \tag{4.32}$$

Where, *As, Ba, Ca a*nd *Ds* are arbitrary constants; *k* is the Lamb wave number; $q = \sqrt{k^2 - k_l^2}$; $s = \sqrt{k^2 - k_t^2}$; and the factor e^{-iwt} is dropped for brevity. Substituting Equations (4.31) and (4.32) into Equations (4.28) to (4.30), the following system of equations are obtained, Equations (4.33) to (4.36).

$$\left(k^2+s^2\right)\cosh qdA_s+\left(k^2+s^2\right)\sinh qdB_a+2iks\sinh sdC_a+2iks\cosh sdD_s=0 \tag{4.33}$$

$$\left(k^2+s^2\right)\cosh qdA_s-\left(k^2+s^2\right)\sinh qdB_a-2iks\sinh sdC_a+2iks\cosh sdD_s=0 \tag{4.34}$$

$$2ikq\sinh qdA_s+2ikq\cosh qdB_a-\left(k^2+s^2\right)\cosh sdC_a-\left(k^2+s^2\right)\sinh sdD_s=0 \tag{4.35}$$

$$-2ikq\sinh qdA_s+2ikq\cosh qdB_a-\left(k^2+s^2\right)\cosh sdC_a+\left(k^2+s^2\right)\sinh sdD=0 \tag{4.36}$$

Where Equation (4.33) and (4.35) satisfy the situation where *z=d*, and Equation (4.34) and (4.36) satisfy the situation where *z=-d*. The system described by Equations (4.33) to (4.36) is satisfied if the subsystems described by Equations (4.37) to (4.40) are satisfied.

$$\left(k^2+s^2\right)A_s\cosh qd+2iksD_s\cosh sd=0 \tag{4.37}$$

$$2ikqA_s\sinh qd-\left(k^2+s^2\right)D_s\sinh sd=0 \tag{4.38}$$

$$\left(k^2+s^2\right)B_a\sinh qd+2iksC_a\sinh sd=0 \tag{4.39}$$

$$2ikqB_a\cosh qd-\left(k^2+s^2\right)C_a\cosh sd=0 \tag{4.40}$$

These have non-trivial solutions only when their determinants are equal to zero; leading to two characteristic equations determining the Eigenvalues of the wave number *k*, Equations (4.41) and (4.42), [86].

$$-\begin{vmatrix}\left(k^2+s^2\right)\cosh qd & 2iks\cosh sd \\ 2ikq\sinh qd & -\left(k^2+s^2\right)\sinh sd\end{vmatrix}=\left(k^2+s^2\right)^2\cosh qd\sinh sd-4k^2qs\sinh qd\cosh sd=0 \tag{4.41}$$

$$-\begin{vmatrix}\left(k^2+s^2\right)\sinh qd & 2iks\sinh sd \\ 2ikq\cosh qd & -\left(k^2+s^2\right)\cosh sd\end{vmatrix}=\left(k^2+s^2\right)^2\sinh qd\cosh sd-4k^2qs\cosh qd\sinh sd=0 \tag{4.42}$$

From Equation (4.41) and (4.42), the subsystem (4.37) and (4.38) provides an expression for D_s in terms of A_s, and subsystem (4.39) and (4.40) provides an expression for C_a in terms of B_a: inserting them into Equations (4.31) and (4.32) yields Equations (4.43) and (4.44) for the desired potentials.

$$\Phi = A_s e^{ik_s x} \cosh q_s z + B_a e^{ik_a x} \sinh q_a z \tag{4.43}$$

$$\Psi = \frac{2ik_s q_s \sinh q_s d}{\left(k_s^2 + s_s^2\right)\sinh s_s d} A_s e^{ik_s x} \sinh s_s z + \frac{2ik_a q_a \cosh q_a d}{\left(k_a^2 + s_a^2\right)\cosh s_a d} B_a e^{ik_a x} \cosh s_a z \tag{4.44}$$

Here, k_s are the values of k satisfying Equation (4.41) and k_a are the values satisfying equation (4.42) where $q_{s,a} = \sqrt{k_{s,a}^2 - k_l^2}\ ;\ s_{s,a} = \sqrt{k_{s,a}^2 - k_t^2}$. The displacement components U and W may be calculated from Equation (4.45) and (4.46) using relations (4.26) and (4.27).

$$U = U_s - U_a \tag{4.45}$$

$$W = W_s + W_a \tag{4.46}$$

Splitting into symmetrical and anti-symmetrical components, the x and z particle displacements can be defined as Equations (4.47) to (4.50).

$$U_s = k_s A\left(\frac{\cosh q_s z}{\sinh q_s d} - \frac{2q_s s_s}{k_s^2 + s_s^2} \cdot \frac{\cosh s_s z}{\sinh s_s d}\right) \cdot e^{ik_s x - i\omega t - i\pi/2} \tag{4.47}$$

$$W_s = -Aq_s\left(\frac{\sinh q_s z}{\sinh q_s d} - \frac{2k_s^2}{k_s^2 + s_s^2} \cdot \frac{\sinh s_s z}{\sinh s_s d}\right) \cdot e^{ik_s x - i\omega t} \tag{4.48}$$

$$U_a = Bk_a\left(\frac{\sinh q_a z}{\cosh q_a d} - \frac{2q_a s_a}{k_a^2 + s_a^2} \cdot \frac{\sinh s_a z}{\cosh s_a d}\right) \cdot e^{i\left(k_a x - \omega t - \frac{\pi}{2}\right)} \tag{4.49}$$

$$W_a = -Bq_a\left(\frac{\cosh q_a z}{\cosh q_a d} - \frac{2k_a^2}{k_a^2 + s_a^2} \cdot \frac{\cosh s_a z}{\cosh s_a d}\right) \cdot e^{ik_a x - i\omega t} \tag{4.50}$$

Where, the dependency factor e^{-iwt}, previously dropped, reappears and constants $A = -k_s A_s \sinh q_s d$ and $B = -k_a B_a \cosh q_a d$ are defined for convenience.

The purpose of the algebraic manipulation leading to expressions (4.47) to (4.50) is to describe two groups of waves each satisfying the wave equations of motion and boundary conditions, i.e. both propagate in the plate independently of one another. Analysing these expressions further, it is observed that Equations (4.47) ad (4.48) describe waves in which particle motion occurs symmetrically with respect to *z*=0 plane (i.e. displacement *U* has the same sign in the upper and lower halves of the plate whilst the displacement *W*, has opposite signs). These waves are termed symmetrical Lamb waves. The second group of expressions, (4.49) and (4.50), describe waves in which the motion is antisymmetrical with respect to the *z*=0 plane (i.e. displacement *U* has opposite signs on both halves of the plate whilst displacement W has the same signs). These waves are termed antisymmetrical Lamb waves. This deformation of the plate during propagation of symmetrical (*s*) and antisymmetrical (*a*) waves is illustrated in Figure 4.7.

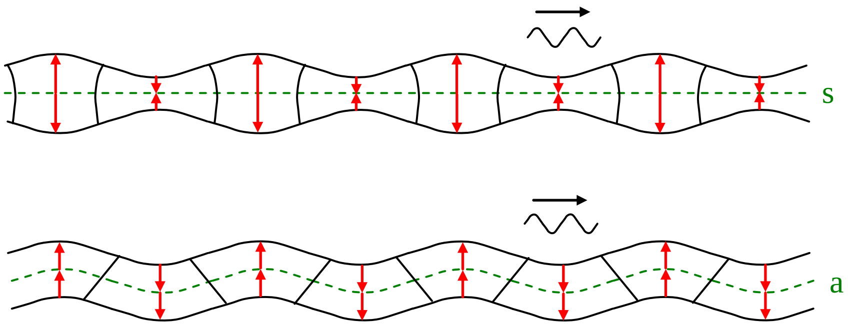

Figure 4.7: Symmetrical (s) and antisymmetrical (a) waves

4.3 Transformation Properties

Often, it is necessary to transform the acoustic field into the coordinate system in accordance with the geometry of the material being analysed. This may involve a rotation of the rectangular coordinate axis. The old and new coordinates are taken to be *x*, *y*, *z* and *x'*, *y'*, *z'* respectively where the relative orientation of the two sets of axes is described by the direction cosines, Figure 4.8.

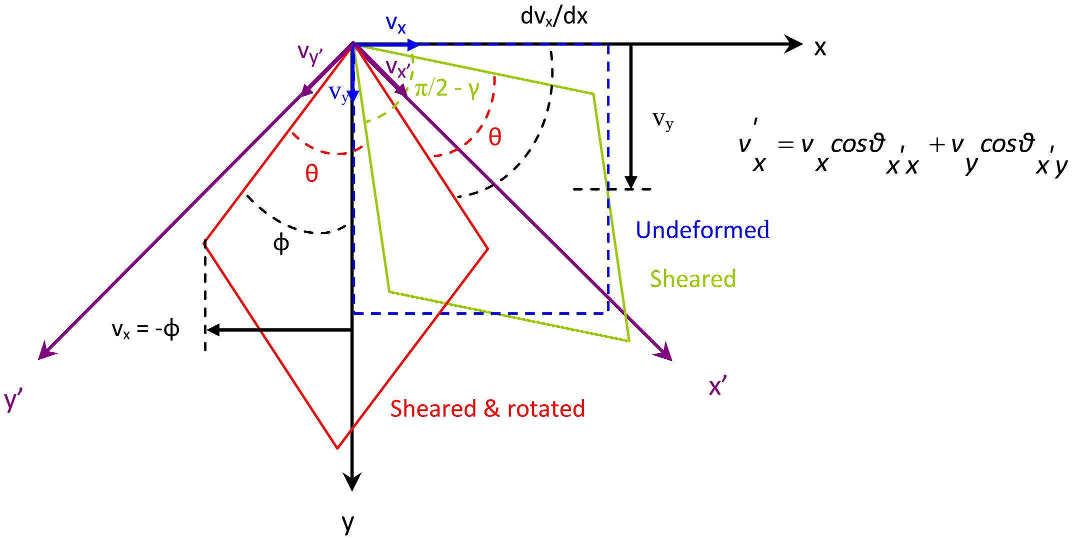

Figure 4.8: Rectangular coordinate transformation corresponding to a clockwise rotation about the z-axis

Both shear deformation and rotation of a rectangular element are shown. The element *dxdy* is deformed at the right-hand side by the downward function $v_y(x,t)$ and by the rightward function $v_x(x,t) = -\varphi y$ where $\varphi(x,t)$ is the rotation of a material cross-section relative to the original normal cross-section. The element is sheared by an angle γ and rotated by an angle ϑ. A vector, v, is represented by the components v_x, v_y, v_z relative to the old coordinate axes and by v_x', v_y', v_z' relative to the new coordinate axes. Each new component can be evaluated in terms of components along the old axes by projecting all of the old components onto the relevant axes of the new system, Equation (4.51). The general vector transformation form is also given.

$$\begin{aligned} v_x' &= \cos\vartheta_{x'x} v_x + \cos\vartheta_{x'y} v_y \\ \Rightarrow v_i' &= a_{ij} v_j \end{aligned} \tag{4.51}$$

Where $i, j = x, y, z$ and the coefficients a_{ij} define a transformation matrix, *[a]*. The transformation of the strain matrix, *[S]*, is now defined as Equation (4.52).

$$\varepsilon_{ij}^{'} = a_{ik} a_{jl} \varepsilon_{kl} \tag{4.52}$$

Where the relationship between the strain (ε) and the particle displacement (*u)* is defined by Equation (4.53)

$$\varepsilon_{kl} = \nabla u \qquad \Rightarrow \qquad \varepsilon_{kl} = \begin{bmatrix} \partial u_X / \partial x \\ \partial u_Y / \partial y \\ \partial u_Z / \partial z \\ \partial u_Y / \partial z + \partial u_Z / \partial y \\ \partial u_X / \partial z + \partial u_Z / \partial x \\ \partial u_X / \partial y + \partial u_Y / \partial x \end{bmatrix} u \tag{4.53}$$

Since Hooke's law applies in all coordinate systems, the stress transformation may be deduced by relating one vector to another. Therefore, the transformed elastic constants are defined as a 4th rank tensor. Equation (4.54) represents just one stress component.

$$\sigma_{mn}^{'} = a_{mi} a_{nj} \sigma_{ij} = a_{mi} a_{nj} c_{ijkl} \varepsilon_{kl} = a_{mi} a_{nj} a_{ko} a_{lp} c_{ijkl} \varepsilon_{op}^{'} \tag{4.54}$$

To evaluate the transformed stress field, a 6x6 Bond transformation matrix, Equation (4.55), is applied Equation (4.14).

$$[M] = \left[\begin{array}{ccc|ccc} a_{xx}^2 & a_{xy}^2 & a_{xz}^2 & 2a_{xy}a_{xz} & 2a_{xz}a_{xx} & 2a_{xx}a_{xy} \\ a_{yx}^2 & a_{yy}^2 & a_{yz}^2 & 2a_{yy}a_{yz} & 2a_{yz}a_{yx} & 2a_{yx}a_{yy} \\ a_{zx}^2 & a_{zy}^2 & a_{zz}^2 & 2a_{zy}a_{zz} & 2a_{zz}a_{zx} & 2a_{zx}a_{zy} \\ \hline a_{yx}a_{zx} & a_{yy}a_{zy} & a_{yz}a_{zz} & a_{yy}a_{zz} + a_{yz}a_{zy} & a_{yx}a_{zz} + a_{yz}a_{zx} & a_{yy}a_{zx} + a_{yx}a_{zy} \\ a_{zx}a_{xx} & a_{zy}a_{xy} & a_{zz}a_{xz} & a_{xy}a_{zz} + a_{xz}a_{zy} & a_{xz}a_{zx} + a_{xx}a_{zz} & a_{xx}a_{zy} + a_{xy}a_{zx} \\ a_{xx}a_{yx} & a_{xy}a_{yy} & a_{xz}a_{yz} & a_{xy}a_{yz} + a_{xz}a_{yy} & a_{xz}a_{yx} + a_{xx}a_{yz} & a_{xx}a_{yy} + a_{xy}a_{yx} \end{array} \right] \tag{4.55}$$

The transformed stress field is $\sigma_H^{'} = M_{HI}\sigma_I$ with a transformed stiffness matrix, $\lfloor c^{'} \rfloor = [M][c][\tilde{M}]$ where $[\tilde{M}]$ is the transpose of $[M]$.

4.3.1 Transversely Isotropic Material

Typically, a laminate will comprise bi-directional lamina: lamina layers placed at an angle to other lamina layers to provide added stiffness. Each lamina may be homogeneously isotropic where the laminated medium can be characterized as homogeneously anisotropic having an axis of elastic symmetry perpendicular to the plane of each lamina. Alternatively, each lamina may be a composite made up of a homogenous matrix reinforced by aligned fibres where each lamina is treated as homogeneously isotropic having an axis of symmetry parallel to the fibre axis. Planes perpendicular to axis of symmetry are considered isotropic. Such an anisotropic material is called transversely isotropic, Figure 4.9, [109].

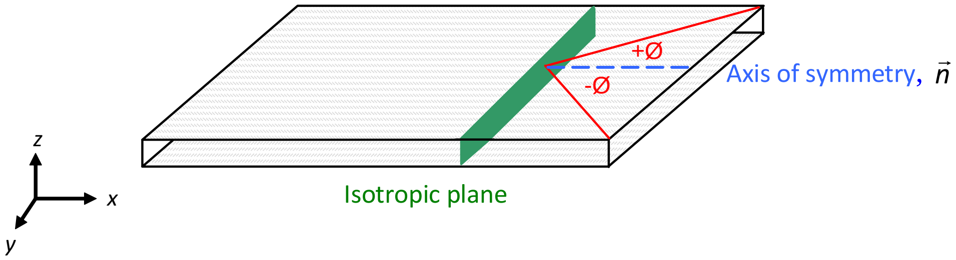

Figure 4.9: Transversely isotropic plate

The accompanying stiffness matrix features five independent elastic constants, Equation (4.56).

$$c=\begin{bmatrix} c_{11} & c_{12} & c_{13} & 0 & 0 & 0 \\ c_{12} & c_{11} & c_{13} & 0 & 0 & 0 \\ c_{13} & c_{13} & c_{33} & 0 & 0 & 0 \\ 0 & 0 & 0 & c_{44} & 0 & 0 \\ 0 & 0 & 0 & 0 & c_{44} & 0 \\ 0 & 0 & 0 & 0 & 0 & \frac{1}{2}\left(c_{11}-c_{12}\right) \end{bmatrix} \tag{4.56}$$

Any general rotation of rectangular coordinates can be performed by applying successive rotations about different coordinate axes For example, the coordinates can be rotated clockwise through an angle of $\emptyset$ about the z-axis then clockwise through an angle ϑ about the transformed y-axis, before finally being rotated clockwise Ψ about the transformed z'-axis, Equations (4.57) to (4.59).

$$\left[a_{z_\phi}\right]=\begin{bmatrix} cos\phi & sin\phi & 0 \\ -sin\phi & cos\phi & 0 \\ 0 & 0 & 1 \end{bmatrix} \tag{4.57}$$

$$\left[a_{y_\theta}\right]=\begin{bmatrix} cos\theta & 0 & -sin\theta \\ 0 & 1 & 0 \\ sin\theta & 0 & cos\theta \end{bmatrix} \tag{4.58}$$

$$\left[a_{z_\psi}\right]=\begin{bmatrix} \cos\psi & \sin\psi & 0 \\ -\sin\psi & \cos\psi & 0 \\ 0 & 0 & 1 \end{bmatrix} \tag{4.59}$$

Therefore, to align the rectangular coordinates with the bidirectional fibre orientation illustrated in Figure 4.9, Equation (4.57) is inserted into Equation (4.55) to provide $[M]$ (and $[\tilde{M}]$) which acts on c in Equation (4.56) using the relationship, $[M][c][\tilde{M}]$, to give the transformed stiffness matrix $c^{'}$, Equation (4.60).

$$c^{'}=\begin{bmatrix} c_{11} & c_{12} & c_{13} & 0 & 0 & c_{16}^{'} \\ c_{12} & c_{11} & c_{13} & 0 & 0 & -c_{16}^{'} \\ c_{13} & c_{13} & c_{33} & 0 & 0 & 0 \\ 0 & 0 & 0 & c_{44} & 0 & 0 \\ 0 & 0 & 0 & 0 & c_{44} & 0 \\ c_{16}^{'} & -c_{16}^{'} & 0 & 0 & 0 & c_{66}^{'} \end{bmatrix} \tag{4.60}$$

Where the relationship between the transformed ($c^{'}$) and original coefficients (c) have the following relationships, Equation (4.61).

$$c_{11}^{'} = c_{11} \qquad c_{12}^{'} = c_{12} \qquad c_{13}^{'} = c_{13} \qquad c_{16}^{'} = -\left(c_{11} - c_{12}\right) sin2\zeta in2\zeta c$$
$$c_{33}^{'} = c_{33} \qquad c_{44}^{'} = c_{44} \qquad c_{66}^{'} = \frac{1}{2}\left(c_{11} - c_{12}\right) \tag{4.61}$$

4.4 Excitation

The active region of a transducer in contact with a material surface introduces localised stress motion resulting in propagation of Guided waves. Two types of excitation are considered.

4.4.1 Point Source

Out-of-plane excitation at a point on a plate will initiate the radial propagation of stress waves within the material. Wave propagation will be spherical if the material is isotropic. In an anisotropic material, the material properties vary throughout the material resulting in directionally dependent wave velocity. If the radius of the active area (*a*) is much less than the wavelength of the excitation, such that $a_r << a_r^2 / \lambda$, then the transducer can be considered to be a point source. In the simplest case, the signal emitted from a point source at point *p*, varies with $e^{j\omega t}$. The field at the receiver is described by Equation (4.62).

$$f\left(p^{'} - p, y\right) = \frac{e^{j\omega\left[\left(p - p^{'}\right)^{2} + y^{2}\right]^{1/2}/v}}{\left[\left(p - p^{'}\right)^{2} + y^{2}\right]^{\frac{1}{4}}} \tag{4.62}$$

Where $p^{'}$ represents a point at some specified distance from p.

4.4.2 Interdigitated

Using spatially-distributed piezoelectric digit pairs to detect the presence of surface acoustic waves, interdigitated transducers reinforce separately excited waves to enable detection of a particular wave mode, or range of modes. The spacing of each digit pair is such that the wave propagates the digit separation distance in precisely the time required for signal repetition to occur. The transducer length is proportional to the number of piezoelectric digit pairs: the greater the length, the more sensitive the sensor is to small changes in over a narrow band of frequencies; the shorter the length, the less sensitive the sensor over a broad range of frequencies, Figure 4.10, [112].

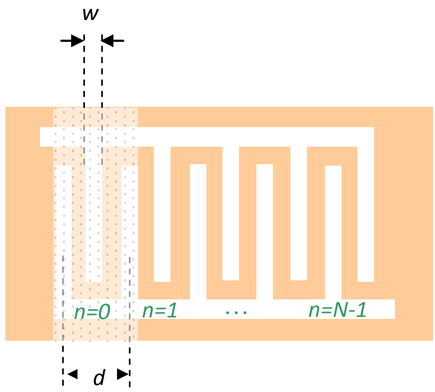

Figure 4.10: Interdigitated transducer with digit pair spacing *d* and digit width *w*

4.4.2.1 Uniform Analysis

A transducer featuring digit pair spacing d with individual digit width w may be uniformly charged at a particular point in time to q and $-q$ with field amplitudes varying at ω Hz. The charge density on one digit can be defined as $\rho = q/d_1$. The signal amplitude contributed by one digit pair (Figure 4.10) at z arising from an elementary signal of frequency ω between z and $z+\Delta z$ as a function of frequency can be defined as Equation (4.63), [112].

$$A(z,\omega) = 2\alpha q e^{-jkz} sin\left(k\frac{d}{4}\right) sinc(w/\lambda) \tag{4.63}$$

Where α is the coupling factor between the charge and the acoustic excitation and k is the wave number. The contribution from all sensor digit pairs with centres at $z^{'} = nd\left(n = 0,1,2\cdots N-1\right)$ is given by Equation (4.64). Upon manipulation of the geometric progression and application of the Double Angle formula, Equation (4.65) is identified as the Fourier Transform of the charge distribution on the digits.

$$A(z,\omega) = 2j\alpha j\alpha^{-jkz} sin\left(k\frac{d}{4}\right) sinc(w/\lambda) \sum_{n=0}^{N-1} e^{jknd} \tag{4.64}$$

$$\Rightarrow \quad A(z,\omega) = j\alpha q e^{-jkz} \frac{sin(kNd/2)}{cos(kd/4)} sinc(w/\lambda) e^{jk(N-1)d/2} \tag{4.65}$$

For a large number of digits, the response $A(z,\omega)$ is a maximum when $kd = 2\pi$ which is the value of k corresponding to the centre frequency with a bandwidth 2/N.

Since interdigitated transducers do not behave as a point source due to their relatively large size, displacement across the active area is non uniform. Raghavan and Cesnik demonstrated using Macro-Fibre Composite (MFC) sensors that wave mode sensitivity was dependent upon digit length, electrode arrangement, frequency and the elastic stiffness characteristics, [113]. Interdigitated sensors, however; can be assumed to behave as a system of point sources, with amplitude and direction of each point defined by a vector p_n, Equation (4.66), [114].

$$p_n = \left(A_n\sqrt{\left(x^2 + (-\upsilon y)^2\right)}, \angle arctan\frac{-\upsilon y}{x}\right) \tag{4.66}$$

where υ is the Poisson's ratio of the active area and A_n is the displacement amplitude

4.4.3 Modelling Techniques

A number of different types of numerical computation techniques can be used for analysis of wave propagation within materials. Modelling has clear advantages over experimental testing: it allows the investigation of different wave propagation instances with relative speed. It also permits the analysis of wave behaviour through the entire thickness of the sample rather than simply on the surface. Analysis of the nature of an elastic wave can also be undertaken when, on occasions, it cannot be determined by other means. Such analysis allows prediction of material response under excitation and defect conditions. The major advantage of simulation is it permits the modelling of a range of wave propagation and combinations. The mathematical equations for Lamb waves must satisfy physical boundary conditions. Computational techniques include finite difference (FD) equations, finite element (FE) analysis, boundary element method (BEM), finite strip elements (FSE), spectral element (SE) methods, mass-spring lattice model (MSLM) and local interaction simulation approach (LISA).

4.4.3.1 Finite Element Analysis

Finite element analysis (FEA) is well suited to analysis of structures with complex geometries. It operates by dividing the shape under analysis into smaller sections called elements comprising either 4 or 8 nodes, Figure 4.11.

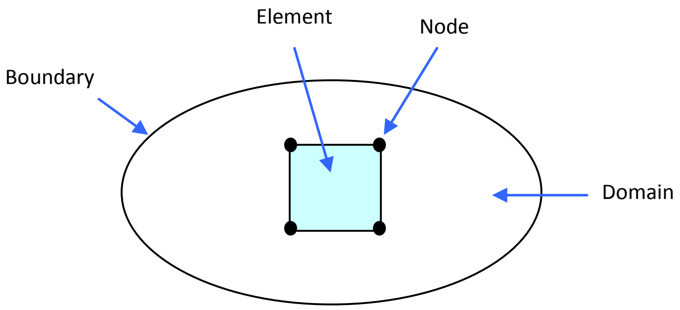

Figure 4.11: Finite Element Modelling (FEM) system, [115]

The software applies mathematical formulae to calculate the given stresses and strains on each element. When a load is applied to an individual node, the software computes the distribution of that load to the surrounding nodes, which in turn calculates the distribution to the next node set and so on, [115].

Hill et al. used FEA to model a steel plate using 20000+ elements, [116]. The excitation detected 20 cm away featured a small S_0 mode and a significant A_0 mode. The result was as expected since the asymmetrical excitation was applied to just one surface, and therefore excited antisymmetric modes.

An analysis of longitudinal and shear wave loss within media using FEA was conducted by Hayward and Hyslop to predict the surface displacement characteristics of different active transducer configurations on ceramic-polymer materials (typically encountered in 1-3 and 2-2 piezoelectric composite array transducers), [117,118]. In the 1-3 composite substrate, the Lamb mode cut off was found to be heavily dependent upon ceramic pillar pitch and volume fraction ratio. Good agreement with the experimental surface displacement was found.

4.4.3.2 Finite Difference Method

Finite Difference (FD) methods describe spring constants by approximating second order or higher order function derivatives using local variables on small grid spacing. FD methods are computationally more expensive for large models and complex geometries. Although convenient for wave propagation in homogeneous materials or media with continuously varying physical properties, the boundaries and discontinuities between different media result in approximate solutions which produce considerable errors.

4.4.3.3 Boundary Element Method

Boundary Element Method (BEM) is computationally more efficient than FE for infinite media. This technique formulates the matrix of the wave equations related to the analysed system in terms of its external boundaries. Different solutions are obtained from the output responses or the modal models. Responses provide amplitudes and phases of reflected and transmitted waves. Modal models give velocities and frequencies of propagating waves, [119].

4.4.3.4 Spectral Element Method

Spectral Element (SE) methods are efficient for wave propagation and are easy to implement. SE approximates functions as a sum of trigonometric functions or Chebyshev polynomials and then differentiates those functions exactly.

4.4.3.5 Mass-Spring Lattice Model

Mass-Spring Lattice Model (MSLM) analyses media inertia using lumped mass particles where the stiffness is modelled using spring elements connecting the particles. MSLM models are similar to FD methods. However, MSLM avoids issues with Lamb waves under traction free conditions by disconnecting the springs.

4.4.3.6 Local Interaction Simulation Approach

Local Interaction Simulation Approach (LISA) avoids the approximation errors produced by FD methods when encountering boundaries or discontinuities in media by heuristically simulating the wave propagation. LISA uses the sharp interface model (SIM) which imposes continuity of displacements and stresses at interfaces and discontinuities, [120]. Complex wave propagation in complex media is modelled accurately and is computationally less expensive.

Lee and Staszewski applied LISA to detect damage simulating wave propagation in an aluminium plate discretised into 151 x 401 elementary 1 mm squares, [119]. The transmitter and receiver transducers were also modelled as piezoceramic discs - with energy transfer to the piezo disc modelled as a 2D Gaussian distribution (typically used for transducer beam profiles). The results showed successful generation of the S_0 mode. Experimental validation of the model using the model configurations gave very good agreement.

4.5 Wind Turbine Blade Considerations

The composite materials comprising the turbine blade exhibit directional characteristics will determine the direction of the propagating stress wave arising from the onset of a defect. The attenuation of the energy within the stress wave varies dependent upon the direction of analysis. It is therefore advantageous to establish a monitoring technique able to exploit the inherent directionality of the material under analysis. Knowledge of the stiffness coefficients characterises the stress / strain relationship for specific material directions. Information from more than one material orientation can be integrated within a finite element model to permit theoretical analysis. The presence of modes and their relative strength can subsequently be ascertained and used to inform appropriate application of sensor coupling.

4.6 Conclusions

Having established the wind turbine blade structural components for monitoring in Chapter 3, this chapter has discussed the tools available that may be applied for defect detection – some more suitable than others. A system of equations was established to enhance understanding of wave propagation within isotropic plate-materials. Although the spar cap of the shear web is a complex structure exhibiting anisotropic properties (where wave propagation characteristics are directionally dependent), establishing symmetry within the laminar lay-up helps to simplify the analysis. Accordingly, the GFRP structure was considered as exhibiting an axis of symmetry in the *x*-direction perpendicular to a plane of isotropy in the *z*-direction - making the material transversely isotropic.

In a transversely isotropic material, it is necessary to transform the stiffness coupling coefficient - relating the stress field to the strain field - in accordance with the material geometry under analysis to accurately represent the acoustic field within a selected coordinate system. To take advantage of the GFRP geometry, directionally dependent transducers can be appropriately aligned to preferentially couple specific wave modes from the material where a change in sensitivity (determined by digit length) is inversely proportional to the usable frequency bandwidth. The active area of such transducers is non-uniform but can be assumed to behave as a system of point sources for modelling purposes.

Modelling allows prediction of material response under different conditions with the advantage that the user may analyse wave propagation over a range of combinations.

However, the nature of component material forming the blade spar-cap is such that it is rarely a standardised structure. As Chapter 3 discussed, there are many modes of failure arising from imperfect manufacturing processes. As such, the geometry of the spar-cap is so specific (and thus not well-characterised) that any limitations of the acoustic technique become evident. Consequently, the next chapter focuses on experimental evaluation of GFRP materials to ascertain the impact of material anisotropy on Guided wave propagation.

5 Experimental Characterisation of Blade Constituent Components

5.1 Overview

This chapter analyses real GFRP components used to construct spar caps of wind turbine blades. Typically, two fibre orientated formations are used: bi-directional (±45°) and quasi-isotropic (0°/±45°/90°). The chapter evaluates signal generation, propagation and reception.

Experimental analysis is performed to test for the presence of dispersion within GFRP materials for different modes of wave propagation with respect to fibre orientation. Laser generation and reception is used to identify the propagating wave modes, the frequencies where mode dispersions occur and the effects of fibre orientation on mode properties (e.g. phase velocity, dispersion). Conventional PZT transducers are applied to bi-directional and quasi-isotropic GFRP in order to determine the sensitivity of received signals dependent upon material orientation. To exploit the directional characteristics of the composite component, directional sensors are then applied. These interdigitated sensors feature different electrode pattern formations and piezoceramic lengths. Experimental analysis is conducted to identify the configuration most sensitive to mode detection with respect to fibre orientation.

A verification process using FE modelling of the GFRP material with the interdigitated sensors (represented by a grid of point sources) provides a comparison of the experimental analysis with the theory.

The experimental findings contribute to a wider context of wind turbine blade inspection, and are used to influence demonstration experiments described in Chapter 6.

5.2 Typical material structure

The design structure of wind turbine blades varies considerably across the industry. However, some components are relatively common. The cross section of a typical wind turbine blade is illustrated in Figure 5.1. Approximately 40 mm thick, the shell comprises plywood sandwiched between layers of glass fibre 1 - 2 mm thick. The strengthening structure, *Shear Web*, connects the leeward and windward laminated wood skins at the mid-chord (via the spar-cap support) for the greater length of the blade.

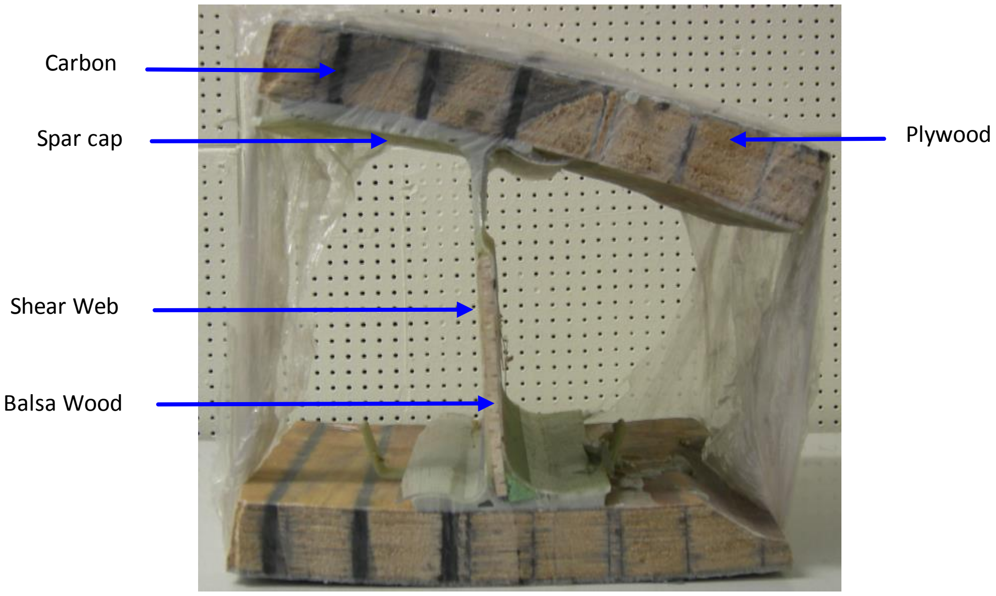

Figure 5.1: Typical wind turbine blade cross-section

Due to the complex shape of the blade and the cyclical loading during operation, glass reinforced epoxy is the most appropriate bonding material. Typically Spabond SP340 is used to attach the shear webs to the spar-cap – which in Figure 5.1 comprises two layers of GFRP, [121]. Manufacturing processes produce a sandwich structure featuring a bond depth that may vary between 3 mm and 20 mm. Of the materials comprising the shear web, GFRP is the only anisotropic material. Therefore, it is necessary to analyse the GFRP component in isolation before progressing to the sandwich structure.

5.3 Glass-Fibre Analysis

Glass-fibre comprises many mineral glasses typically based on silica (SiO_2) and combines with oxides (calcium, boron, sodium, iron and aluminium). Typical compositions of three well-known glasses used for glass fibre in composite materials are given in Table 5.1.

Table 5.1: Glass composition in percentage weight, [122]

Oxide	E-glass	C-glass	S-glass
SiO_2	52.4	64.4	64.4
Al_2O_3, Fe_2O_3	14.4	4.1	25.0
CaO	17.2	13.4	-
MgO	4.6	3.3	10.3
Na_2O, K_2O	0.8	9.6	0.3
Ba_2O_3	10.6	4.7	-
BaO	-	0.9	-

The strength of the glass is determined by the three-dimensional structure of the constituent oxides. The mechanical properties of the composite are dominated by the contribution of the fibre to the composite, Figure 5.2.

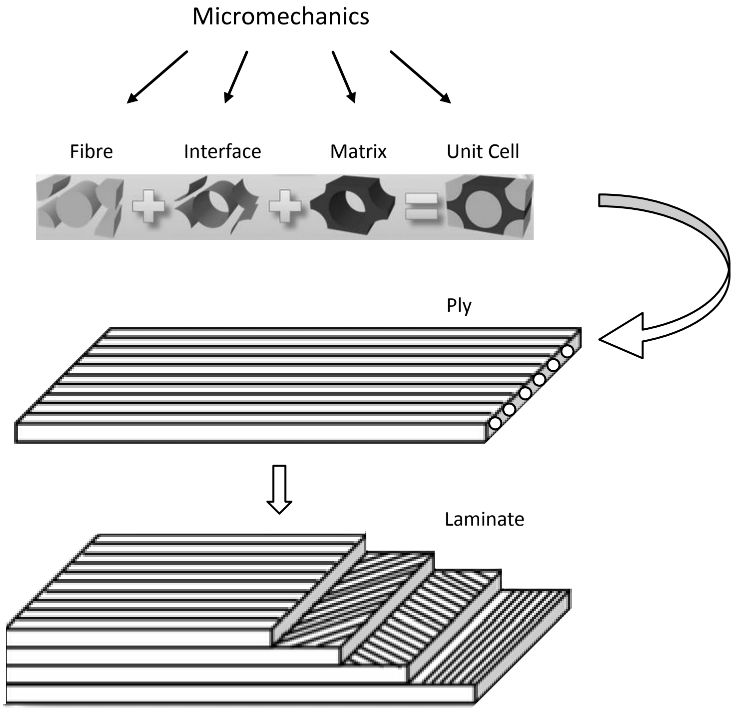

Figure 5.2: Micromechanics-based analysis for composite structures, [123]

Other factors determining composite strength include: the surface interaction of fibre and resin controlled by the degree of bonding; the amount of fibre in the composite (Fibre Volume Fraction); and the orientation of the fibres in the composite.

Generally, the stiffness and strength of a laminate will increase proportionally with the amount of fibre present. However, when the fibre volume fraction increases above 60-70%, the laminate strength will start to decrease due to insufficient resin holding the fibres properly together.

Within the laminate, reinforcing fibres are designed to be loaded along their length; their orientation creating highly directional properties. This anisotropy can be exploited within designs: the majority of fibres directed along the orientation of the main load paths thus minimising fibre material orientated where there is little or no load, Figure 5.3, [124].

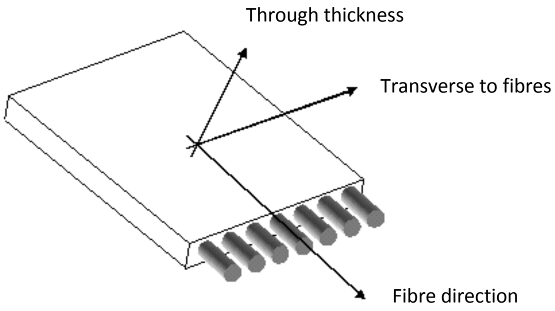

Figure 5.3: Unidirectional lamina

The effects on the characteristics of an elastic wave as it progresses through a GFRP sample is of interest particularly with respect to geometrical spreading, energy absorption and dispersion.

5.3.1 Attenuation effects of wave propagation in GFRP

To assess the impact of wave propagation and attenuation effects in GFRP materials, a study was undertaken using two different geometry materials. The first material was a unidirectional (UD) sample where the majority of fibres run in one direction (0° along the roll – a warp UD) and a small amount of fibre runs in another direction (90° across the roll – a weft UD). The purpose is to hold the primary fibres (0°) in position. An illustration of the 8 ply GFRP epoxy laminate is given in Figure 5.4 with details provided in Table 5.2

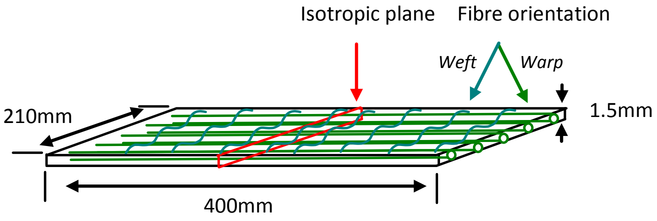

Figure 5.4: Unidirectional 8-ply GFRP

Table 5.2: Material properties for unidirectional GFRP

Gurit UT-E250	Measurement	unit
Lamina thickness	0.2	mm
Fibre	Warp: 600	tex
	Weft: 10	
Thread count	4.16 x 0.56	cm^{-1}

The second GFRP material was a 2 ply ±45° balanced laminate with thickness 2 mm. Transversely isotropic, the material exhibits symmetry about an axis normal to a plane of symmetry, Figure 5.5 and Table 5.3. (This material was representative of the materials often encountered in wind turbine blade components).

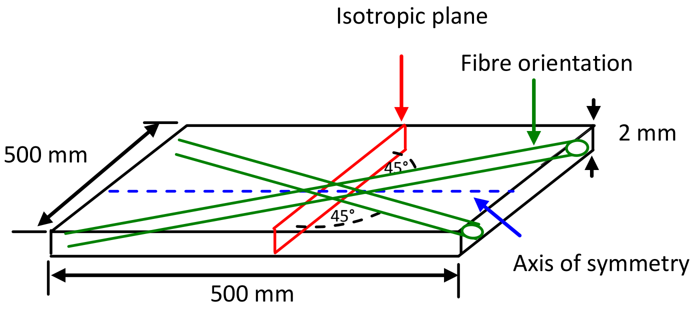

Figure 5.5: Transversely isotropic GFRP

Table 5.3: Material properties for bidirectional GFRP

St Germain Vetrotex RO99 688	Measurement	unit
Lamina thickness	1	mm
Continuous strand (diameter)	17	µm
Fibre	600	tex

The experimental set-up to generate and receive the fundamental symmetric mode in these samples is detailed in Appendix B1.

The initial separation between the two transducers was 60 mm increased in 10 mm increments to 250 mm and 300 mm respectively for UD and ±45° plates and the response recorded. For the ±45° material measurements were performed both along the fibre axis, and at 45° to the fibre axis. For the UD material the size of the plate prevented off fibre axis measurements being performed. Figure 5.6 illustrates the amplitude difference between the initial transducer displacement at 60 mm and the final displacement at 300 mm for the ±45° sample measured in the off-fibre axis direction. Attenuation in the material is clearly observed resulting in loss of wave characteristics

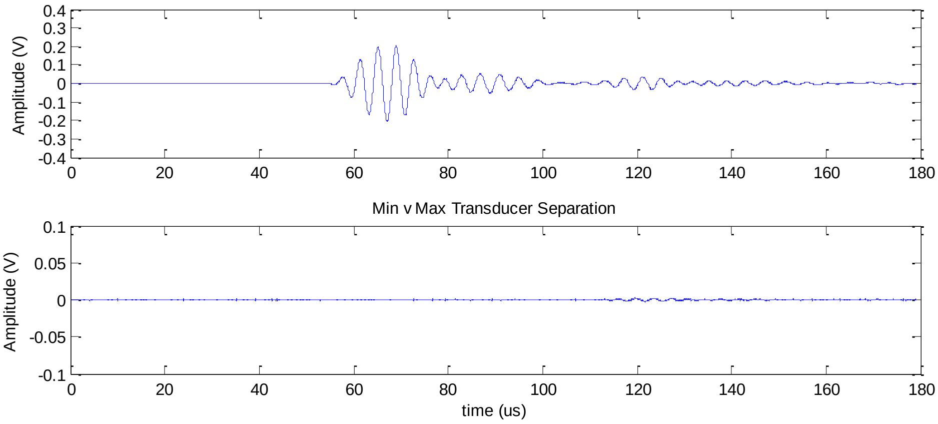

Figure 5.6: Variation in signal amplitude for ±45° plate, off-fibre direction. Transducer separation = 60 mm (top); transducer separation = 300 mm (bottom)

Figure 5.7 illustrates the peak-to-peak signal amplitude as a function of the transducer separation and Figure 5.8 shows the corresponding logarithmic relationship.

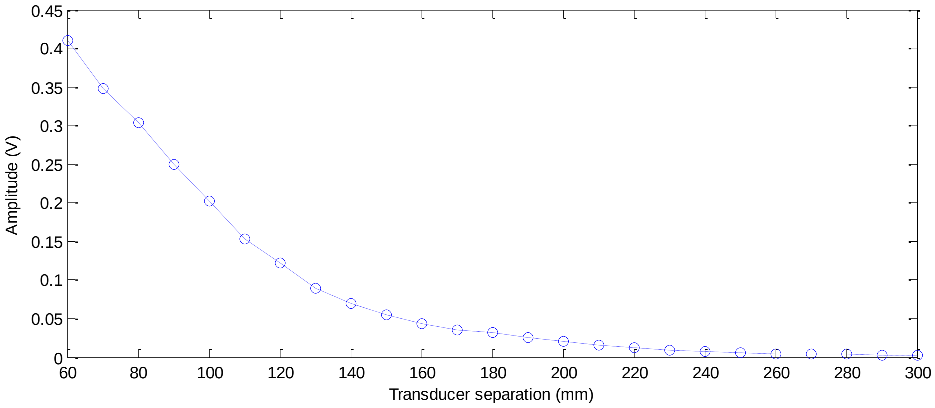

Figure 5.7: Attenuation for ±45° plate, off-fibre direction (amplitude)

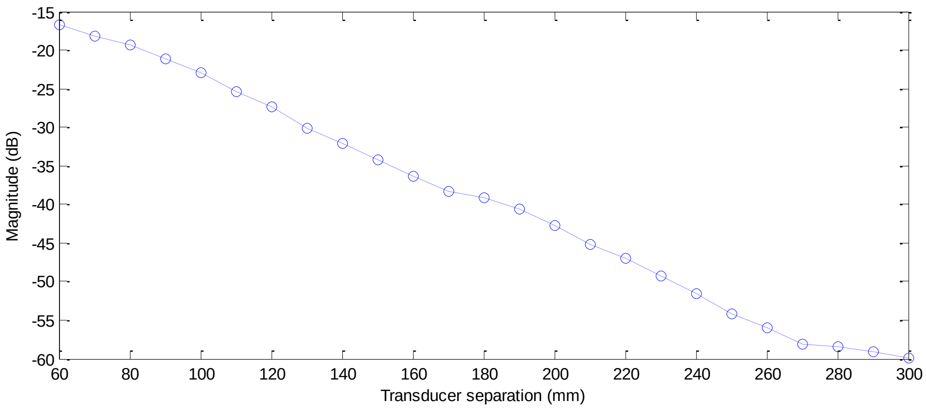

Figure 5.8: Attenuation for ±45° plate, off-fibre (dB)

The attenuation due to beam spreading would be expected to have a 1/√r relationship (where r is the radius of the measured point from the excitation). Of course, attenuation due to the GFRP micro-structure would also be expected and the anisotropy of the material is such that this structure would vary at different points of measure (e.g. measurement taken point at a point where two fibres intersect). Also the amplitude of the background noise can vary due to the appearance (disappearance) of a new wave mode (previously existing wave mode).

Figure 5.9 illustrates the amplitude difference between the initial transducer displacement at 60 mm and the final displacement at 300 mm for the ±45° sample measured in the on-fibre axis direction. Figure 5.10 and Figure 5.11 show the attenuation characteristics. It is observed that the final displacement amplitude is approximately 30 dB greater in the on-fibre analysis compared with the off-fibre analysis – due to the large differences in the elastic properties of the matrix compared with the fibres. Again, the amplitude varies from the geometrical attenuation expected due to the composite signal (of more than one wave mode) regularly contributing to the overall amplitude of the fastest (and largest) mode. The effects of scattering (e.g. fibre ends) also contribute to the overall mode amplitude.

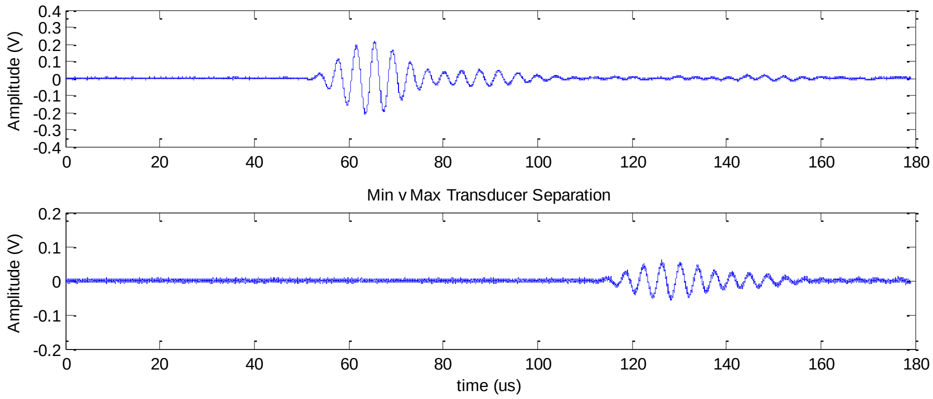

Figure 5.9: Variation in signal amplitude for ±45° plate, on-fibre direction. Transducer separation = 60 mm (top); transducer separation = 300 mm (bottom)

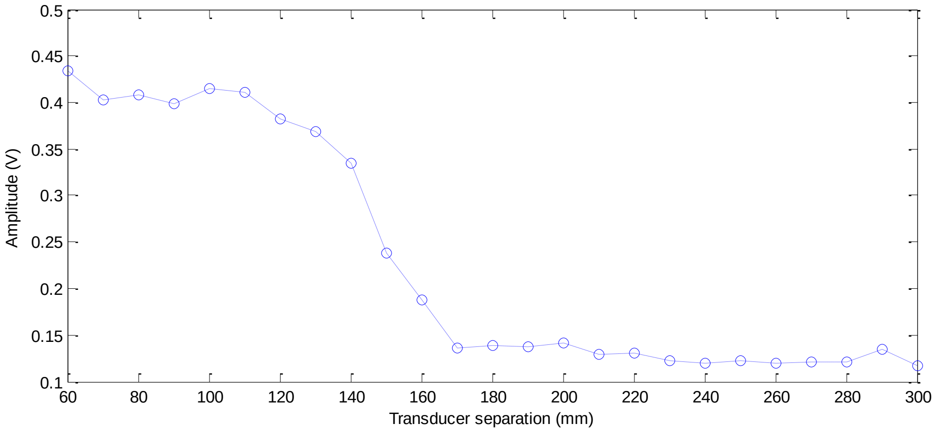

Figure 5.10: Attenuation for ±45° plate, on-fibre axis direction (amplitude)

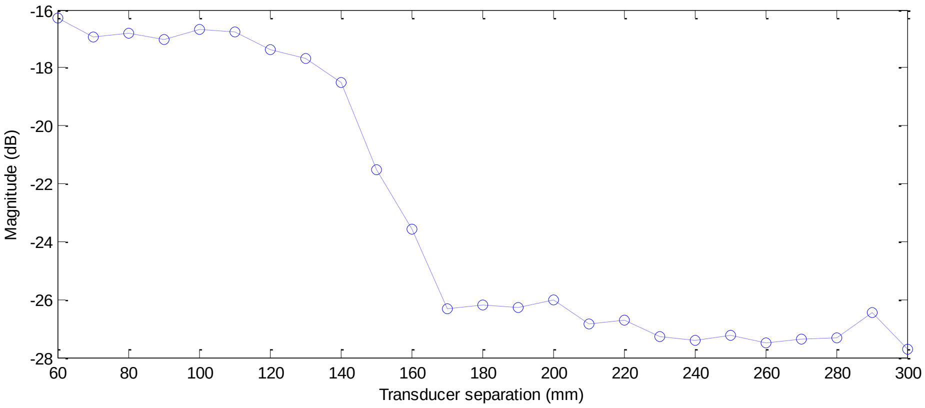

Figure 5.11: Attenuation for ±45° plate, on-fibre (dB)

Figure 5.12 illustrates the amplitude difference between the initial transducer displacement at 60 mm and the final displacement at 250 mm for the UD sample. Figure 5.13 and Figure 5.14 show the attenuation characteristics. It is observed that the final displacement amplitude is approximately 4 dB greater in the UD sample than for the on-fibre bi-directional sample at transducer separation of 250 mm.

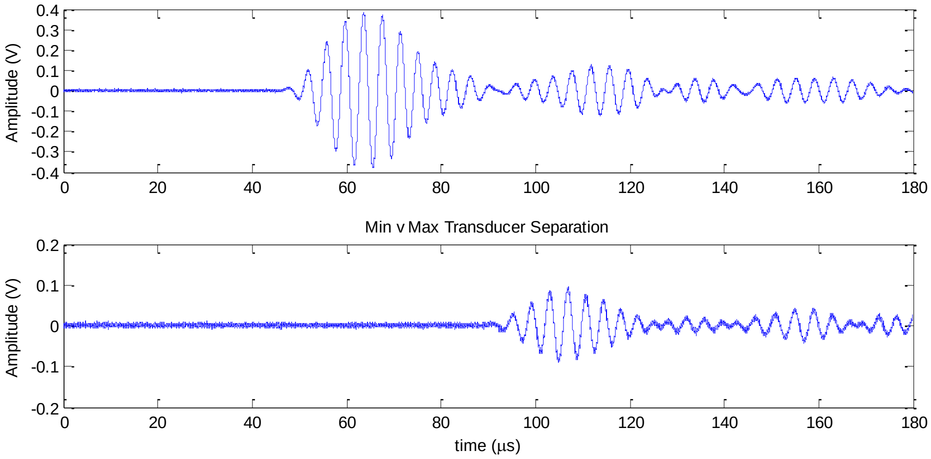

Figure 5.12: Variation in signal amplitude for UD plate. Transducer separation = 60 mm (top); transducer separation = 250 mm (bottom)

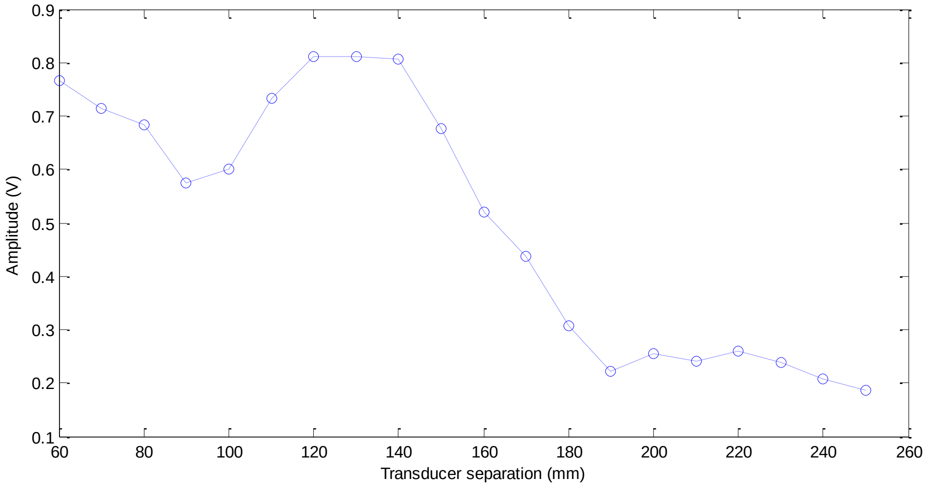

Figure 5.13: Attenuation for UD plate (amplitude)

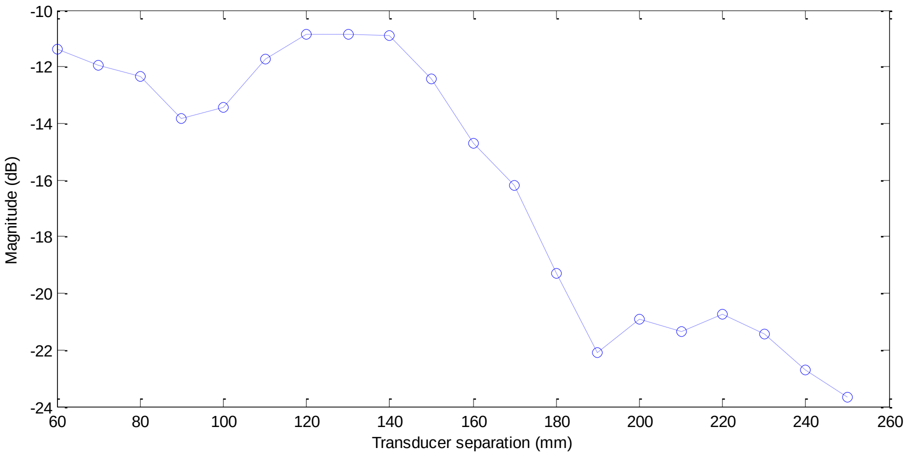

Figure 5.14: Attenuation for UD plate (dB)

The velocity measurements for the fastest mode are evaluated as illustrated in Figure 5.15.

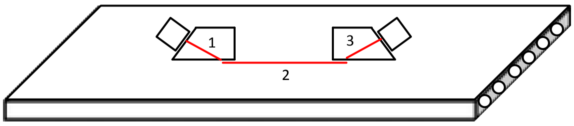

d1 = 49mm
d2 = 60mm
d3 = 49mm

Figure 5.15: Distance considered in time plots: d1, d2 & d3.

d_2 is the distance travelled through the GFRP specimen by the signal. The associated time is evaluated as:

$$t_2 = t_{arrival} - \left(t_1 + t_2\right) = 50\mu s - \left(18.35 + 18.35\right)\mu s = 13.3\mu s$$

$$v_{GFRP\,(UD)} = \frac{d_2}{t_2} = \frac{60mm}{13.3\mu s} = 4511ms^{-1}$$

Table 5.4 summarises the mean measured velocities together with the attenuation figures for both the bidirectional and UD samples.

Table 5.4: Velocity and attenuation measurements in GFRP materials at 250 kHz

Material	Fastest Mode Velocity (ms^{-1})	Attenuation (dB/m)
Unidirectional	4530	48
±45° (on-fibre axis)	4140	40
0° (off-fibre axis)	3430	145

To better understand the directional properties of GFRP characteristics, it is helpful at this stage to record what information can be extracted from the bidirectional GFRP (Table 5.3) and input them into a finite element model (FEM). Information as to mode sensitivity dependent upon orientation of wave propagation path can then be used to influence sensor positioning on the sample during experimental analysis

5.4 Characterising GFRP - FEA Modelling

In order to provide suitable material data for input to the FEM, an experiment was conducted to obtain the mechanical properties of bidirectional GFRP (described by Table 5.3). Details of the experiment are provided in Appendix B2. The longitudinal velocity, c_l, was measured as 4023.9 ms^{-1} and the maximum shear velocity, c_s, was 2136.9 ms^{-1}.

The following mechanical properties were recorded on-fibre:

- Young's Modulus, E = 2.097 e^{10}
- Shear Modulus, G = 8.043 e^{9}
- Bulk Modulus, B = 1.779 e^{10}
- Poisson's Ratio, ν = 0.3036
- Acoustic Impedance, Z = 7.087 e^{6}

Using Equations (5.1), (5.2), (5.3), the stiffness coefficients are provided in Table 5.5.

$$c_{11} = \frac{(1-v)E}{(1+v)(1-2v)} \tag{5.1}$$

$$c_{12} = \frac{vE}{(1+v)(1-2v)} \tag{5. 2}$$

$$c_{44}, c_{55}, c_{66} = \frac{1}{2}(c_{11} - c_{12}) \tag{5. 3}$$

Table 5.5: On-fibre GFRP stiffness coefficients

$2.8519e^{10}$	$1.2433e^{10}$	$1.2433e^{10}$	0	0	0
	$2.8519e^{10}$	$1.2433e^{10}$	0	0	0
		$2.8519e^{10}$	0	0	0
			$0.8043e^{10}$	0	0
				$0.8043e^{10}$	0
					$0.8043e^{10}$

The following mechanical properties were recorded off-fibre:

- Young's Modulus, E = 1.776 e^{10}
- Shear Modulus, G = 6.578 e^{9}
- Bulk Modulus, B = 1.975 e^{10}
- Poisson's Ratio, v = 0.3501
- Acoustic Impedance, Z = 7.087 e^{6}

Equations (5.1) to (5.3) provided the off-fibre stiffness coefficients in Table 5.6.

Table 5.6: Off-Fibre GFRP stiffness coefficients

$2.8519e^{10}$	$1.5362e^{10}$	$1.5362e^{10}$	0	0	0
	$2.8519e^{10}$	$1.5362e^{10}$	0	0	0
		$2.8519e^{10}$	0	0	0
			$0.6578e^{10}$	0	0
				$0.6578e^{10}$	0
					$0.6578e^{10}$

The information contained within Table 5.5 and Table 5.6 was used to characterise the model.

A single laminar model - generated using PZFlex (Weidlinger Associates) - with a bidirectional fibrous lay-up was created with an accompanying fibre volume ratio of

1:1, Figure 5.16. The model was defined using the off-fibre characteristics of Table 5.6 with on-fibre characteristics superimposed using the data in Table 5.7.

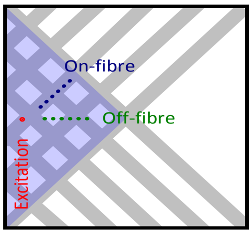

Figure 5.16: ±45° fibre arrangement with fibre volume 1:1

The analysis is conducted within the quarter area of the model where a ±45° fibre arrangement exists. A pseudo-delta function of amplitude 1 V, frequency 0.25 MHz and -90° phase impacted the model (as simulation of surface perturbation). The particle displacement data for 256 locations in the off-fibre direction, with a spatial resolution of 0.381 mm was recorded. The data was then transformed using a 2DFFT within a MatLab script file (provided in Appendix E). Figure 5.17 illustrates the propagating modes in the off-fibre direction, whilst Figure 5.18 shows the modes present in the on-fibre direction.

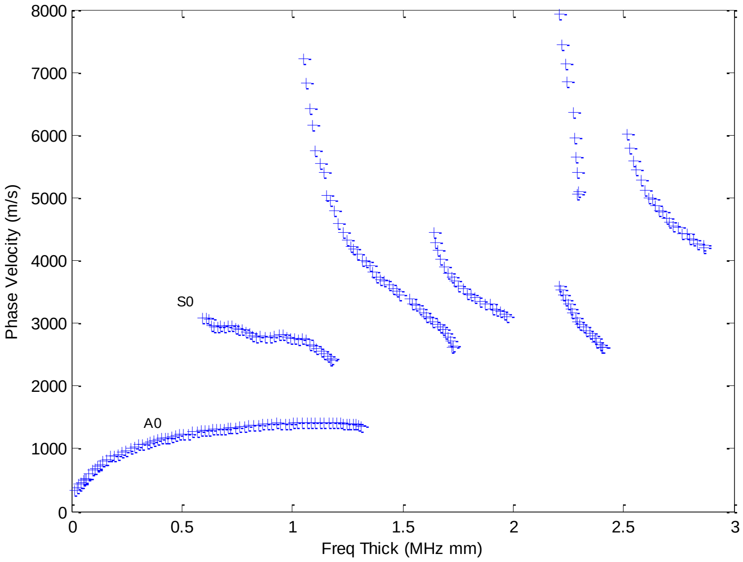

Figure 5.17: Excited wave modes within GFRP model for off-fibre direction

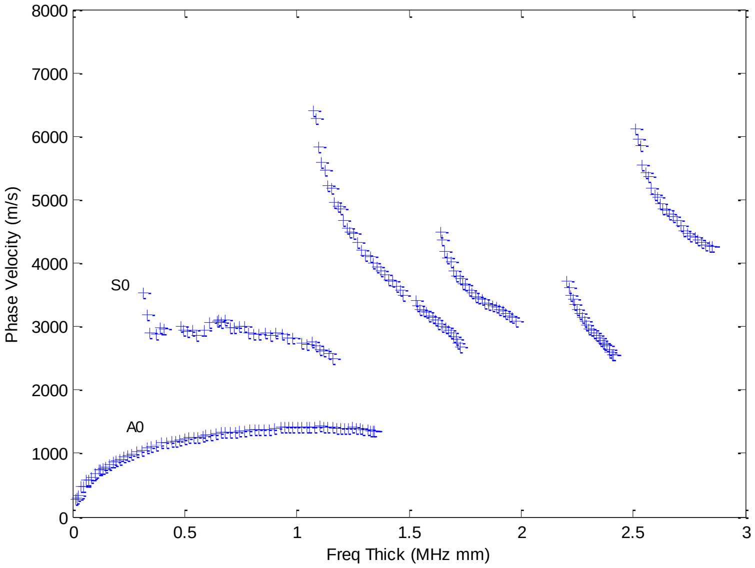

Figure 5.18: Excited wave modes within GFRP model for off-fibre direction

Both on- and off-fibre analysis show the S_0 and A_0 modes together with higher order modes. The cut-off frequencies of the higher order modes are greater than 1 MHz. In addition, these modes exhibit considerable dispersion when compared with the S_0 & A_0 modes. Since a typical characteristic of defect onset is dispersion, the higher order modes are less suited for structural analysis.

Figure 5.19 compares the on- and off-fibre characteristics of the S_0 and A_0 modes. It is observed that the A_0 mode is almost identical for both orientations – providing approximately the same bandwidth. The S_0 mode for both orientations exhibits similar phase velocity between 600 kHz and 1.2 MHz (off-fibre bandwidth). However, the on-fibre plot shows greater bandwidth extending down to 300 kHz, suggesting greater signal strength.

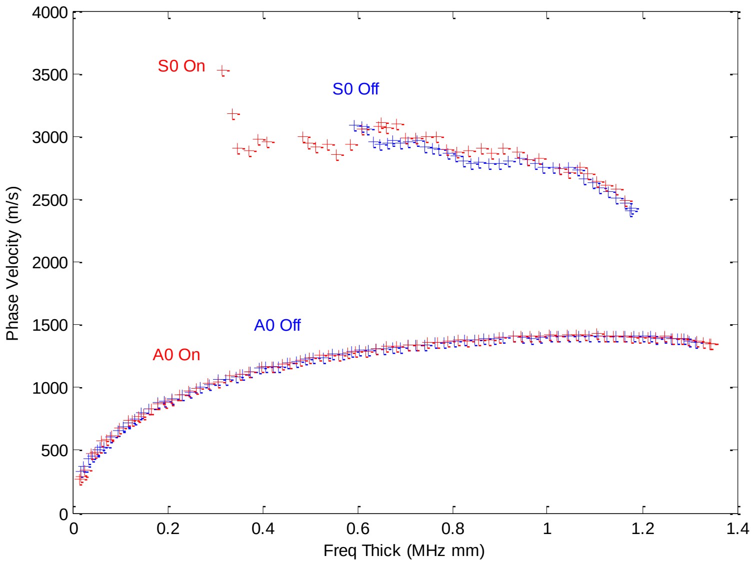

Figure 5.19: S_0 & A_0 mode comparison for on- versus off-fibre

Finite element analysis of bidirectional GFRP suggests a sensor arrangement aligned with on-fibre orientation to detect propagating stress waves arising from defect onset.

To ascertain precisely which modes are excited within a perturbed bidirectional GFRP requires experimental precision. Consequently, laser generation and reception is the chosen method of excitation to achieve the required level of spatial and temporal resolution.

5.5 Material analysis using laser generation/reception

In order to obtain definite information on in-plane particle motion in GFRP materials, pulsed lasers were used to excite nano-scale displacement within the sample's surface. The set-up offers precise spatial resolution which contributes towards the quality of output data. Lamb wave velocities are dependent on wave frequency and plate thickness. A variation of wave mode phase velocity over a range of frequencies for a particular plate-thickness is known as dispersion. Since the presence of dispersion may be an indicator of the presence of damage (e.g. a change in material thickness due to tensile loading), it is necessary to identify and avoid the range of frequencies over which dispersion for a particular mode in a particular material normally occurs when using the preferred sensors for structural integrity monitoring.

The process of laser excitation is achieved by rapidly heating a localised area on the surface via a pulse of precise frequency. At low incident powers, the generation of thermal and elastic waves can be achieved. This is known as the *Thermoelastic Regime*. The electromagnetic energy generated by the laser interacts with the surface of a non-reflective material of which some of the energy is absorbed by resistive losses (scattering processes). Energy not absorbed is reflected. The absorbed energy is progressively attenuated as it penetrates into the sample such that absorption and reflection of energy takes place within the surface layer or skin of the sample. Skin depth is defined such that at a depth δ, the wave amplitude is attenuated $1/e$ of the surface amplitude, where e is the energy density. For shallow absorption, the energy density can be very high, creating a pressure, Equation (5.4).

$$p = \rho \Gamma e \tag{5. 4}$$

Where ρ is the density and Γ is Gruneisen’s coefficient. The rapidly heated local volume element generates stresses and strains that act as the ultrasonic source, Figure 5.20. The principal stress components (D_{11}, D_{22}) are parallel to the surface while the normal surface component (D_{33}) is negligible.

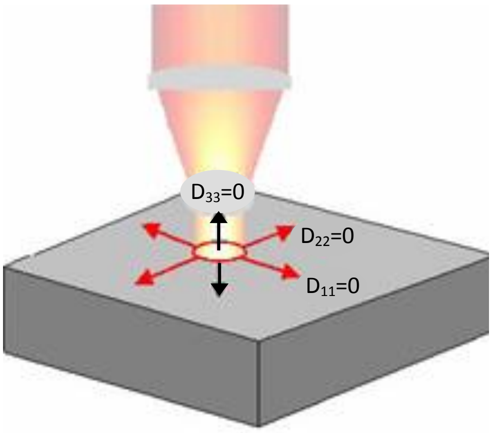

Figure 5.20: Thermoelastic Regime, [125]

In practice, vaporization of the sample surface is easily produced when using pulsed lasers. The average power in a typical 200 mJ, 10 ns duration pulse is 20 MW. This is above the threshold for vaporisation which produces plasma known as the Ablation Regime - a formation with stresses predominantly normal to the surface of the sample, Figure 5.21.

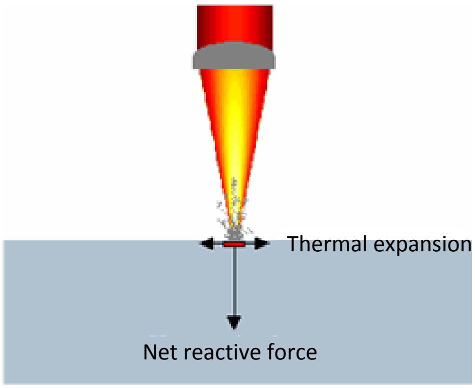

Figure 5.21: Ablative Regime, [125]

The ablation regime causes damage but in applications where surface conditions are not important, this technique can be considered non-destructive, [126]. Optical absorption, conversion to ultrasonic energy and ultrasonic propagation are all affected by changes at the material surface. Thus in order to maximize the absorption of the sample a layer of paint is applied to the material surface. A coating of matt black paint increases the absorption to almost 100%, [125]. As a result of the absorptivity of the layer of paint, sufficient energy exists to vaporise the coating which is blown off causing a normal reaction on the surface. Thus, subsequent pulses are incident on the original material surface. Therefore, the combination of stresses on the surface for the first shot is likely to be an amalgam of both in-plane and normal stresses.

Laser-excited ultrasound was utilised to ascertain the material properties of the 500 mm x 500 mm x 2 mm GFRP sample - coated with matt black spray paint to ensure absorption - and determine the characteristics of the fibre alignment. Elastic waves were generated optically using a Quantel Brilliant B Q-switched ND:YAG laser – able to deliver a pulse energy of 850 mJ at 1065 nm with a pulse width duration of 5 ns and a repetition rate of 10 Hz giving a peak power of 170 MW and an average power of 8.5 W. The sample was affixed to a stepper motor positioner using 4 screws penetrating the full thickness of the sample. The reflections that may arise from the off-fibre location of these screws was considered as having little impact on the fastest wave propagating modes due to the extended propagating path any reflected signal would travel and the associated attenuation when off-fibre.

The laser focus configuration was adjusted for the purposes of comparative analysis.

5.5.1 Unfocussed Laser Tests

The set-up for an unfocused laser exhibits the lowest energy density and lowest ablation profile. The purpose of this set-up is to favour the thermoelastic regime and observe the presence of the dominant in-plane motion which will naturally couple more efficiently into the symmetric Lamb wave modes. Due to the non-homogeneity of the sample, analysis of the on-fibre data (±45°) is compared with the off-fibre data (0° and 90°) to observe any differences.

The high power laser perturbed 256 points on the GFRP surface at 0.5 mm intervals. Light from the pulsed Nd:YAG laser was directed onto the sample surface. Control of the surface power density determined the thermoelastic regime operation by controlling the laser output power. This was accomplished by altering the Q-switch timing with respect to the main flashlamp synchronisation in the laser. Details of the experimental set-up are provided in Appendix B3. A post data-capture image of the analysed GFRP is shown in Figure 5.22.

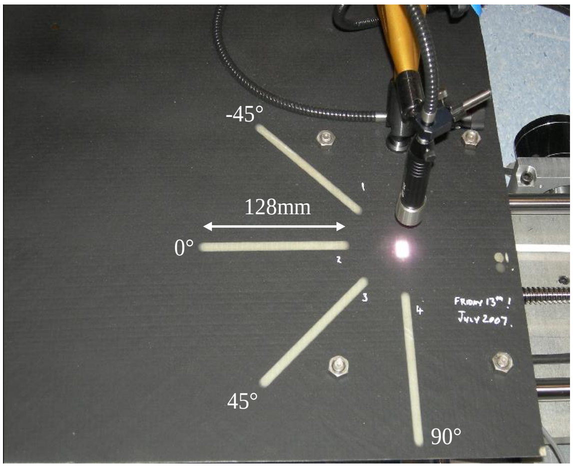

Figure 5.22: Sample showing test directions -45°, 0°, 45°, 90°

A typical received time signal from a single point measurement, termed an A-Scan, is illustrated in Figure 5.23. The first arrival at 117 μs is the S_0 mode.

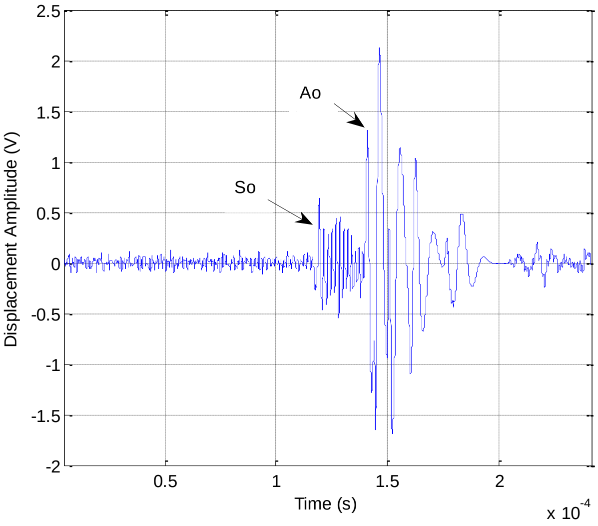

Figure 5.23: Single point measurement on GFRP

The S_0 mode is observed to arrive first followed by the A_0 mode. The A_0 mode has significantly larger amplitude, attributed to the dominant normal out-of-plane displacement characteristics at low frequency-thickness product values (when compared with the S_0 mode).

The B-Scan for the normalized A-scans in the off-fibre direction is observed in Figure 5.24. As expected, the ultrasonic energy within the B-scan propagating in the on-fibre (45°) direction, Figure 5.25, is significantly greater than the ultrasonic energy illustrated for the off-fibre (0°) direction. A significant drop in energy magnitude for the S_0 mode may be observed.

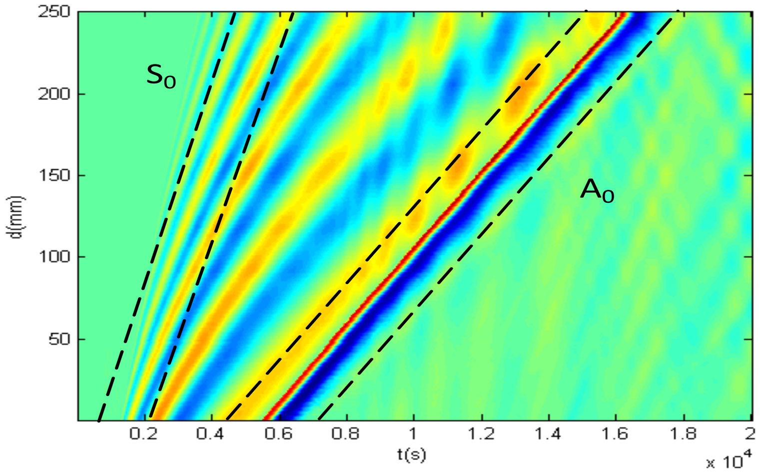

Figure 5.24: Off-fibre (0°) B-scan

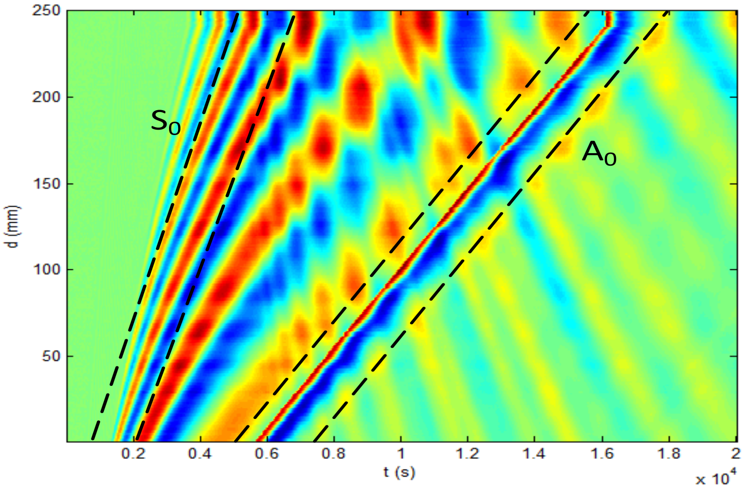

Figure 5.25: On-fibre (45°) B-scan

5.5.1.1 Applied Signal Processing Techniques

In order to extract more information from the data pertaining to the propagating modes, it must be analysed temporally and spatially. A two dimensional function $h(x,y)$ has a two dimensional transform $H(u,v)$, analogous to the one-dimensional case, given by Equation (5.5). Figure 5.26(a) illustrates an example of a two dimensional cosine surface.

$$H(u,v)=\int_{-\infty}^{\infty}\int_{-\infty}^{\infty}h(x,y)e^{-j2\pi(ux+vy)}dx\,dy \tag{5.5}$$

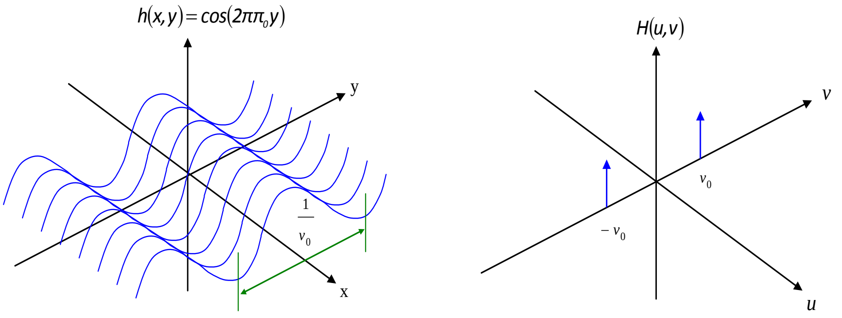

(a) (b)

Figure 5.26: Two Dimensional Fourier Transform of a cosine surface

Extracting a section from the $y-h$ plane shows that the function oscillates at v_0 cycles per unit length along the *y*-axis. Frequencies associated with functions of time and length, are termed temporal and spatial respectively. Figure 5.26(b) illustrates the two dimensional transform of this cosine surface. Figure 5.27 shows the cosine surface rotated by θ°.

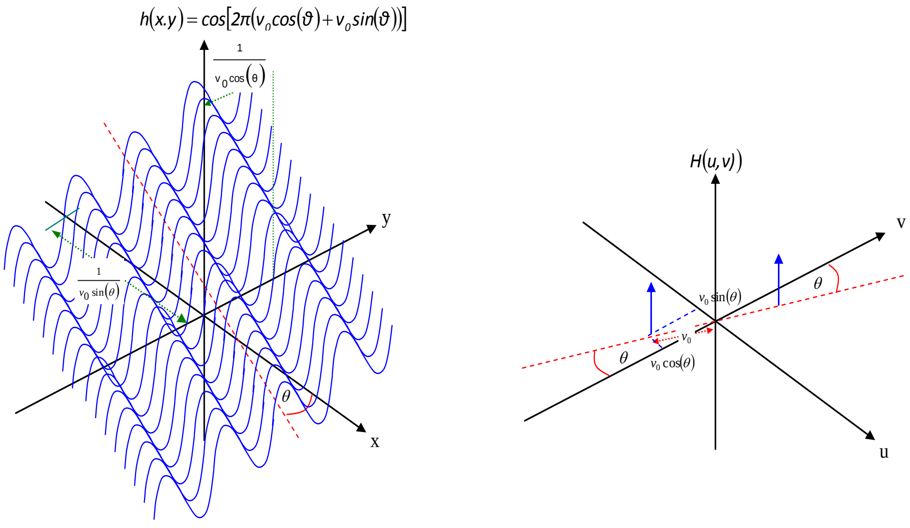

(a) (b)

Figure 5.27: Two Dimensional Fourier transform of cosine surface rotated through θ°

If a section is cut through the $x-h$ plane, it observed that the waveform oscillates with a spatial frequency of $v_0 sin(\vartheta)$ cycles per unit of x. Similarly, a section cut through the $y-h$ plane oscillates with a frequency of $v_0 cos(\vartheta)$ cycles per unit of y. The two-dimensional Fourier transform is observed in Figure 5.27(b). The spatial frequency at which the surface oscillates perpendicular to the lines of zero phase is given by $v_0 = \left[v_0 cos^2(\vartheta) + v_0 sin^2(\vartheta)\right]^{\frac{1}{2}}$. The impulse functions have swung through θ°, [127]. The two-dimensional Fourier transform, $H(u,v)$, can be viewed as two successive one dimensional transforms, Equations (5.6) to (5.8).

$$H(u,v) = \int_{-\infty}^{\infty} e^{-j2\pi 2\pi}\left[\int_{-\infty}^{\infty} h(x,y)e^{-j2\pi 2\pi}\,dx\right]dy \tag{5.6}$$

$$Z(u,y) = \int_{-\infty}^{\infty} h(x,y)e^{-j2\pi 2\pi}\,dx \tag{5.7}$$

$$\Rightarrow \quad H(u,v) = \int_{-\infty}^{\infty} Z(u,y)e^{-j2\pi 2\pi}\,dy \tag{5.8}$$

The term within the brackets of Equation (5.6) is merely the one-dimensional Fourier transform of $h(x,y)$ with respect to *x*, as indicated in Equation (5.7). Subsequently, Equation (5.8) is the one-dimensional Fourier transform of $z(u,y)$ with respect to *y*. This interpretation can be extended to the two-dimensional FFT (2DFFT) by assuming that the surface function has been sampled in the *x* dimension with sample interval T_x, and sampled in the y dimension with sample interval T_y. The sampled function is $h(pT_x, qT_y)$ where $p = 0,1,\ldots,N-1$ and $q = 0,1,\ldots,M-1$ leading to the resulting 2DFFT of Equation (5.9).

$$H\left[n/NT_x, m/MT_y\right] = \sum_{q=0}^{M-1}\sum_{p=0}^{N-1} h\left[pT_x, qT_y\right] e^{-j2\pi\left(\frac{mq}{M}+\frac{Np}{N}\right)} \tag{5.9}$$

5.5.1.2 Wave Mode Analysis

A 2DFFT MATLAB script-file was implemented on each spatially incremented temporal dataset. Whilst the ultrasonic laser source excites waves of all frequency-wave number combinations, only a few well-defined curves present significant amplitude. Using Equation (5.10), the data was manipulated to provide a relationship between phase velocity and frequency-thickness, Figure 5.28.

$$k = \frac{\omega}{v} \tag{5.10}$$

Where, ω is the wave mode frequency, v is the wave mode velocity and k is the wave number.

It is observed that there are two wave modes which extend to very low frequencies: S_0 and A_0.

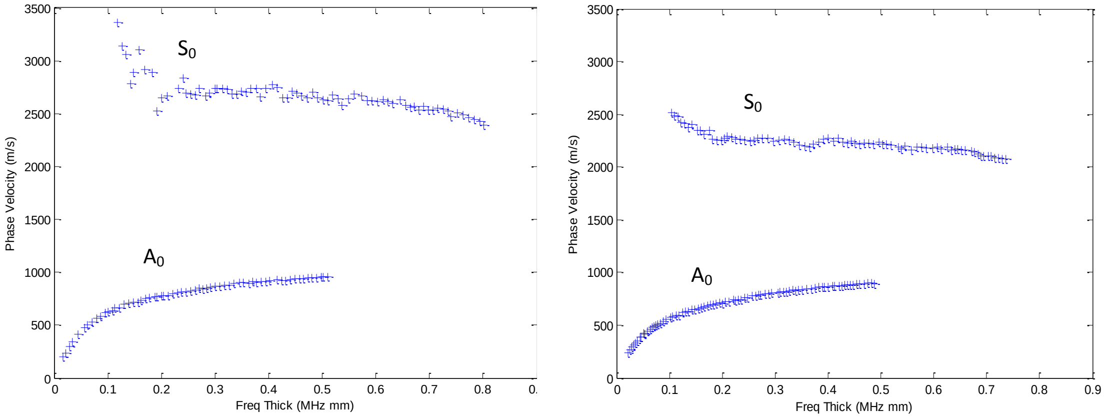

(a) – Phase velocity vs Freq Thick at 45°

(b) – Phase velocity vs Freq Thick at 0°

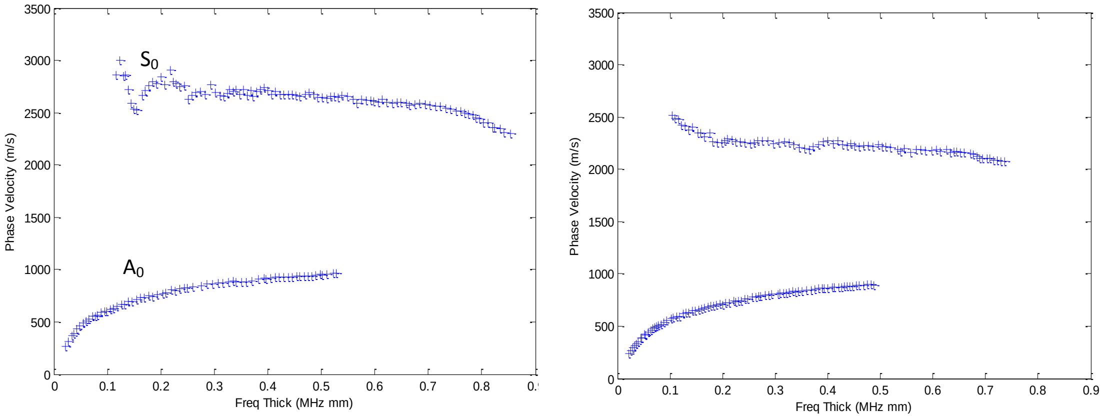

(c) – Phase velocity vs Freq Thick at -45°

(d) – Phase velocity vs Freq Thick at 90°

Figure 5.28: Phase velocity vs. frequency-thickness: on-fibre, (a) & (c); off-fibre, (b) & (d)

Generally, the phase velocities for the ±45° directions (on-fibre) are greater than the phase velocities for 0°/90° directions for the same frequency-thickness value.

The S$_0$ mode shows some scatter in the dispersive region. This phenomenon occurs because the dispersion curves are naturally presented in the wave-number/frequency-thickness domain. Wave-number and phase velocity are equated through $c_n = f_n \big/ k_m$. The discrete relationship is given by Equation (5.11).

$$c = \frac{n \big/ NT_s}{m \big/ M\Delta\Delta} \quad ms^{-1} \tag{5.11}$$

Where, n is defined by $1 \le n \le N$, and m is defined by $1 \le m \le M$.

However, the conversion is not linear. The frequencies associated with the wave-number domain are spatially uniform and exhibit a constant resolvable error between bins. This is mapped onto the spatially non-uniform frequency grid of the phase velocity domain, exhibiting a non-constant irresolvable error between bins. The conversion from wave-number domain into phase velocity domain changes the constant wave-number error into a non-constant phase velocity error, Figure 5.29, [126].

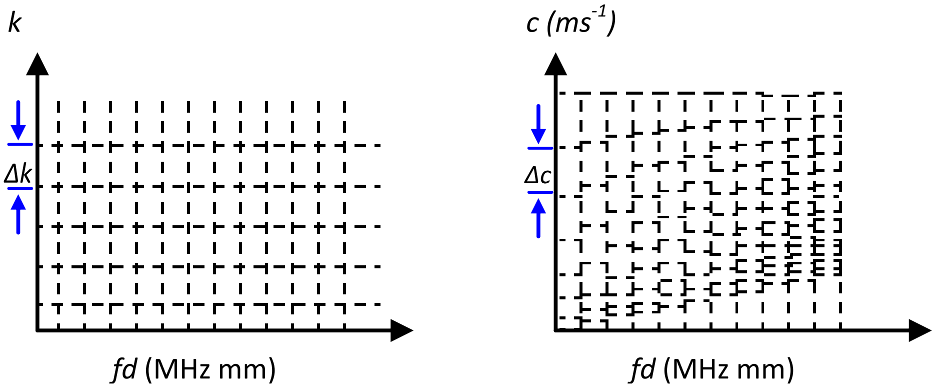

Figure 5.29: Conversion of frequency bins – wave no. domain (left) to phase velocity domain (right)

The error is represented by Equation (5.12).

$$\Delta c = c(nf, k(m+1)) - c(nf, km) = \frac{c}{(m+1)} = \frac{nf}{k(m^2 + m)} \qquad (5.12)$$

As the wave-number increases for a certain frequency, the error Δc decreases. Conversely, for a certain wave-number, as the frequency increases, Δc increases.

Figure 5.30 illustrates the contour levels of the irresolvable error given by Equation (5.12) together with the experimental dispersion curves.

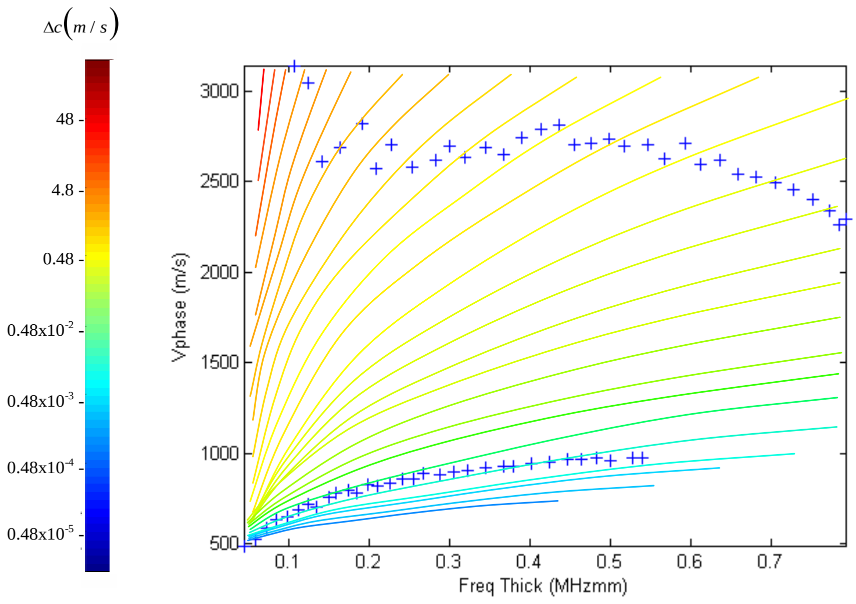

Test Scan 45°

Figure 5.30: Experimental dispersion curves with irresolvable error *Δc*

It is observed that the area immediately surrounding the vertical asymptotic region of the S_0 mode exhibits the greatest errors, increasing logarithmically from low phase velocities to high phase velocities at low frequency-thickness values.

5.5.2 Spot Focused Laser Tests

If the source laser beam is focused to a very small spatial spot dimension, a spatial impulse source is created that allows the excitation of a wide variety of spatial modes. However, when the laser beam is focused in this way, the incident optical power increases, the surface temperature rises until the boiling point of the sample is reached and some material is vaporised, ionised and a plasma is formed, Figure 5.21 , [125].

Details of the spot-focus laser set-up (similar to the unfocussed set-up but with increased laser energy) are provided in Appendix B3. The extracted wave modes using a 2DFFT are shown for both on-fibre and off-fibre directions in Figure 5.31.

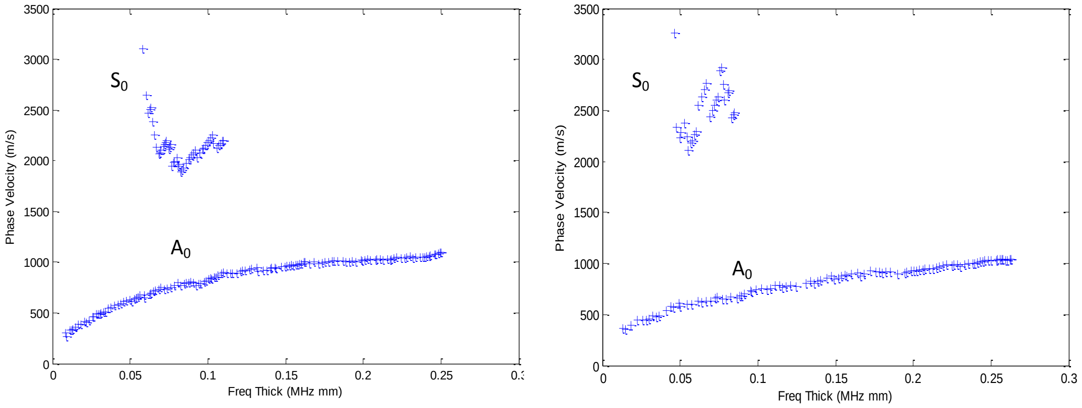

Figure 5.31: Spot focused laser tests: on-fibre (left); off-fibre (right)

A strong A_0 is observed where close analysis of the on-fibre (45°) and off-fibre (90°) directions - for like frequency-thickness values – illustrates greater phase velocity values in the on-fibre +45° direction. There is less of an S_0 mode presence than there was for the unfocused tests. This is perhaps explained by the fact that the laser signal is focused upon a smaller area which thus creates a greater intensity of energy such that the laser source is operating within the Ablative Regime (Figure 5.21). The plasma formation initiates stresses that are predominantly normal to the surface of the sample due to the fact that the depth of the heated area is not negligible with respect to the heated surface (i.e. the dipole normal to the surface, D_{33} is dominant, Figure 5.20). In the unfocused set-up, the depth of the heated area was negligible with respect to the heated area and more likely to create in-plane stresses (i.e. D_{33} is less dominant).

5.5.3 Line Focused Laser Tests

To improve the directivity of the laser energy, in favour of the directional properties of the sample material, a cylindrical lens was used to focus the beam into a line source. The line focus encourages propagation perpendicular to the axis along which the line focus is generated and where the interferometer sensing spot is focused. Details of the line-focused laser set-up are provided in Appendix B3.

The extracted wave modes using a two dimensional FFT are shown for both on-fibre and off-fibre directions in Figure 5.32.

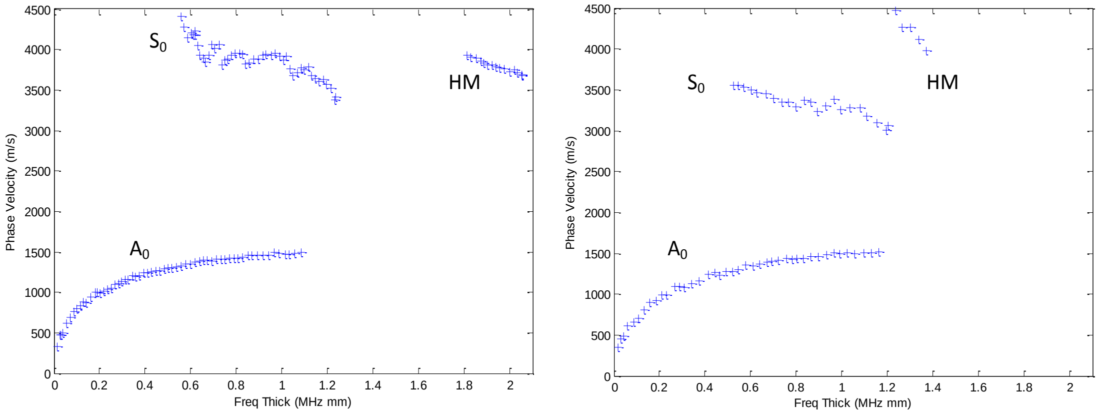

Figure 5.32: Line Focus Tests; on-fibre (left); off-fibre (right)

A strong A_0 is observed for both 45° (on-fibre) and 90° (off-fibre) directions with the phase velocity being slightly higher in the former for specific frequency-thickness values. The S_0 mode is also observed, again showing scatter in the dispersive region due to the non-constant irresolvable error between bins (Δc). A higher order mode (HM) is also observed for both on-fibre and off-fibre orientations. There is a greater likelihood that due to the increased in-plane energy, stress waves propagated through the GFRP plate in an increased number of symmetric wave modes. It is not immediately evident that it is the same mode which appears in each plot.

The directionality of the line-source (plane waveforms generated parallel to the line) decreases the spreading attenuation in comparison with an omnidirectional circular spot source. As a result, the ablation is relatively weak: the ablation volume is similar to that for the spot focus experiment but it is spread over a wider area and produces less intense plasma. Thus a combination of improved directionality, reduced geometrical attenuation, and weak ablation has produced greater in-plane displacement.

5.5.4 Comparison of laser experimental data with FE model

The FE model introduced in Section 5.4, and characterised by Table 5.5 and Table 5.6, was compared with the spot-focused laser tests of Section 5.5.2 to assess the degree of correlation, Figure 5.33 and Figure 5.34.

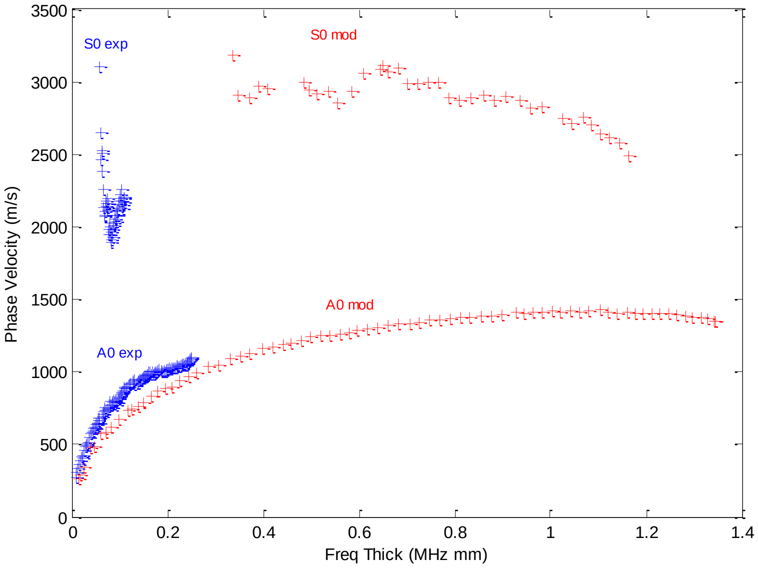

Figure 5.33: Spot focus laser data (blue) against FE model (red) – On-fibre

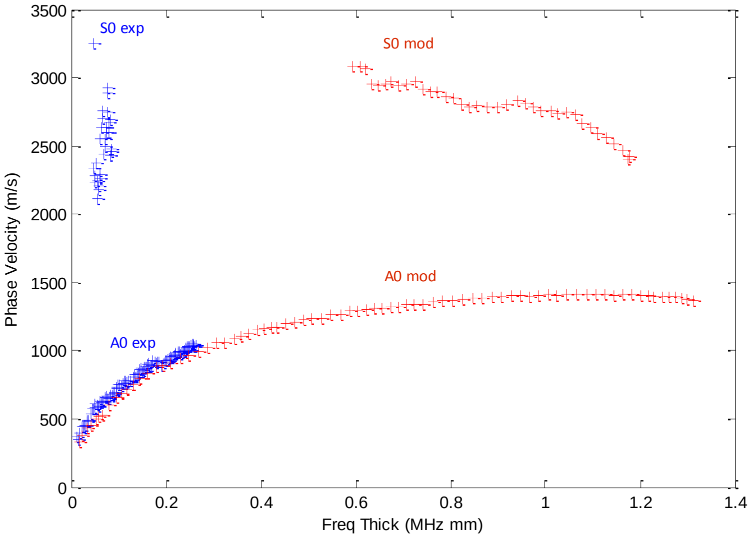

Figure 5.34: Spot focus laser data (blue) against FE model (red) - Off-Fibre

The spot-focused experimental data was the preferred dataset for analysis because the laser configuration more closely resembles the excitation used to analyse the model - described in Section 5.5.1. There is reasonable A_0 mode agreement for both the on-fibre and off-fibre analysis. However, there is very little agreement for the S_0 mode in either analysis.

The model exhibits a number of weaknesses: off-fibre directions (angle ≠ 45°) are all defined by the same elastic constants (those for 0°); the volume fraction ratio was 1:1, and the fibres featured a rectangular cross-section (rather than circular).

5.5.5 Material Analysis using PZT transducers

Having identified that it is possible to extract fundamental wave-mode information (S_0, A_0) from a bi-directional GFRP laminate using a laser, it is necessary to establish whether such information can be acquired using techniques that facilitate field operation. The following sections analyse wave mode characteristics within GFRP samples using piezo-electric transducers for both excitation and detection. In particular, two different sensor arrangements were studied: a PZT with omnidirectional properties; and an interdigitated sensor with particular directional properties.

An experiment was set up to establish the effects of material anisotropy on Guided Wave propagation using PZT transducers. This analysis involved two different GFRP lamina lay-ups: bidirectional with 0°/0° lamina arrangement and ±45° fibre orientation; quasi-isotropic with 0°/±45°/90° fibre arrangement.

5.5.5.1 Bidirectional GFRP Sample

A bi-directional GFRP plate was considered for analysis, the details of which are provided in Table 5.7.

Table 5.7: Material properties for bidirectional GFRP sample

HexPly M34/40%/600T2/G	Measurement	unit
Areal weight (glass fibre)	590±29	gm^{-2}
Plain Weave	2 x 2 Twill	
Fibre type	Glass fibre epoxy prepreg	
Fibre	Warp: 1200	tex
	Weft: 1200	tex
Thread count	2.5 x 2.4	cm^{-1}
Areal Weight (prepreg)	983±46	gm^{-2}

The objective of the experiment was to observe the propagating wave modes propagating within a bidirectional GFRP sample. Details of the experimental set-up are provided in Appendix B4.

The left image of Figure 5.35 illustrates the dispersion curves for the on-fibre, whilst the image on the right illustrates the dispersion curves for the off-fibre case over a normalised frequency-thickness scale.

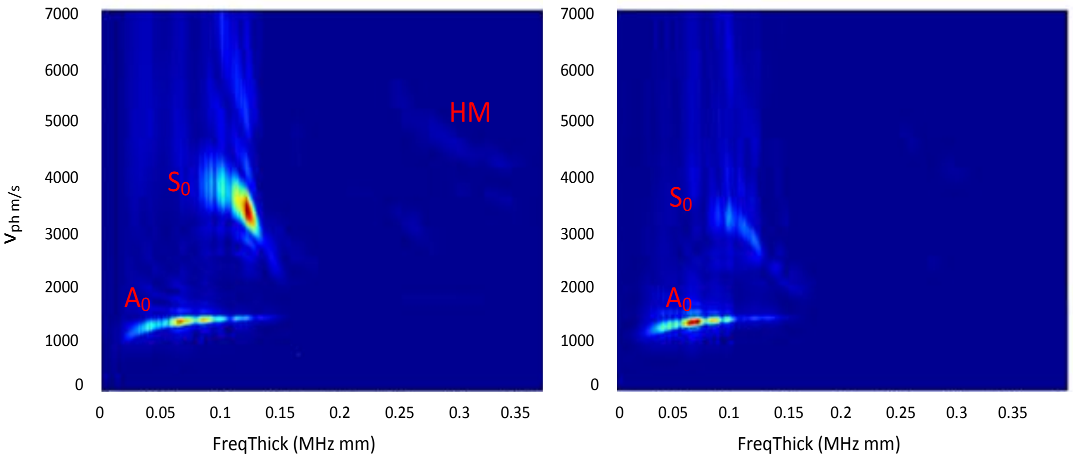

Figure 5.35: Dispersion Curves for Bidirectional GFRP laminate: on-axis direction, left; off-axis direction, right.

The left image of Figure 5.35 shows a strong A_0 mode and S_0 for the on-fibre analysis together with some higher order modes (HM). The right image of Figure 5.35 shows only the presence of both the A_0 and S_0 modes for the off-fibre analysis, i.e. no discernible presence of higher order modes. For the off-fibre analysis, reduced energy in the S_0 mode may also be observed. Avoiding dispersion, the usable bandwidths are: $f \geq 80$ kHz for A_0; and $f \leq 80$ kHz for S_0.

5.5.5.2 Quasi-isotropic GFRP Sample

A quasi-isotropic plate was subsequently considered for analysis. The material layup is given in Table 5.8.

Table 5.8: Stacking sequence for quasi-isotropic sample

Ply number	Orientation of layers
1	Woven (0º/90º)
2	Biaxial (± 45º)
3	Woven (0º/90º)
4	Woven (0º/90º)
5	Biaxial (± 45º)
6	Woven (0º/90º)

Full details of the GFRP sample are provided in Table 5.9 and Table 5.10.

Table 5.9: Material properties for GFRP sample - weave

WRE581T	Measurement	unit
Areal weight (glass fibre)	576	gm^{-2}
Plain Weave	2 x 2 Twill	
Fibre type	E-glass	
Fibre	Warp: 600	tex
	Weft: 600	tex
Thread count	5 x 4.6	cm^{-1}

Table 5.10: Material properties for GFRP sample - biaxial

XE905	Measurement	unit
Areal weight (glass fibre)	912	gm^{-2}
Style	±45° Biaxial	
Fibre type	E-glass	

The same ultrasonic measurement system (with accompanying PZT29 transducers) of was used to observe the propagating wave modes within the quasi-isotropic GFRP sample (Appendix B4). The resulting 2DFFT analysis is shown in Figure 5.36.

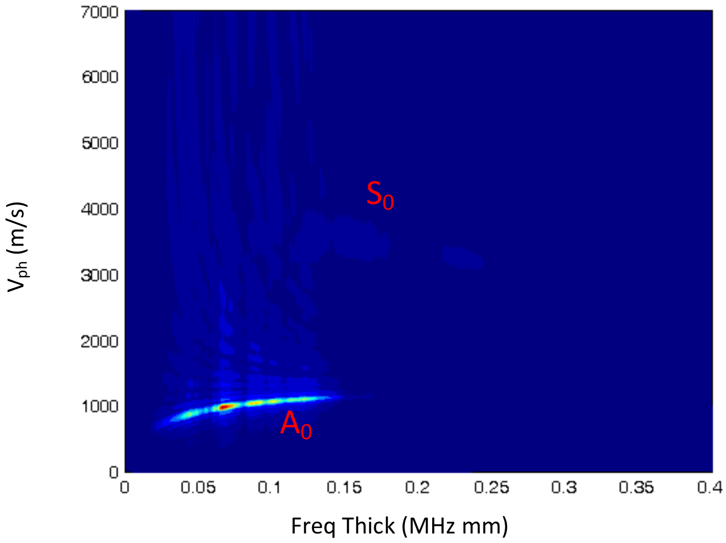

Figure 5.36: Dispersion Curves for on-axis direction – quasi-isotropic GFRP laminate

For the on-fibre analysis, there exists a strong A_0 mode whilst the S_0 mode exhibits significantly less energy and is not as dispersive at high frequencies (compared with the bidirectional GFRP material). Avoiding dispersion, the usable bandwidths are: $f \geq$ 80 kHz for A_0; and $f \leq$ 150 kHz for $S_{0.}$

5.5.6 Material Analysis using MFC transducers

Macro Fibre Composite (MFC) sensors are interdigitated transducers which are able to excite and sense in-plane displacement. The directional characteristics of the sensor are such that it is sensitive to in-plane displacement in the 0°−180° axis for isotropic materials, [114]. Therefore, the directional properties of the sensor can be oriented to match the directional properties of the GFRP material to which it is attached to increase sensitivity. Comprising several layers, the piezocomposite design ensures that the sensor is flexible and able to conform to a material surface whilst also remaining durable. The piezoceramic fibres are laid out in a rectangular cross-section and sandwiched between layers of homogenous epoxy for structural reinforcement. Orthotropic polymide layers, etched with an electrode pattern, are then laminated to the top and bottom configured perpendicularly to the piezoceramic fibres, Figure 5.37.

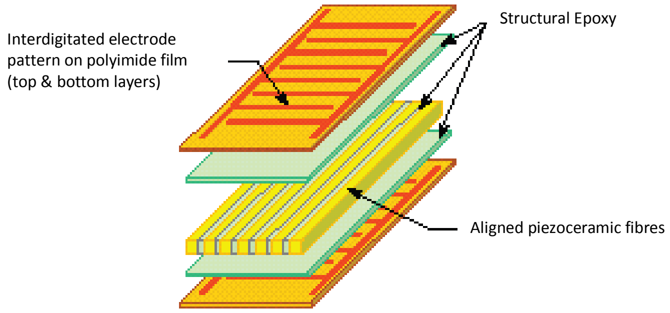

Figure 5.37: Layered construction of a typical MFC , [128]

This structure provides the characteristics of a monolithic transducer coupled with improved flexibility. MFCs are designed to detect displacement that is predominantly in-plane. They are, therefore, most sensitive to the detection of the S_0 mode.

5.5.6.1 MFC Sensor Type

To establish the MFC sensor type with the greatest sensitivity to GFRP, three different sensors were identified:

- M8507 sensor with 85 mm length and 7 mm width
- M2807 sensor with 28 mm length and 7 mm width
- M2814 sensor with 28 mm length and 14 mm width

An experiment was conducted to assess whether the active length of an MFC sensor had any impact upon its performance. Due to its length, (85 mm), the M8507 sensor is particularly suitable for this purpose. The sensor was bonded to the bidirectional GFRP surface using Locktite super glue. An applied force of 45 kN (to facilitate a successful bond and good coupling) was achieved using of a flexible load manipulator and measured using a load cell. Figure 5.38 illustrates the set-up.

Figure 5.38: MFC bonded to GFRP sample using flexible load manipulator

A transmitter and a receiver was bonded to a bidirectional GFRP structure separated by 700 mm. Signal details are provided in Appendix B6. The sensor response to the fastest propagating wave mode is illustrated in Figure 5.39 and shows the greatest SNR occurring at 25 kHz. It is observed that the response fluctuates considerably across the spectrum.

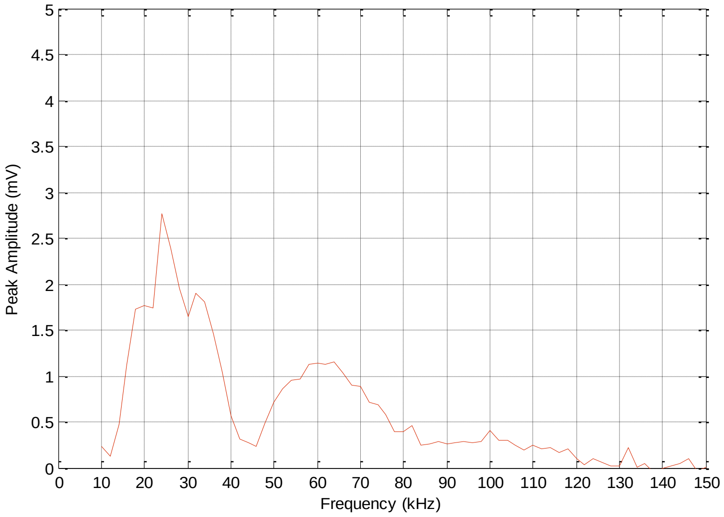

Figure 5.39: M8507 frequency response for an active length of 85 mm

The length of the sensor was subsequently shortened in six successive 10 mm increments to observe the effect on the frequency response. Both the transmitter and the receiver were simultaneously cut in such a way as to maintain the integrity of the sensor during the course of the experiment, Figure 5.40.

Figure 5.40: M8507 MFC sensor active area shortened in 10mm steps

This process was repeated until the active sensor length was shortened to 25 mm. The results are presented in Figure 5.41. As the sensor length is shortened, it may be observed that the frequency at which the peak response occurs increases. This observation is better illustrated in Figure 5.42. The peak A-scan amplitude for each sensor length is shown in Figure 5.43 where it is indicated that the greatest SNR is achieved at a sensor length of approximately 50mm.

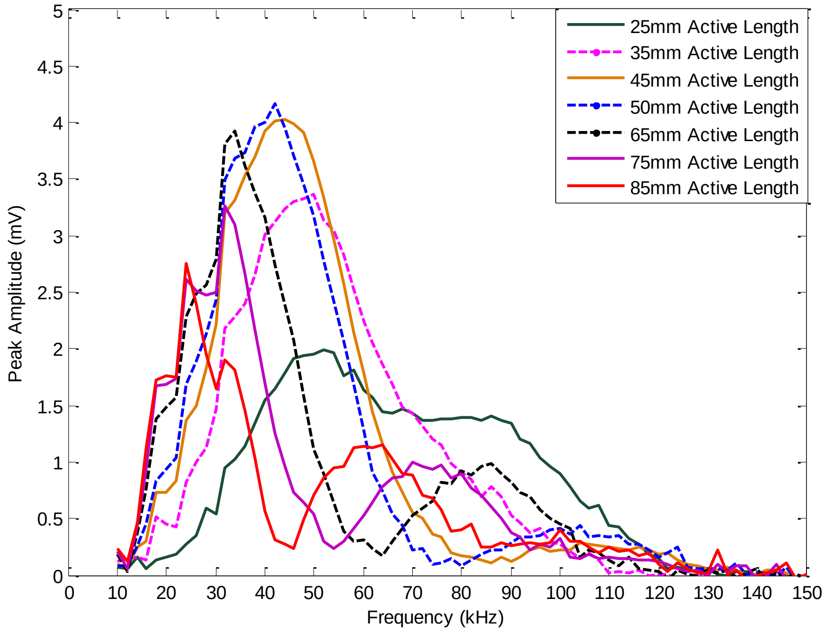

Figure 5.41: Fastest mode frequency response for different M8507 lengths vs. frequency on a GFRP sample. Tx and Rx separated by 700 mm Pitch-Catch on a GFRP plate.

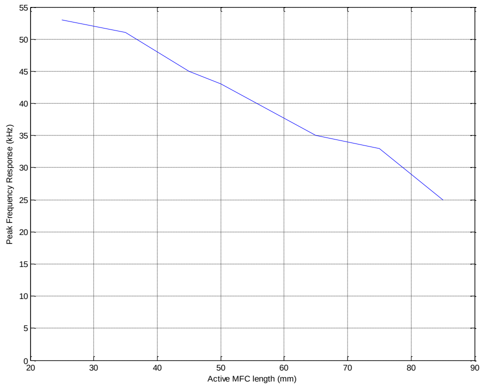

Figure 5.42: Identified frequencies for greatest sensitivity based upon M8507 active length

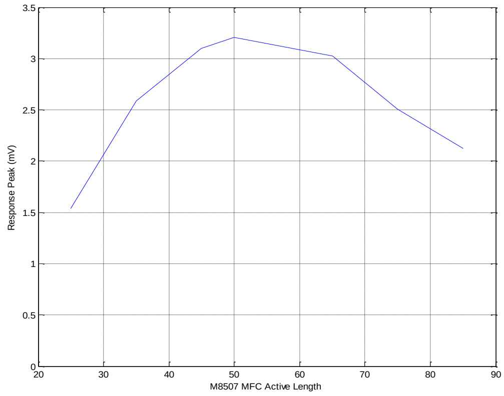

Figure 5.43: Response peak for different M8507 lengths

Extending the analysis to include three different pairs of MFC sensor types, sensors were bonded to the GFRP sample: M2814, M2807 and M8507, Figure 5.44. Each transmitting sensor was separated from its receiver by 700 mm.

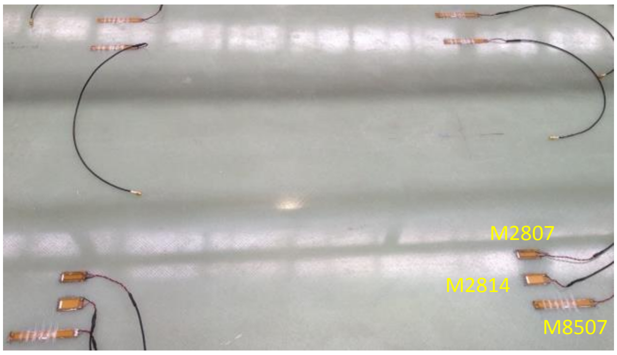

Figure 5.44: Three types of MFC sensor analysed: M2807 (top); M2814 (middle); M8507 (bottom)

Figure 5.45 shows the frequency response of three MFC sensors: 85 mm M8507 (blue); M2807 (green); M2814 (red). For completeness, Figure 5.46 includes all active lengths of the M8507 (25 mm – 85 mm). It is clearly observed that the M2814 has a frequency response with a four-fold improvement over the next best sensor response: M2807.

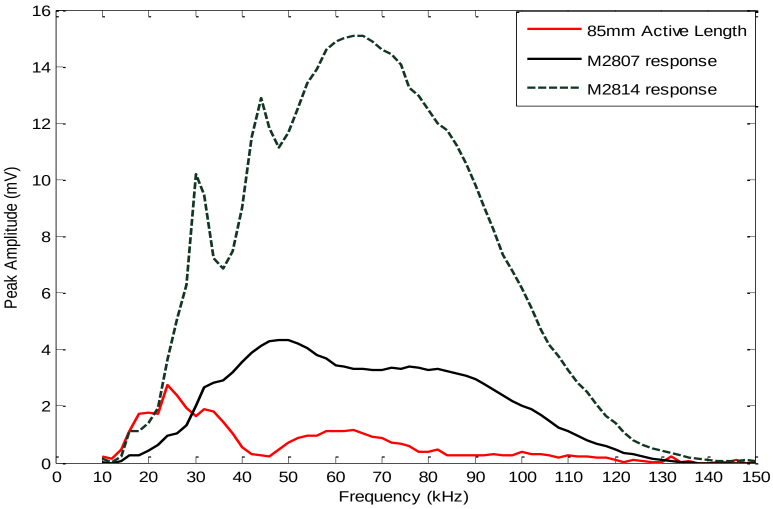

Figure 5.45: Frequency responses for M8507 (blue), M2807 (green) & M2814 (red) sensors over a bandwidth of 140 kHz in 2 kHz steps

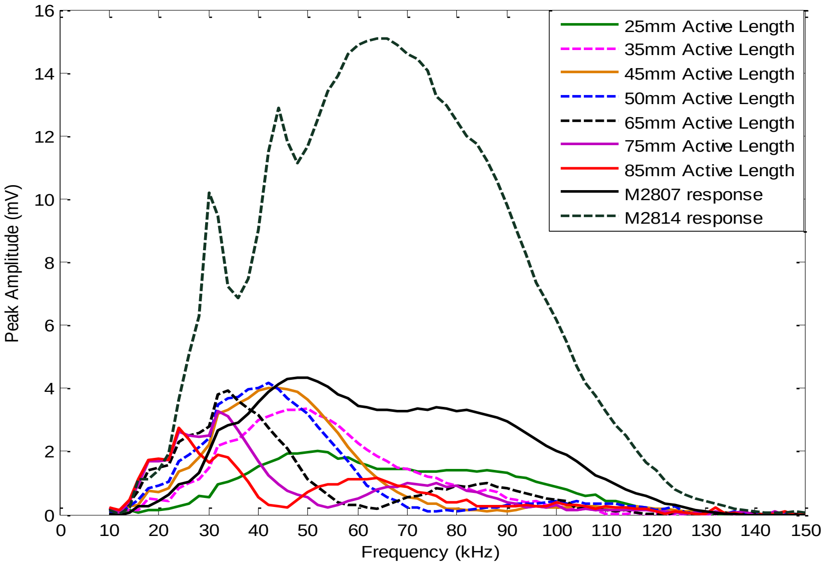

Figure 5.46: Frequency Responses for all length of M8507, and M2807 and M2814 sensor

Closer analysis of the M2814 sensor response shows that the bandwidth with maximum response is between 55 kHz and 75 kHz. To be certain of the fidelity of the M2814 response, the same unaltered sensor arrangement was tested after a period of four months and then again after an additional three month period, Figure 5.47.

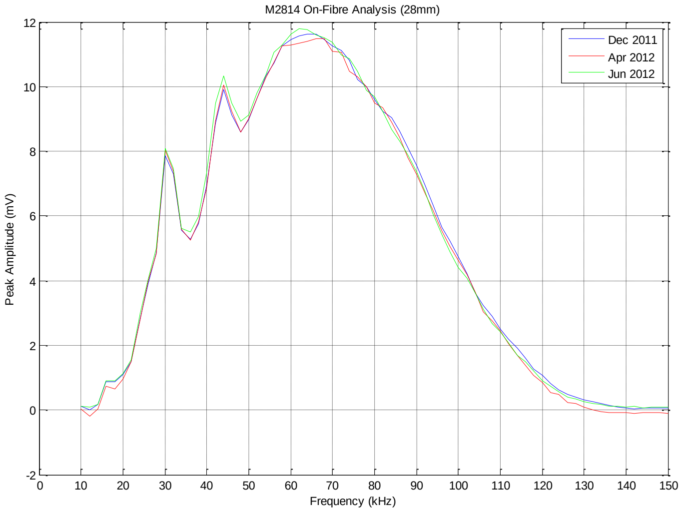

Figure 5.47: Frequency responses for the M2814 MFC sensor pair separated by a period of 4 months

The frequency responses for the M2814 at three different time periods are almost identical suggesting reasonable reliability from the sensor on a GFRP surface.

As the MFC is segmented by interdigital electrodes, the strain of a passing wave causes a voltage across each segment and the voltage across the whole of the MFC is the net voltage across each MFC segment, Figure 5.48.

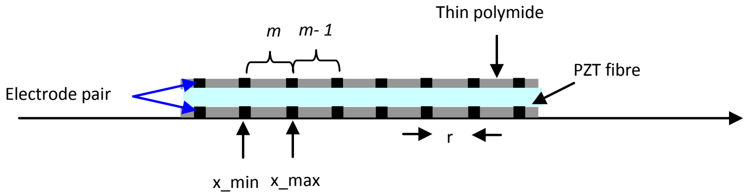

Figure 5.48: analysis of MFC showing sections

The stress across the *m*th segment is defined by Equation (5.13).

$$\sigma_m\left(\omega,t,x_{Tx}\right)=E\int_{x_{m\_min}}^{x_{m\_max}}\varepsilon_{r_x}\left(w,t,x_{T_x}\right)dx \qquad (5.13)$$

Where, σ is the stress, *E* is Young's modulus, *ε,* is the strain at point *x*, x_{T_x} is the transmit point along axis, *x*. The dielectric displacement caused by stress, σ, gives a voltage across the *m*th segment defined by Equation (5.14).

$$V_m=r\,\frac{d}{\varsigma_\sigma}\sigma_{m_{rx}}\left(\omega,t,x_{t_x}\right) \qquad (5.14)$$

Where, *d* is the piezoelectric charge constant and ς_σ is the permittivity in the absence of stress. Every segment is assumed to have identical electrical characteristics. Therefore, the voltage across the electrodes is the mean voltage developed across all segments, Equation (5.15).

$$V_{r_x}\left(\omega,t,x_{t_x}\right)=\frac{1}{M}\sum_{m=1}^{M}V_m\left(\omega,t,x_{t_x}\right) \tag{5.15}$$

The voltage measured by the MFC sensor is proportional to the average stress across the segments contained within the MFC. The conditions for maximum sensitivity are illustrated in Figure 5.49.

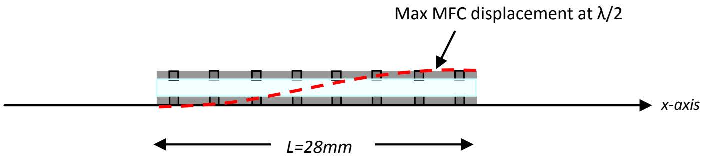

Figure 5.49: Conditions for maximum sensitivity

From Figure 5.47, the chosen experimental frequency of operation is 56 kHz. Considering the phase velocity of the S_0 mode as approximately 3200 ms^{-1}, this gives a wavelength of approximately 57 mm. The wavelength of greatest sensitivity to detect the S_0 mode is: $\lambda = 2L$ = 2 x 28 mm = 56 mm.

5.5.6.2 Material Directionality of a Bidirectional GFRP Sample

A pitch-catch M2814 MFC sensor arrangement was implemented where the transmitting sensor was centred on the bidirectional GFRP sample, described in Table 5.7. The receiving sensor was located 450 mm from the transmitter and was rotated in 5° angular steps (concurrently with the transmitter). Both sensors were coupled to the sample using an applied load of 4 kg as illustrated in Figure 5.50(a). Details of the signal used to analyse the sample are given in Appendix B7.

72 A-scan signals were recorded around the perimeter of the GFRP sample, Figure 5.50.

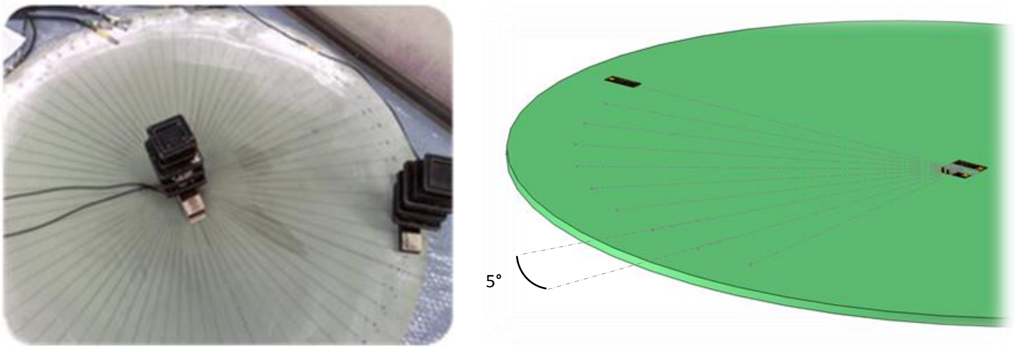

(a) (b)

Figure 5.50: 1 m dia. GFRP (bi-directional) sample – measurements taken at 5° intervals

Evaluating the group velocity, the variation in amplitude of the S_0 mode with fibre orientation was studied. Using MatLab, a time window was applied to each A-scan to capture the S_0 and A_0 modes, the results are presented in Figure 5.51.

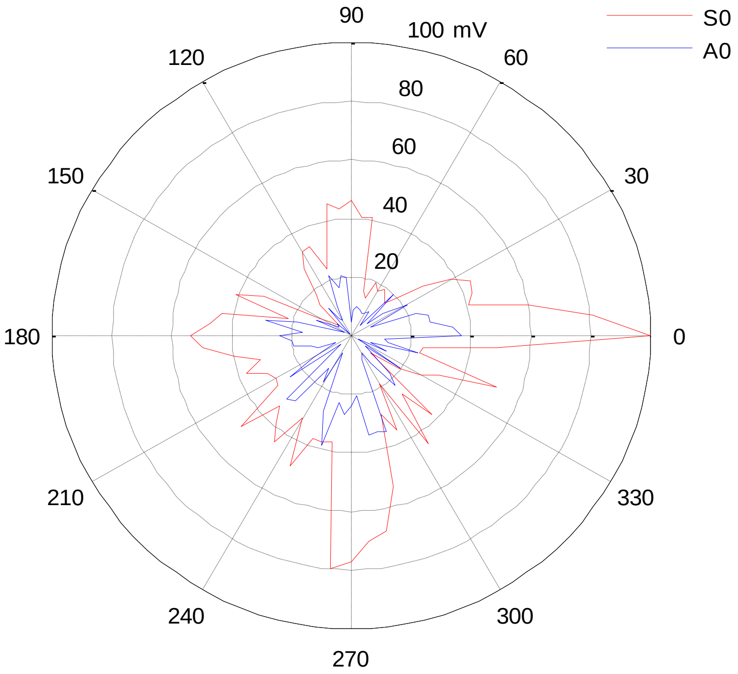

Figure 5.51: Directional characteristics of bidirectional GFRP sample for the A_0 mode

It is observed that the S_0 mode exhibits greater sensitivity to changes in material properties than the A_0 mode. The greatest S_0 magnitudes are recorded at integer multiples of 90° - coinciding with the fibre direction of the sample. However, the peak amplitudes are observed for angles of 0° and 270°. This could be due to coupling conditions whereby the MFC sensor is not equally bonded to the GFRP sample creating phase differentials that impact upon signal amplitude. The polar plot of Figure 5.51 indicates that the directional properties of the sample can reduce the received signal by as much as 16 dB when comparing on-fibre measurements with off-fibre measurements. The A_0 mode is less obviously directional than the S_0 mode; it also exhibits lower amplitude. For example, at 0°, the A_0 mode is 9 dB lower than the S_0 mode.

5.5.6.3 Material Directionality of a Quasi-Isotropic GFRP Sample

To compare the sensitivity of MFC sensors coupled to bidirectional GFRP with that of a different composite lay-up, a pitch-catch M2814 sensor arrangement was implemented on a quasi-isotropic GFRP sample (detailed in Table 5.8, Table 5.9 and Table 5.10). The transmitting sensor – located at the centre of the sample - and the receiver (450 mm from the transmitter) were rotated concurrently and circumferentially in 5° angular steps. Both sensors were coupled to the sample using an applied load of 4 kg. Details of the signal used to analyse the sample are given in Appendix B7.

Analysing 72 A-scan signals around the perimeter of the GFRP sample, the time-of-arrival for each S_0 wave was recorded and the group velocity evaluated. The results are shown in Figure 5.52.

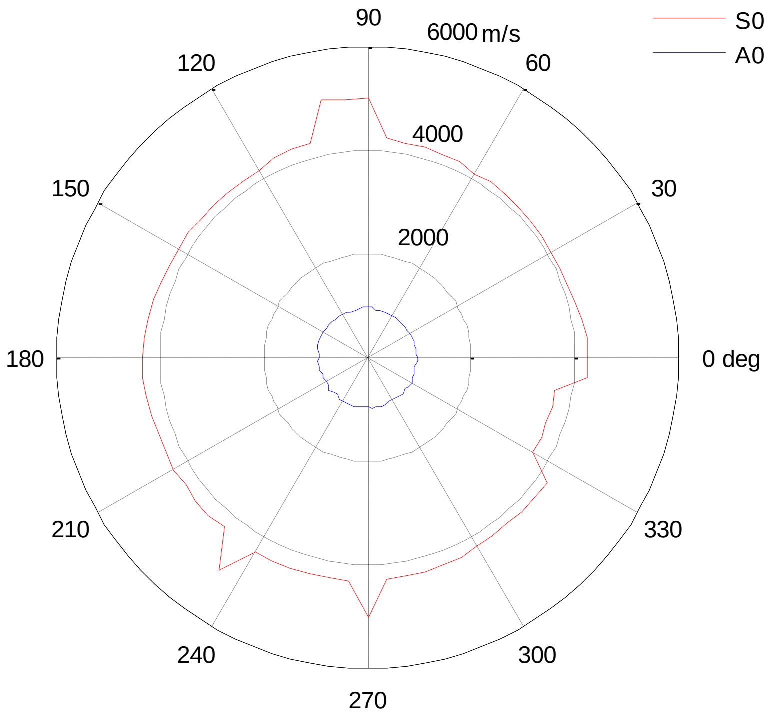

Figure 5.52: *S_0* mode (red) and *A_0* mode (blue) group velocities for quasi-isotropic GFRP sample

As may be observed, there is now very little change in the time of arrival for the S_0 mode (≈ 4050 ms^{-1}). There is an unexpected increase in group velocity at 90°, 235° and 270°, however; it is possible the sample is not uniform perhaps resulting in scatter occurring from abnormalities within the material resulting in a change of wave characteristics. The A_0 mode shows very little variation in directional dependency with a group velocity of ~ 1000 ms^{-1}.

The accompanying amplitude response for both modes is shown in Figure 5.53.

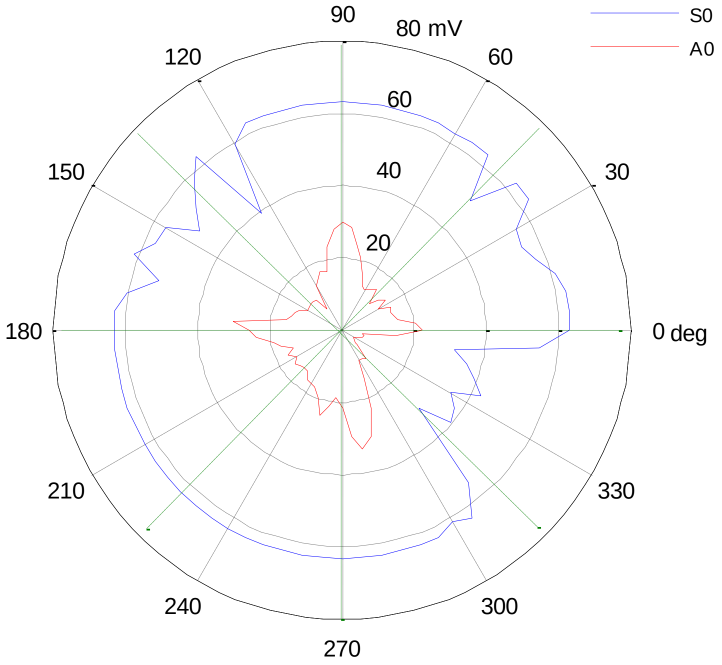

Figure 5.53: Amplitude response for *S₀* mode (blue) and *A₀* mode (red). Dashed green line indicates sample fibre orientation

The S_0 mode amplitude response was relatively independent of fibre orientation with a reduction occurring only between 310° and 350° and at 130°. However, the four 0°/90° woven (from six) layers of the quasi-isotropic sample had a greater effect on the amplitude of the A_0 mode where the largest amplitudes occurred at 0°, 90°, 180° & 270°. The amplitude reduction in both S_0 and A_0 modes between 310° and 350° is unexpected. Interestingly, Figure 5.52 shows a drop in the S_0 mode group velocity plot between 320° and 355°. This suggests that there is an unintended change in material characteristics within this region of the quasi-isotropic plate (to which the S_0, in particular, is sensitive).

5.5.6.4 Combined Sensor and GFRP Directionality – FEM Analysis

The directional properties of the GFRP sample have to be considered in conjunction with the directional properties of the interdigitated MFC sensor. Having developed an FE model for the bidirectional GFRP (Section 5.4), it is helpful to model the M2814 MFC sensor attached to the material to predict the effects of directionality. An x-ray of the MFC (Figure 5.37) and the layout of the fibre contained within are shown in, Figure 5.54, [129].

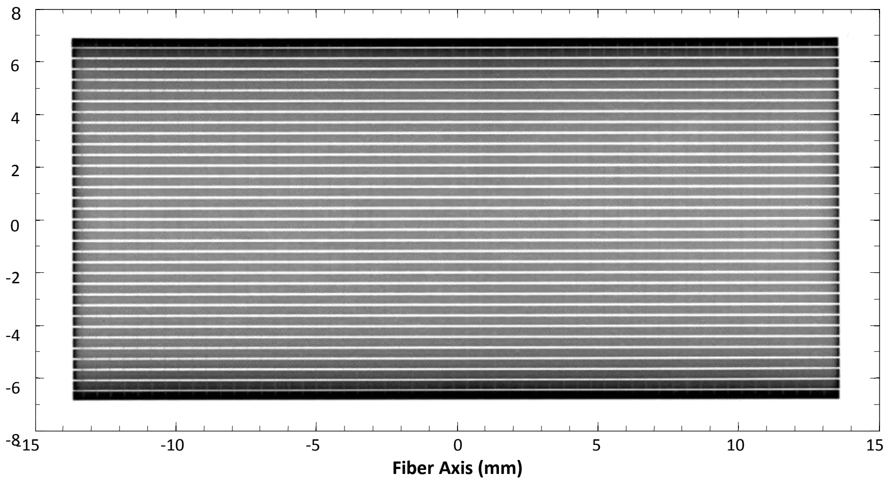

Figure 5.54: X-ray of MFC active region

The active region of the sensor was represented by a discrete grid of point sources from which displacement can be measured. A grid array of 84 by 42 points was used. Each point separated from an adjacent point by 1mm.

The displacement amplitude (A_n) and direction of each point source is defined by the vector, p_n, Equation (5.16).

$$p_n = \left(A_n \sqrt{\left(x^2 + (-vy)^2\right)}, \angle arctan \frac{-vy}{z} \right) \tag{5.16}$$

Where v=0.312 for the active region, [130]. Each point source is represented by different amplitude. A simple mesh with clearly defined element numbering was established whereupon formulae were applied to assign material properties and loading. The displacement in the length of the MFC, parallel to piezoceramic fibres and identified as the x-axis, ranges from -1 at one end to 1 at the opposite end. The displacement in the sensor width (y-axis) is scaled by the Poisson ratio of the active area (υ=0.312): ranging from 0.312 to -0.312. As the MFC expands along the x-axis, it contracts along the y-axis (Equation 5.16). The signal used to excite each point was a 50 kHz, 5-cycle Hann-windowed sine wave. The GFRP material was modelled as described in Figure 5.55 but with a circular geometry with the purpose of establishing the modelled sensor field.

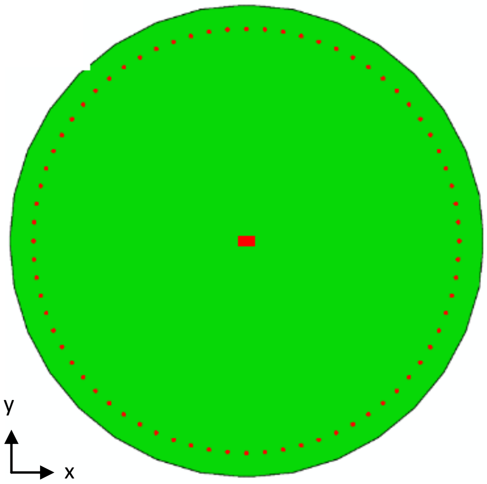

Figure 5.55: Modelled sensor and GFRP sample (on-fibre)

The sensor length is orientated along the fibre direction and the summation of displacement of each point within the discrete grid was evaluated at each of the receiving points located 50 mm from the perimeter of the sample (adjacently separated by 5°). Figure 5.56 illustrates the degree of S_0 mode directionality predicted by the model. Similarly Figure 5.57 shows the A_0 mode directionality.

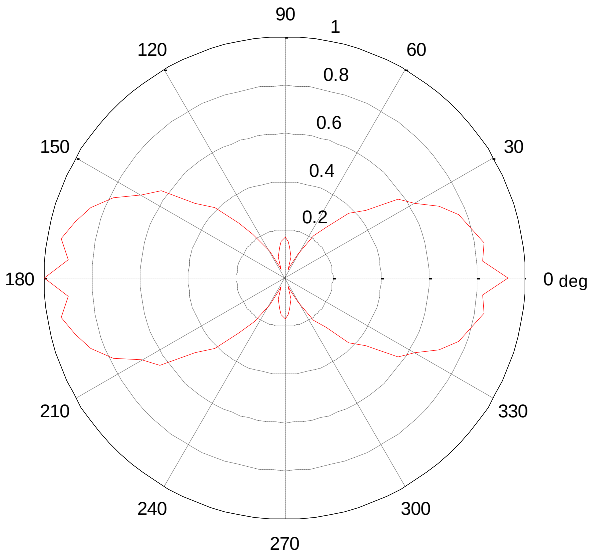

Figure 5.56: Directional sensitivity of modelled MFC and bidirectional GFRP for S_0 mode

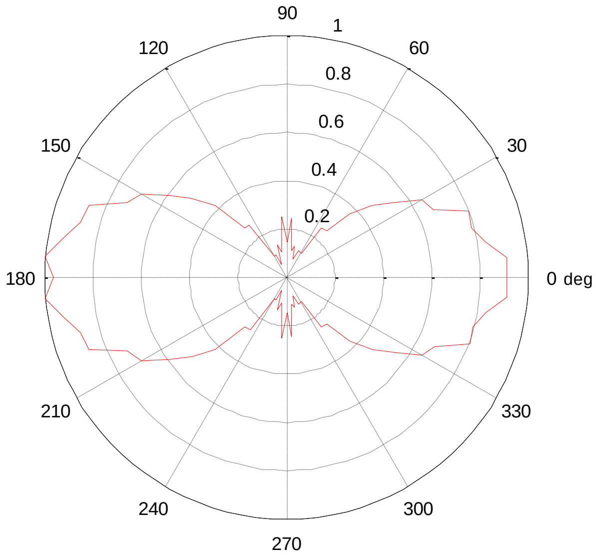

Figure 5.57: Directional sensitivity of modelled MFC and bidirectional GFRP for A_0 mode

The results show greatest mode sensitivity occurs at 0° and 180° for both S_0 and A_0 modes. The lowest sensitivity is recorded at 90° and 270°.

The modelled data can now be compared with experimental data similarly focusing on the arrival time of the received signal using an MFC for excitation around the GFRP circumference.

5.5.6.5 Combined Sensor and GFRP Directionality – Experimental Analysis

The experimental aim is to identify the effects of the $0/90_4$ fibre lay-up on the field pattern of the MFC sensor. To establish the MFC sensor field plot for an anisotropic composite, an M2814 MFC sensor was dry-coupled (using 4.5 kg of weights) at the centre of the bidirectional GFRP sample, described in Table 5.7, and remained static for the duration of the experiment. A receiving MFC sensor was rotated around the sample in 5° increments at a distance of 450 mm from the transmitter (details provided in Appendix B7). The resulting plot is shown in Figure 5.58.

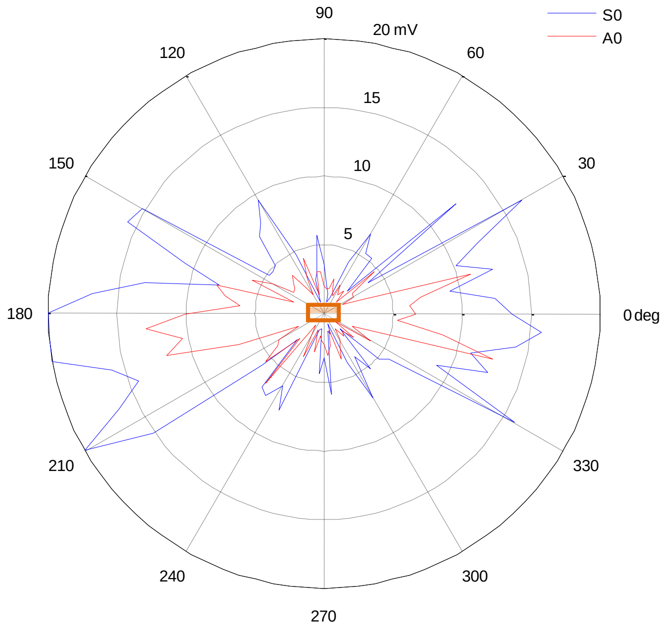

Figure 5.58: Directional S_0 mode (blue) and A_0 mode (red) characteristics of MFC sensor (orange rectangle) on bidirectional GFRP; transmitting sensor orientated along the 0^o-180^o axis

Figure 5.58 illustrates the S_0 field pattern exhibiting greater sensitivity to changes in material properties than the A_0 mode. The greatest S_0 signal sensitivity is achieved when the receiver is orientated in the same direction as the transmitter: a maximum SNR of -24 dBm occurs at 180^o with a measurement of -26 dBm recorded at -5^o. The A_0 mode, although lower in amplitude, has a similar variation in SNR based upon receiver-transmitter orientation (a maximum of -27.5 dBm at 185^o). The slightly unbalanced plot for both S_0 and A_0 is perhaps due to unequal bonding across the MFC sensor surface.

To establish to what extent a change in bonding conditions can change the field pattern of the M2814 sensor on bidirectional GFRP, several different bonding techniques were applied to the transmitting sensor. Three different coupling techniques were compared:

- Dry coupling using 4.5 kg of weight
- Adhesive coupling using double-sided tape
- Adhesive bonding using super-glue

Figure 5.59 shows the S_0 field plots for the adhesive and dry coupled conditions. For the permanently bonded condition, the S_0 field pattern is relatively symmetrical through the 90^o - 270^o axis when compared with the field patterns for the dry coupled configuration.

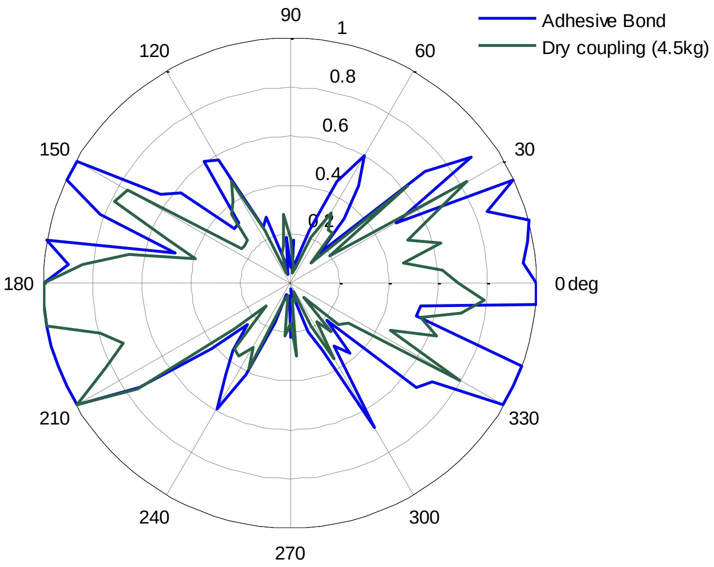

Figure 5.59: Directional S_0 mode characteristics for permanently bonded (blue) and dry-coupled (green) transmitting sensors on bi-directional GFRP. Sensor orientated along the 0^o-180^o axis

Figure 5.60 compares the adhesive bonded sensor with the taped bond. It is observed that the taped bond is significantly less sensitive.

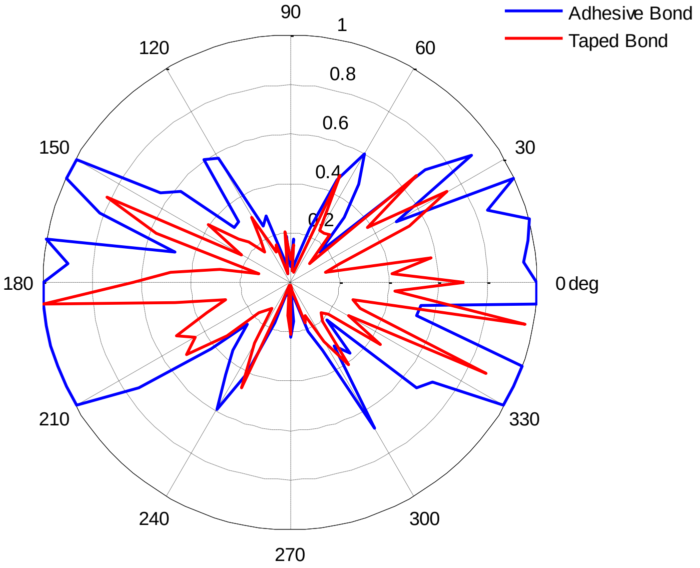

Figure 5.60: Directional S_0 mode characteristics for permanently bonded (blue) and taped (green) transmitting sensors on bi-directional GFRP. Sensor orientated along the 0^o-180^o axis

This experiment in sensor coupling to the GFRP illustrates that the adhesive bond using superglue yields superior evenly distributed signal sensitivity.

Lastly, comparing the A_0 mode and S_0 mode for a permanently bonded transmitting sensor orientated along the 0^o-180^o axis, Figure 5.61, it is observed that generally the S_0 mode yields greater sensitivity and a more symmetrical characteristic corresponding to GFRP fibre directionality.

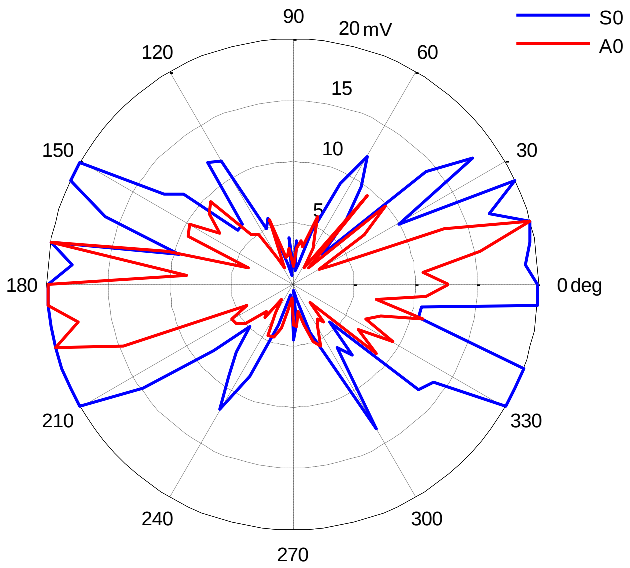

Figure 5.61: Directional S_0 mode (blue) and A_0 mode (red) characteristics of MFC sensor on bi-directional GFRP sample. Transmitting sensor orientated along the 0^o-180^o axis

Comparison of the experimental data with the FE model of Section 5.5.6.4, Figure 5.62 and Figure 5.63 show that whilst the main lobes are broadly aligned, there is little similarity of detail. One explanation is that the model does not incorporate a 'coupling coefficient' – an inherent attribute of sensor attachment during experimental set-up. Together with the stiffness coefficient error arising from the bidirectional GFRP model (Table 5.5 and Table 5.6); the combined result will be to smooth out the amplitude peaks and troughs. Provision of additional detail within the model would be expected to yield a better agreement between the model and the experimental results.

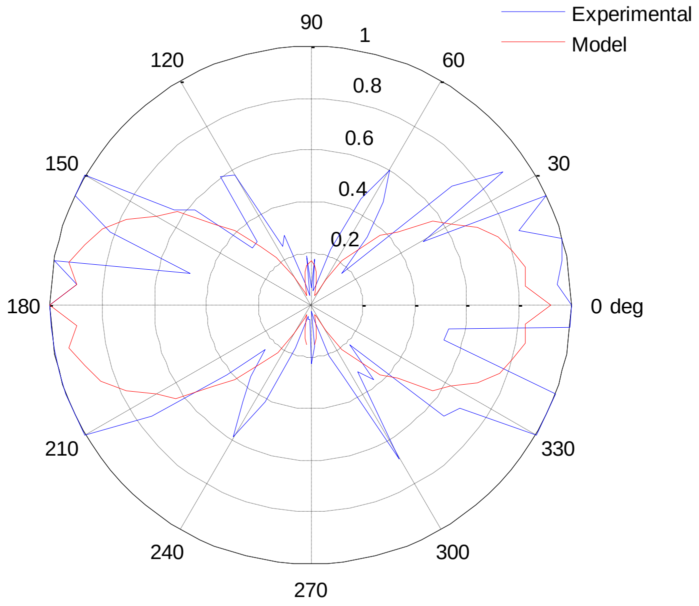

Figure 5.62: Experimental versus modelled sensor & GFRP – S_0 mode

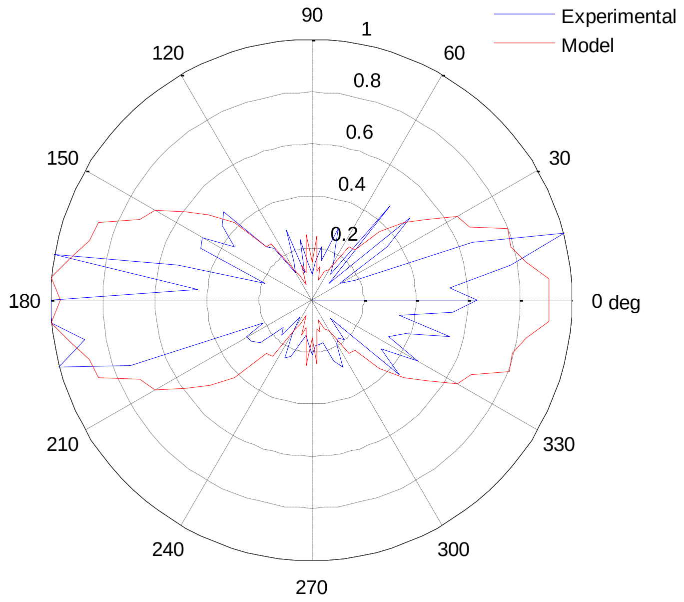

Figure 5.63: Experimental versus modelled sensor & GFRP – A_0 mode

Finally, to observe the field plot of a different GFRP configuration, the quasi-isotropic GFRP sample (Section 5.5.5.2) was experimentally analysed. The transmitting sensor was placed at the plate centre to observe how the field plot changes with a change in fibre lay-up, Figure 5.64. Less scatter was observed in the field plot of the A_0 and S_0 modes. With the exceptions of the region from 310° to 350° (where there is up to 6 dB of difference between the two plots), the field plots of both modes are broadly similar. As with the bidirectional GFRP, the greatest sensitivity occurs at 0° ± 20° and 180° ± 20°.

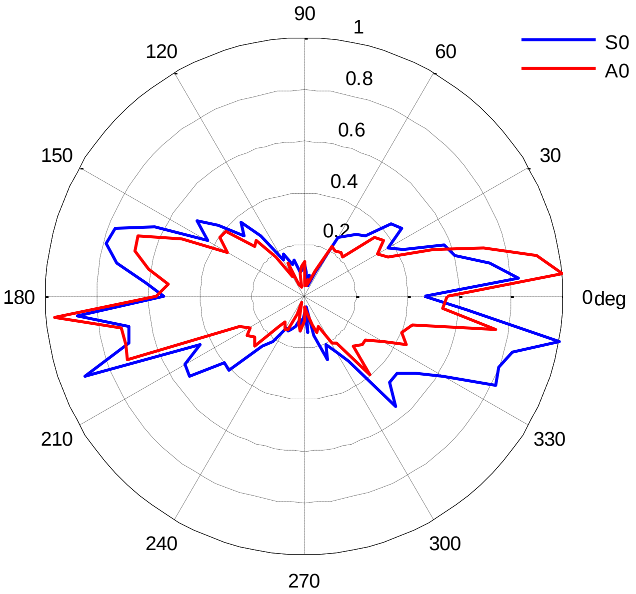

Figure 5.64: Directional S_0 (blue) and A_0 mode (red) characteristics of MFC sensor on quasi-isotropic GFRP; Tx sensor along the 0° to 180° axis

In summary, the field pattern of the S_0 and A_0 Lamb wave modes generated by the M2814 MFC sensor is strongly influenced by the fibre orientation of the GFRP sample under analysis. For the bidirectional sample, there was greater evidence of signal scattering at certain angle orientations not aligned with the sensor, however; the greatest SNR was observed along the 0°-180° axis which compares with the field pattern of the MFC on an isotropic plate. Bonding conditions have an impact on the symmetry of the field pattern over the 0°-180° axis. When the MFC sensor was permanently bonded to the structure, general symmetry was achieved for both S_0 and A_0 modes.

For the quasi-isotropic sensor, there was a significant reduction in energy scatter and the observed field pattern approximates the isotropic field pattern using the same sensor type. Along the sensor longitudinal axis, there was greater energy propagation through the quasi-isotropic sample than that recorded for the bidirectional sample.

For both samples, the S_0 mode exhibited a greater sensitivity to sensor orientation (than the A_0 mode). The analysis conducted within this chapter has been used to inform the sensor array design to be used on a wind turbine blade.

Analysis, so far, has focused on the wave propagation characteristics of GFRP under static conditions. The next section analyses the change in stress wave characteristics in GFRP under load conditions.

5.6 Real-time Monitoring during Loading

Due to the environment in which wind turbines are sited, they regularly experience loading due to variable wind speeds and direction. As a result of the force of the wind, secondary loading conditions arise from vibrations. Loading also arises when the rotor is ‘pitched’ to face the direction of the wind when in service.

A particular concern is to ensure that these loading effects are not misinterpreted for the onset of a defect. It may be that the presence of loading will initiate a defect but this will be established over a period of time.

This section analyses the effects of tensile loading on bidirectional GFRP samples similar to that found within spar-caps strengthening the turbine blade. Parametric monitoring is used to indicate the presence of loading. A number of 800 mm x 70 mm x 4 mm bidirectional GFRP samples were manufactured for the purposes of destructive testing, Figure 5.65.

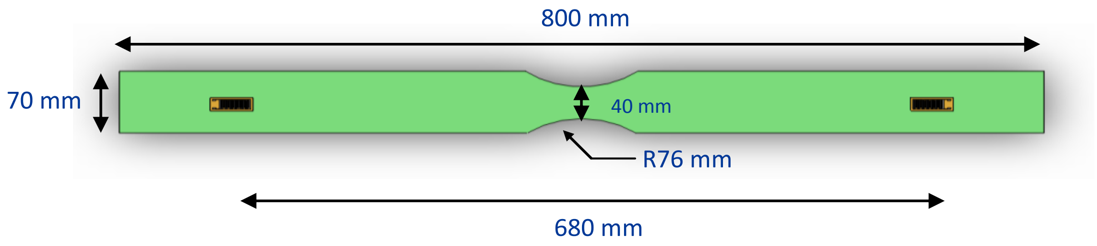

Figure 5.65: GFRP coupons for the purposes of exploring the effects of loading on propagating Guided waves

The GFRP sample dimensions were dictated by the capacity of the Instron 8508 tensile machine used to apply loading, Figure 5.66. Each sample, at its centre, was waisted to a radius of 76 mm to ensure fracture did not occur at the grip point. Details of the experimental set-up are provided in Appendix B9.

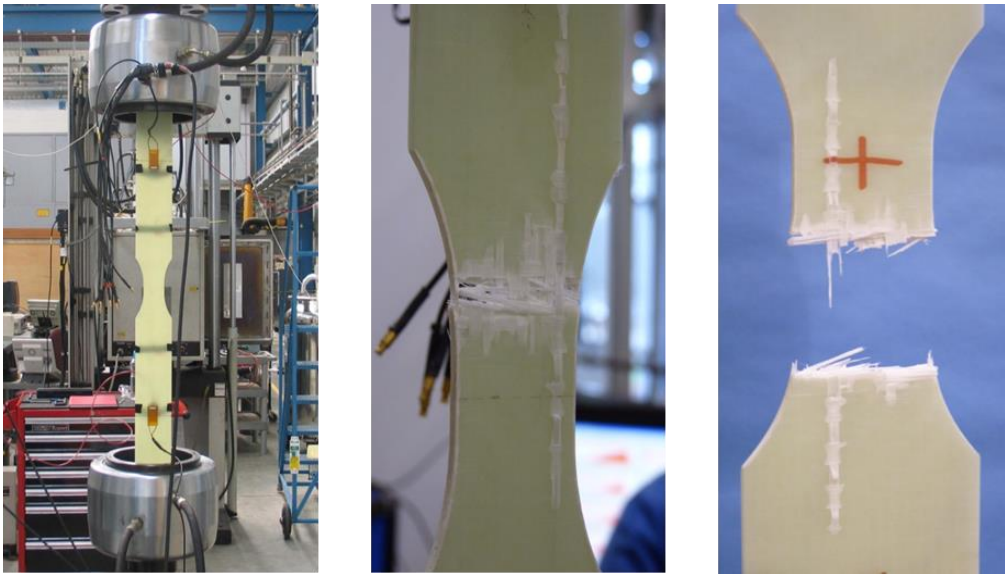

Figure 5.66: Instron 8508 loading machine, right; coupon after loading, centre, right.

To introduce a level of damage (and be able to assess the effectiveness of the sensors), three different load-cycles were subjected to the coupon: uniform increasing load; increasing step-wise load; and cyclic load.

5.6.1 Uniform Increasing Load

A uniformly increasing tensile load was applied to a GFRP coupon, Figure 5.67. The sample fractured at a load of 49 kN at 6 minutes 20 seconds. The complete recorded time-series data for the duration of the applied tensile load is shown in Figure 5.68.

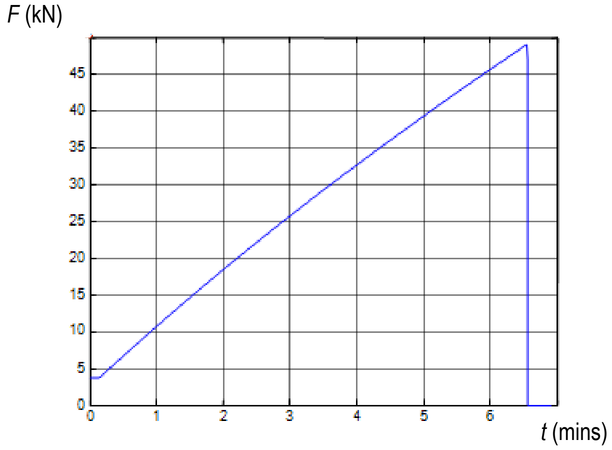

Figure 5.67: Applied tensile load - uniformly increasing

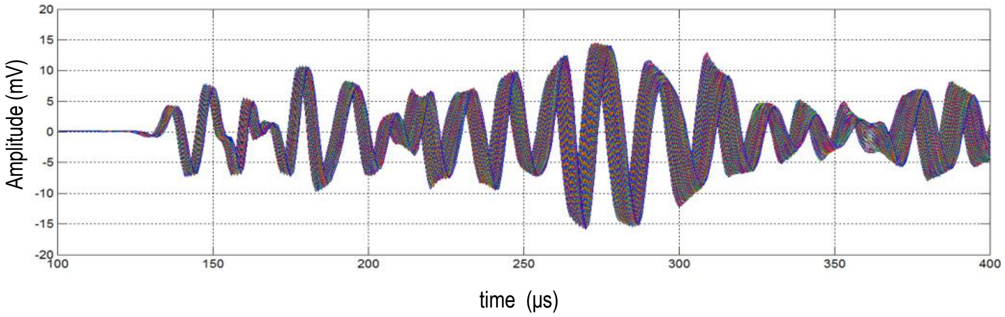

Figure 5.68: All interspersed time-series data

The peak-to-peak amplitude of each A-scan captured throughout the duration of the load cycle was generally constant. Analysing the arrival time of each A-scan, it was observed to increase linearly with increasing load, Figure 5.69: 137 μs to 140 μs.

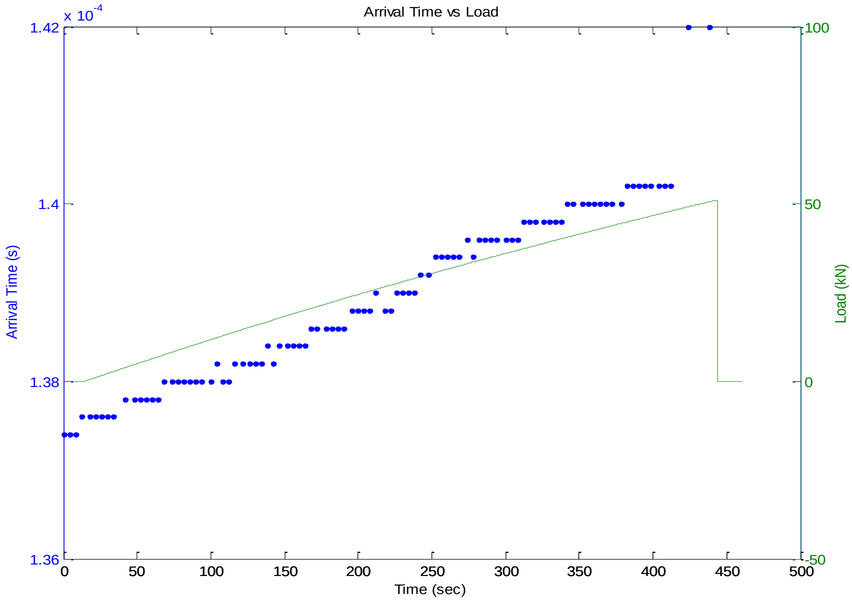

Figure 5.69: Change in load (green axis) versus change in arrival time (blue axis)

5.6.2 Increasing Step-wise Load

To observe material response upon repeated cycles of applied increased monotonic load and load removal, the profile of Figure 5.70 was used on the GFRP coupon.

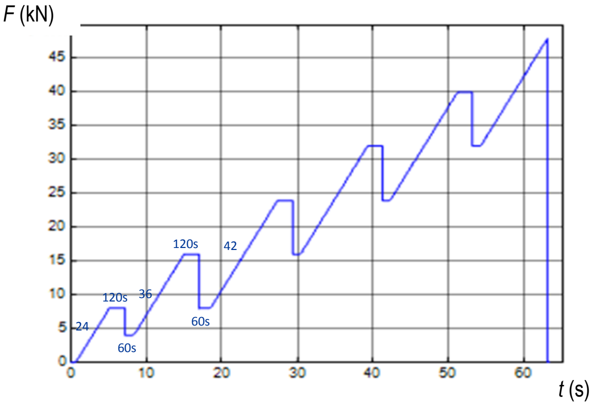

Figure 5.70: Increased step-wise tensile load showing the duration of the load increase and the steps

The sample fractured at a load of 47.9 kN in a time of 63 minutes 13 seconds. From Figure 5.71, the arrival time was observed to increase and decrease in accordance with the load. The arrival time of a Guided wave appeared to be an effective indicator of the presence of load at any particular time.

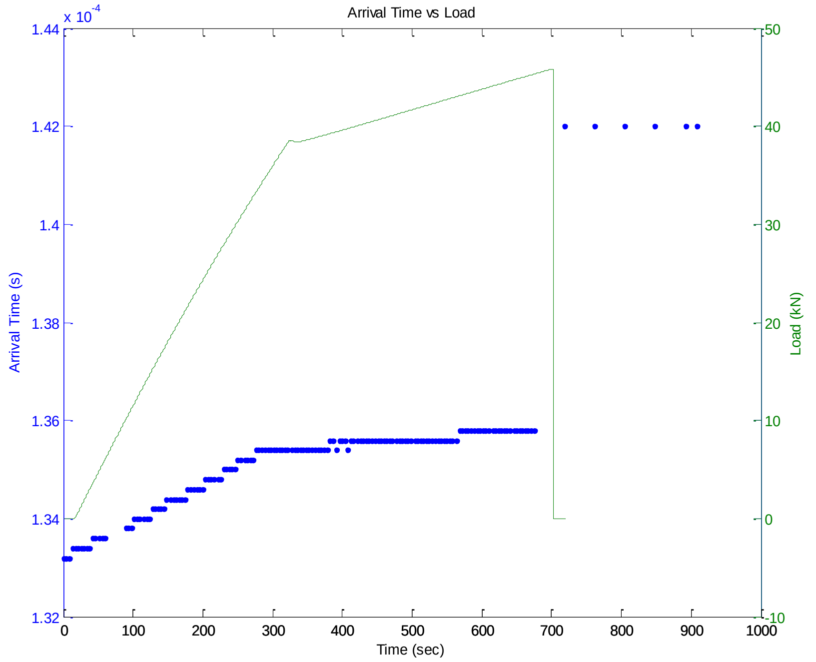

Figure 5.71: Change in load (green axis) versus change in arrival time (blue axis)

5.6.3 Cyclic Load

A cyclic tensile load was applied to the GFRP coupon to observe the effects of fatigue with repetitively applied loads, Figure 5.72. The procedure involved applying five identical load cycles, if where after no change of output was observed, the 6th load cycle was increased to a new peak. If again, no deterioration in output was observed, a final 7th and greater load cycle was applied until the point of fracture occurred.

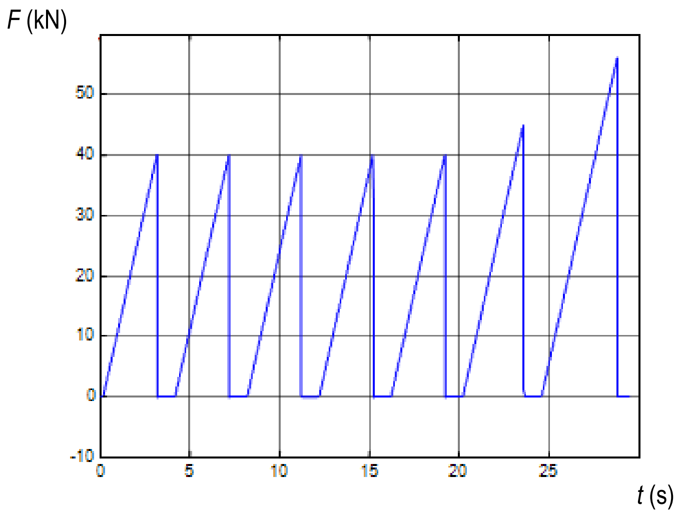

Figure 5.72: Applied cyclic tensile load: 5 even cycles of 40 kN; one cycle of 40 kN

The sample fractured at a load of 56.1 kN at 29 minutes 5 seconds. Figure 5.73 clearly illustrates the arrival time of the fastest wave mode (blue axis) increasing and decreasing in accordance with the applied load (green axis).

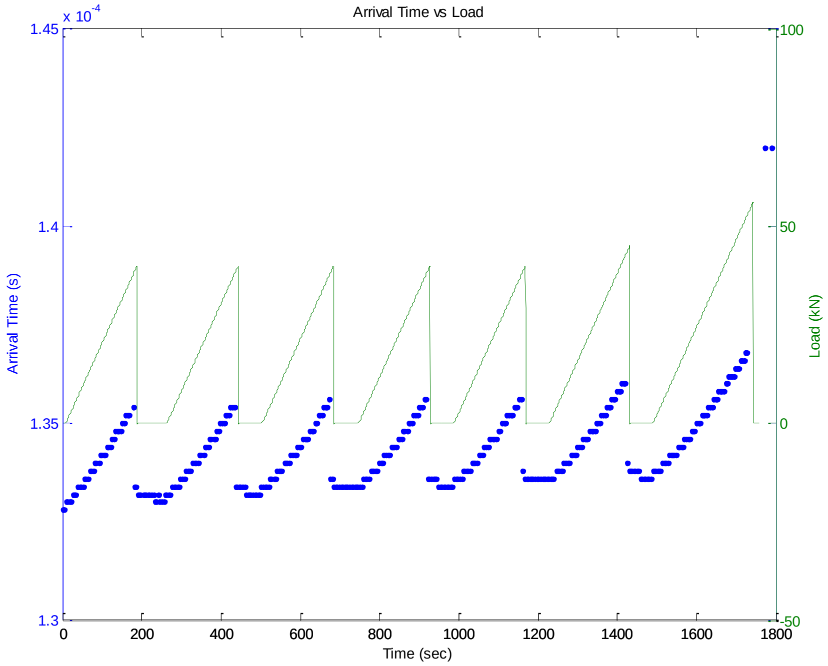

Figure 5.73: Change in load versus change in arrival time

5.6.4 Summary

The parameter which clearly indicates the presence of component loading is the arrival time. Indicatively proportional to the applied tensile load, the arrival time increased by several microseconds upon load presence and reduced upon load removal. This behaviour agrees with Hooke's law (Equation 4.14) where the stiffness coefficient matrix is transversely isotropic (Equation 4.56).

5.7 Conclusions

This Chapter has detailed the various issues for consideration when characterising GFRP material typically found within wind turbine blades. As a first-step approach to installing sensors, it was necessary to establish how far a signal will propagate before falling below a required threshold for the purposes of signal evaluation. Two different GFRP lay-ups were analysed: 8 ply unidirectional GFRP and 12-ply bidirectional ±45° GFRP. The lowest level of attenuation was recorded for the on-fibre ±45° GFRP (55.9 dB/m) indicating that detection of structural degradation due to an extraneous event is best identified at a sensor location that is on-fibre.

To achieve the required level of spatial and temporal resolution to identify which wave modes contribute towards the composite waveform, laser generation and reception was performed on a 500 mm x 500 mm GFRP sample. The excitation technique involved three different focusing techniques: unfocused, spot-focus and line-focus. The line-focused tests were observed to excite greater in-plane displacement (where the S_0 mode is clearly perceived over an increased bandwidth) due to improved directionality, reduced geometrical attenuation, and weak ablation when compared with either the unfocussed or spot-focus tests.

An FE model of the bidirectional GFRP was created to better understand the directional properties of GFRP characteristics. Stiffness coefficients were evaluated upon analysing a small section of the GFRP sample and applying them to the model.

Comparison of spot-focused laser tests with the model showed that whilst there was reasonable agreement with the experimental data for the A_0 mode, there was very poor agreement with the S_0 mode - likely due to insufficient stiffness information (model was not transversely isotropic).

With out-of-plane and in-plane wave mode resolution established, experiments were conducted to analyse elastic wave propagation due to material excitation using piezoceramic sensors. The bidirectional GFRP showed strong S_0 and A_0 modes at a distance of 250 mm from the excitation source. Higher order modes were also observed. The same set-up for quasi-isotropic (0°, ±45°, 90°) GFRP revealed a strong A_0 mode together with a weak S_0 spanning a shorter bandwidth.

To exploit the directionality of the GFRP samples under test, the performance of an interdigitated piezoceramic sensor was analysed. Of three MFC sensors investigated, the M2814 (with active area 28 mm x 14 mm) was identified as the sensor with the best resonance performance at low frequencies. The MFC sensor was modelled as a rectangular grid of point sources and used as an excitation source at the centre of the previously developed bidirectional GFRP FE model but now circular in geometry. Identified receive points - 490 mm away, spaced 5° around the perimeter - summed the displacement from each transmitting point source. Both S_0 and A_0 modes exhibited directional lobes aligned with the 0° – 180° axis.

The related experimental analysis provided group velocity and amplitude data (at 72 different circumferential points) where the transmitting and receiving sensors were aligned and rotated concurrently. For the bidirectional GFRP sample, the S_0 mode was identified as being highly sensitive to the fibre orientation. The A_0 mode group velocity was largely insensitive to fibre orientation. The amplitude response of both modes was greatest when the receiver was aligned with material fibre direction. For the quasi-isotropic GFRP sample, the group velocities for the S_0 and A_0 modes were predominantly insensitive to the increased radial resolution of fibre filaments. The accompanying amplitude response for the S_0 was relatively independent of fibre orientation. However, the quasi-isotropic sample had a greater effect on the amplitude of the A_0 mode where the largest amplitudes occurred at 0°, 90°, 180° & 270°.

To provide information on signal attenuation at a receiver with respect to its alignment with a fixed transmitter, amplitude responses were recorded for both the bidirectional GFRP sample and the quasi-isotropic GFRP sample. For the former sample, misalignment between transmitter and receiver by greater than ±30°, resulted in a drop in amplitude for both S_0 and A_0 modes. For the latter sample, misalignment between transmitter and receiver by greater than ±20°, resulted in a significant drop-off in amplitude for both S_0 and A_0 modes. Permanent adhesive bonding was found to provide the most consistent sensor response.

Comparison with the results from the combined (point source) sensor and FE model showed broad alignment of the main lobes. However; there was a lack of correlation – likely due to insufficient stiffness information (model was not transversely isotropic) and the lack of a 'coupling coefficient'. The combined effect will be to 'smooth out' the amplitude response. In addition, the model assumes some homogeneity for certain geometrical areas which may not otherwise exist.

Final analysis was given to the inspection of a GFRP component under continuing loading conditions. Upon application of a tensile load on a narrow coupon (a challenging geometry which yielded a complex Guided wave), the arrival time of Guided waves was the only A-scan parameter to provide information relating to the stressed condition of the component. Several tensile tests were applied (uniformly increasing load, step-wise load, cyclic load) and, in each case, information as to the changing load recorded. These results indicated that the time-of-arrival of Guided waves was a reliable indicator for a change in material characteristics due to operational conditions, and that MFC sensors were able to differentiate between cyclic loading conditions and the onset of defects.

Having established fundamental propagation characteristics, the next chapter considers defect detection within a full-length wind turbine blade.

6 Defect Detection within a Full Size Wind Turbine Rotor Blade

6.1 Overview

The directionality of MFC sensors were demonstrated as being suitably sensitive to the fibre characteristics of GFRP components in the previous Chapter. This Chapter analyses the structural lay-up of a typical wind turbine rotor blade. The spar cap has been identified as a ‘failing’ component by wind turbine manufacturers. To establish the distance a stress induced propagating elastic wave will travel, a spatial array was configured over an area of 3.76 m x 0.78 m - partially covering both the spar-cap and the aerodynamic frame. Sensor placement with respect to the GFRP fibre direction and component boundaries are analysed for the purposes of array optimisation

Chapter 6 concludes with the analysis of a GFRP structure upon a continuingly applied load to ascertain the presence and, where occurring, subsequent absence of such a load.

6.2 Wind Turbine Blade Structure

Prior to implementing a sensor array for the purposes of detecting the onset of defects, the structure of the turbine blade was first studied. Appendix C1 provides details of the selected decoupled wind-turbine blade. The aero-dynamic structure has a length of 9.8 m and uses an internal spar-box arrangement to support loads within its environment. The spar box comprises two parts: a ‘U’ –shaped GFRP configuration topped with a GFRP spar-cap.

The dimensions of the blade and the location of the spar-box support are illustrated in Figure 6.1

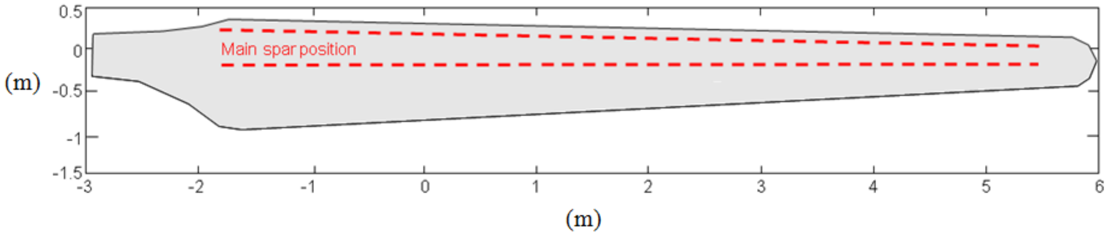

Figure 6.1: Blade showing location of internal spar-box

In order to identify how well the MFC sensors would respond to the onset of defects within a composite wind turbine blade, a sparse array was configured with respect to the blade geometry.

6.3 Sensor Location on Wind Turbine Blade

An array of 10 MFC sensors was distributed across the blade to ascertain the maximum separation whilst having the capability to detect incipient defects. The sensor positions on the blade surface are identified in Figure 6.2 (a larger image is provided in Appendix C2).

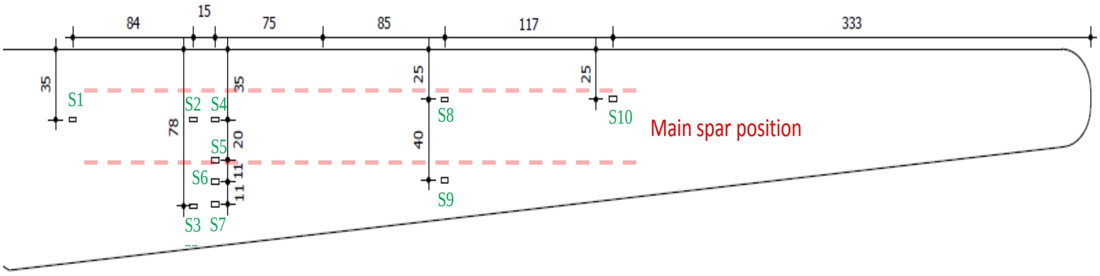

Figure 6.2: Sensor positions on turbine blade surface (sensor locations, grey (mm); sensor id, green)

Sensor distribution is such that the blade characteristics and their interaction with propagating Guided waves can be observed. For example, transmitting on Sensor S1 and receiving on Sensor S10 will establish the ability to detect signals over long distances; and transmitting on S1 whilst receiving on Sensor S9 will provide information on the effects of the material change (from the spar cap to aerodynamic structure) on Guided waves.

The maximum sensor separation - between S1 and S10 - is 3.76 m, Figure 6.3.

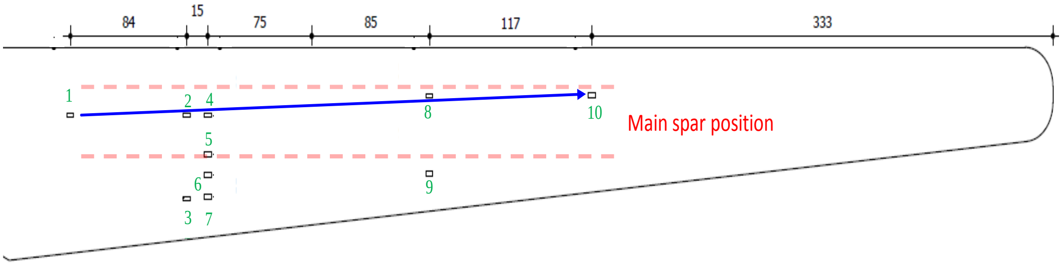

Figure 6.3: Sensor S1 to Sensor S10

Using TWI's Teletest pulser-receiver unit, the blade structure is configured for pitch-catch excitation (details provided in Appendix C3). The recorded response is illustrated in Figure 6.4.

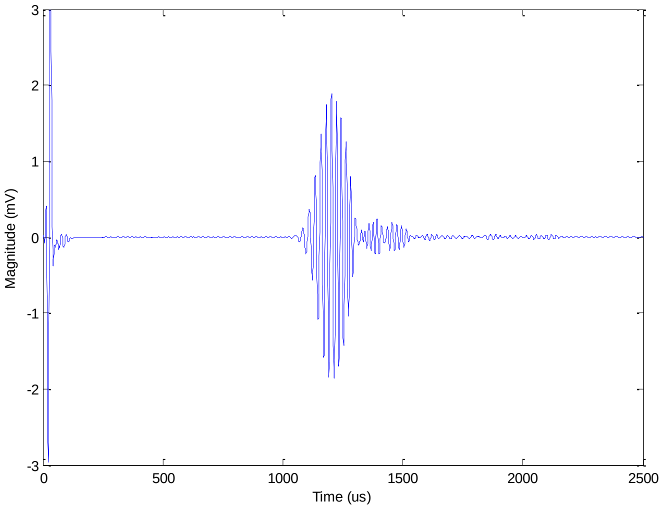

Figure 6.4: Received signal over a distance of 3.76 m (pitch-catch)

Figure 6.4 is the response over the load-carrying spar-cap. The received signal presents a good level of SNR. The arrival time of the fastest mode is 3420 ms^{-1} which agrees with the modal data of Figure 5.35, indicating the expected arrival time of the S_0 mode at 50 kHz. A gain of 40 dB (with 64 averages) was applied to the received signal demonstrating that good signal integrity is achieved for a sensor spacing of 3.8 m.

The received signal was then observed upon traversing the load-carrying spar cap/aerodynamic structure boundary, Figure 6.5, a distance of 2.61 m)

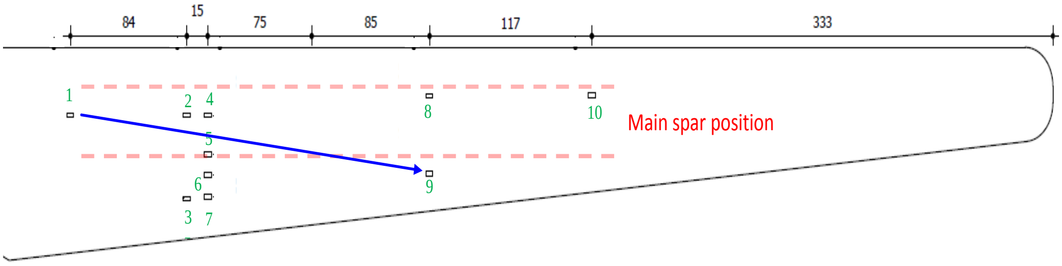

Figure 6.5: Sensor S1 (spar cap) to Sensor S9 (aerodynamic structure)

It may be observed from Figure 6.6 that although the distance between the two sensors has been reduced by over 1 m, the signal amplitude has dropped significantly (-20 dB).

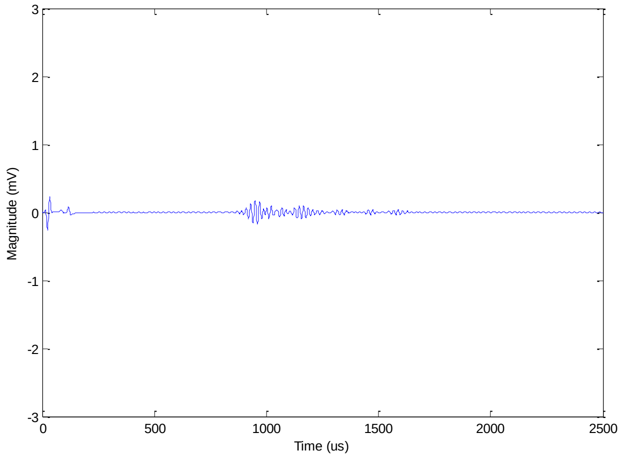

Figure 6.6: Received signal across boundary of spar cap over a distance of 2.61 m (pitch-catch)

Furthermore, upon using S1 as transmitter and receiving on Sensors S2 to S10, it was observed that receivers located on the spar cap (S2, S4, S8 & S10), recorded a greater phase velocity for the S_0 mode than receivers located over the aerodynamic form (S3, S5, S6, S7 & S9), Figure 6.7.

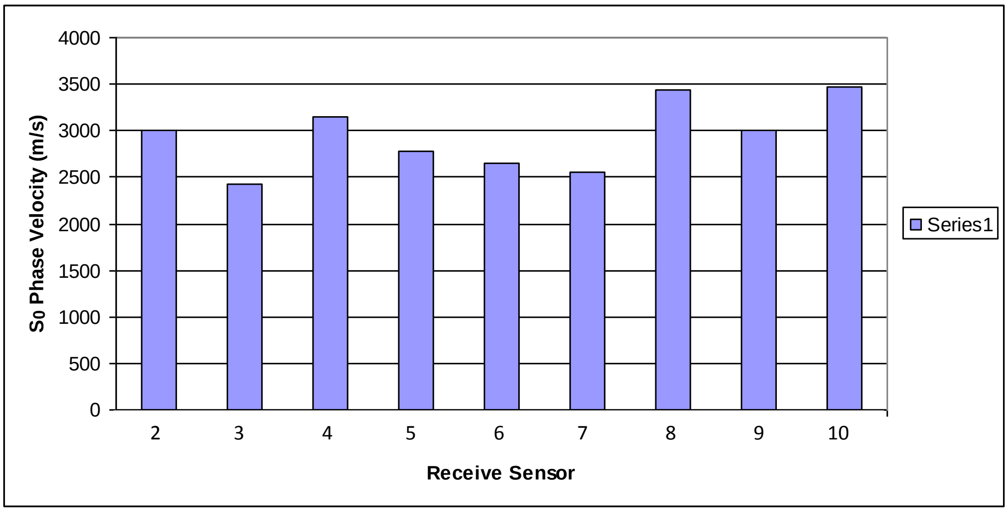

Figure 6.7: Recorded Guided wave velocities from Sensor S2 to Sensor S10

In addition, it may be observed from Figure 6.6 that the received signals at the various locations over the aerodynamic structure exhibit a series of reflections. It is therefore possible, using a receiver, to discern between different component locations.

6.4 Blade Material Lay-up

To gain a better understanding of the blade structure lay-up, material was extracted from two different areas of the blade: one over the load-carrying spar cap; and one from the aerodynamic frame. Two different samples were analysed: *Sample A* from the aerodynamic structure; and *Sample B* from the spar-cap. The material analysis showed *Sample A* to be a sandwich structure comprising an arrangement of GFRP-Foam-GFRP. The glass fibre lay-up for the top GFRP sandwich layer is shown in Figure 6.8 with details provided in Table 6.1. The lay-up of the bottom GFRP sandwich layer (inner surface) is shown in Figure 6.9 with details provided in Table 6.2.

The total thickness of the resin skin for the bottom side is 2.16 mm. The related fibre volume ratio is 21.8%. The total thickness of the composite sandwich structure (Sample A) is 14.48 mm. It may be observed from both Table 6.1 and Table 6.2 that Sample A comprises predominantly unidirectional fibre along the chord of the blade structure providing it with support. Woven fibre at 60° is also regularly present.

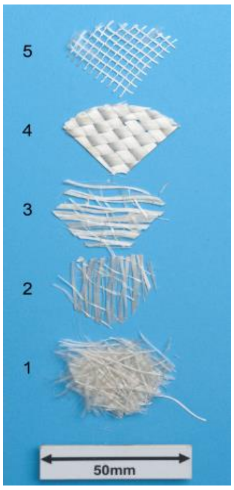

Figure 6.8: Fibre configuration for sandwich top layer

Table 6.1: Sample A Fibre lay-up (top)

Foam Cored Sample A - Top side		
Layer no.	*Thickness (mm)*	*Description*
1	0.59	Random fibre layup
2	0.19	Mainly UD with occasional cross weave at ~60°
3	0.23	Mainly UD with occasional cross weave at ~60°
4	0.50	Tight even weave at ~60°
5	0.12	Fine even open weave with at ~60°

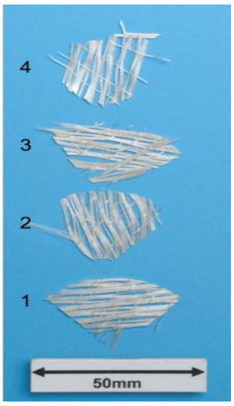

Figure 6.9: Fibre configuration for sandwich bottom layer

Table 6.2: Sample A Fibre lay-up (bottom)

Foam Cored Sample A - Bottom side (inner surface)		
Layer no.	*Thickness (mm)*	*Description*
1	0.25	Mainly UD with occasional cross weave at ~60°
2	0.22	Mainly UD with occasional cross weave at ~60°
3	0.30	Mainly UD with occasional cross weave at ~60°
4	0.21	Mainly UD with occasional cross weave at ~60°

Material analysis showed *Sample B* to comprise GFRP only. The glass fibre lay-up is detailed in Table 6.3 and Figure 6.10. There are 17 layers of fibre contributing towards a sample thickness (with resin skin) of 13.39 mm. The related fibre volume ratio is 53.8% (i.e. approximately double that of the aerodynamic frame). As observed for the aerodynamic frame, the predominant lay-up is unidirectional fibre running the length of the blade and providing the spar cap with strength. Again, regular cross-weaves at fibre orientation of 60° are present within the ply.

Table 6.3: Sample B fibre lay-up

Solid core sample (B)		
Layer no.	*Thickness (mm)*	*Description*
1	0.33	Random fibre layup
2	0.31	Random fibre layup
3	0.22	Mainly UD with occasional cross weave at ~60°
4	0.23	Mainly UD with occasional cross weave at ~60°
5	0.45	Tight even weave at ~60°
6	0.26	Mainly UD with occasional cross weave at ~60°
7	0.28	Mainly UD with occasional cross weave at ~60°
8	0.20	Mainly UD with occasional cross weave at ~60°
9	0.20	Mainly UD with occasional cross weave at ~60°
10	1.28	Thick UD no weave
11	0.24	Tight even weave at ~60°
12	0.26	Tight even weave at ~60°
13	1.15	Thick UD no weave
14	1.00	Thick UD no weave
15	0.21	Mainly UD with occasional cross weave at ~60°
16	0.21	Mainly UD with occasional cross weave at ~60°
17	2.21	Thick UD no weave

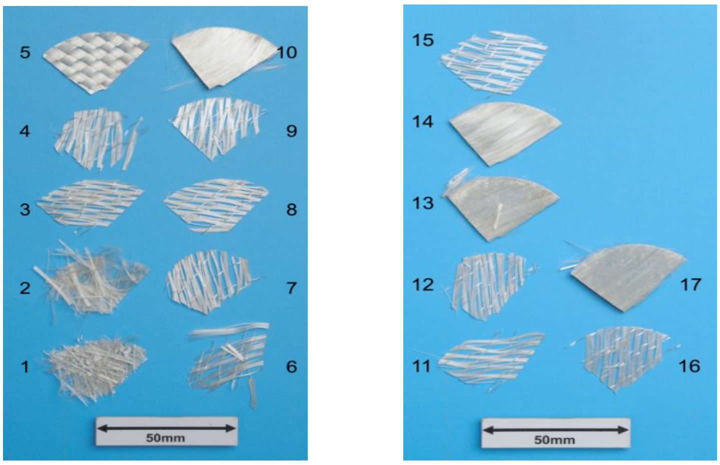

Figure 6.10: Fibre lay-up of material over spar cap

The information contained within Table 6.1 through Table 6.3 suggests that sensors placed along the length of the blade (and in line with the transmitter) will receive a signal of strength greater than that of an equivalently spaced sensor at an angle to the transmitter.

Figure 6.11 illustrates how the fibres in both the load-carrying spar-box and the aerodynamic frame relate to each other. The spar-box features predominant unidirectional (UD) fibres with no weave orientated along the length of the blade to provide the structure with strength. The angles of all other fibres (contributing to the spar box) are orientated with respect to the UD fibres. Together with adjacent layer contributions, it is clearly observed from Figure 6.11 that the predominant fibre orientation is in the 0°-180° axis (black). A tight weave also contributes to this orientation – with orthogonal fibres at 90° to the spar-box length (green). Additional loose cross weaves provide fibres oriented at 30° (red) and -75° (blue).

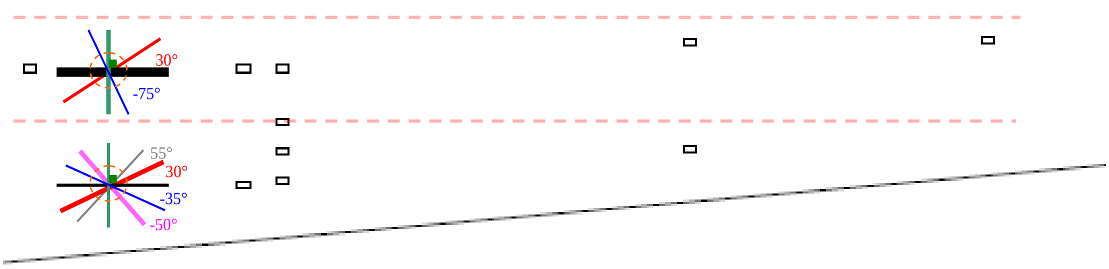

Load-carrying Spar-box:

– – – Random fibre lay-up – *Layer 1,2*
▬ UD at 0° (with no weave) along blade chord – *Layer 10,13,14,17*
— — Tight weave at 90° and 0° to spar box – *Layer 5*
— — UD at 30° to spar box with occasional cross weave at 0° spar box – *Layer 4,7,9,12,16*
— — UD at -75° to spar box with occasional cross weave 0° spar box – *Layer 3,6,8,11,15*

Aerodynamic frame:

– – – Random fibre lay-up – *Layer 1*
— — UD at +90° to blade chord with occasional cross weave at -35° - *Layer 2*
— — UD at 0° to blade chord with occasional weave at -50° – *Layer 3*
— — Tight even weave: -50° and +30° to blade chord– *Layer 4*
— — Fine even open weave at +55° and -35° to blade chord – *Layer 5*

Figure 6.11: Illustration and description of fibre lay-up both on the load-carrying spar-box and on the aerodynamic frame

The orientation of the spar-box fibres approaches bi-directionality. Figure 6.12 shows the spar-box fibre-orientation (indicatively weighted) with the directionality of the M2814 sensors for the S_0 mode (Figure 5.61) and the S_0 plot from FE model (Figure 5.56). From this analysis, stronger wave energy detection may be expected by receiver sensors orientated at approximately 0° along the spar-box from the transmitter. The expectation is that the sensor field pattern favours energy detection at 30° from the transmitter. However, energy propagation in this direction may be limited due to the reduced fibre bulk (compared with the UD at 0°). The orthogonal fibres – although with a tight bulk weave – would not be expected to deliver significant levels of wave energy due to the lack of sensor sensitivity at 90° and 270°.

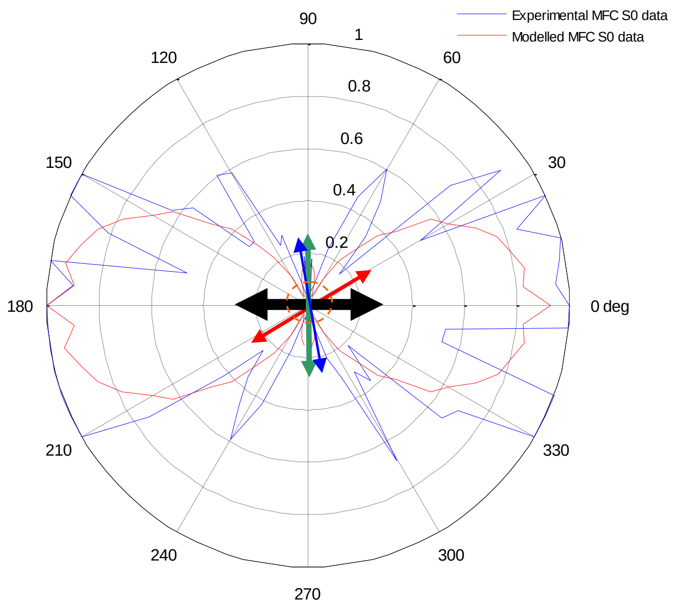

Figure 6.12: Fibre orientation of spar box combined with directionality of M2814 sensor on bidirectional GFRP

Examining the fibre orientation in the aerodynamic frame (Figure 6.11), a more evenly radial distribution of fibres is observed. There are UD fibres at 0° and 90° to the blade length (black and green respectively) with a tight even weave at -50° (pink) and 30° (red). A fine weave contributes to directional strength at 55° (grey) and -35° (blue). Occasional cross-weaves contribute at -35° and -50°. The material, therefore, can be considered to be quasi-isotropic. Figure 6.13 illustrates the coupling of the aerodynamic frame fibre-orientation (indicatively weighted) with the directionality of the M2814 sensors for the S_0 mode (Figure 5.64). Although the fibre orientation is more evenly distributed in all directions, due to the sensor field sensitivity, stronger wave energy detection may be expected by receiver sensors orientated at approximately 0° and 180° from the transmitter.

The sensor may also be expected to favour energy detection at 30° from the transmitter (with reduced sensitivity). Some wave energy may also be detected by sensors located at 55° to the transmitter. However, at this angle the SNR has dropped by 10 dB from comparative wave detection at 0°. The UD orthogonal fibres would not be expected to deliver significant levels of wave energy due to the lack of sensor sensitivity at 90° and 270°.

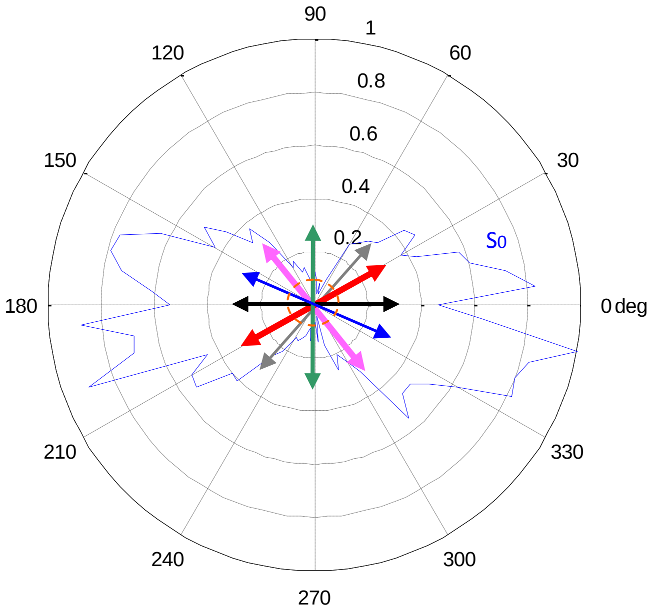

Figure 6.13: Fibre orientation of spar box combined with directionality of M2814 sensor on quasi-isotropic GFRP

The location of the sensors with respect to the fibre orientations of the blade component parts plays a significant role as regards the sensor sensitivity. The scope of the array is 3.76 m on the near bi-directional, load-carrying, spar cap and yields an SNR of -45 dBm. The longitudinal unidirectional fibre is the predominant medium of wave energy transfer.

Therefore, sensors orientated 0° to each other on the spar-cap will be most sensitive to changes in material characteristics. The aerodynamic frame is a sandwich structure with a GFRP quasi-isotropic top layer. The reduced fibre bulk in any one direction - together with additional boundary conditions - incurs a decrease in SNR of 20 dB for an oblique path distance at 70% of the distance of the longitudinal spar-cap analysis. The omnidirectional nature of this blade section ensures that energy propagates in a more uniform fashion and thus has less influence on the placement of sensors.

The quality of the received signal will depend upon sensor location with respect to the blade boundary separating the spar cap from the aerodynamic frame. If the propagating signal traverses a boundary from source to receiver, a more complex signal with additional scattering and reflections can be expected. Subsequent analysis focuses on the effect of boundary conditions upon a propagating ultrasonic wave to observe how it changes within the presence of a defect.

6.5 Baseline Reference Analysis of Sensor Array

The sparse sensor array extends a distance of 3.76 m (Figure 6.2) along the blade length and spans 530 mm across its width. It is therefore instructive to be able to observe the sensitivity of each sensor for different excitation locations. The angle of each of the transmitters to all other receiver sensors is illustrated in Figure 6.14.

The location of the receiving sensor with respect to the transmitting sensor has an impact on the received signal strength. The subsections which follow focus on sensor alignment and the effect of the presence of a boundary.

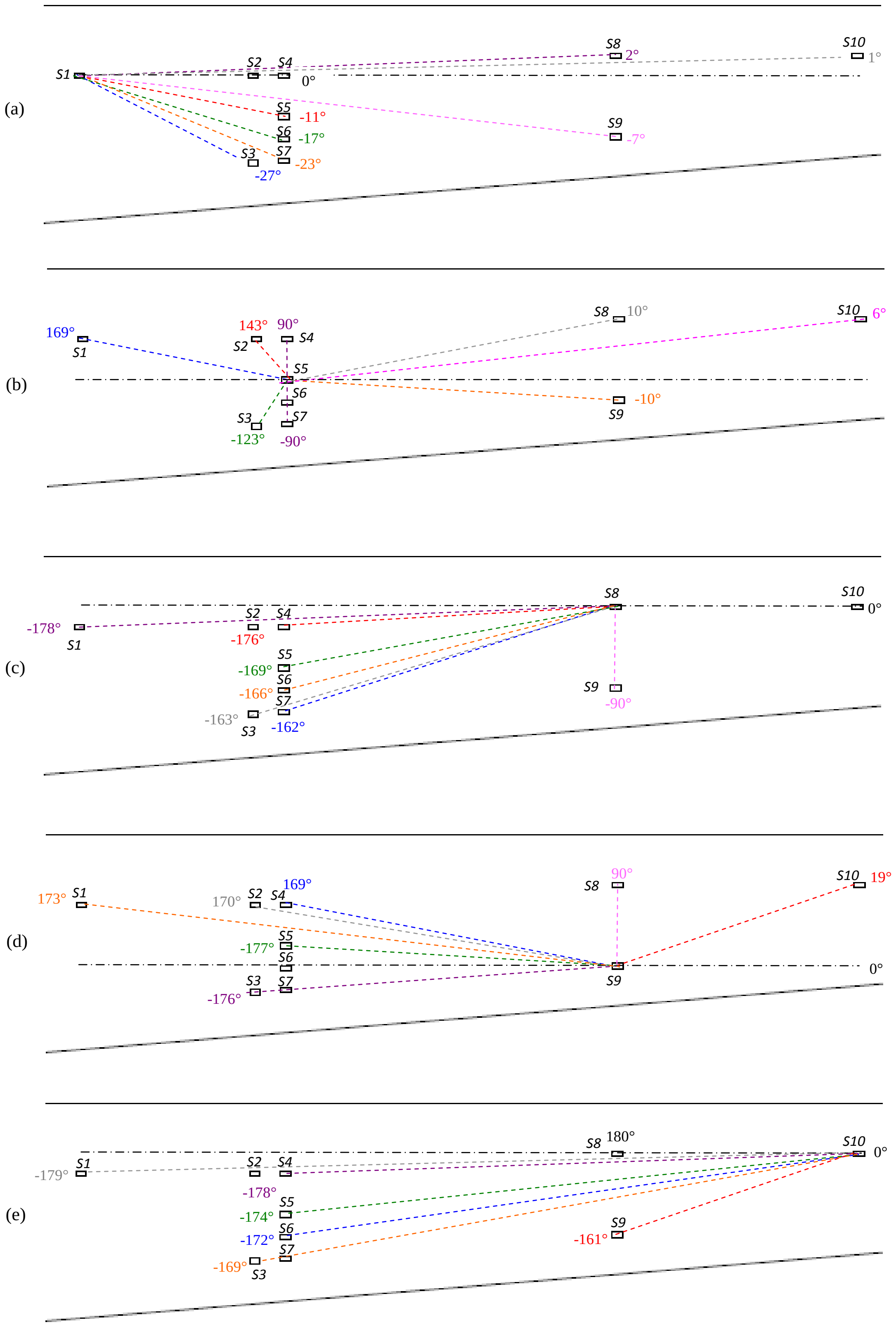

Figure 6.14: Receiving sensors with respect to the transmitting sensor: S1, (a); S5, (b); S8, (c); S9, (d); S10, (e)

6.5.1 Spar Cap Sensor Analysis

The turbine blade features a spar-box which serves as the strengthening member of the blade. This internal structure spans 7 m along the blade length. In this region of the blade, the sole material present is GFRP. Using the configuration illustrated in Figure 6.14(a) to ascertain the sensitivity of the array, the signals recorded by receive sensors S2, S8 and S10 were analysed, Figure 6.15. The signal used to excite S1 is detailed in Appendix C3.

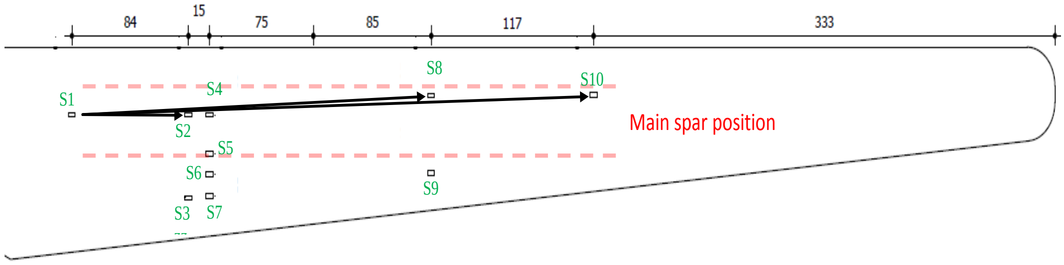

Figure 6.15: Transmit on Sensor 1 and receive on Sensors 2, 8 & 10

Figure 6.16 provides a single image indicating: Tx sensor to Rx sensor alignment (dashed lines); the GFRP fibre direction (weighted arrows); the S_0 mode orientation appropriate for bidirectional GFRP; and the S_0 plot from FE model (Figure 5.56). As

Figure 6.16 indicates; sensor alignment, dominant fibre direction (0° - 180°), and S_0 mode plot are all in reasonable agreement. Figure 6.17 shows a strong signal at S2 (0.84 m), at S8 (2.59 m) and at S10 (3.76 m). Each response provides a high SNR and clearly features the S_0 mode. In addition, the attenuation can be determined for this area of the blade: -7.5 dBm^{-1}.

Signal integrity issues were experienced with the cable used to collect data from Sensor S4. Further information is provided in Appendix C4.

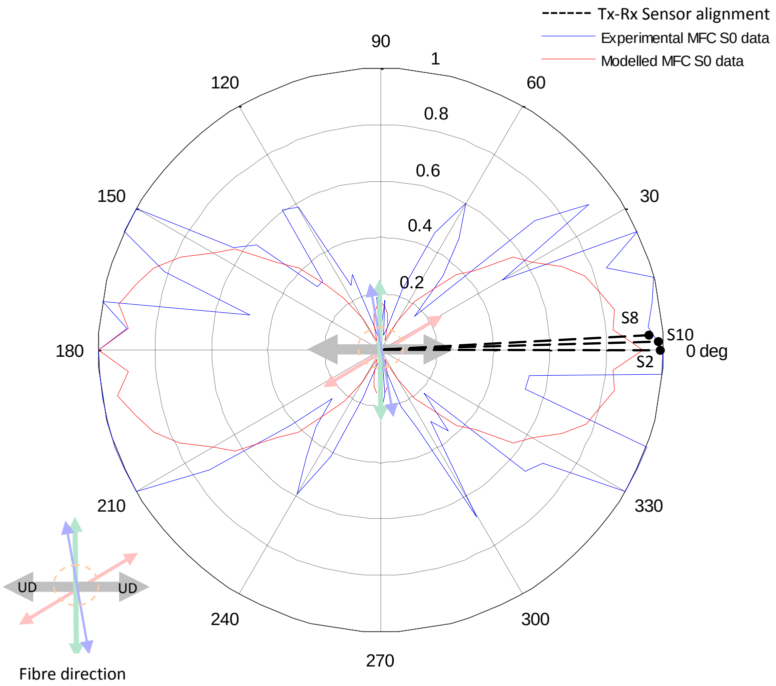

Figure 6.16: Rx sensor alignment to Tx corresponding to spar-box UD fibre direction and maximum sensor sensitivity. Sensor S1 (Tx) at centre. Arrows indicate weighted fibre orientation within blade. Bidirectional GFRP experimental MFC S_0 response, blue; modelled MFC S_0 response, red.

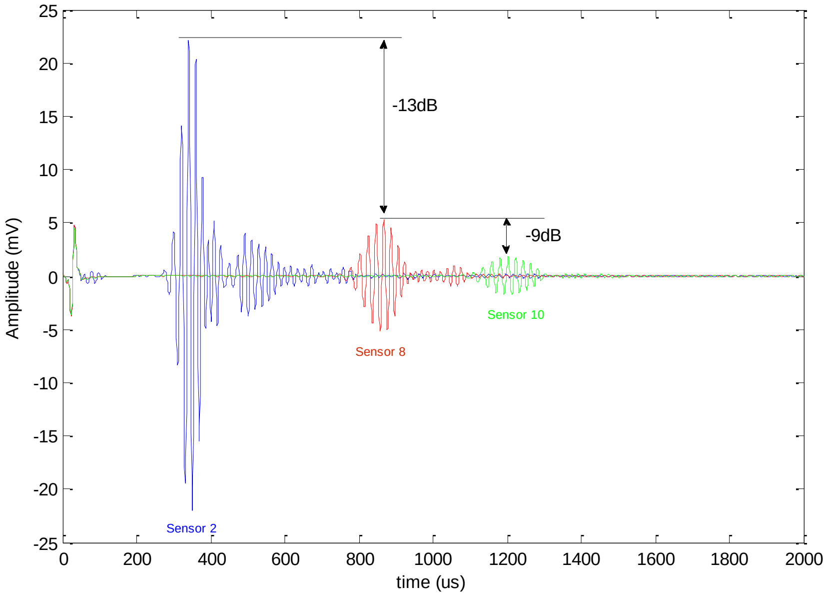

Figure 6.17: A-scans recorded at Sensors 2, 8 & 10 for transmission on Sensor 1

The remaining sensors (S3, S5, S6, S7 and S9) are outwith the spar cap region and are considered in the following subsection.

6.5.2 Aerodynamic Frame

To observe the signals excited and received within the aerodynamic frame, the configuration illustrated in Figure 6.14(d) was used: sensor S9 selected as transmitter and sensors S3 (1.75 m from S9), S5 (1.6 m), S6 (1.6 m) and S7 (1.6 m) selected as receivers, Figure 6.18.

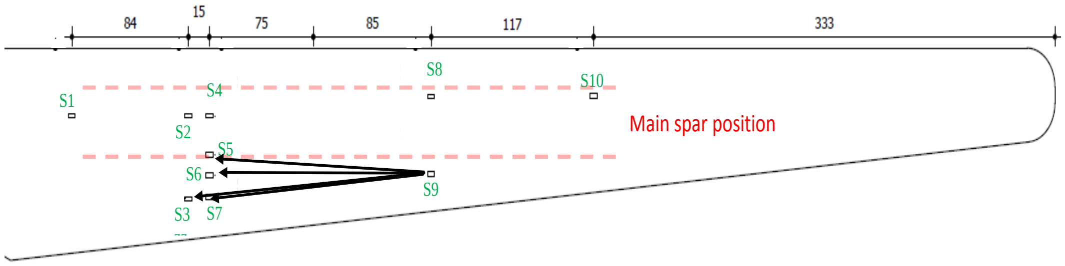

Figure 6.18: Transmit on sensor S9 and receive on sensors S3, S5, S6 & S7

Figure 6.19 provides a single image indicating: Tx sensor to Rx sensor alignment (dashed lines); the GFRP fibre direction (weighted arrows); and the MFC S_0 mode orientation appropriate for quasi-isotropic GFRP. As Figure 6.19 indicates; sensor alignment and S_0 mode plot are in reasonable agreement. However, the fibre orientation of the aerodynamic frame is evenly distributed. The SNR of stress waves propagating along fibre directions oriented in the 0°-180° (±20°) direction is expected to be greater than those waves propagating in other directions.

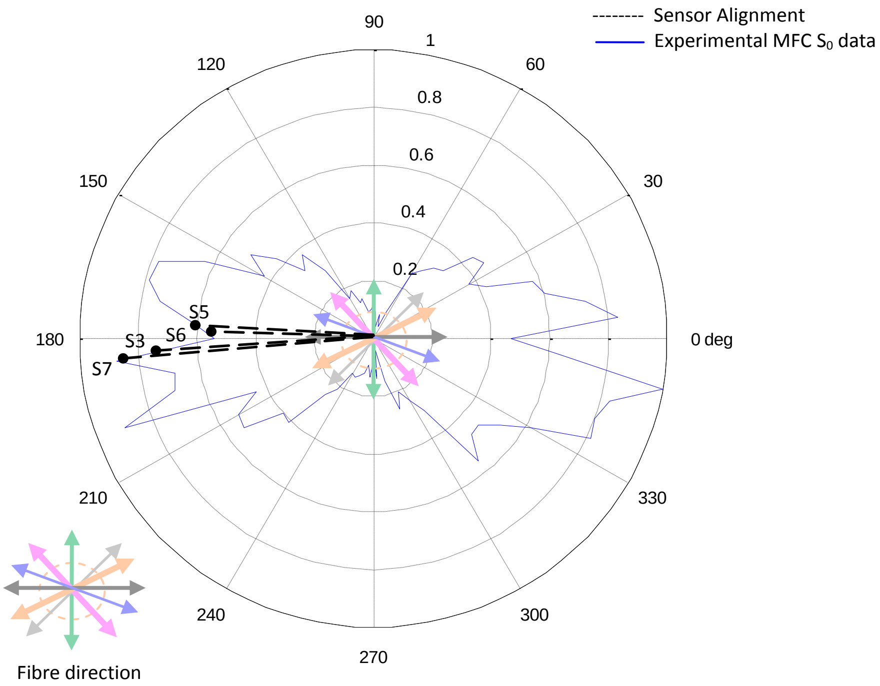

Figure 6.19: Rx sensor alignment to Tx on aerodynamic frame with respect to sensor sensitivity. Arrows indicate weighted fibre orientation within blade. Sensor S9 (Tx) at centre. Quasi-isotropic GFRP experimental MFC S_0 response, blue.

The presence of the S_0 mode is observed in the A-scans for sensors S3, S5, S6 and S7, Figure 6.20. Sensor S6 is on-fibre (1° misalignment, Figure 6.18) whereas S7 has a misalignment of 4°. Consequently, the signal magnitude recorded at S6 is 6 dB greater than that recorded at S7. Being on the boundary of the spar-cap, S5 has a complex waveform featuring reflections and mode conversion.

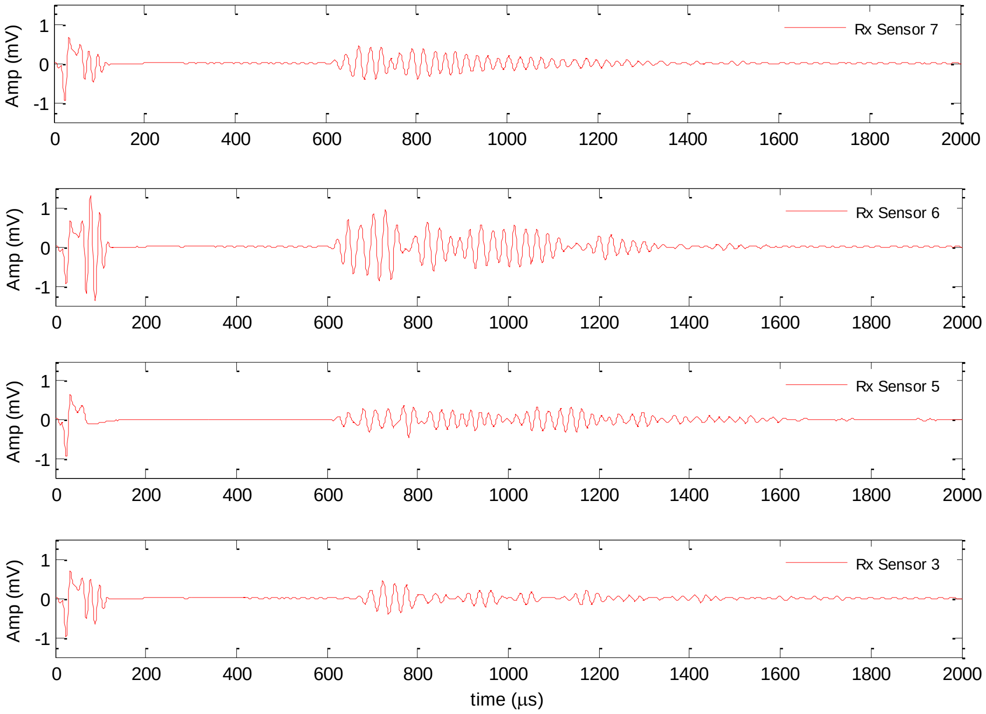

Figure 6.20: A-scans recorded at sensors S3, S5, S6, and S7 for transmission on sensor S9

6.5.3 Boundary Effects: Spar Cap to Aerodynamic Frame

To observe the effects of a propagating wave crossing the spar-cap boundary into the aerodynamic frame (a GFRP-Foam-GFRP sandwich structure), configuration Figure 6.14 (c) was used: sensor S8 as transmitter (Appendix C3); and S3, S6, S7 & S9 as receivers on the aerodynamic structure, Figure 6.21.

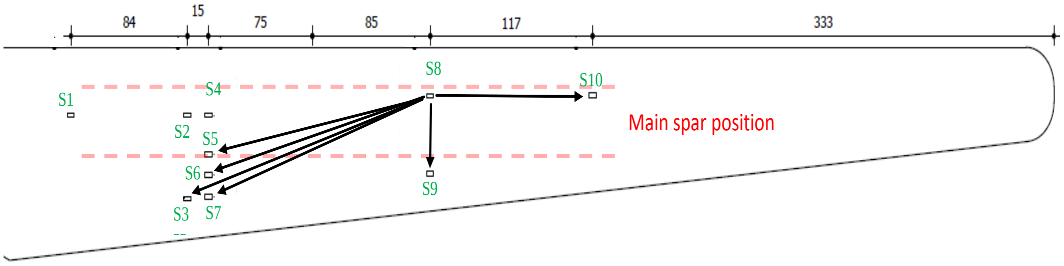

Figure 6.21: Transmit on S8 and receive on Sensors S3, S5, S6, S7, S9 & S10

For comparison, sensor S10, situated on the same blade area as the transmitter, was also configured as a receiver.

The wave propagation path from S8 to S10 is contained within the bidirectional spar cap component, summarised by Figure 6.22. However, two component structures (spar cap and quasi-isotropic aerodynamic frame) have to be considered for the wave propagation path from S8 to S3, S6, S7 and S9, Figure 6.22 and Figure 6.23.

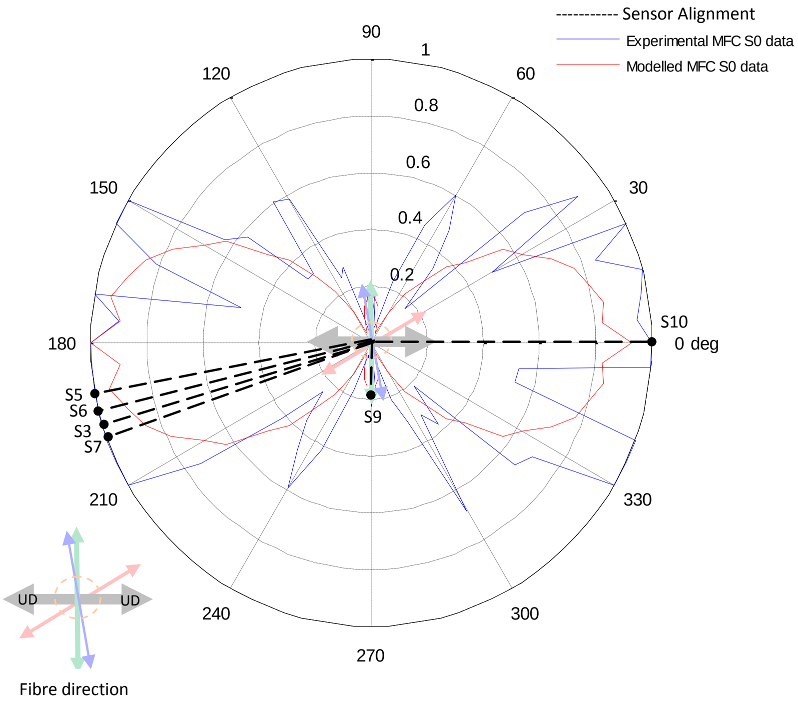

Figure 6.22: Spar cap blade configuration for: wave propagation path (part 1) for S3, S5, S6, S7 & S9 Tx – Rx sensor alignment; and full wave propagation path for S10. Sensor S8 (Tx) at centre. Bidirectional GFRP experimental MFC S_0 response in blue. Modelled MFC S_0 response in red. Arrows indicate weighted fibre orientation within blade.

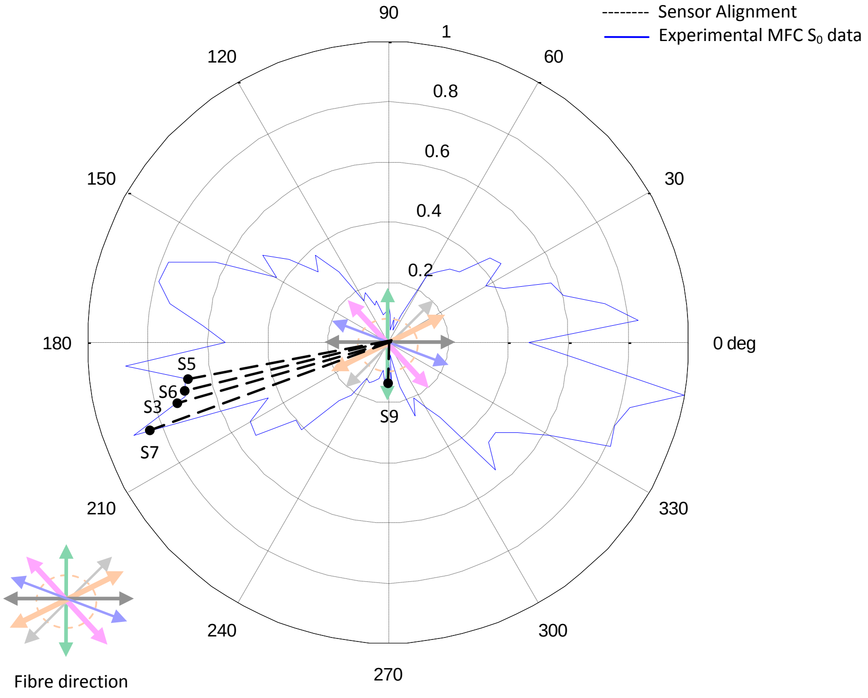

Figure 6.23: **Spar cap blade configuration for: wave propagation path (part 2) for S3, S5, S6, S7 & S9 Tx – Rx sensor alignment; and full wave propagation path for S10. Sensor S8 (Tx) at centre. Quasi-isotropic GFRP experimental MFC S_0 response in blue. Arrows indicate weighted fibre orientation within blade.**

Figure 6.24 shows the response for sensors S9 (0.4 m from S8), S10 (1.17 m), S6 (1.65 m), S7 (1.68 m) and S3 (1.83 m). Although S9 is closest to S8, it is located just 100mm from the spar-cap boundary initiating reflections and causing mode conversion. Both S3 and S7 provide the poorest SNR response, however; each response clearly shows a small S_0 mode. The response of S6 - located 110 mm from the spar cap boundary – also includes a clear S_0 mode with reflections present.

Sensor S5 (1.63 m), located at the interface between the spar-cap and the aerodynamic structure, does not show clear modal data due to the immediate onset of reflections.

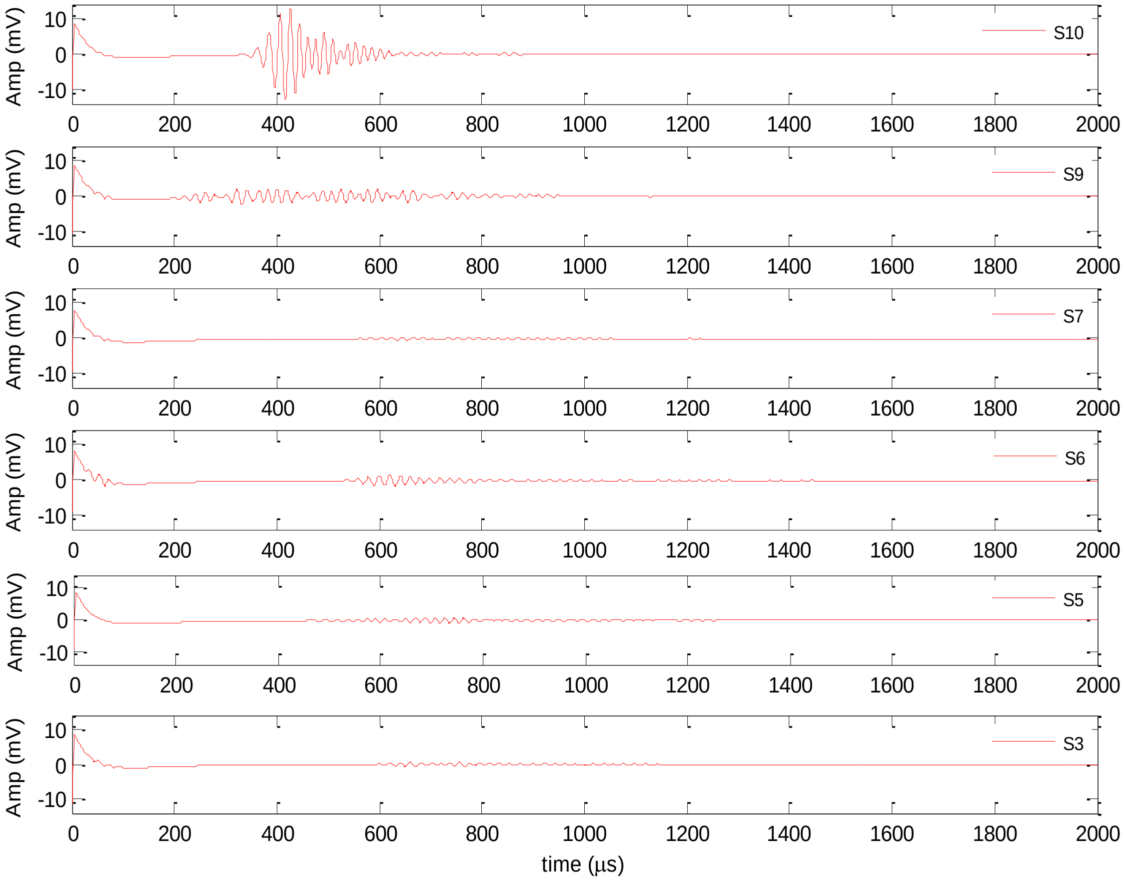

Figure 6.24: A-scans recorded at Sensors 3, 6, 7, 9 & 10; excitation on Sensor 8

Sensor S10, included for comparison and located on the same blade component as Tx sensor, is displaced from S8 by a distance greater than twice that of S9. However, the SNR of the S_0 mode, recorded at S10, is significantly greater than that recorded at S9, clearly indicating a drop in SNR when a stress wave propagates from one blade component into another.

6.5.4 Boundary Effects: Aerodynamic Frame to Spar Cap

To observe the signals excited within the aerodynamic frame propagating into the spar-cap, configuration Figure 6.14(d) was used. Transmitting on sensor S9, signals were observed at receivers, S1 (2.61 m), S2 (1.78 m), S8 (0.4 m) and S10 (1.24 m), Figure 6.25.

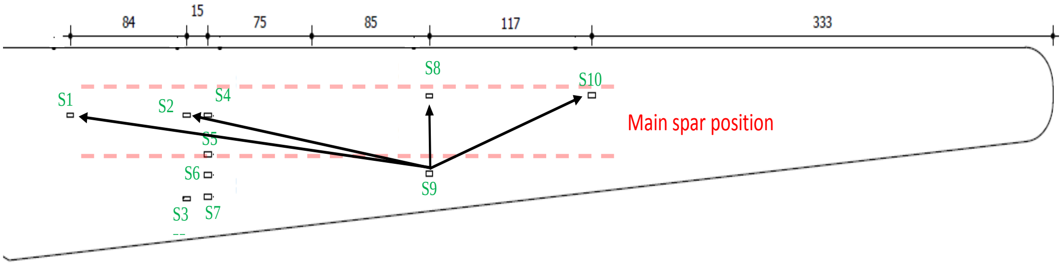

Figure 6.25: Transmit on S9 and receive on Sensors S1, S4, S8 & S10

Two blade component structures (spar cap and quasi-isotropic aerodynamic frame) have to be considered for the wave propagation path from S9 to S1, S2, S8 and S10, Figure 6.26 and Figure 6.27.

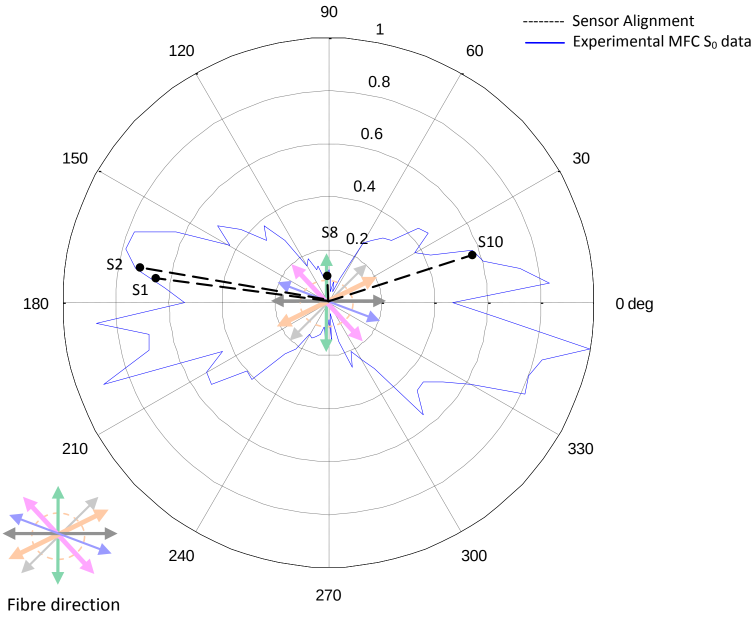

Figure 6.26: Spar cap blade configuration for wave propagation path (part 1) for S1, S2, S8 & S10 Tx – Rx sensor alignment. Sensor S9 (Tx) at centre. Quasi-isotropic GFRP experimental MFC S_0 response in blue. Arrows indicate weighted fibre orientation within blade.

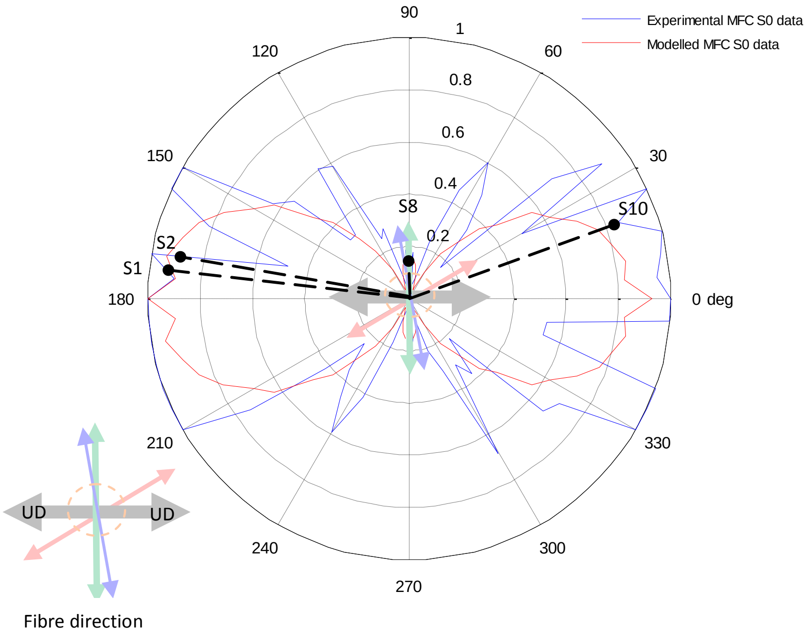

Figure 6.27: Spar cap blade configuration for: wave propagation path (part 1) for S1, S2, S8 & S10 Tx – Rx sensor alignment. Sensor S9 (Tx) at centre. Bidirectional GFRP experimental MFC S_0 response in blue. Modelled MFC S_0 response in red. Arrows indicate weighted fibre orientation within blade.

Figure 6.28 shows wave reflections at each receiver. The longer distances between S9 and S1, S2 and S10 permit observation of the S_0 mode. The presence of the boundary together with change of fibre orientation, significantly impact upon the strength of the recorded signals. Sensor S8 is oriented 90° to the transmitter where signal sensitivity is at its minimum. As a result, the SNR at S5 is only 2.5 dB higher than the signal recorded at S10 (despite S10 being positioned three times farther from the transmitter).

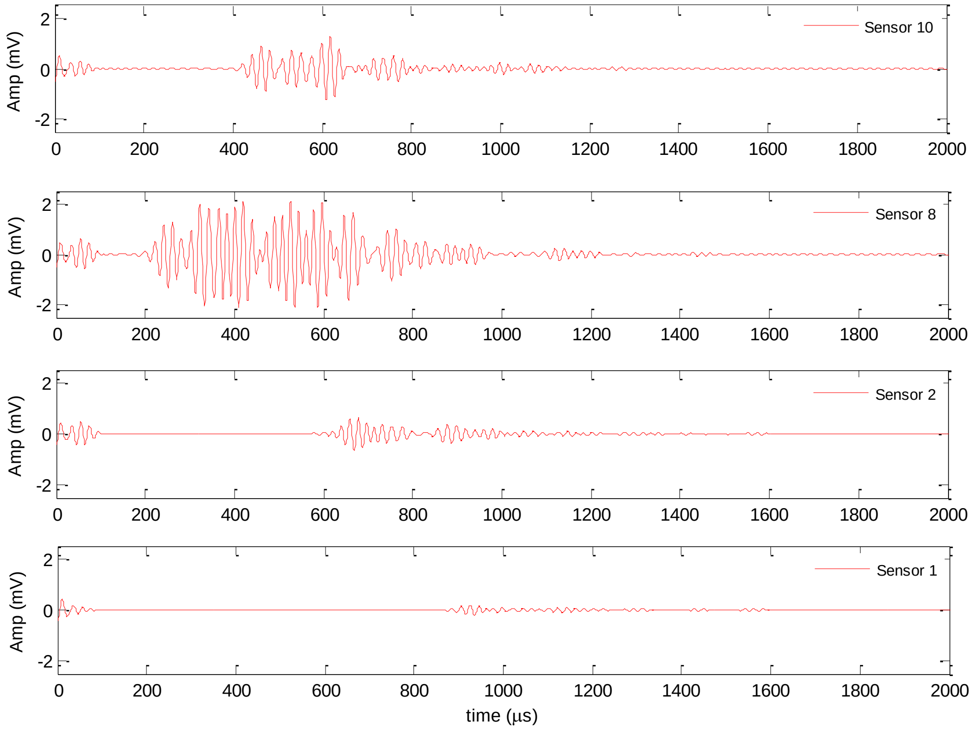

Figure 6.28: A-scans recorded at Sensors 1, 2, 8, 10 for transmission on Sensor 9

6.5.5 Sensor Array Symmetry

To ascertain the symmetry of the sensor array with respect to the spar cap, a converse arrangement to Figure 6.15 was established (using configuration of Figure 6.14(e)) where sensor S10 was configured as transmitter and sensors S1, S2 and S8 were configured as receivers, Figure 6.29.

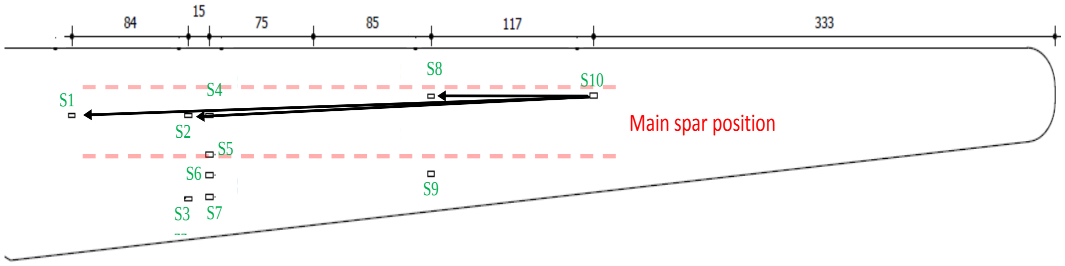

Figure 6.29: Transmit on Sensor S10 and receive on sensors S8, S2 & S1

Comparing S8 in Figure 6.30 with S2 in Figure 6.17 reveals a 5 dB difference in SNR. This can be explained by observing (from Figure 6.2) that S8 is located 1.17 m from transmitter S10 whilst S2 is located 0.84 m from transmitter S1. There is good agreement between the signal recorded at S1 (Figure 6.30) and that recorded at S10 in Figure 6.17. Thus, the sparse array exhibits symmetry across the spar-cap.

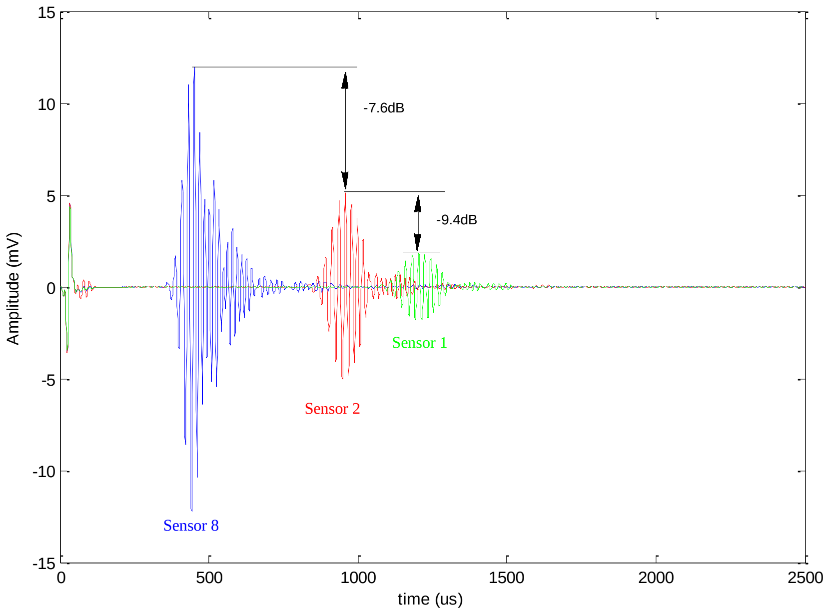

Figure 6.30: A-scans recorded at sensors S1, S2, and S8. Transmission on S10.

A similar analysis was conducted with respect to the aerodynamic frame with respect to sensors S1 and S9, Figure 6.31.

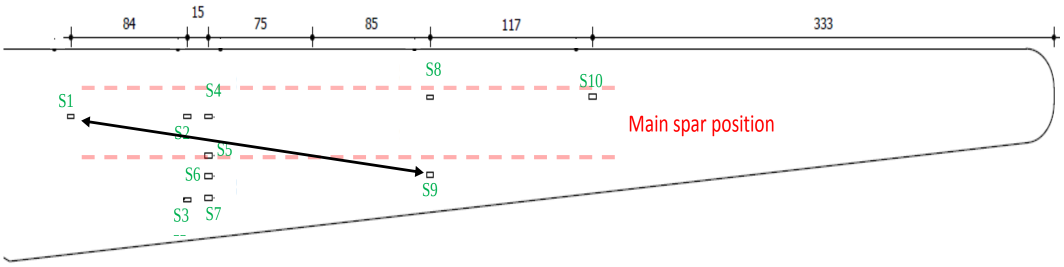

Figure 6.31: Transmit on sensor S1 and receive on sensor S9, and vice versa.

Figure 6.32 shows the two signals to be almost identical, indicating symmetry between sensors on either side of the spar cap boundary.

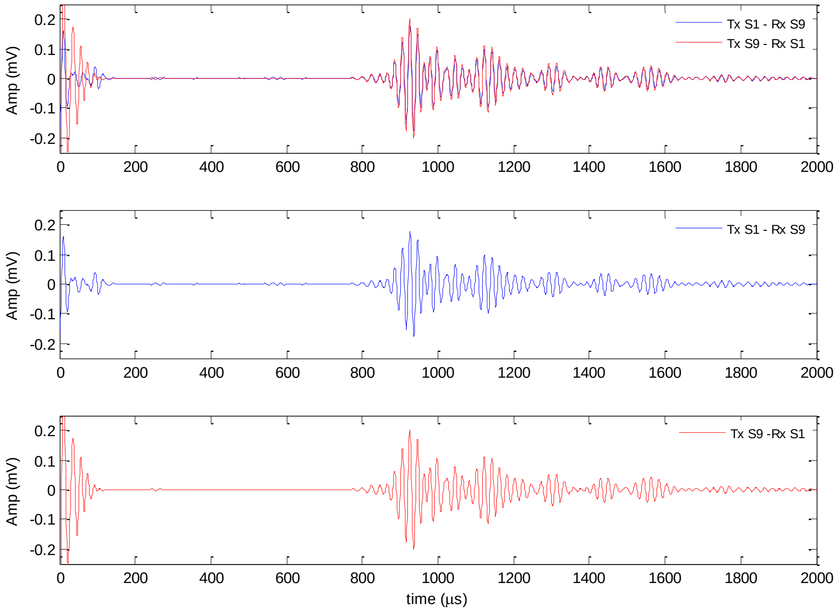

Figure 6.32: Transmit on S1 and receive on S9, blue; transmit on S9 and receive on S1, red; comparison, top.

Finally, a comparison was made between two propagating waves travelling 1.65 m: S8 to S2 on the spar cap; and S9 to S3 on the aerodynamic frame, Figure 6.33.

It is observed that there is a 29 dB difference for the same transmit-receive sensor separation. Given Figure 6.14(c) and (d) show the orientation of each receiver as -176° to the transmitter (with maximum sensor sensitivity); it is assumed that this difference in amplitude response can be attributed to the different material types with separately defined fibre orientations.

The different material properties of the spar cap and aerodynamic frame have also impacted the signal arrival time where the latter exhibits lower velocity properties.

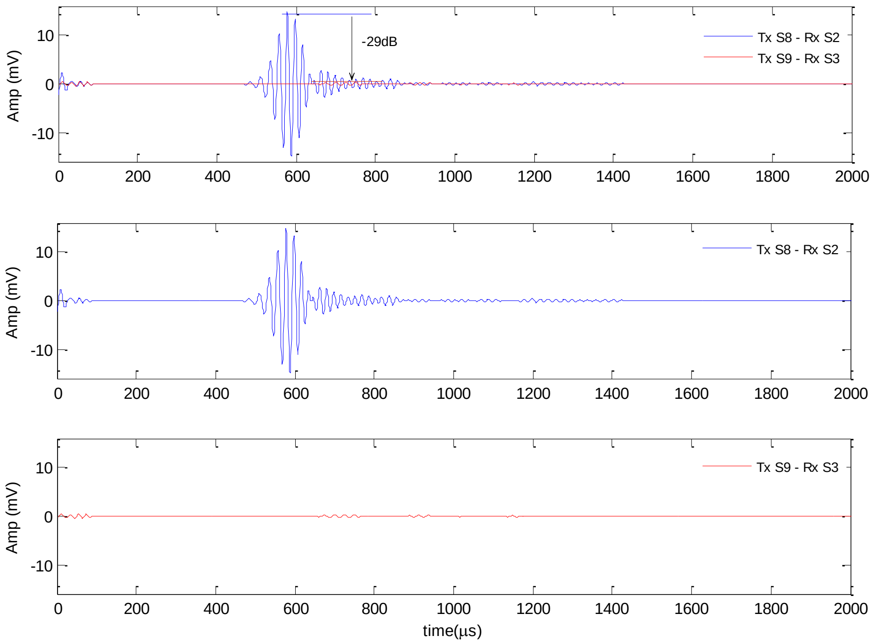

Figure 6.33: Transmit on S8 and receive on S2, blue; transmit on S9 and receive on S3, red; comparison, top.

Clear transmission of the S_0 was achieved for the full length of the sparse array on the spar-cap. Comparison of transmit/receive sensor configuration on the spar cap with the aerodynamic frame yielded greater SNR for the S_0 with respect to the latter. Lastly, the array exhibited a significant level of spatial symmetry.

6.5.6 Summary

Transmitting and receiving on the spar-cap yields a significantly increased SNR (29 dB) than transmitting and receiving on the aerodynamic frame - for the same sensor separation. This is predominantly due to the increased density of fibres orientated in the direction of the spar-cap. The aerodynamic foil comprises a top layer of GFRP which has a relatively more equal axial distribution of fibres. As the transmitter approached the boundary, signal reflections were observed to increase. As a result, it became increasingly difficult to distinguish between the propagating wave modes.

Whilst it may be acknowledged that blades vary in design with different fibre orientation, eliciting individual signatures, the conclusion of this section indicates that knowledge of blade design can help optimise Guided wave monitoring techniques. To assist, blade information can be obtained from the blade manufacturer.

6.6 Conclusion

An analysis of Macro-Fibre Composite (MFC) transducers together with the rotor blade material characteristics was performed. Throughout the experimental study, the unobtrusive, conformable and lightweight interdigitated sensor coupled well to the curved geometry of the blade making it a physically realisable solution for defect detection as part of a spatial array.

A sparse array of sensors was distributed across a detached wind-turbine blade (3.76 m x 0.78 m) to provide significant coverage of the turbine blade both on the load-carrying spar-cap and on the aerodynamic frame. The directionality of the sensor together with the orientation of fibres within the vicinity of the sensor - and at more remote locations – was considered. Baseline reference analysis was performed to assess the capability of the array. The sensor array exhibited approximate symmetry upon analysing the signal response along one direction of the blade compared with the opposite direction.

7 Response of Guided Waves to Onset of Blade Defects

7.1 Overview

The preceding chapter considered the implications of sensor location. This chapter analyses the characteristic changes to propagating Guided waves when a defect is applied within the vicinity of the sparse array described Figure 6.2 and Figure 6.14.

Thus far, analysis has predominantly focused on the amplitude and arrival time of received signals. However, Section 6.5 revealed the limitation of such analysis due to the presence of the boundary between the spar-cap and the aerodynamic frame; which sets up reflections obfuscating specific modal information. Therefore, this chapter applies signal processing techniques to the received Guided waves to establish its disparity from a baseline reference signal. The cross-correlation function was identified as a technique sensitive to slight variations between a pair of A-scan signals. Analysis considered 5 different excitation locations on the blade to identify signatures due to component differences. Three defects were considered: 2 mm indentation damage, 12 mm indentation damage and through-hole damage.

To optimise signature differences between baseline reference data and defect data, a sliding-window cross-correlation function was applied to pairs of A-scans with the aim of scrutinising time-windows containing modal data.

7.2 Cross-Correlation Function

The cross correlation is a standard method of estimating the degree to which two series are correlated. The cross correlation function of two series *x(k)* and *y(k)* (for *k= 0,1,2…N-1*) is shown in Equation (7.1)

$$r(d)=\frac{\sum_k (x(k)-\bar{x})(y(k-d)-\bar{y})}{\sqrt{\sum_k (x(k)-\bar{x})^2}\sqrt{\sum_k (y(k-d)-\bar{y})^2}} \tag{7.1}$$

Where, the variable d represents the delay. Which, when evaluated for all delays $d = 0,1,2 \cdots N-1$, the cross correlation sequence will have twice the length of the original series. Figure 7.1 illustrates the cross correlation between two signals received on sensor S8 (Figure 6.2) whilst transmitting on S1 for the no-defect case.

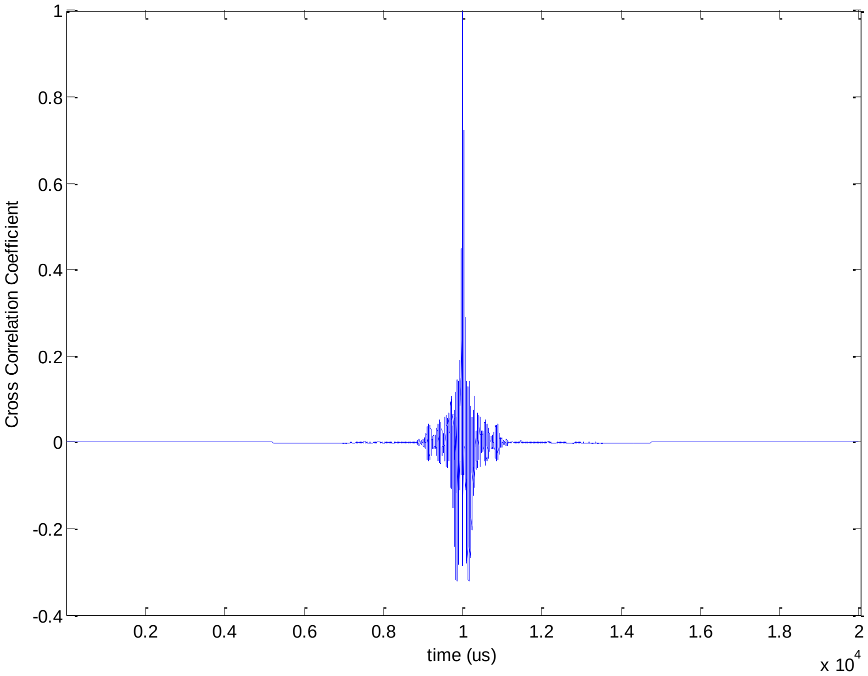

Figure 7.1: No defect cross-correlation function for Rx sensor S8 when exciting on sensor S1

As expected, the correlation coefficient was very high when there was no delay between the two data sequences: *r(d)* = 0.9999. When a delay was introduced, the coefficient dropped rapidly. Essentially the cross-correlation function statistically measures the degree of match between the two samples. The highest value in the correlation plane can then be used as a direct estimate of the particle image displacement. This method of analysis of change between two sequences – one of which will contain information relating to an applied defect – will be used to assess detection.

Four different defects were analysed: hole damage in the spar-cap; 2 mm indentation damage in the aerodynamic frame; 12 mm indentation damage in the aerodynamic frame; and hole damage in the aerodynamic frame.

7.2.1 Defect 1 – Through Hole

A 60mm diameter hole was drilled through the spar-cap section of the turbine blade between sensors S4 and S8, Figure 7.2. The objective was to assess which sensors were able to detect the presence of the hole.

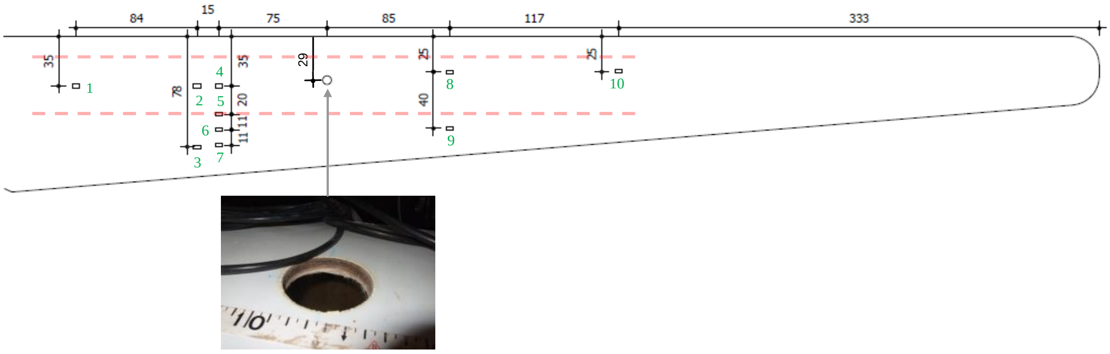

Figure 7.2: Blade layout showing position of hole defect

With sensor S1 configured as transmitter (excitation shown in Appendix C3) and S10 configured as receiver, the recorded A-scan was directly compared with the A-scan of the no-defect set-up, Figure 7.3. The amplitude was observed to drop by 3 dB.

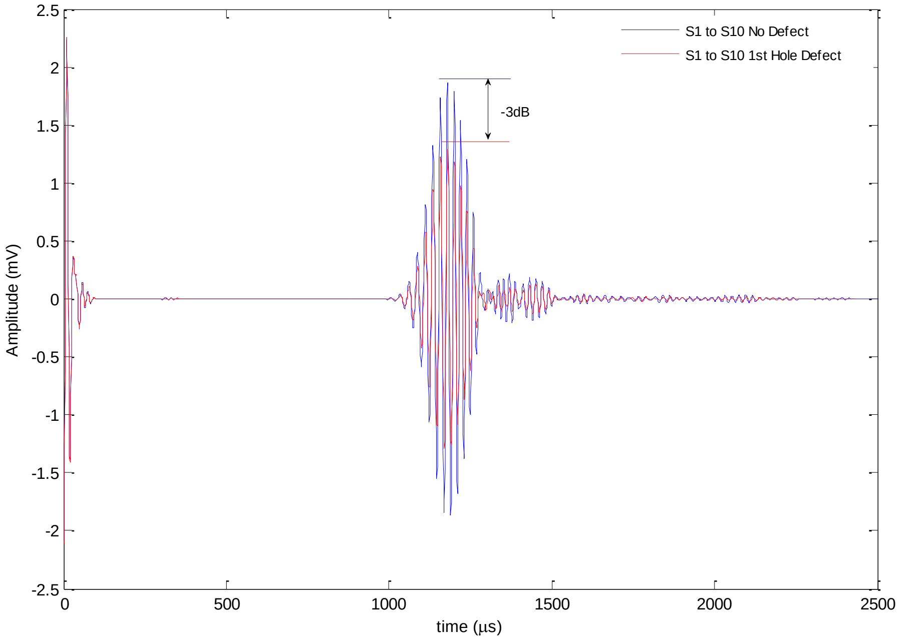

Figure 7.3: Comparison of baseline and hole defect A-scans for across the length of the spar-cap using the cross correlation function (Equation 7.1)

Table D.1 (Appendix D) provides the relevant data. To better visually demonstrate the data, the squared inverse of the cross correlation function was evaluated using Equation (7.2), Figure 7.4.

$$\left(\frac{1}{r(d)}-1\right)^2 \tag{7.2}$$

It is observed that receive sensors located on the spar-cap (where the hole defect occurs) were capable of detecting the presence of the defect. Sensor S1 to S4 and S8 showed significant drop in the cross correlation coefficient, *r(d)*. Symmetrically similar, sensor S10 to S4 and S2 also showed a significant drop in *r(d)*. Finally, sensor S8 to S2 and S4 showed a similar drop in *r(d)*, as did sensor S8 to S1.

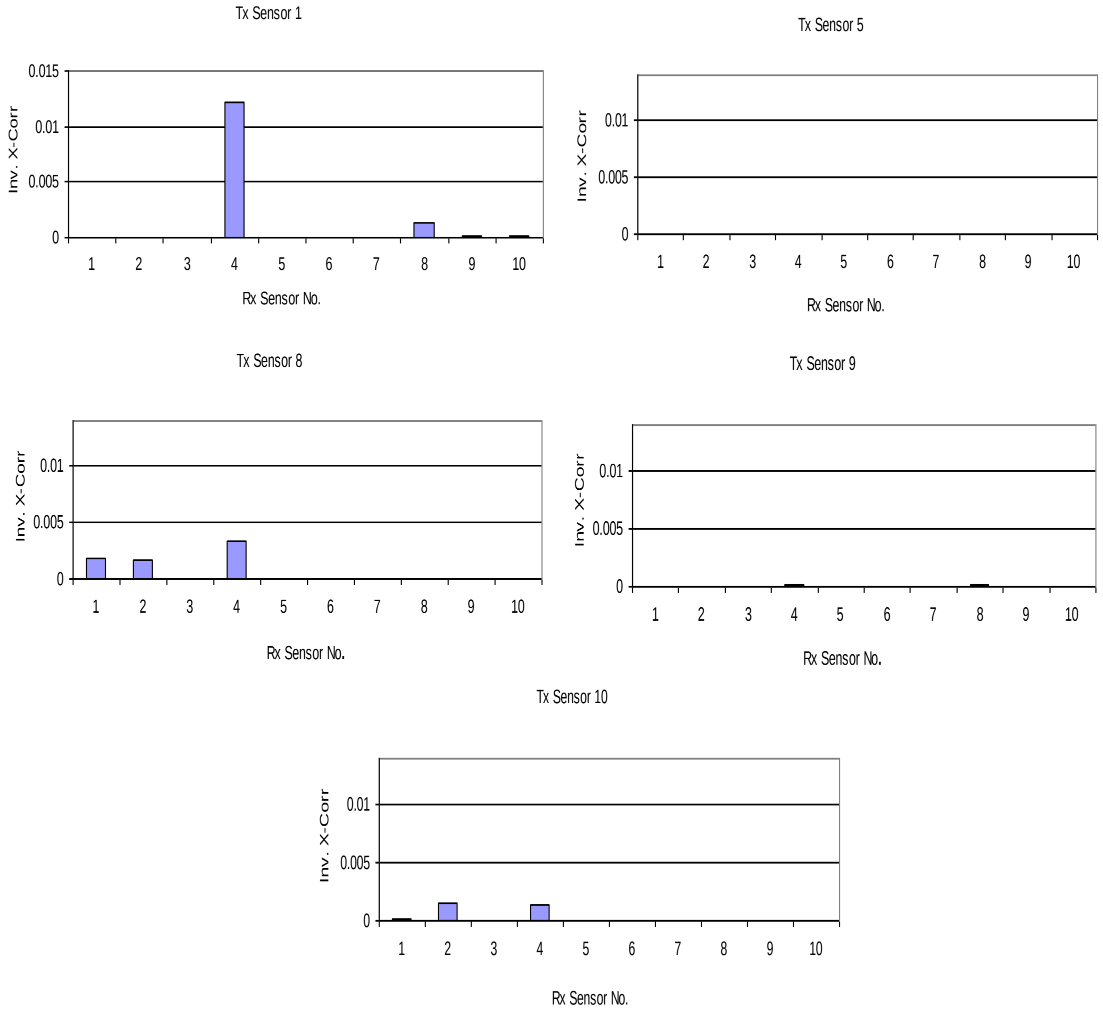

Figure 7.4: Inverse cross correlation representation for sequential Tx Sensors 1, 5, 8, 9 & 10. All other sensors configured as Rx

In summary, a defect signature was clearly visible between transmit sensors (S1, S8 & S10) and receive sensors (S1, S2, S4 & S8) surrounding the defect all located on the spar-cap. Dominated by UD fibre running along the length of the blade, appropriately aligned sensors on this section of the blade provides optimised signal sensitivity, (Figure 6.16).

7.2.2 Defect 2 – 2 mm Blade Indentation

A 60mm diameter, 2 mm circumferential indentation was drilled through the aerodynamic surface of the blade between sensors S6 and S9, Figure 7.5.

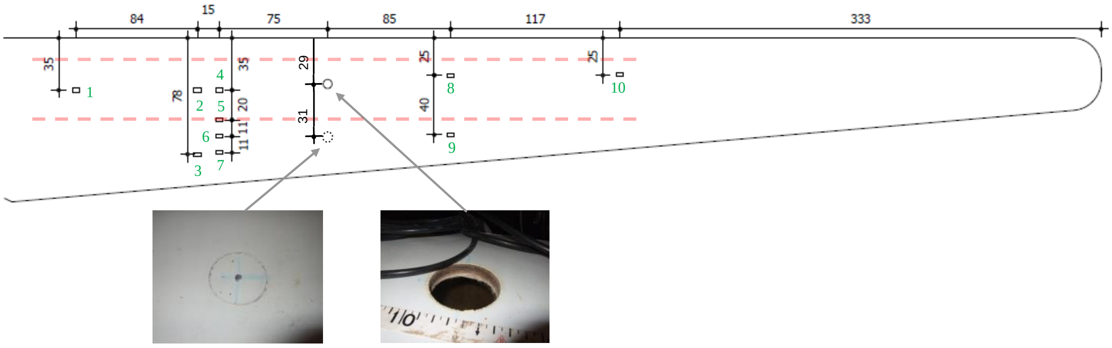

Figure 7.5: Blade layout showing position of 2 mm fibre defect located 31cm from the through-hole.

Comparing the A-scans of the baseline data (sensors S9 to S6 and S7) to the data acquired after application of the 2mm defect, Figure 7.6 and Figure 7.7.

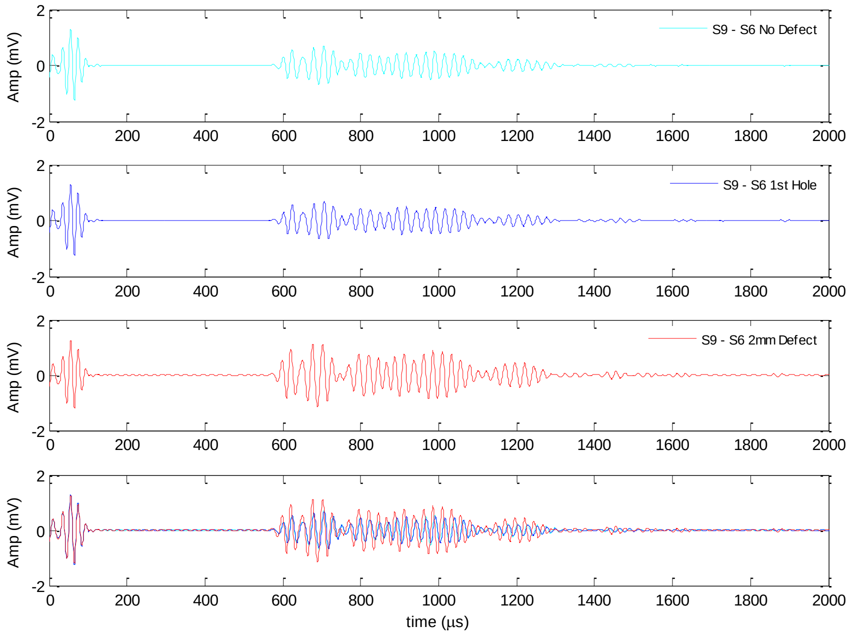

Figure 7.6: Comparison of No Defect (cyan), 1st Hole Defect (blue) and 60mm diameter 2 mm circumferential defect (red) A-scans across aerodynamic blade frame. Tx Sensor 9 to Rx Sensor 6.

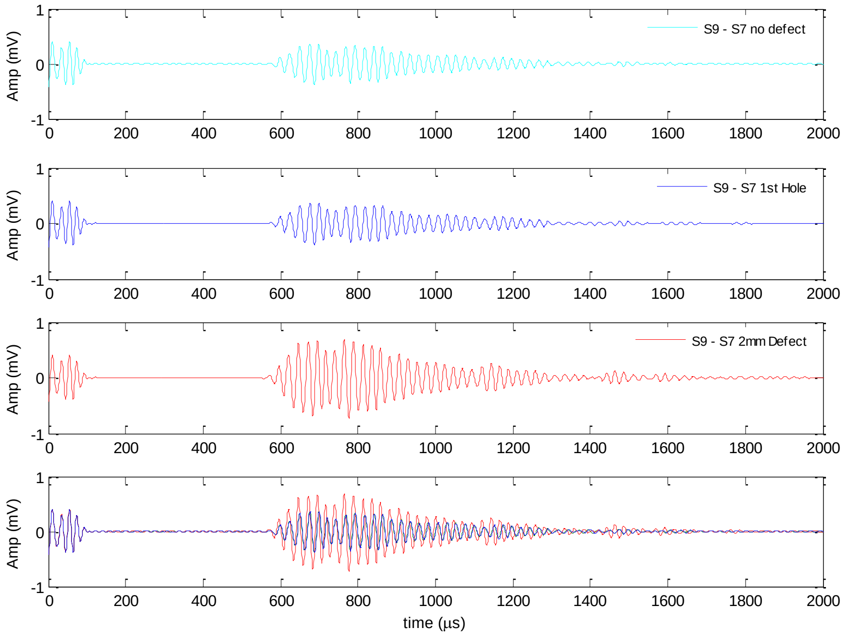

Figure 7.7: Comparison of No Defect (cyan), 1st Hole Defect (blue) and 60 mm diameter 2 mm circumferential defect (red) A-scans across aerodynamic blade frame. Tx Sensor 9 to Rx Sensor 7.

It is observed that upon application of the 2 mm defect, increased amplitude is recorded. Using the cross correlation function described in Equation (6.2). Table D.2 (Appendix D) provides the relevant data. A graphical representation of is illustrated in Figure 7.8.

Sensor S5, configured as Tx, recorded the largest discrepancy between the baseline and 2 mm defect data sequences – particularly on the receivers closest to the defect (sensors S3, S6 & S7). Information for '*Tx Sensor 1*', '*Tx Sensor 8*' and '*Tx Sensor 9*' were similar. The expectation was that the data returned by S9 would show greater evidence of defect presence due to closer proximity to the defect. However, the damage to the blade surface was to the blade skin only. This material is isotropic and therefore the order of greatest sensitivity to the defect (with respect to the transmitter location) should be: *Tx Sensor 5*, followed by *Tx-Sensor 9*, *Tx-Sensor 8*, *Tx-Sensor 1* and finally *Tx-Sensor 10*. This order of expected defect sensitivity was in broad agreement with the recorded data of Figure 7.8.

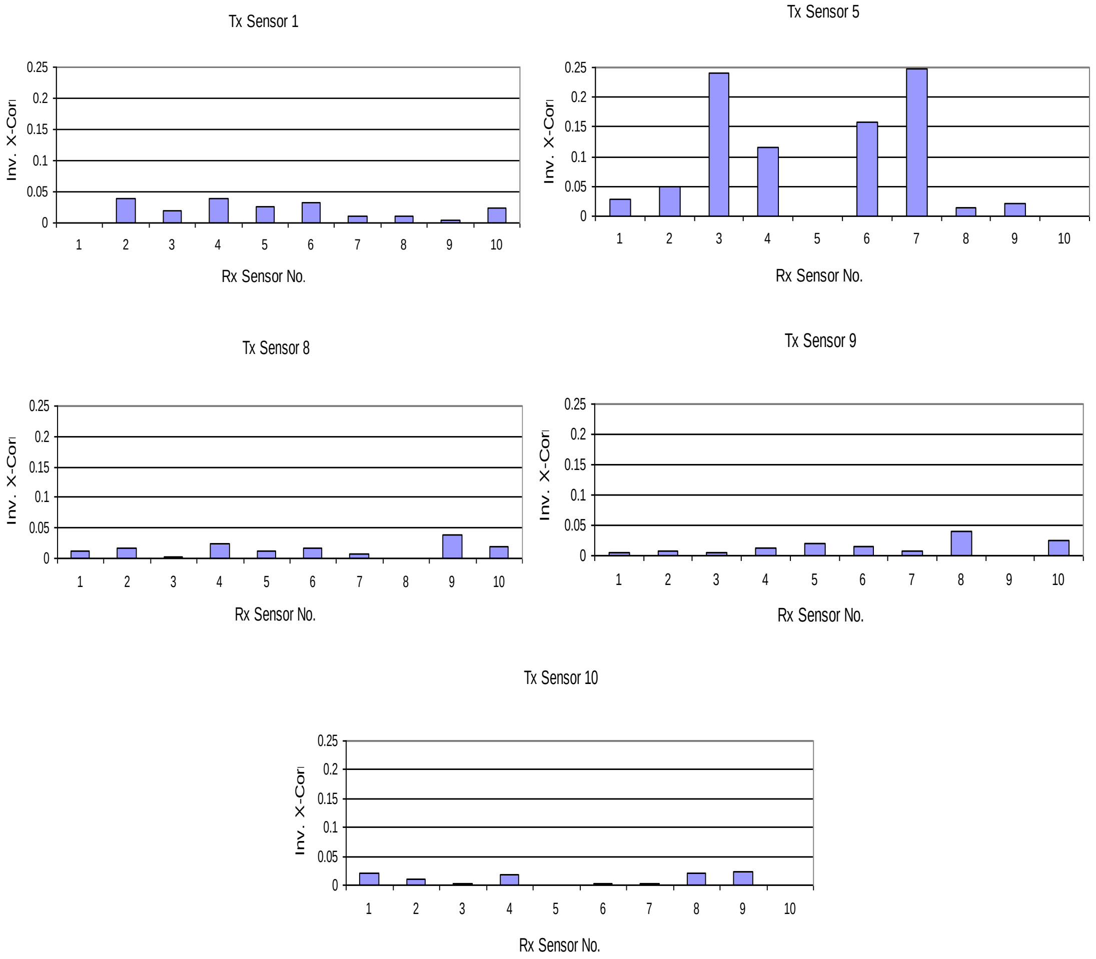

Figure 7.8: Inverse cross correlation representation for sequential Tx Sensors 1, 5, 8, 9 & 10. All other sensors configured as Rx

7.2.3 Defect 3 – Deep Blade Indentation

The 60 mm diameter circumferential defect was deepened to create an indentation of 12 mm resulting in fibre damage within the aerodynamic structure of the blade, Figure 7.9.

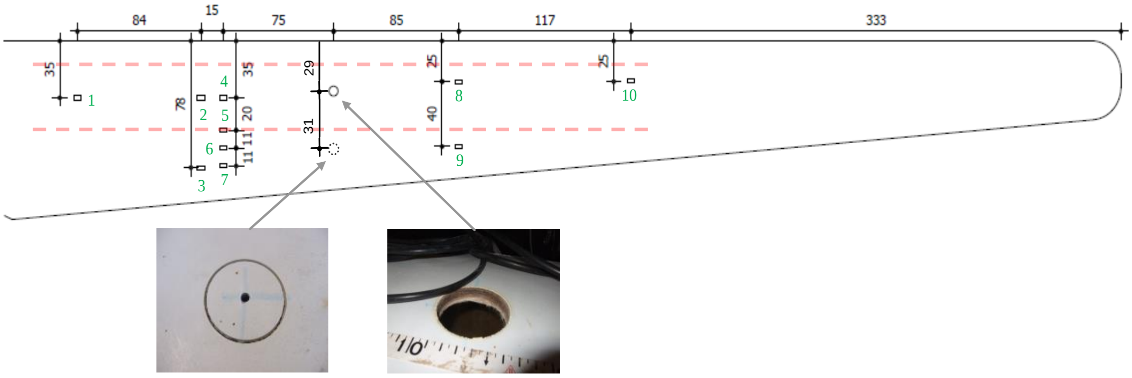

Figure 7.9: Blade layout showing position of 12 mm fibre defect located 31 cm from the through-hole.

Comparing the A-scans of the baseline data (2mm defect) to the data acquired after application of a 12 mm indentation defect, Figure 7.10, it may be observed that there was a 3 dB difference in amplitude when transmitting on sensor S9 and receiving on S6. Little difference was observed in amplitude when the receiver was switched to S7, Figure 7.11.

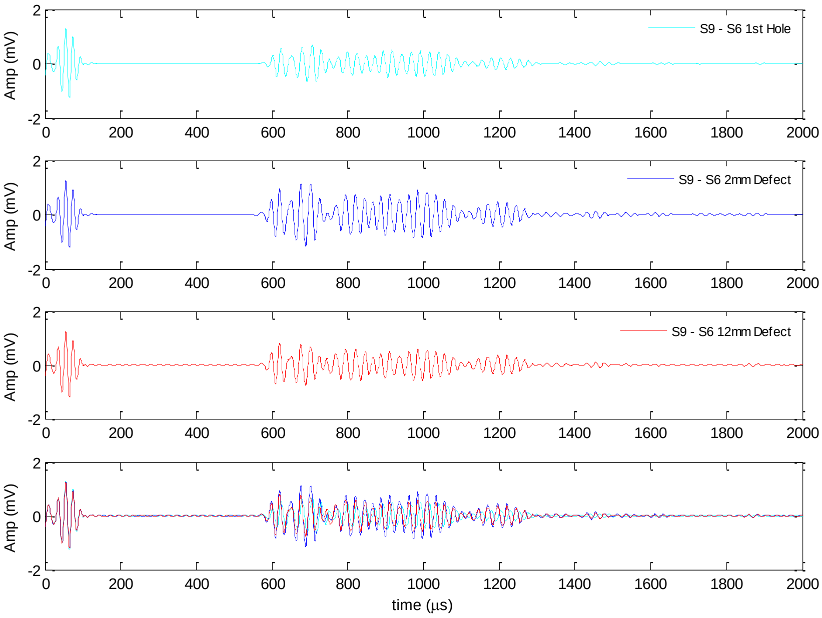

Figure 7.10: Comparison of 1st Hole (cyan), 2mm Defect (blue) and 60 mm diameter 12 mm circumferential defect (red) A-scans across aerodynamic blade frame. Tx Sensor 9 to Rx Sensor 6.

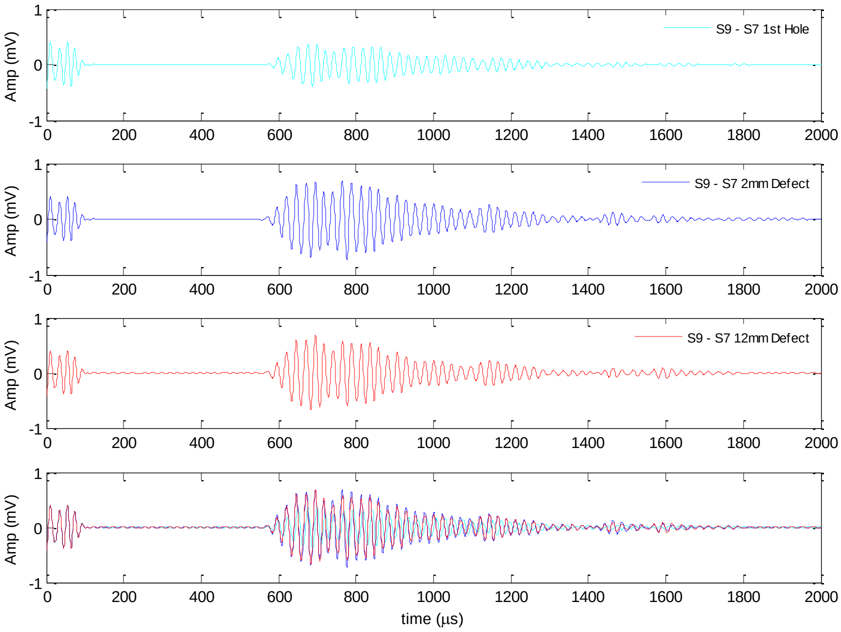

Figure 7.11: Comparison of 1st Hole (cyan), 2 mm Defect (blue) and 60 mm diameter 12 mm circumferential defect (red) A-scans across aerodynamic blade frame. Tx Sensor 9 to Rx Sensor 7.

Table D.3 (Appendix D) provides the relevant cross correlation data. From Figure 7.12, the largest calculated coefficients occurred when sensor S5 was excited and S9 was configured as receiver; and when sensor S9 was excited and S5, S6 and S7 were configured as receivers. For all other transmit sensors (S1, S5 and S10), there was no visible evidence of mismatch. The orientation of sensor S5 with respect to S9 (Figure 6.14(d)), whilst slightly misaligned with respect to the MFC S_0 mode plot, would be expected to provide maximum sensitivity. The quasi-isotropic characteristic of the aerodynamic frame ensured that any effect on the propagating wave (due to slight sensor misalignment) was insignificant. Transmitting on sensor S9 to receivers S3, S5, S6 and S7 approximated good sensor alignment for maximum signal strength (Figure 6.19). Sensors S1, S8, and S10, positioned on the spar-cap, were not suitably located to pick up defects occurring within aerodynamic structure.

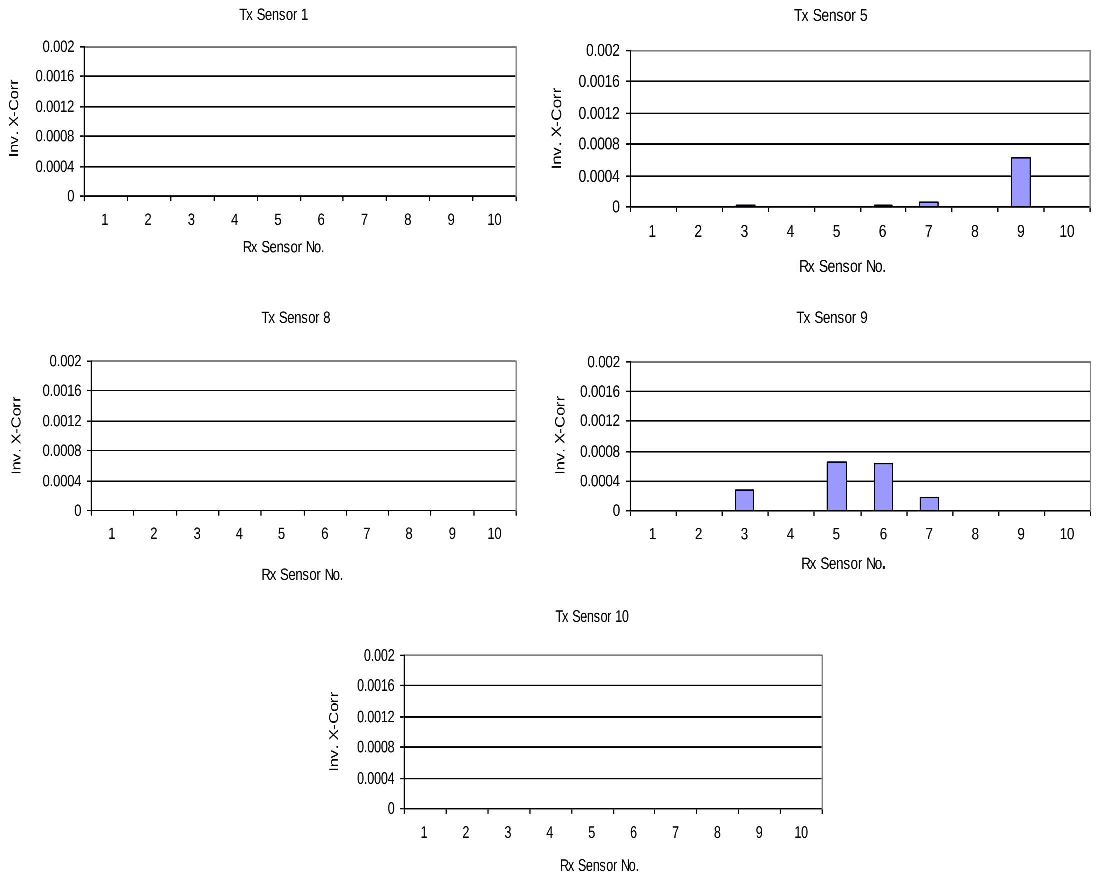

Figure 7.12: Inverse cross correlation representation for sequential Tx Sensors 1, 5, 8, 9 & 10. All other sensors configured as Rx

7.2.4 Defect 3 – Hole in Aerodynamic Blade Frame

The 12 mm circumferential indentation was deepened to create a through-hole within the aerodynamic frame, Figure 7.13.

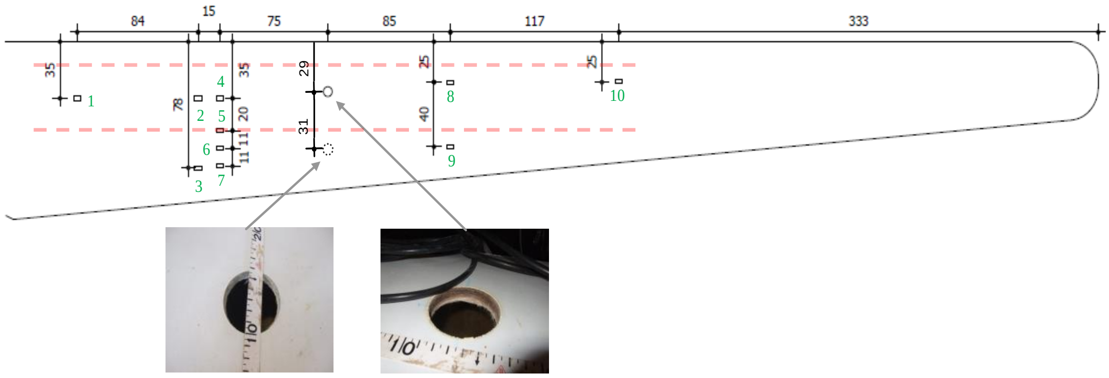

Figure 7.13: Blade layout showing position of through-hole within aerodynamic structure from through-hole within spar-cap

Comparing the A-scans of 12 mm defect to the data acquired after application of the through-hole, Figure 7.14, little difference in amplitude was observed when transmitting on sensor S9 and receiving on S6.

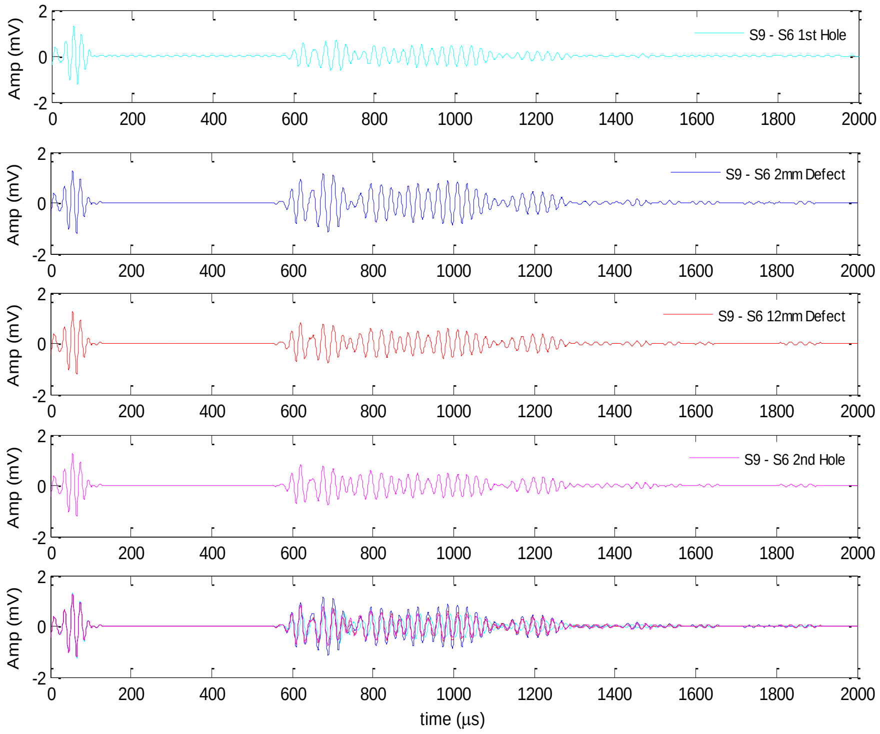

Figure 7.14: Comparison of 12 mm fibre-break and 2nd through-hole defect A-scans across aerodynamic blade frame. Tx Sensor 9 to Rx Sensor 6.

Similarly, there was little difference in the A-scans between the 12 mm defect and aerodynamic (2nd) hole, when sensor S9 was configured as the transmitter and S7 as the receiver, Figure 7.15.

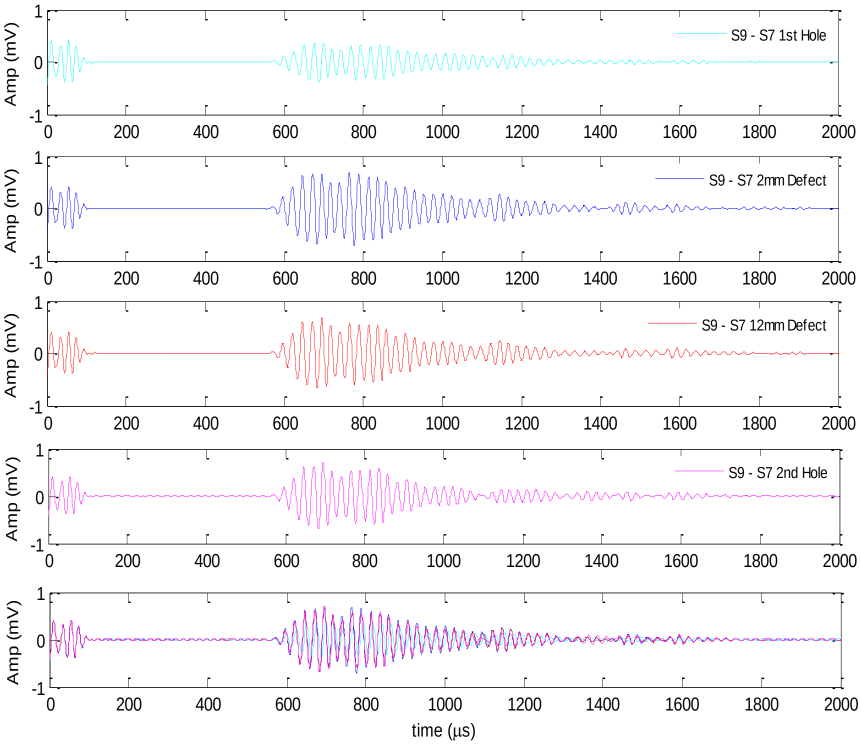

Figure 7.15: Comparison of 12 mm fibre-break baseline and 2nd through-hole defect A-scans across aerodynamic blade frame. Tx Sensor 9 to Rx Sensor 7.

The cross correlation data (Table D.4, Appendix D) shows that there was a high degree of match between the 12 mm fibre-breakage defect data and the aerodynamic frame hole defect data. The greatest mismatch was measured when sensor S5 was excited with S9 configured as a receiver, and when S9 was excited with S3, S5, S6 and S7 configured as receivers.

Figure 7.16 illustrates that there were two orders of magnitude in match-sensitivity when compared with the damage between the 2 mm defect and 12 mm defect (Figure 7.12).

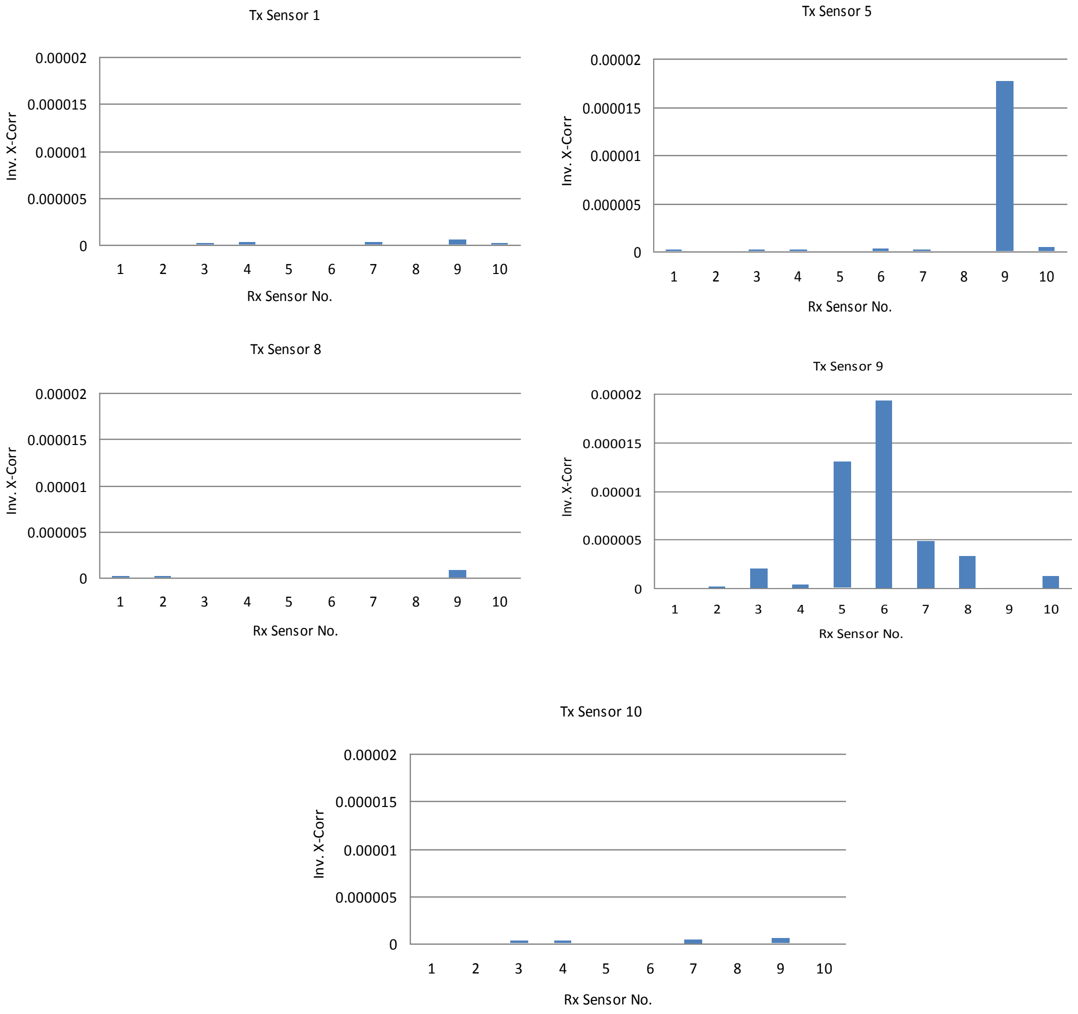

Figure 7.16: Inverse cross correlation representation for sequential Tx Sensors 1, 5, 8, 9 & 10. All other sensors configured as Rx

For all other transmit sensors (S1, S5 and S8), there was very little visible evidence of mismatch. The sensor alignment (and material fibre directionality) provided maximum sensitivity. As with the 12 mm fibre-break defect, the information arising from the aerodynamic hole defect suggested that the positioning of sensors S1, S8, and S10 on the spar-cap were not suitably located to pick up defects occurring within aerodynamic structure.

7.3 Sliding-Window Cross-Correlation Analysis

The cross correlation data presented in Section 7.2.1 – Section 7.2.4 provided just one coefficient per comparison of baseline/defect full data-sequence. Whilst valid information, it was difficult to determine where the greatest contribution to mismatch occurred. One method for acquiring information on localised data mismatch is to create a correlation sub-window covering a fraction of the two data sequences, record the corresponding coefficient before sliding the window forwards until the data sequence index has been expired. To achieve the desired outcome, adjacent correlation windows contain a substantial degree of overlap such that an evolving depiction of data match or mismatch emerges. The application of this moving window is illustrated in Figure 7.17.

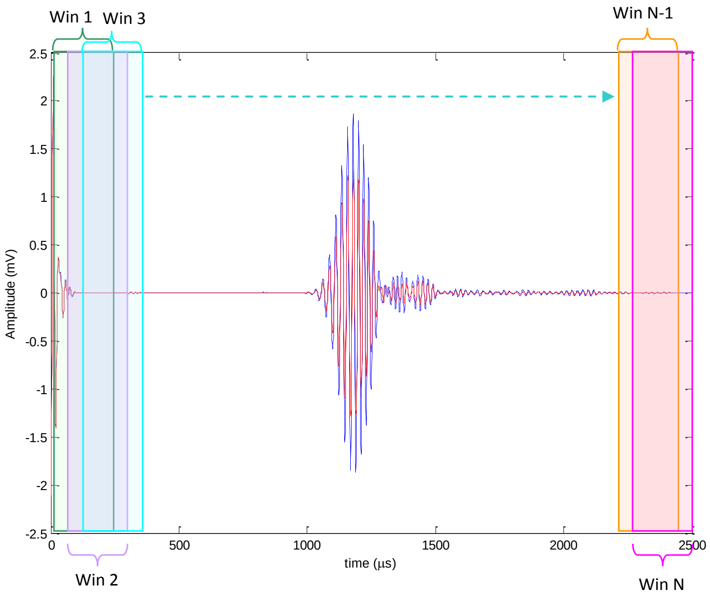

Figure 7.17: Sliding-window cross-correlation window showing a high amount of overlap

Subsequent analysis revisits the recorded data-sets of Section 7.2.1 to 7.2.4 to establish whether further information on the structural integrity of the blade can be uncovered using a moving cross-correlation window.

7.3.1 Spar Cap Analysis

Applying the approach of Figure 7.17, 200 correlation windows were used to compare the propagating wave characteristics in the blade before a defect was applied and after a hole defect through the spar cap, using sensor S1 as source of excitation (Appendix C3) and S10 as receiver, Figure 7.18.

The pink trace represents the cross-correlation for two sets of data prior to application of a defect. The ideal case would provide a cross correlation value of 1 where modal data exists (prior to the S_0 arrival time, noise occurs and correlation in this region is expected to be significantly below 1: windows 20 - 74). Where the S_0 mode occurs, the coefficient is equal to 1.

The data recorded upon application of the hole-defect was cross-correlated with data recorded when no defect was present (blue trace). The correlation coefficient ranged from 0.98 to 0.93 for windows which capture the S_0 mode (windows 74 – 88). The coefficient for all other modes dropped to 0.65 (windows 89 - 106).

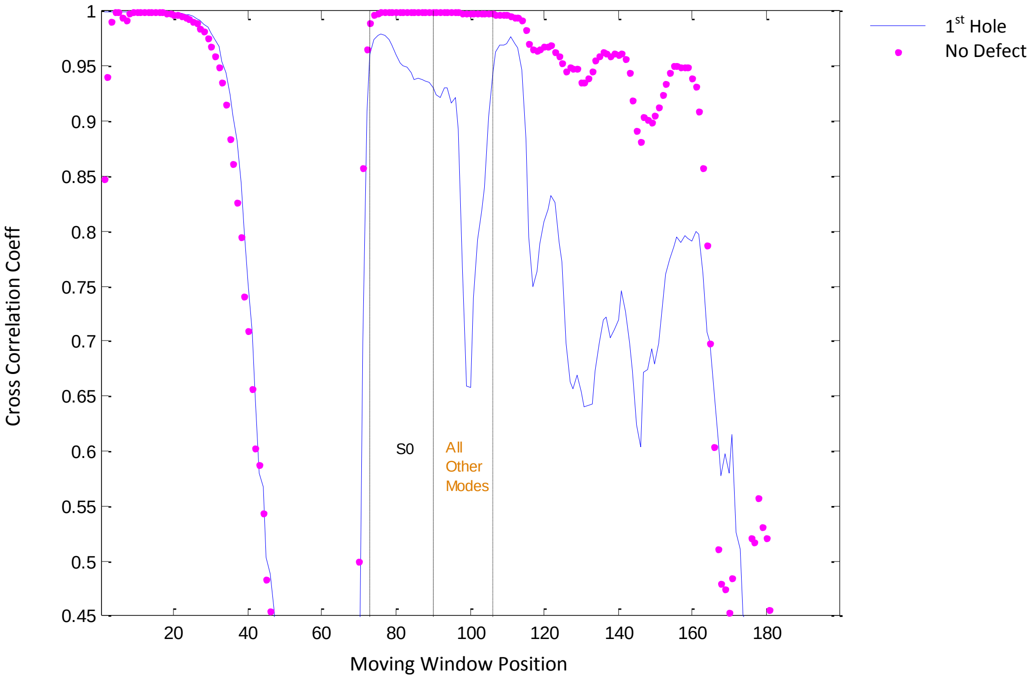

Figure 7.18: Sliding-window correlation analysis of no defect vs. through-hole on spar cap. Tx is sensor 1, Rx is Sensor 10

Figure 7.19 shows the response for a pair of sensors located farther from the spar-cap hole defect: aerodynamic frame where a signal is received on S6 upon exciting S9. The cross correlation coefficient is 0.97 or above during the time period where the S_0 mode appears (windows 37–48). It is observed that the defect was more clearly detected by sensors located on the blade component where the defect occurred (i.e. the spar-cap).

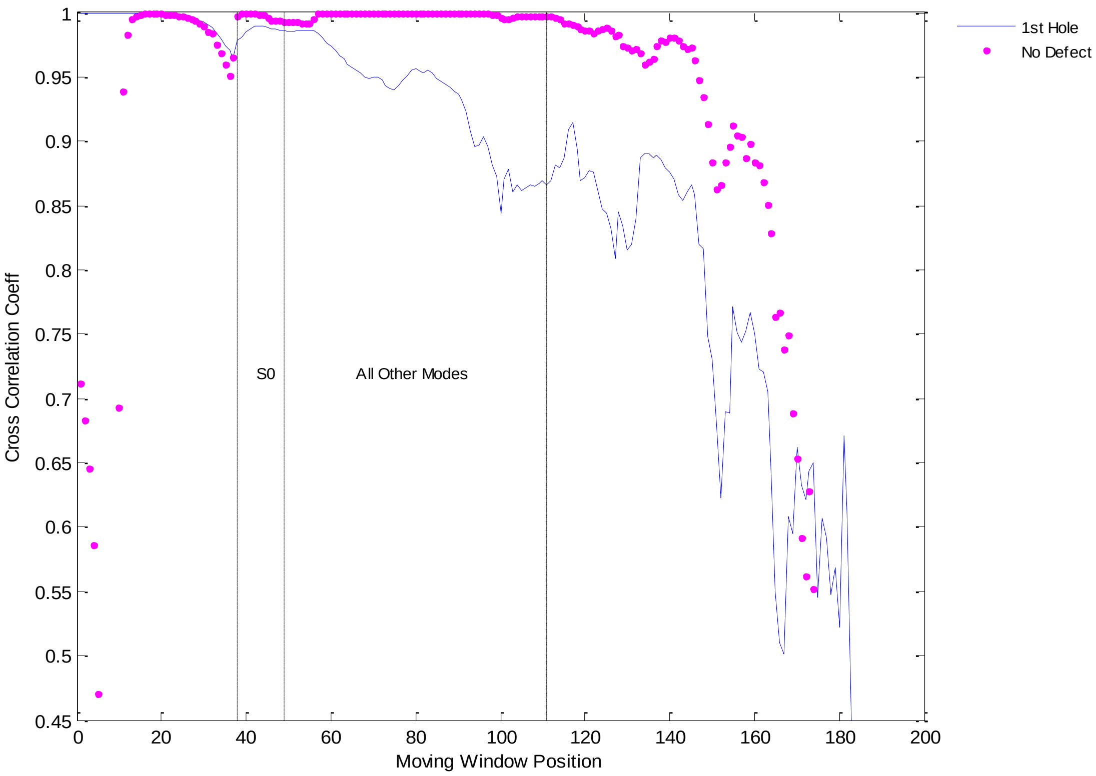

Figure 7.19: Sliding-window correlation analysis of no defect vs. through-hole on spar cap. Tx is Sensor 9, Rx is Sensor 6

7.3.2 Aerodynamic Structural Analysis

Figure 7.20 considers the case for the blade aerodynamic frame. Cross correlation was conducted between: two data sets where there was no blade defect (pink); 2

mm defect dataset and 12 mm defect dataset (blue); and 2 mm defect dataset and 2nd hole dataset (red).

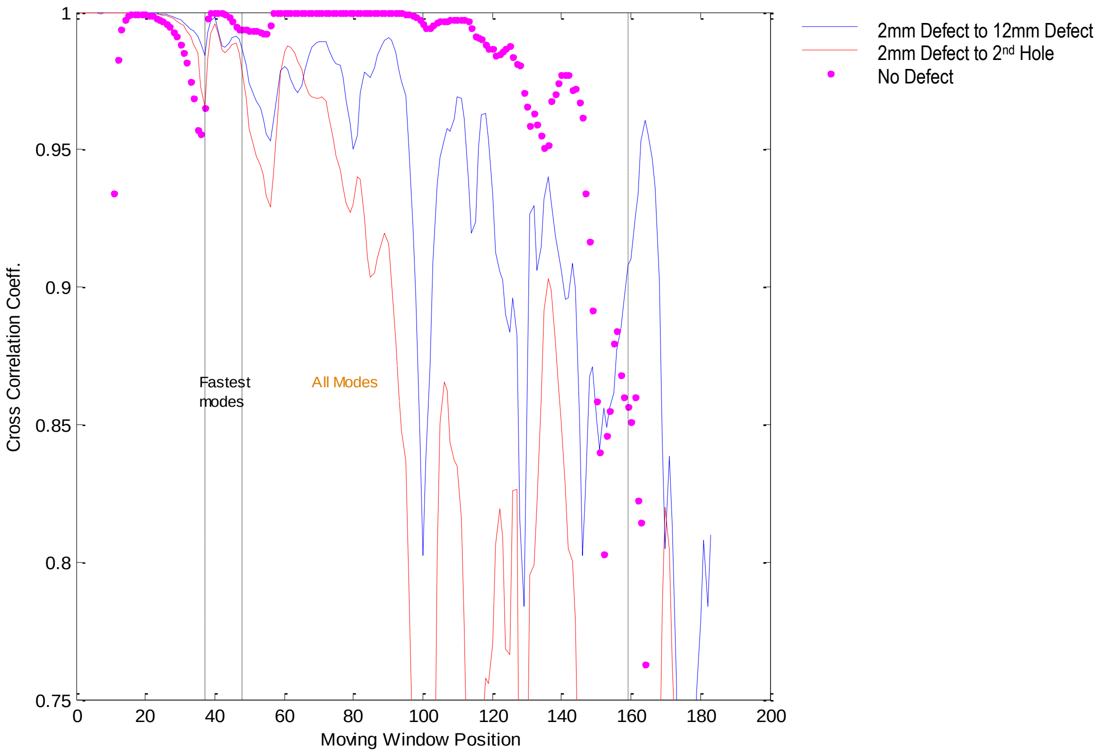

Figure 7.20: Sliding-window correlation analysis: 2 mm skin damage defect to 12 mm fibre breakage (blue); 2 mm skin damage defect to aerodynamic structural hole (red). Tx - Sensor 9; Rx - Sensor 6

The characteristics for no defect showed a correlation coefficient which did not dip below 0.995. Exciting on sensor S9 and receiving on S6, analysis of the Fastest Mode coefficients for 2 mm Defect to 12 mm Defect and 2 mm Defect to 2nd Hole revealed similar characteristics (0.985 to 0.965). For the remaining modes (All Modes) the coefficients for the two plots increasingly diverged as the Moving Window Position progressed.

Retaining sensor S9 as the transmitter and now receiving on S7, Figure 7.21, correlation between two no-defect datasets (pink) exhibited a minimum coefficient (across all modes) of 0.997.

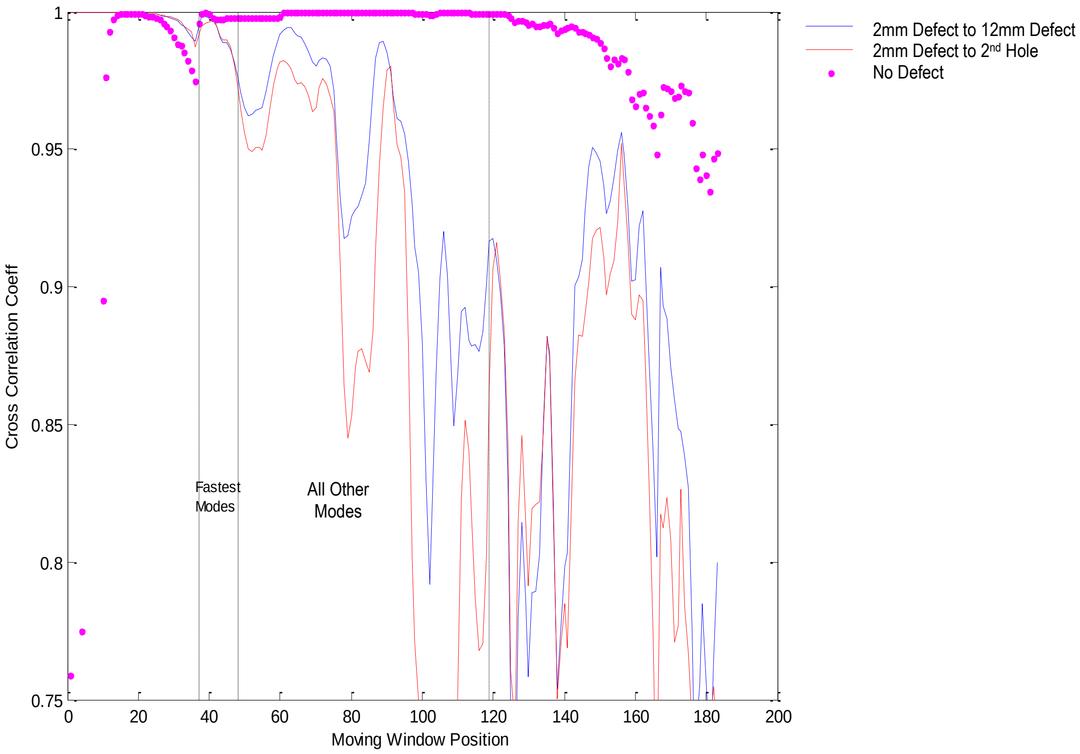

Figure 7.21: Sliding-window correlation analysis: 2 mm skin damage defect to 12 mm fibre breakage (blue); 2 mm skin damage defect to aerodynamic structural hole (red). Tx is Sensor 9, Rx is Sensor 7

The effects of dispersion ensured the S_0 mode was not clearly resolved. The case for the Fastest Modes was then considered. The cross correlation of the 2 mm Defect and 12 mm Defect datasets produced a coefficient of 0.97. A similar response yielded a cross correlation coefficient of 0.97 for the 2 mm defect to 2nd Hole defect. Both plots share similar characteristics in this region. The remaining modes (All Other Modes) produced greater coefficient values for both comparison pairs.

Again, retaining sensor S9 as transmitter, Figure 7.22, illustrates the results of an adjacent receiver on the aerodynamic frame, S3. Cross correlation between two no-defect datasets (pink) exhibited a minimum coefficient (across all modes) of 0.997. A cross correlation of 0.976 and above was returned for the S_0 mode comparing the 2 mm Defect to 12 mm Defect datasets.

Considering the same plot region, a coefficient of 0.974 was recorded for the 2 mm Defect to 2nd Hole datasets. Cross correlation comparison of the two dataset pairs for the S_0 window region (windows 41–50) were very similar. The coefficients for All Other Modes, whilst smaller, showed some divergence.

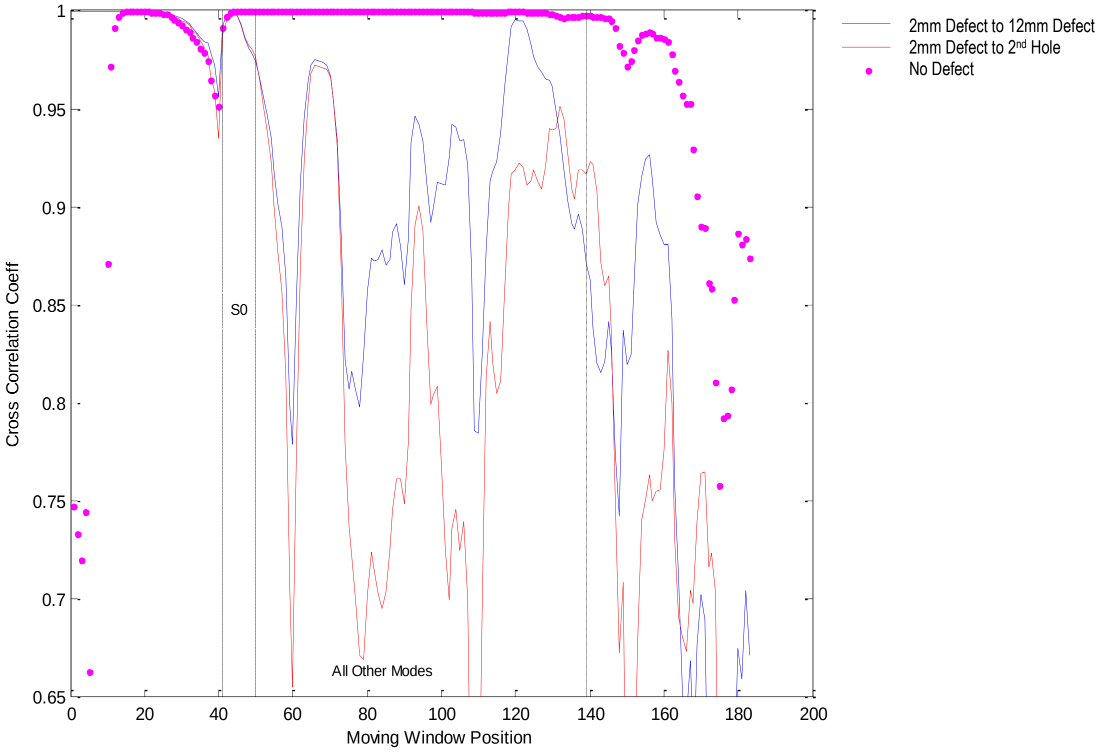

Figure 7.22: Sliding-window correlation analysis: 2 mm skin damage defect to 12 mm fibre breakage (blue); 2 mm skin damage defect to aerodynamic structural hole (red). Tx is Sensor 9, Rx is Sensor 3

Sensor S5, located on the boundary between the spar-cap and the aerodynamic frame, was then configured as the transmitter, Figure 7.23. As a result of its position, a change in cross correlation characteristics was expected. Cross correlation between two no-defect datasets (pink) exhibited a minimum coefficient (across all modes) of 0.995. The coefficient outputs for cross correlation of both the 2 mm Defect to the 12 mm Defect (blue) and the 2 mm Defect to the 2nd Hole Defect (red) were (min = 0.905) for the plot region containing the Fastest Modes were similar (0.905 versus 0.892). Coefficients of the two different defect datasets for All Other Modes yielded significantly smaller coefficients.

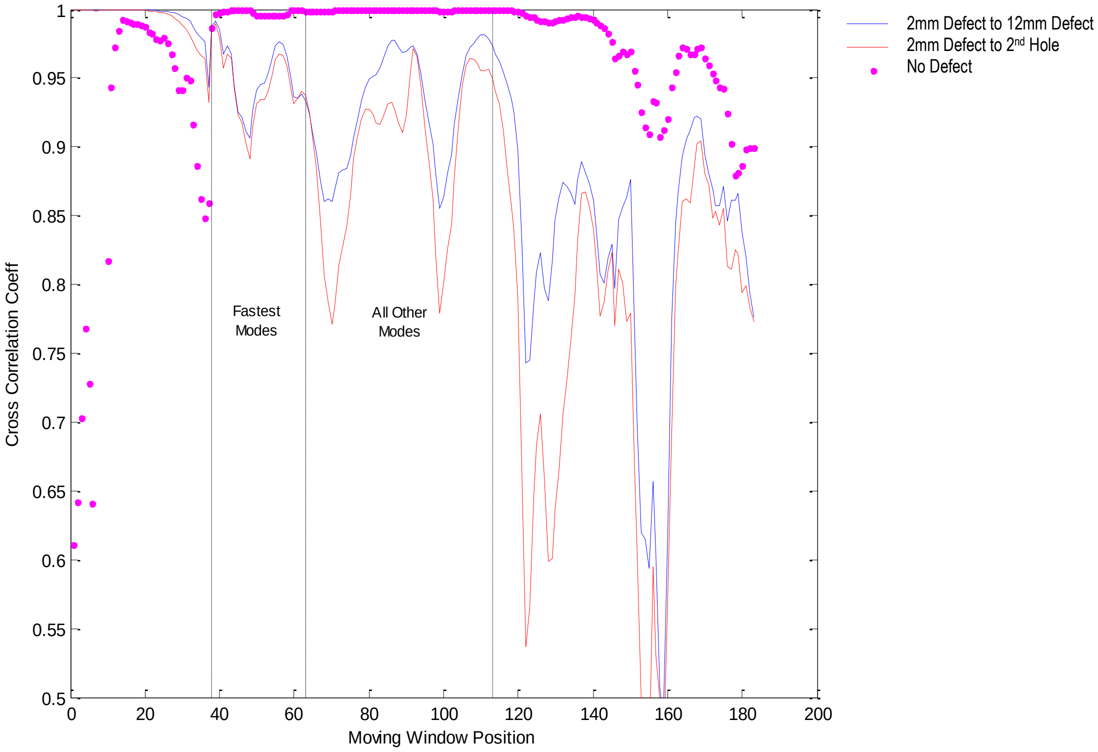

Figure 7.23: Sliding-window correlation analysis: 2 mm skin damage defect to 12 mm fibre breakage (blue); 2 mm skin damage defect to aerodynamic structural hole (red). Tx is Sensor 5, Rx is Sensor 9

Finally, to observe the response recorded by sensors located on the adjacent spar-cap, responses for transmission on sensor S1 and reception on S10 are presented in Figure 7.24. The plot region containing the S_0 mode illustrated that the cross-correlation of 2 mm defect and 12 mm defect (min=0.998); and 2 mm defect to 2nd Hole (min = 0.997) produced coefficient plots almost identical to the no defect plot (min = 0.999). Interestingly, the plots for the remaining modes (All Other Modes) featured coefficient plots with a high degree of match (min = 0.993).

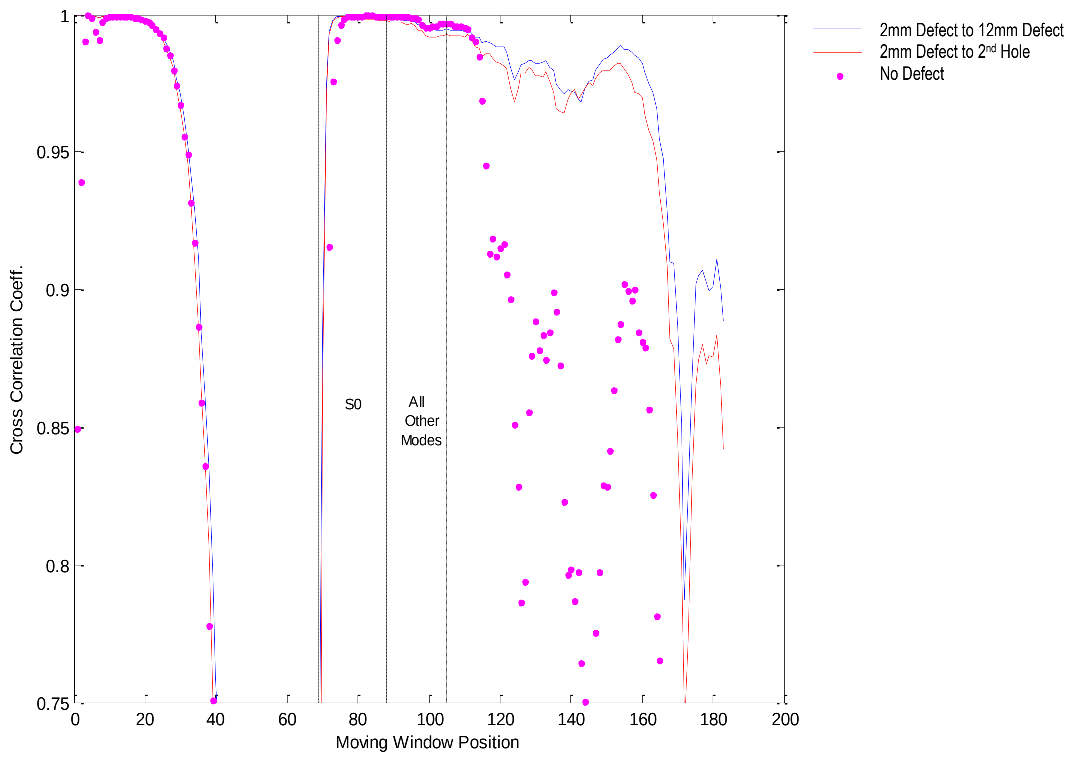

Figure 7.24: Sliding-window correlation analysis: 2 mm skin damage defect to 12 mm fibre breakage (blue); 2 mm skin damage defect to aerodynamic structural hole (red). Tx is Sensor 1, Rx is Sensor 10

As with the spar-cap analysis (Section 7.3.1), the defects were more clearly detected by sensors located on the component material where the defect has occurred (in this case, the aerodynamic frame).

The spatial array of sensors attached to the turbine blade has shown that it was possible to extract additional information on blade structural integrity using a sliding window to output a sequence of cross-correlation coefficients analysing local variations between two data-sets. Furthermore, it was possible to establish the region of the blade where the blade defect had arisen.

7.4 Conclusions

To test the sensitivity of the array, three different defect-types were analysed: 2 mm defect; 12 mm defect; and through-hole structural damage. The cross-correlation and inverse cross-correlation functions were used to detect the presence of defects within the blade structure. The region of defect location could be determined by the increasing lack of signal correlation (with respect to 'no defect' measurements), the closer the proximity of the sensor to the defect location.

The occurrence of fibre damage within the aerodynamic structure yielded a cross correlation coefficient of 0.975 from a closely positioned Tx/Rx sensor pair on the same structure. Using the same transmitter and analysing a receiver positioned farther and on the spar-cap, a coefficient of 0.999 was recorded. The corollary using the same transmitter but with a receiver located nearby on the spar cap yielded a coefficient of 0.998 - significantly higher than the coefficient of a receiver placed on the aerodynamic frame and displaced a further 1.2 m from the defect. This suggests that both the distance of the sensor to the defect and the presence of a boundary affect the coefficient measurement when considering the defect location.

When an acute defect (through-hole) was introduced to the spar-cap of the blade, the receiving sensors positioned closest to the defect recorded the lowest cross-correlation coefficients (0.889 at a distance of 0.99 m; 0.988 at 2.02 m). However, when the 12 mm fibre-break defect in the aerodynamic frame was deepened to become a through-hole defect, the resulting change in cross-correlation coefficient was nominal indicating that the structural integrity of the sandwich layer physically in contact with the sensor acts as the most sensitive indicator of damage.

The location of the 2 mm defect was less well identified by the spatial array. This is likely due to the fact that such depth of indentation affects only the blade skin. This layer is isotropic and therefore the boundary conditions will have less of an impact upon the signal sensitivity at each of the sensors. The sensors located most closely to the defect provided a greater indicator of damage. However, a greater degree of defect location was apparent when fibre damage within the GFRP layer occurred.

To establish additional information upon the occurrence of defects within the blade structure, the cross-correlation window was reduced to a fraction of the dataset and then applied across the full dataset index. Using this sub-window approach, the cross-correlation function was better able to highlight dissimilarities between modes within experimental datasets.

The extension from 2 mm defect damage to 12 mm defect damage on the aerodynamic frame illustrated, for the same receiver sensor coupled to the frame, a drop in the cross correlation coefficient for A-scan time-windows containing the S_0 mode. As the proximity of the sensor to the defect increased, the correlation coefficient dropped. Comparable with a single coefficient between two data-sets, there was no clear visible coefficient deterioration (for the S_0 mode) when damage was advanced to a hole defect. As expected, for each blade component, the cross-correlation of two baseline datasets (prior to application of a defect) yielded a coefficient very close to 1. Furthermore, the coefficients of sensors coupled to the blade component adjacent to the section containing a defect, closely matched the no defect coefficient sequence.

8 Conclusions and Future Work

8.1 Conclusions

The objective of the research contained within this thesis was to identify the turbine component most likely to fail and subsequently incur significant O&M costs for operators of both onshore and offshore wind farms. The rotor blade was identified as a structurally important part that is at present insufficiently inspected. Having identified a key component for inspection, it was necessary to identify the most commonly reported blade-faults.

OEMs and utility companies have regularly reported instances of disbond between the supporting member and the blade inner shell as a particular issue with coincidental occurrences of delamination within the spar cap. Consequently, identification of a non-destructive technique for the detection of defect onset within the spar-cap area of the blade is the identified area for research.

A number of NDT techniques were considered for autonomous inspection. The prerequisites for consideration required the inspection method to be continuous, to reduce the number of hands-on maintenance checks, and that the sensors have wide-coverage to ensure a relatively low density of affixed sensors to the blade.

Changes in the mechanical properties of a blade composite structural component, initiates the onset of elastic waves which when confined by plate-like boundaries, generates Lamb waves able to propagate long distances within the material - suitable for the examination of large cross-sectional areas. Within GFRP materials, it was established that the fundamental Lamb wave modes (A_0, S_0) were clearly apparent for a broad range of frequencies. However, unlike the A_0 mode which suffers the effects of dispersion for a broad-range of low frequencies, the S_0 mode experiences the effects of dispersion for only a narrow bandwidth of frequencies. This makes it a particularly suitable mode for structural integrity analysis, since dispersion may well be one of the by-products of defect onset.

The chosen sensors for interrogation of structural integrity, piezoceramic transducers, are robust, light-weight and unobtrusive. They feature the requisite level of sensitivity for successful detection of multi-mode Lamb waves propagating through GFRP - a regular component material within rotor blades. To exploit the inbuilt fibrous properties of the GFRP support material, interdigitated Macro Fibre Composite (MFC) sensors were selected to optimise the sensitivity of the spatial sensor array where Lamb waves propagate with less attenuation when the direction of travel is parallel to fibre orientation. MFC sensors are flexible and can conform to curved surfaces to which they may be attached making them particularly suitable for use on blade structures. The construction of an MFC sensor is such that it preferentially excites the S_0 mode.

The dimensions of the MFC active area were identified as a variable that may affect transducer performance. Three different dimensions were examined. The sensitivity of the MFC was found to be significantly dependent upon the ratio of the active length to the wavelength, permitting the interdigitated sensor to be adapted to preferentially excite one wave mode over others. An MFC with active area dimensions 28 mm x 14 mm (M2814) was identified as exhibiting the best resonance performance at low frequencies. Exploring the effects of different ply-configurations within GFRP materials (quasi-isotropy against fibre bidirectionality), the S_0 mode was found to be more sensitive to the effects of increasing anisotropy than was the A_0 mode when analysing both group velocity and amplitude response. Sensor alignment with respect to the excitation source indicated a significant fall-off in signal amplitude for misalignments of greater than 20° for quasi-isotropic GFRP and misalignments of greater than 30° for bidirectional GFRP – increased occurrences of scatter occurred at greater misaligned angles. Permanent adhesive bonding of the MFC to a GFRP component provided consistently uniform coupling conditions yielding data sensitivity to indicate a change in material characteristics.

FEA was used to gain a better understanding of the directional characteristics of bidirectional GFRP. An FE model was created to analyse modal sensitivity to fibre alignment. Good agreement with the experimental GFRP data was achieved for the A_0 mode. However, there was poor S_0 agreement. The directional properties of an MFC were modelled (as a grid of point sources) and superimposed onto the GFRP model. Whilst indicative, the model did not predict the levels of scatter present within the experimental field plot, suggesting the in-plane mechanical properties of the GFRP material are more complex than that captured in the model.

A study of loading conditions on GFRP (which may be experienced within the environment) using MFCs revealed that the mechanical effects of loading, where present, were identifiable within the recorded dataset. Upon subsequent removal of loading, the erstwhile changes observed in the dataset coincidentally disappeared; indicating that the effects of loading can be identified separately from defect onset. An algorithm, using cross correlation, can be applied to determine load presence as an oscillating point in time against baseline reference data.

A decommissioned turbine rotor blade (3.76 m x 0.78 m) was populated with a sparse array of sensors and subsequently analysed. The aim was to ascertain some baseline reference (no defect) data, with respect to different blade components, upon configuring selected sensors for transmission whilst receiving on all other sensors within the array. The S_0 mode amplitude was found to vary by up to 36 dB depending upon receiver position in relation to the load-carrying spar-cap and the aerodynamic frame.

Using signal processing, a system of analysis involving the cross-correlation function and its inverse, was established where the array was able to detect fibre-break with an indication as to its proximity to the sensor being analysed. Furthermore, the cross correlation coefficient provided information on the presence of a component boundary within the blade.

Modifying the cross-correlation technique to provide a sequence of coefficients between two datasets - each representing a window of time - increased the discernible level of sensitivity to the presence of defects. The S_0 mode showed greater variations between defect and baseline reference datasets. Furthermore, a regular decrease in correlation was recorded the greater the proximity of an observed sensor to the defect location.

The reliability of cross-correlation analysis as a technique for defect detection was tested whereby baseline data recorded for each blade section - prior to application of a defect - yielded a coefficient very close to 1.

The outcome of the work contained within this thesis is that a lightweight NDT system, using a sparse array of low-profile flexible piezoceramic transducers, has been developed that is able to detect structural defects to GFRP components within blade structures using signal processing techniques. The system is able to detect fibre-breakage down to 2 mm. Furthermore, the sliding-window cross-correlation technique illustrated that certain modes can, upon inspection, be indicative of particular types defects. The fundamental modes clearly responded to fibre damage within the blade material, whilst higher order (slower) modes were also responsive to defect onset. This technique can be exploited such that the occurrence of mode change may be identified for a refined failure mode e.g. identification of mode change to: surface damage, fibre damage, sudden material discontinuity. Some wave mode response may arise for all damage types (for example S_0), but occurrence together with the presence of other changed modes - and their response level to damage severity – can lead to a specific signature for a particular damage mode. Algorithms, as part of the overall wind turbine SHM system, can be used to recognise the occurrence of these signatures and provide an early damage prognosis to the operator (end user) whereupon appropriate preventative action can be taken.

8.2 Future Work

There was limited time and access to the turbine blade analysed within this thesis: the blade was housed within a project partner's premises in rural Greece. The strategy undertaken (and outlined) was deemed the most appropriate to yield significant results. For this reason, options such as full matrix capture were not considered given the requisite configuration time. Similarly, fibre damage, as methodical cutting into the blade, was the chosen method of damage control due to budget considerations and resource availability.

In addition to full matrix capture, there are a number of other considerations. The piezoceramic pillars of the interdigital transducers were aligned approximately with the GFRP fibre direction to optimise the transfer of mechanical energy from the blade structure to the MFC sensor. Smart Material, who manufactures MFC sensors, produces another MFC kind known as 'P2', [131,132]. Although these sensors have the same dimensions as the sensors analysed within this thesis, they exhibit a different level of sensitivity (e.g. different capacitance characteristics). Repeating the experiments conducted in Chapter 6 with the 'P2' sensors may help further fine-tune the sensor array.

The MFC sensors were used for their flexible and robust properties, however; the harsh environments in which they would be expected to continually operate would require that they are protected accordingly. There are a number of considerations regarding suitable housings. It is a requirement that their implementation retains sensor flexibility and does not significantly compromise signal integrity. A particularly significant area of work concerns the adhesive used to bond the sensor housings to the blade: it must not be deleterious to operation nor be unprepossessing. If blade manufacturers believe that there is a risk to life-cycle –

despite intent – their apprehension will serve to restrict the implementation of such a monitoring technique. The inclusion of additional materials would require sensor re-characterisation due to changes in coupling conditions. The subsequent results may result in changes to the spatial sensor array.

There is scope for further development of signal processing techniques. For example, the cross correlation technique was enhanced to highlight local variability using a smaller analytical window. This technique could be further optimised to identify characteristic signals specifically related to particular defects. The work within this thesis identified a variation of the S_0 mode due to fibre damage. However, significant changes in higher order modes were also observed: the combined changes of these modes may subtly distinguish between one defect type and another (surface, fibre, material discontinuity). The change in fundamental and higher order wave modes to blade damage provides the potential to ascertain the level of damage severity. An algorithm providing a specific signature to damage and severity, whilst indicative of early defect onset, may also be able to alert the end user as to the best time for intervention to optimise O&M costs.

The experimental data (Chapter 6 and Chapter 7) can be used to fine-tune both the FE model of the GFRP component and the MFC sensor coupled to it. For example, experimental information on the drop-off of signal amplitude with sensor misalignment can be used to tweak the stiffness coefficients for off-fibre directions of the GFRP. In addition, the rectangular grid array of point sources used for sensors representation can be enhanced to include a coupling coefficient related to a mode-excitability coefficient to better determine the displacement field at a monitored point (using Equation (5.13)). As the model is optimised to more accurately reflect recorded experimental data, it is used to enhance knowledge of the blade materials and the conditions under which they operate. This is an approach that can be accurately used to determine the point at which a turbine should be taken out of service for detailed inspection.

Appendix A – Blade Loss or Failure

The table below is a non-exhaustive list of incidents which have been reported to have occurred in Europe over the last 10 years. Not all incidents are reported and obtaining full information is not an easy task, [133].

Fault	Year	Location Report
Blade Failure	1992	Delabole, Cornwall Blades damaged by lightning
Blade Failure	1993	Cemmaes, Wales Blade parts thrown over 400m
Blade Failure	1995	Rudersdorf, Germany 11m long piece of blade landed next to childrens nursery
Blade Failure	1995	Tarifa, Spain 2 separate occurrences of blades breaking off
Blade Failure	1995	Greece Cracked blades
Blade Failure	1996	East Friesland, Holland Parts of rotor blade reported landing in peoples garden
Blade Failure	1996	Eesmond, Holland 2 blade failures in September
Blade Failure	1996	Schllewsig-Flensburg, Germany Turbine blades broke and fell. Pieces landed on road and damaged adjacent turbine
Blade Failure	1997	Nordstrand, Germany 2 of 3 blades came off. Parts flew over 300m, across a road
Blade Failure	1997	Waldaubach, Germany Blade flew off. Parts found 400m to 500m away. Parts landed in summer house
Blade Failure	1997	Kaiser Wilhelm Koog, Germany Blade parts flew up to 500m. 1 person killed
Blade Failure	1997	Wanderup, Germany 66% of blade flew 50m. Road only 20m away
Blade Failure	1997	Taff Ely, Wales Lightning strike
Blade Failure	1997	Four Burrows, Cornwall Lightning strike
Blade Failure	1998	Goonhilly, Cornwall Lightning strike
Blade Failure	1999	Lower Saxony, Germany Blade parts blown off. Parts found 100m away
Blade Failure	1999	Brandenburg, Germany At least 20 separate blade parts up to 1m long, blown more than 300m
Blade Failure	1999	Hachenburg, Germany Blade parts flew almost 40m onto heavily used footpath. lightning strike
Blade Failure	1999	Burmonken, Germany Blade broke. Parts flew off
Blade Failure	1999	Lower Saxony, Germany Frozen blade detached and disintegrated. Parts flew 100m
Blade Failure	1999	Wijnaldum, Holland lightning strike destroyed turbine blades
Blade Failure	1999	Lelystad, Holland Blades from 4 turbines badly damaged by lightning
Blade Failure	1999	Seglabera. Sweden Blade parts flew almost 150m
Blade Failure	1999	Sustrum, Germany 7m long blade section flew more than 200m and 10 other pieces up to 1m long were recovered
Blade Failure	1999	Allstedt, Germany 2 blade parts more than 20m long blown off and flew more than 150m
Blade Failure	1999	Blankenheim, Germany Blade fell to the ground
Blade Failure	1999	Germany lightning strike damaged blades
Blade Failure	1999	Schleswig-Holstein, Germany Brake failure. Turbine turning 4x normal speed. 60 residents within 500m evacuated
Blade Failure	1999	Cuxhavn, Germany Blade blown off. Parts flew 200m
Blade Failure	1999	Zennhusen, Germany 2 turbines damaged by lightning. One lost a blade and 2 others shattered
Blade Failure	1999	Lower Saxony, Germany Blade destroyed by lightning
Blade Failure	1999	Stoffin, Germany Blade bent, hit tower. Debris over 50m circle
Blade Failure	1999	Leewarden, Holland Sereious damage to blades following lightning strike
Blade Failure	2000	Samso, Denmark Complete rotor and housing broken. 1 blade piece went through a window and landed In swimming pool. Another piece was thrown 600m
Blade Failure	2000	Lower Saxony, Germany Storm tore nacell cover off. 1 blade flew 150m to 200m hitting factory and house, piercing 24cm thick stone wall, timber floor and roof. Turbines subsequently shut down following court ruling on safety grounds.
Blade Failure	2000	Lower Saxony, Germany 21m blade section weighing 2t flew approx 100m
Blade Failure	2001	Lower Saxony, Germany 33m blade piece broke off and flew 100m
Blade Failure	2001	Lower Saxony, Germany 33m blade piece weighing 4t broke off and ffell to ground
Blade Failure	2001	Hessen, Germany 4m x 1m blade piece broke off and flew 150m
Blade Failure	2001	Bad Doberan, Germany Turbine blade broke off. Nearby motorway closed off
Blade Failure	2002	Blyth, Northumberland Broken blade on UK first offshore turbine
Blade Failure	2002	Lower Saxony, Germany Blade shattered with an audible crack. Debris scattered across surrounding fields
Blade Failure	2002	Wormhout, France Blade torn off during a storm
Blade Failure	2002	Aachen, Germany Turbine blade torn off during storm. 7.5m section flew 40m
Blade Failure	2002	Westfalia, Germany Loss of blade. 30m long section weighing 5.5t fell off. Smaller blade parts covered an area to 400m from tower
Blade Failure	2002	Westfalia, Germany lightning strike broke off 1m of blade
Blade Failure	2002	Saxony, Germany Technical defect led to blade damage
Blade Failure	2002	Westfalia, Germany Blade broke off during storm
Blade Failure	2002	Westfalia, Germany Blade bent and fell to ground. Local farm evacuated
Blade Failure	2002	Kaiserslautem, Germany Blade broke off due to storm damage
Blade Failure	2002	Brandenburg, Germany 2 of 3 turbine blades tore off in a storm and thrown "far"
Blade Failure	2002	Westfalia, Germany Blade bent then broke in a storm
Blade Failure	2002	Austria Turbine blades damaged during storm
Blade Failure	2002	Esbjerg, Denmark 3 blades experienced damage during commissioning
Blade Failure	2003	Aude, France 3 blades from 3 separate turbines broke off during storm. 7 out of 10 turbines on this site were shut down and dismantled
Blade Failure	2003	Lower Saxony, Germany Lightning damage. Blade parts scattered over 150m
Blade Failure	2003	Lower Saxony, Germany Lightning strike broke off blade tips
Blade Failure	2003	Rheinland-Pfalz, Germany Lightning strike to 2 turbines damaging multiple blades on each
Blade Failure	2003	Saxony, Germany Lightning damage to blade tips

Blade Failure	2003	Westfalia, Germany Lightning damage to blade
Blade Failure	2003	Westfalia, Germany 37m long blade section bent in storm
Blade Failure	2003	Saxony, Germany Lightning strike destroyed blade, started fire and damaged turbine housing. 1 blade bent. Another fell off.
Blade Failure	2003	Boulogne sur Mer, France Blade parts weighing several tons fell ino an area used by fishermen and walkers
Blade Failure	2004	East Belgium Lightning strike led to exploding blade
Blade Failure	2004	Zeeland, Holland 3 blades exploded ue to lightning strike
Blade Failure	2004	Lower Saxony, Germany 2t piece of blade broke off and flew 66m
Blade Failure	2004	Hessen, Germany Blades torn off in a storm
Blade Failure	2004	Saxony, Germany 10m section of blade flew 20m. 6m piece flew 40m. Smaller pieces flew out to 200m. Suspected lightning damage a week earlier.
Blade Failure	2004	Saxony, Germany Rotor bent during storm, some pieces flew off
Blade Failure	2004	Saxony, Germany 10m blade section broke off
Blade Failure	2004	Lower Saxony, Germany Lightning strike destroyed blades close to motorway
Blade Failure	2004	Rheinland-Pfalz, Germany Broken rotor
Blade Failure	2004	Brittany, France Blade bent and damaged tower
Blade Failure	2004	Brittany, France 2nd incident in 10 days. 2.5m long pieces of blade found in field
Blade Failure	2004	Zeebrugge, Belgium 3t rotor blade became detached and flew 100m landing not far from nearby gas terminal
Blade Failure	2004	Mecklenburg, Germany Blade thrown from turbine
Blade Failure	2004	Montjoyer, France Turbine caught fire followed by all 3 blades falling off
Blade Failure	2005	Udby, Denmark Turbine lot control. 3 blades broke off. Pieces thrown over large area. Residents evacuated
Blade Failure	2005	Crystal Rig, Berwickshire 40m blade shattered. Parts thrown hundreds of metres

Appendix B – Experimental Details

B.1 – Attenuation of wave propagation in GFRP

The equipment and its configuration used to conduct attenuation experiments on unidirectional and bi-directional GFRP is illustrated in Figure B1, Figure B2, and Figure B3.

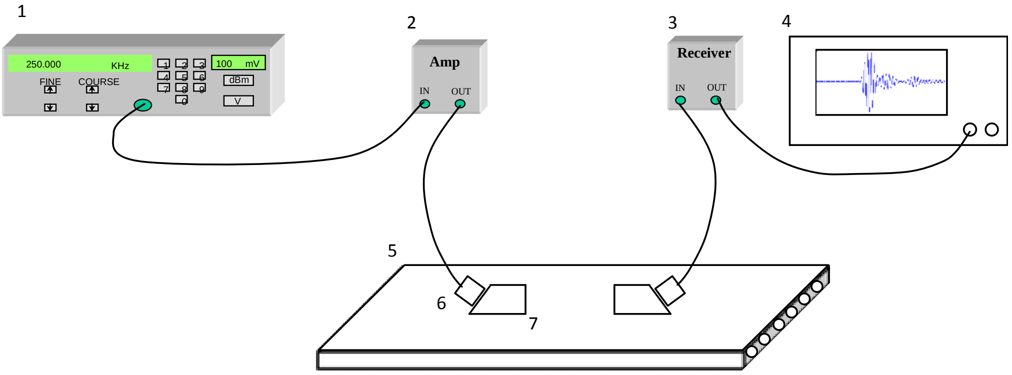

Figure B1: Experimental set-up for attenuation measurements on unidirectional GFRP

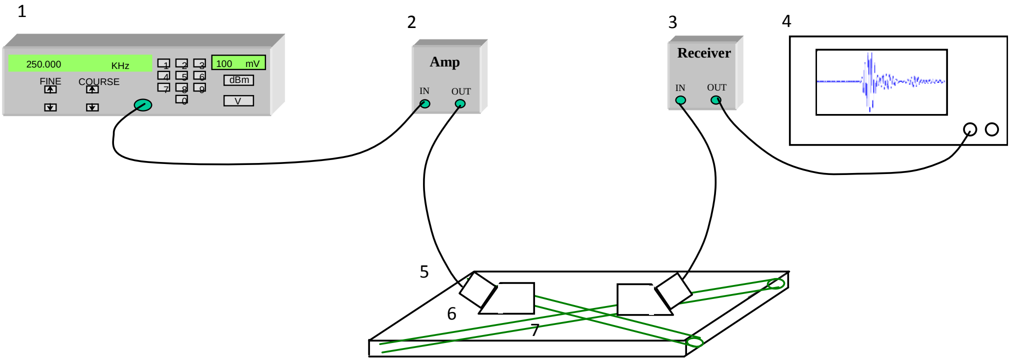

Figure B2: Experimental set-up for attenuation measurements on bi-directional GFRP: off-fibre

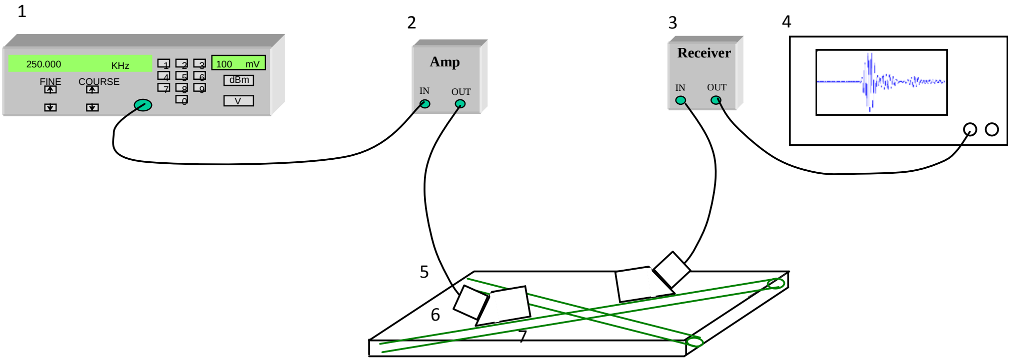

Figure B3: Experimental set-up for attenuation measurements on bid-directional GFRP: on-fibre

1. Tektronix AFG3102 function generator
2. Kalmus Wideband RF Amplifier. Gain = 50 dB.
3. JSR PR35 Pulser/Receiver unit. Gain = 70 dB.
4. Agilent Infiniium 1 GHz 4 GS/s oscilloscope
5. 400 mm x 210 mm unidirectional GFRP
6. 2 x narrowband Ultran transducers operating at 250 kHz, angled at 58° to the GFRP plate
7. Plexiglass wedges.

Initial separation between the two transducers was 60 mm, increasing to 250 mm. in 10 mm increments. The dimensions of the GFRP plate prevented off-fibre axis measurements being performed.

The 4-cycle, Hann-windowed, amplified excitation signal output by the generator is shown in Figure B4.

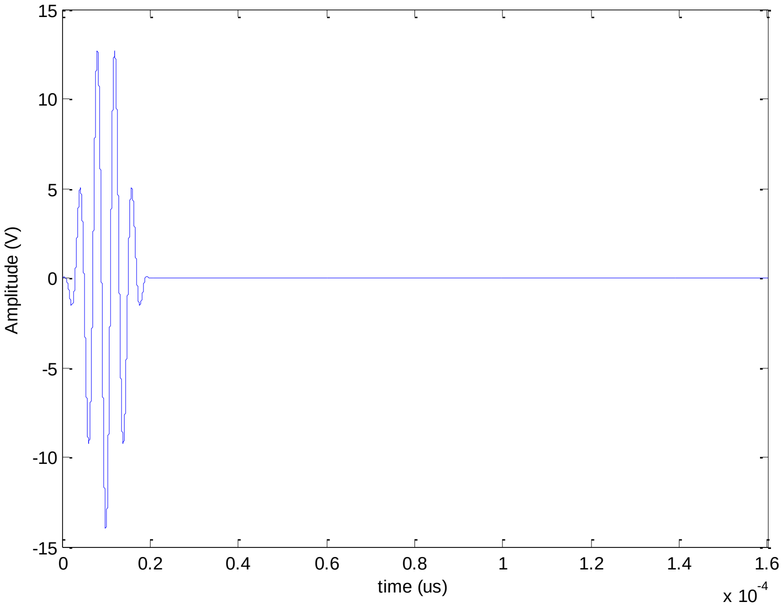

Figure B4: Signal excited into the unidirectional GFRP plate

B.2 – Characterising a bidirectional GFRP sample

To establish the characteristics of a bidirectional GFRP sample, a test set-up was configured to measure the longitudinal and shear velocity within the sample, Figure B5. A 50 mm GFRP specimen (described by Table 5.3) was inserted into the rotational wheel to characterize the velocity of ultrasound with respect to the angle of incidence.

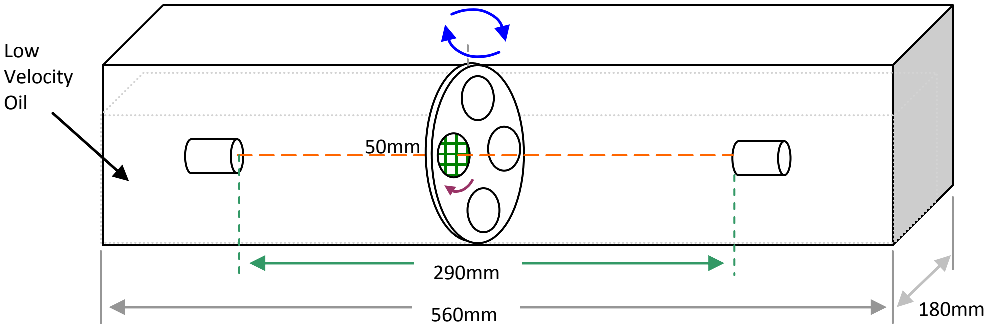

Figure B5: Test-rig to analyse velocity in GFRP

Panametrix immersion transducers were used as the Tx and Rx. The excitation signal is described by Figure B6. The coupling medium, Krytox 8996, was low-velocity oil used to excite a range of frequencies. The longitudinal velocity, c_l, was measured as 4023.9 ms^{-1} and the maximum shear velocity, c_S, was 2136.9 ms^{-1}.

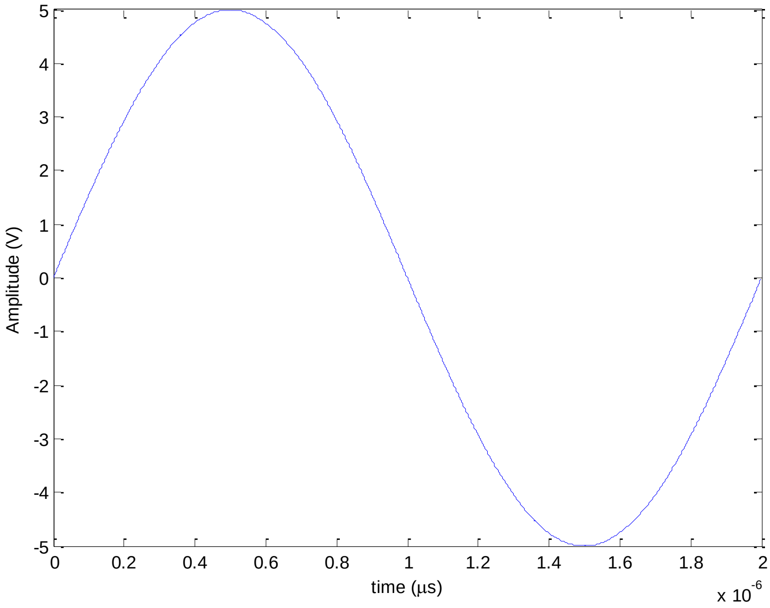

Figure B6: 10 V_{pp}, 1-cycle, 500 kHz sine wave excitation signal

B.3 – Laser excited ultrasound in GFRP

Unfocused Laser Tests

Laser excited ultrasound was generated using the configuration illustrated in Figure B7.

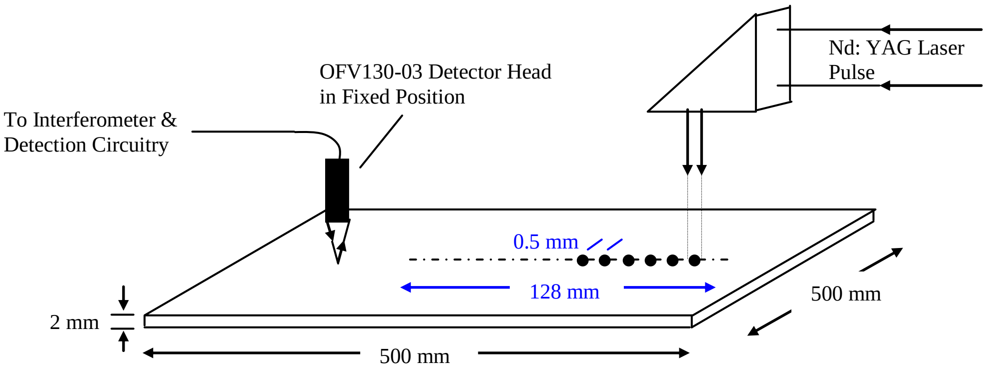

Figure B7: Unfocused laser configuration set-up on GFRP plate

Light from the pulsed Nd:YAG laser was directed onto the sample surface. Control of the surface power density determined the thermoelastic regime operation by controlling the laser output power. This was accomplished by altering the Q-switch timing with respect to the main flash lamp synchronisation in the laser. Figure B8 shows directions 1 and 3 oriented at -45° and +45° respectively and directions 2 and 4 orientated 0° and 90° respectively.

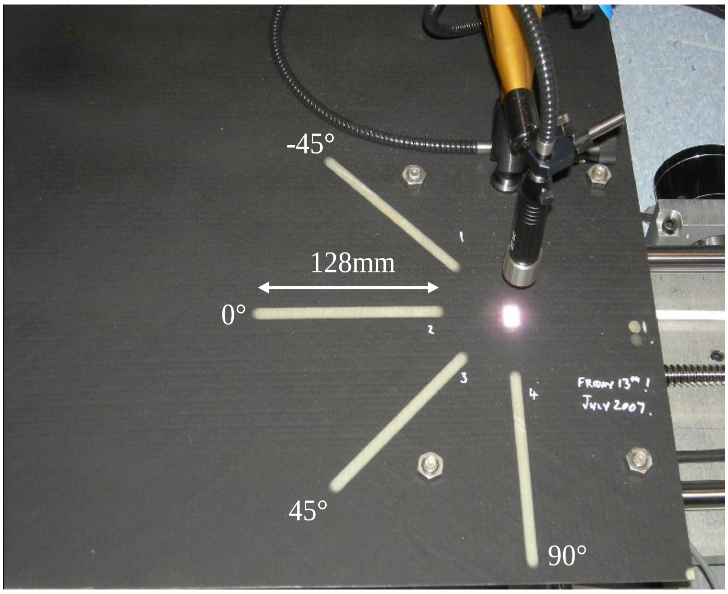

Figure B8: Sample showing test directions -45°, 0°, 45°, 90°

The sample was passed under the laser using a stepper motor controlled source positioner. The propagating stress waves were monitored by an optical interferometer (affixed to the sample) scanned across the sample surface with a spatial sampling interval of Δx=0.5 mm. Measurements were recorded using a commercial laser vibrometer system: Polytec OFV302 with OFV2700-2 OVD 30 displacement decoder. This unit provided excellent repeatability when scanned across the sample surface and provided a displacement sensitivity of 0.25nm operating over a 50 kHz to 20 MHz bandwidth. Ultrasound transients of signal length 15 k samples at 40 M samples per second were recorded using Physical Acoustics diagnostic software with 64 averages used to improve SNR

Spot-focused Laser Tests

The laser light was adjusted so that the focus of the laser spot sat directly on the surface of the glass-fibre sample. The ultrasonic wave was detected using a PolyTec OFV-303 laser head connected to a PolyTec OFV-3001 vibrometer controller having a maximum detection limit of 20 MHz. The stepper motor controlled source positioner was not used. The laser started at a point 149 mm from the detector and travelled the maximum allowable distance of 95.25 mm in 250 equal step sizes of 0.381 mm. The final laser position was 53.75 mm from the detector. The signal was captured on an Agilent Infiniium oscilloscope while a trigger detector circuit used to detect the pulse from the laser, Figure B9.

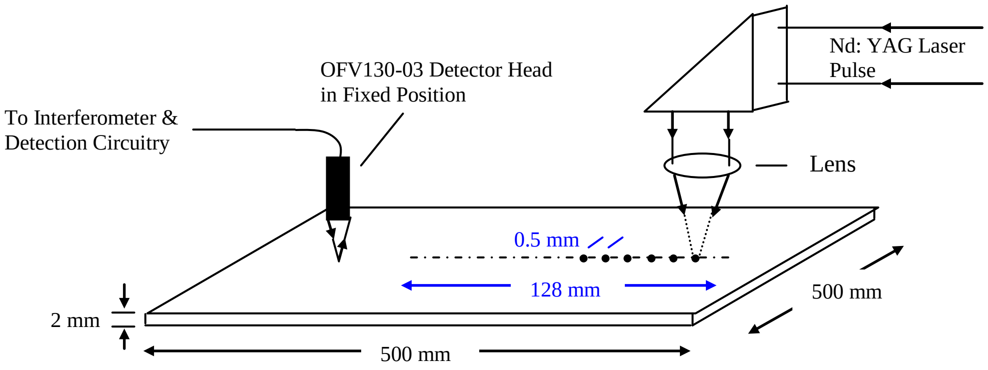

Figure B9: Laser excitation using a lens to create a spot-focus

Line-focused Laser Tests

To provide a line-focus, an 8 mm long, 0.6 mm wide lens was attached to the laser head supplying a power density of 12.9 GW/cm^2. The line focus encourages propagation perpendicular to the axis along which the line focus is generated and where the interferometer sensing spot is focused. The PolyTec OFV-303 laser head and PolyTec OFV-3001 controller was used to detect the ultrasonic wave.

The experiment performed at 45° (on-fibre) and 90° (off-fibre) directions on the GFRP sample is illustrated in Figure B10.

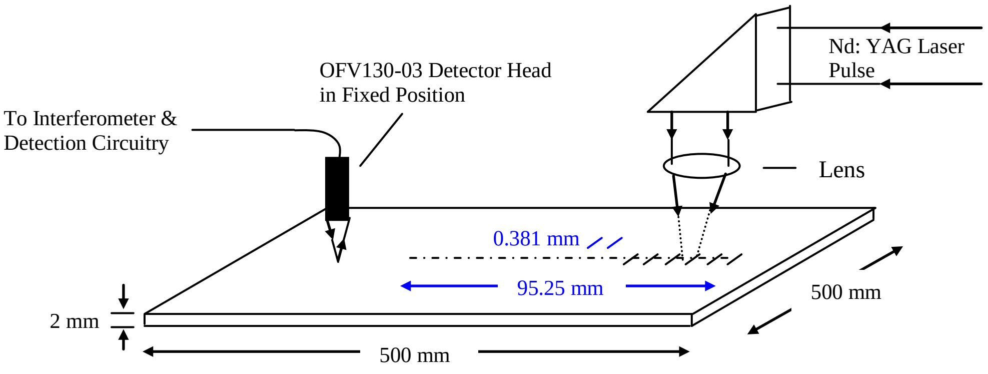

Figure B10: Laser experiment – 14 mm line focus lens

B.4 – Bidirectional GFRP Analysis using PZT Transducers

A low frequency ultrasonic measurement system (employing a single-axis scanner with adjustable transducer holders) was used to observe wave modes propagating within a bidirectional GFRP sample, Figure B11. PZT29 transducers were coupled to the structure using glycerol.

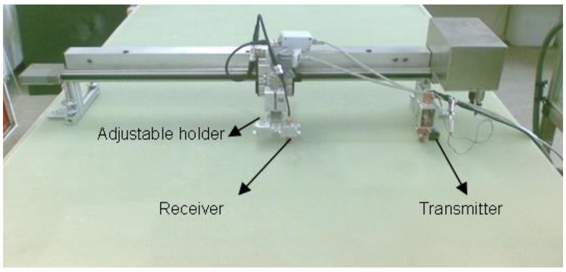

Figure B11: Single axis scanner with PZT transducers on GFRP sample

The excitation signal comprised a Hann-windowed, 100 kHz, 5-cycle sine-wave with amplitude 100 V_{PP} and gain 10 dB, Figure B12.

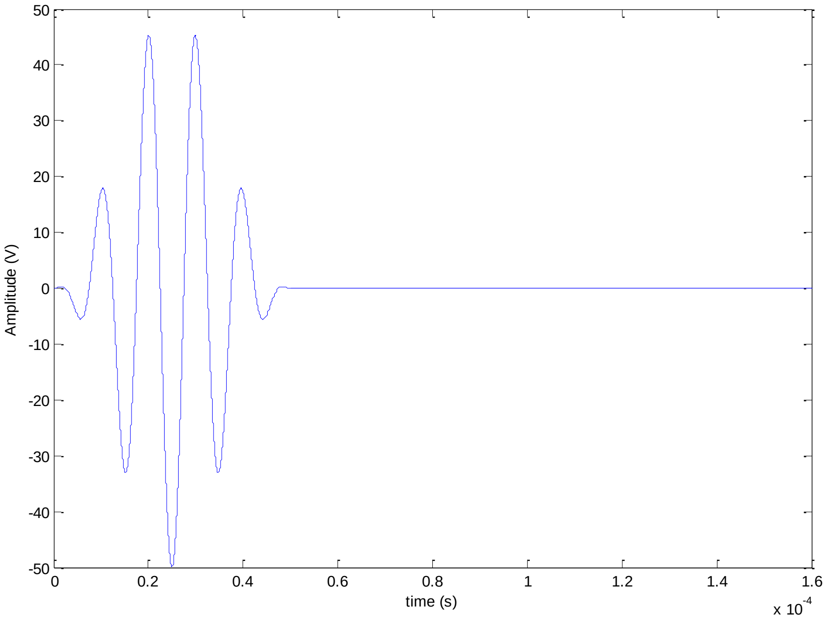

Figure B12: Signal excited into the Bidirectional GFRP plate

The tests were performed so that the line of propagation between the transmitter and the receiver was parallel to the on-fibre (0° or 90°) directions. The fixed transmitter was placed at a distance of 250 mm from the receiver starting position (which was then incrementally moved towards the transmitter in 1 mm steps) covering a distance of 200 mm. The data was analysed using MatLab where a two-dimensional FFT was used to detect the presence of Lamb wave modes propagating within the sample.

B.5 – Quasi-isotropic GFRP Analysis using PZT Transducers

A low frequency ultrasonic measurement system (single-axis scanner with adjustable transducer holders) was used to observe wave modes propagating within a quasi-isotropic GFRP sample, Figure B11. PZT29 transducers were coupled to the structure using glycerol. The excitation signal comprised a Hann-windowed, 100 kHz, 5-cycle sine-wave with amplitude 100 V_{PP} and gain 10 dB, Figure B12.

The tests were performed so that the line of propagation between the transmitter and the receiver was parallel to the on-fibre (0°, 45° or 90°) directions. The fixed transmitter was placed at a distance of 250 mm from the receiver - incrementally moved towards the transmitter in 1 mm steps, covering a distance of 200 mm.

B.6 – Effect of MFC Active length on sensor performance

A 5-cycle, Hann-windowed sine wave was applied to an MFC transmitter sweeping a frequency from 10 kHz – 150 kHz in 2 kHz steps, Figure B13.

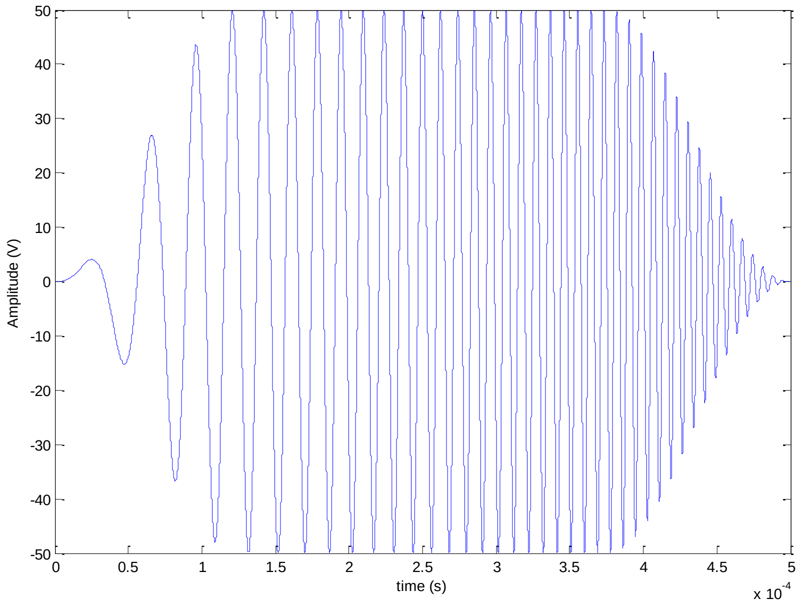

Figure B13: Swept input signal: 10 kHz to 150 kHz

The received signal was amplified by 40 dB and averaged 16 times – a configuration that provided capture of a satisfactory signal strength within a practical test-time.

B.7 – Material directionality of a GFRP sample

A 5-cycle, 250 V_{pp}, 56 kHz, Hann-windowed sine wave was applied to an MFC, Figure B14.

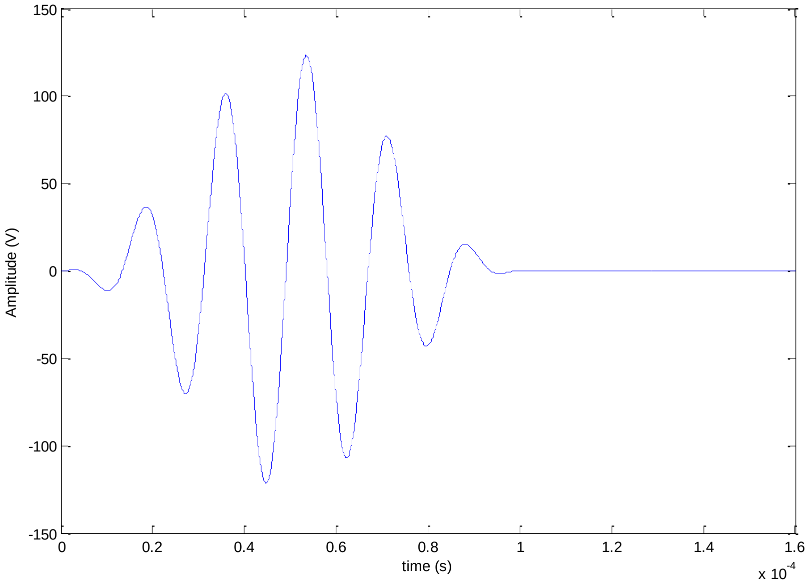

Figure B14: Input signal to assess GFRP directionality

The usable bandwidth of the illustrated signal is described using Equation (B1)

$$Bandwidth\ (BW) = \frac{2f_c}{N} \tag{B1}$$

Where, f_c=56 kHz and N=5; giving a BW = 22.4 kHz.

B.8 – MFC sensor field plot on bidirectional GFRP

The MFC sensor field plot was produced by maintaining a static MFC transmitter at the sample centre and rotating a receiving MFC sensor located 450 mm away towards the sample perimeter. The excitation signal used was a 250 V_{PP}, 56 kHz, 5-cycle, Hann-windowed, sine wave, Figure B15.

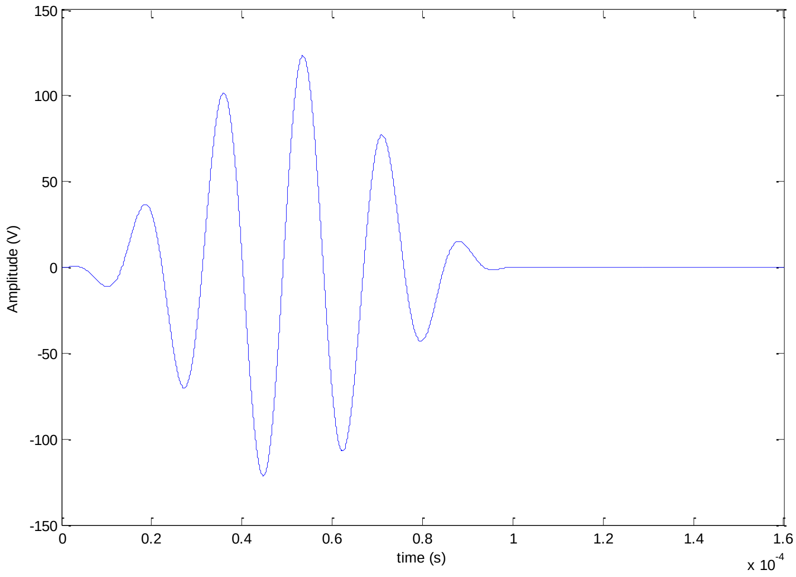

Figure B15: Excitation signal used for sensor field plot on bidirectional GFRP

The receiver was then rotated by 5° increments in an anti-clockwise direction and the signal recorded. This process was repeated up to 360°.

Note: experimental analysis suggested that MFC sensors can be placed and replaced for approximately two full rotations (i.e. 144 times). Thereafter the MFC performance was affected and generally had to be replaced.

B.9 – Loading of Bidirectional GFRP samples

The experimental set-up for applied loading of bidirectional GFRP samples with dimensions 800 mm x 70 mm x 4 mm - each waisted at the centre to ensure fracture did not occur at the grip point – is illustrated in Figure B16.

Figure B16: Instron 8508 Tensile loading machine gripping a waisted GFRP coupon

Each sample underwent:

- Loading using up to 4 different types of tensile tests
- Real time monitoring during each loading cycle
- Continuous acquisition of Guided Wave pulses as emitted from MFCs using Teletest pulser/receiver
- Loading (and monitoring) to failure

M2814 MFC sensors were bonded at each end of the GFRP sample using double-side adhesive tape: one configured as a transmitter and the other as a receiver. The MFC excitation signal was a 250 V_{PP}, 56 kHz, 5-cycle, Hann-windowed, sine wave, Figure B17.

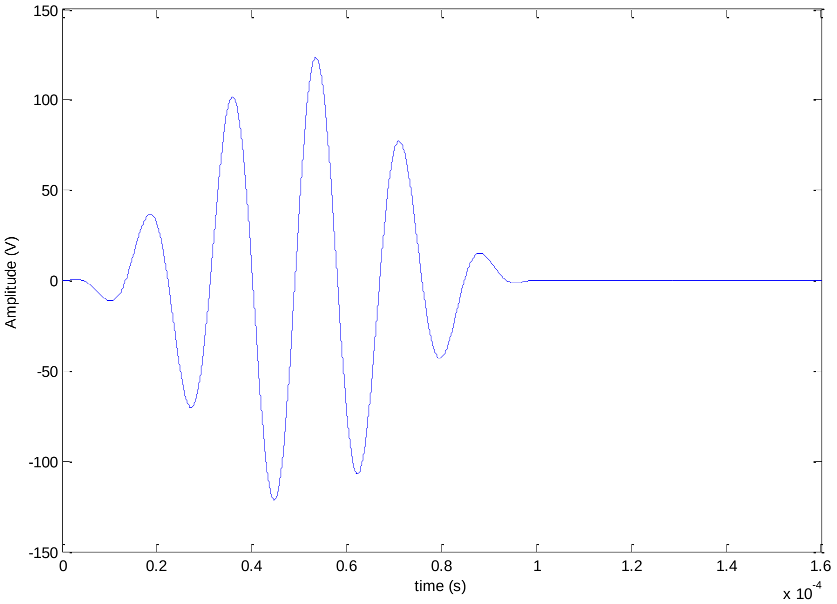

Figure B17: Excitation signal used during loading of GFRP coupon

Data was collected using a pulser/receiver system. Excitation was routinely conducted every 5 seconds for the duration of each tensile test. The data analysed included amplitude variation due to a change in load and variation of the signal time-of-arrival.

Appendix C – Wind Turbine Blade Configuration

C.1 – Wind Turbine Blade Structure

An image of the decoupled wind-turbine blade is shown in Figure C1. The blade length is 9.8 m supported by an internal spar-box, comprising two parts: a 'U' – shaped GFRP configuration topped with a GFRP spar-cap, Figure C2.

Figure C1: Detached 9.8 m wind turbine blade

Figure C2: Support structure – a 'U' configuration topped with a spar cap

C.2 – MFC sensor array configuration

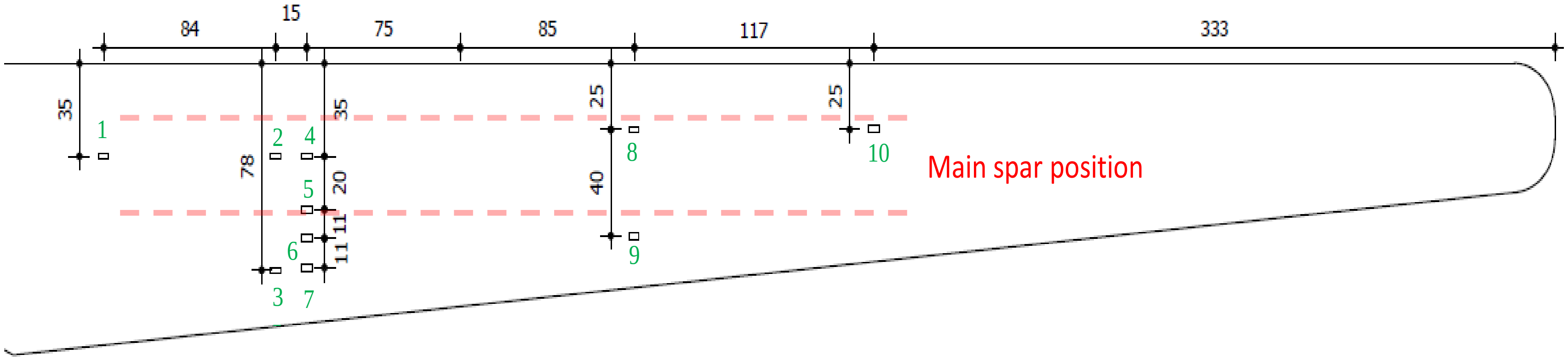

Figure C3: Sensor positions on turbine blade surface (sensor locations, grey (mm); sensor id green)

C.3 – Excitation of Wind Turbine Blade

The signal used for sensor excitation on the decoupled 9.8 m wind turbine blade is given in Figure C4.

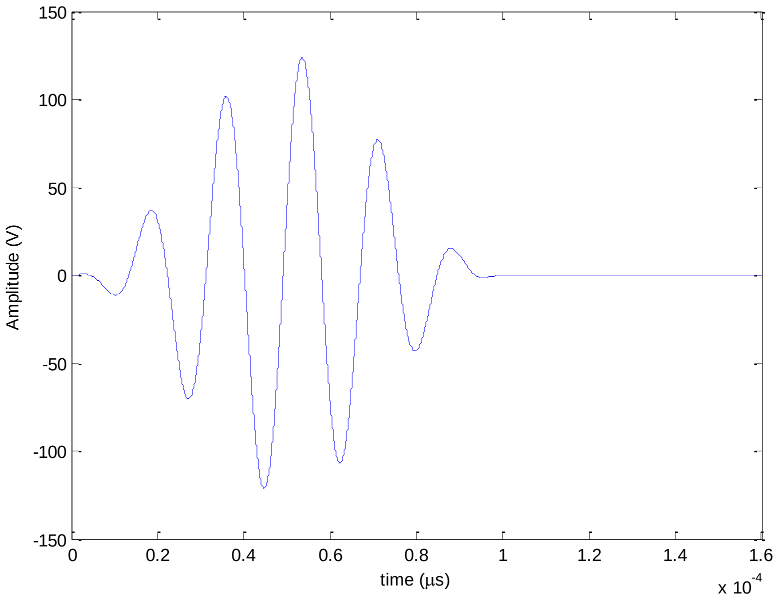

Figure C4: Input signal to assess GFRP directionality

TWI's Teletest pulser-receiver unit was used to generate a 5-cycle, 250 V_{pp}, 56 kHz, Hann-windowed sine wave to each transmitting M2814 MFC sensor.

C.4 – Signal Analysis on Spar Cap

Sensors 2, 4, 8 and 10, located on the spar cap (Figure 6.2), were analysed upon using Sensor 1 as the transmitter (excitation described in Appendix C3). The results are observed in Figure C5.

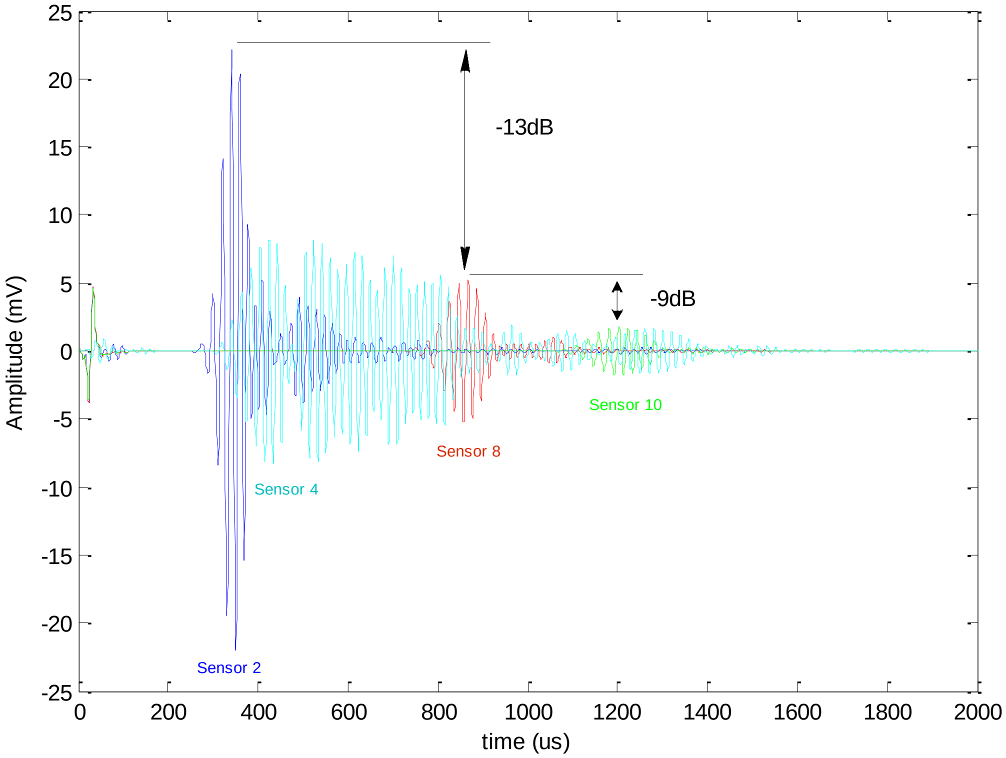

Figure C5: Ascans recorded at Sensors 2, 4, 8 & 10

The signal from Sensor 4 was particularly 'noisy' compared with those of other sensors. During the experiment it was discovered that the coaxial cable connected to Sensor 4 suffered signal integrity issues. This was verified by swapping cables. The same effects were observed on whichever sensor was connected to that particular cable. No cable replacement was possible as experiments took place at a blade manufacturer's premises in rural Greece.

Appendix D – Blade Failure Detection using Cross Correlation

The following tables list the recorded cross-correlation coefficients for a series of transmitting and receiving MFC sensors (as a sparse array) on a decommissioned full length wind-turbine blade, Figure C3.

Table D.1: Cross correlation data between Tx Sensors 1, 5, 8, 9 & 10 and all other sensors configured as Rx

Tx *Rx*	1	5	8	9	10
1		0.9971	0.9572	0.9983	0.9911
2	0.9956	0.9972	0.9596	0.9923	0.9615
3	0.9924	0.9933	0.9983	0.9989	0.9947
4	0.8894	0.9948	0.9426	0.9897	0.964
5	0.9983		0.9951	0.997	0.9989
6	0.9982	0.9957	0.9959	0.994	0.9982
7	0.9947	0.9934	0.9995	0.9983	0.9968
8	0.9636	0.9953		0.9874	0.9967
9	0.9911	0.9989	0.994		0.9965
10	0.9888	0.9986	0.9948	0.9969	

Table D.2: 2 mm defect cross correlation between Tx Sensors 1, 5, 8, 9 & 10 all other sensors configured as Rx

Tx *Rx*	1	5	8	9	10
1		0.8348	0.8945	0.9312	0.8532
2	0.8012	0.7772	0.8682	0.9088	0.8992
3	0.8591	0.509	0.9406	0.9237	0.9484
4	0.8045	0.6596	0.8454	0.892	0.8657
5	0.8412		0.8878	0.8559	0.9772
6	0.8198	0.6016	0.8727	0.8767	0.9446
7	0.8938	0.5019	0.914	0.907	0.9461
8	0.896	0.8813		0.7998	0.8539
9	0.9377	0.8529	0.8068		0.8508
10	0.8427	0.9668	0.8572	0.8406	

Table D.3: 12 mm defect cross correlation between Tx Sensors 1, 5, 8, 9 & 10 all other sensors configured as Rx

Tx Rx	1	5	8	9	10
1		0.9995	0.9995	0.9986	0.999
2	0.9983	0.9985	0.9993	0.9983	0.9988
3	0.998	0.9949	0.999	0.9831	0.9989
4	0.9975	0.9977	0.9988	0.9984	0.9982
5	0.9989		0.9996	0.9746	0.9997
6	0.9989	0.9952	0.9995	0.9747	0.9994
7	0.998	0.9924	0.9985	0.9865	0.9987
8	0.9987	0.9994		0.9983	0.9988
9	0.9984	0.9751	0.9969		0.9977
10	0.9986	0.9971	0.9995	0.9991	

Table D.4: 2nd Hole defect cross correlation between Tx Sensors 1, 5, 8, 9 & 10 all other sensors configured as Rx

Tx Rx	1	5	8	9	10
1		0.9997	0.9997	0.9998	0.9999
2	0.9999	0.9998	0.9997	0.9996	0.9998
3	0.9996	0.9996	0.9999	0.9986	0.9995
4	0.9995	0.9997	0.9998	0.9994	0.9995
5	0.9999		0.9999	0.9964	0.9999
6	0.9999	0.9995	0.9998	0.9956	0.9999
7	0.9995	0.9996	0.9999	0.9978	0.9994
8	0.9999	0.9998		0.9982	0.9999
9	0.9993	0.9958	0.9991		0.9993
10	0.9997	0.9994	0.9998	0.9989	

Appendix E – MatLab code to perform 2DFFT

```
disp('*********************************************')
disp('---------------------------------------------')
disp('  Generation of Lamb Wave Dispersion Curves  ')
disp('---------------------------------------------')
disp('*********************************************')
disp('')
%
%clear all
data=[];
%
file=input('Filename of time-history file(s): ','s');
start=input('Time-history no. FURTHEST from source: ');
stop=input('Time-history no. NEAREST source: ');
inc=input('Increment number: ');
disp('---------------------------------------------')
disp('            Time & Spatial Padding           ')
disp('---------------------------------------------')
rnum=input('Number of time-sample points (^2): ');
cnum=input('Number of spatial-sample points (^2): ');
thick=input('Plate thickness (mm): ');
pos=input('Spatial sampling distance (mm): ');
filtdat=input('Apply low-pass Butterworth filter?, (y/n): ','s');
 if filtdat == 'yes' | filtdat == 'y' | filtdat == 'Y' | filtdat ==
'1'
  minf=input('Upper cut-off frequency, (Hz): ');
 end
%
disp(' ')
disp('++Kaiser window applied to both temporal and spatial
planes++')
dbs=input('Minimum side-lobe attenuation (-dB): ');
dbs=abs(dbs);
disp(' ')
%
% Read in each nodal time-history
% Assume files have extension '.dat'
%
tic     % Start timer
%
disp(' ')
disp('**Reading & normalising discreet time-histories**')
disp(' ')
for i=start:inc:stop               %Sets up the file no. variable
  datai=[file int2str(i)];         %Concat file no to file name
  fin=[datai '.txt'];              %Concat file type to file name.
  if ~exist(fin)                   %Condition when filename does
                                    %not exist
  disp(' ')
  disp('Filename does not exist!')
  disp(' ')
  break
  end
  eval(['load ' fin]);             %Load the complete file name.
  temp=eval(datai);                %Assigns what ever is in datai
```

```
                                   %to temp.
  time=temp(:,1);                  %Time sampling coln 1 (select
                                   %time data)
  X=temp(:,2);                     %Data column 2 (select
                                   %magnitude data)
  PTP=max(X)-min(X);               %Peak to peak data amplitude
  X=X./PTP;                        %Normalise each time history
 if filtdat == 'yes' | filtdat == 'y' | filtdat == 'Y' | filtdat ==
'1'
                                   %Assess filter requirements.
  if i==start;
   tdur=max(time)-min(time);       %Duration of time history
   dt=abs(tdur/(length(time)-1));  %Evaluate time step
   fsamp=1/dt;                     %Evaluate sampling frequency
   Wp=minf/(fsamp/2);              %Upper cut-off frequency
   Ws=(minf+(minf*0.1))/(fsamp/2); %Roll-off
   Rp=3;                           %Passband attenuation, dB
   Rs=20;                          %Stopband attenuation, dB
   [n,Wn]=buttord(Wp,Ws,Rp,Rs);
   [B,A]=butter(n,Wn);             %Bandpass Butterworth filter
  end
  X=filtfilt(B,A,X);               %Apply filter forward & reverse
                                   %directions
end
  data=[data,X];
  fprintf('\nReading file: %s',fin);
%
%  subplot(2,1,1)
%  plot(X(:,1),windat,'k-');   % Plot time-histories
%  set(gca,'XColor','black','YColor','black');
%  hold on;
%
%  ftdat=fft(windat,rnum);
%  ftmag=abs(ftdat);               %FT Magnitude
%  ftphase=unwrap(angle(ftmag));   %FT Phase
%
%  subplot(2,1,2)
%  plot(f(1:(rnum/10)),ftmag(1:(rnum/10)),'k-');
%  set(gca,'XColor','black','YColor','black');
%  hold on;                        %Draw on same graph
%
%
   clear fin;
end
%
disp(' ')
disp(' ')
disp('++++Processing Data++++')
disp(' ')
%
% Apply spatial and temporal windowing function
%
data=data';                   % Transpose DATA set
%
if dbs>50                     % Minimum side-lobe attenuation
  beta=0.1102*(dbs-8.7);      % dbs > 50
elseif dbs<21
  beta=0;
else
```

```
  beta=0.5842*(dbs-21) ^ 0.4 + 0.07886*(dbs-21);    % 21<dbs<50
end
%
[snum,tnum]=size(data);       % Size of data set: Assign to 'snum'
                              % the no of rows of ‘data’; assign
                              % to 'tnum' the no of colns of data
spwind=kaiser(snum,beta);     % Spatial kaiser window
twind=kaiser(tnum,beta);      % Temporal kaiser window
[A,B]=meshgrid(spwind,twind);
spdat=data.*A'.*B';             % Kaiser windowed data set
%
disp('++Applied Kaiser Window Temporally and Spatially++')
disp(' ')
%
% Calculate X-axis (freq) and Y-axis (wavenumber)
%
tdur=max(time)-min(time);       % Duration of time history
dt=abs(tdur/(length(time)-1));  % Time step
fsamp=1/dt;                     % Sampling frequency
f=fsamp*(0:((rnum/2)-1))/rnum;  % Frequency scale for the fft
ftp=(f*thick)/1e6;              % Freq thickness product scale
possamp=(2*pi)/(pos*1e-3);      % Wavenumber = 2pi/lambda
waveno=possamp*(0:((cnum/2)-1))/cnum;
%
% Apply 2D FFT to data set
%
ft2dat=fft2(spdat,cnum,rnum);  % 2D FFT on temp & spatial windowed
                               % data set
ft2mag=abs(ft2dat);            % 2D FFT Magnitude
% ft2ph=unwrap(angle(ft2mag)); % 2D FFT Phase
%
disp('++Performed 2D FFT++')
disp(' ')
%
% Data input in time (columns) vs distance (rows)
% First FFT (up dist columns) gives freq vs distance,
% second FFT (along freq rows) gives freq vs wavenumber
% However, have transposed the data set prior to 2D FFT,
% therefore data is now in distance (cols) vs time (rows)
%
[maxftp,sftp]=max(ftp);
[maxwav,swav]=max(waveno);
%
etim=toc;      % Elapsed time
disp('+++++Finished Processing+++++')
fprintf('**Elapsed time: %g secs**', etim);
%
disp(' ')
disp(' ')
disp('---------------------------------------------')
disp('             Plotting Information            ')
disp('---------------------------------------------')
flag1=1;
flag2=1;
flag3=1;
while 1
disp(' ')
 disp('Plot Graph(s)')
 disp('....(0) 3D Plot : Wavenumber vs FTP')
```

```
 disp('....(1) Contour Plot : Wavenumber vs FTP')
 disp('....(2) Both')
 disp('....(3) Phase Velocity vs FTP')
 disp('...(-1) Exit Plotting Option')
 grph=input('Enter: ');
%
if grph<0, break,end
%
 ftpmin=input('Minimum FTP of interest (MHzmm): ');
 fprintf('\nMaximum FTP: %g:',maxftp);
 ftpmax=input('Maximum FTP of interest (MHzmm): ');
 wavmin=input('Minimum wave-number of interest: ');
 fprintf('\nMaximum wave-number: %g:',maxwav);
 wavmax=input('Maximum wave-number of interest: ');
 scale=input('Log-scale amplitude data ?: ','s');
%
 xmin=(ftpmin/ftp(2))+1;     % x-axis is FTP
 xmax=(ftpmax/ftp(2))+1;
 ymin=(wavmin/waveno(2))+1;  % y-axis is waveno
 ymax=(wavmax/waveno(2))+1;
%
 if xmin < 1
 xmin=1;
 end
 if xmax > sftp
 xmax=sftp;
 end
 if ymin < 1
 ymin=1;
 end
 if ymax > swav
 ymax=swav;
end
%
xmin=round(xmin);
xmax=round(xmax);
ymin=round(ymin);
ymax=round(ymax);
%
 xaxis=ftp(xmin:xmax);
 yaxis=waveno(ymin:ymax);
%
 [temp,num_x]=max(xaxis);
 [temp,num_y]=max(yaxis);
%
 set(0,'DefaultFigureColor','white')
 set(0,'DefaultLineColor','black')
%
if grph==0 | grph==2
if flag1==1
 figure (1)
end
flag1=0;
 set(gcf,'name','3D Lamb Wave Dispersion Curve(s)')
 set(gcf,'InvertHardCopy','off')
 set(gcf,'DefaultTextColor','black')
 [x,y]=meshgrid(xaxis,yaxis);
if scale == 'yes' | scale == 'y' | scale == 'Y' | scale == '1'
 meshh=mesh(x,y,20*log10(1+(ft2mag(ymin:ymax,xmin:xmax))));
```

```
% length freq=x-axis, waveno=y-axis
else
 meshh=mesh(x,y,ft2mag(ymin:ymax,xmin:xmax));
end
 set(meshh,'EdgeColor','black','FaceColor','none','LineStyle','-');
 title('Lamb Wave Dispersion Curves: 3D Plot');
 xlabel('Frequency Thickness Product (MHzmm)')
 ylabel('Wavenumber (2pi/m)')
 zlabel('Amplitude')
% set(gca,'XColor','black','YColor','black','ZColor','black'); %Axes
colour
end
%
if grph==1 | grph==2
ncont=input('Number of Contour Lines in Plot: ');
if flag2==1
 figure (2)
end
flag2=0;
 set(gcf,'name','Contour Plot : Lamb Wave Dispersion Curves')
 set(gcf,'InvertHardCopy','off')
 set(gcf,'DefaultTextColor','black')
if scale == 'yes' | scale == 'y' | scale == 'Y' | scale == '1'
 ylabel('Wavenumber (2pi/m)')

conth=contour(xaxis,yaxis,20*log10(1+(ft2mag(ymin:ymax,xmin:xmax))),
ncont,'k-');
 % Wavenumber
else
 ylabel('Wavenumber (2pi/m)')
 conth=contour(xaxis,yaxis,ft2mag(ymin:ymax,xmin:xmax),ncont,'k.');
 % Wavenumber
end
 title('Lamb Wave Dispersion Curves: Contour Plot')
 xlabel('Frequency Thickness Product (MHzmm)')
 set(gca,'XColor','black','YColor','black','ZColor','black');
 % Axes colour
%
   while 1
   grph4=input('Load External Wavenumber Data [1=yes, 0=no]: ');
   if grph4<1, break,end;
   exdat=input('External filename: ','s');
   exfile=[exdat '.set'];
   if ~exist(exfile)
   disp(' ')
   disp('Filename does not exist!')
   disp(' ')
   break
   end
   eval(['load ' exfile]);
   exdata=eval(exdat);
   hold on;
   xlabel('Frequency Thickness Product (MHzmm)')
   ylabel('Wavenumber (2pi/m)')
   set(gca,'XColor','black','YColor','black','ZColor','black');
   plot(exdata(:,1),exdata(:,2)/thick,'r-');
   % Imported data in line with 2D FFT data, account for plate
     thickness
   hold off;
```

```
   end
end
%

if grph==3
nleont=input('Number of Contour Lines in Plot: ');
k=ft2mag(ymin:ymax,xmin:xmax);
[i j]=size(k);
phasev=zeros(i,j);
matEmpt=zeros(i,j);
for J=1:length(waveno)
    [maxval,row]=max(k);   % Max value & row position
    for I=1:length(row)
    if waveno(row(I))==0
        waveno(row(I))=1;
    end
    end
    phasev(J,row)=(f(xmin:xmax).*2*pi)./waveno(row); % Convert to
                                                     % phase vel
    for rowInd=1:length(row)
        matEmpt(row(rowInd),rowInd)=maxval(rowInd);
    end
    k=k-matEmpt;
    matEmpt=zeros(i,j);
end

 if flag3==1
 figure (3)
 end
flag3=0;
%set(gcf,'name','2D Plot : Lamb Wave Phase Velocity')
%set(gcf,'InvertHardCopy','off')
%set(gcf,'DefaultTextColor','black')

set(gcf,'name','Contour Plot : Lamb Wave Phase Velocity')
set(gcf,'InvertHardCopy','off')
set(gcf,'DefaultTextColor','black')

conth=contour(xaxis,phasev(1,:),ft2mag(ymin:ymax,xmin:xmax),ncont,'k
-');

title('Lamb Wave Dispersion Curves: Contour Plot')
ylabel('Vphase (m/s)')
xlabel('Frequency Thickness Product (MHzmm)')
set(gca,'XColor','black','YColor','black','ZColor','black'); % Axes
colour

for plotInd=1:length(waveno)
plot(f(xmin:xmax),phasev(plotInd,:),'.'); hold on    %Plot 2D phase
                                                     %vel
% goOn=input('Conitnue (y=1, n=0):');
%if goOn==0; break, end;
end
xlabel('Frequency Thickness Product (MHzmm)')
ylabel('Phase Velocity (m/s)')
set(gca,'XColor','black','YColor','black');
%
 while 1
```

```
 grph5=input('Load External Phase Velocity Data [1=yes, 0=no]: ');
 if grph5<1, break,end;
 exdat=input('External filename: ','s');
 exfile=[exdat '.set'];
 if ~exist(exfile)
 disp(' ')
 disp('Filename does not exist!')
 disp(' ')
 break
 end
 eval(['load ' exfile]);
 exdata=eval(exdat);
 hold on;
 xlabel('Frequency Thickness Product (MHzmm)')
 ylabel('Phase Velocity (km/s)')
 set(gca,'XColor','black','YColor','black');
 plot(exdata(:,1),exdata(:,2),'r-');
 hold off;
 end
end
%
 end    % End if statement
% end     % End while loop
%
%
while 1
 disp(' ')
 disp('Save Options')
 disp('....(0) Save Full Data Set')
 disp('....(1) Pick Discreet Points & Save')
 disp('...(-1) Exit Program & Clear Data')
 save=input('Enter: ');
%
if save<0, break,end
%
 if save==0
 fout=input('Filename [.dsp]: ','s');
  xpos=x(:);
  ypos=y(:);
  dout=ft2mag(xmin:xmax,ymin:ymax)';
  dout=dout(:);
  dout=[xpos ypos dout]';
  fid=fopen([fout '.dsp'],'w');
  fprintf(fid,'%g\n',num_x);
  fprintf(fid,'%g\n',num_y);
  fprintf(fid,'%g %g %g\n',dout);
  status=fclose(fid);
  end
%
 if save==1
 hold on;
disp('Pick points: ')
disp('...Mouse: LH button select : RH button terminate')
disp('...Keyboard: Arrow keys : CR terminate')
 x=[];
 y=[];
 n=0;
 but=1;
 while but==1;
```

```
  [xi,yi,but]=ginput(1);
  plot(xi,yi,'r+','era','back');
  n=n+1;
%  text(xi,yi,[' ' int2str(n)],'era','back','color','red');
  x=[x;xi];
  y=[y;yi];
 end
 disp(' ')
 disp('End of Data Entry')
 disp(' ')
%
 xfreq=x/thick;   % Remove plate thickness from FTP scale
 Vph=(xfreq.*(2*pi*1e6))./y;              %Evaluated Vphase
 pdat=[x Vph]';                           %Horizontally concat
                                          %freqthick with Vphase
                                          %data, then transpose
 fout=input('Filename [mat]: ','s');      %Enter root name of file
                                          %to save.
 index=input('Enter file no.: ');         %Enter the file number.
 fullfile=[fout int2str(index)];          %Combine root name & no.
                                          %for full file name.
 fid=fopen([fullfile '.mat'],'w');        %Save as a .mat file.
 fprintf(fid,'%g %g\n',pdat);             %Reads Row1,Coln1 of
                                          %trunc & puts into Row1
                                          %Coln1 then reads Row2,
                                          %Coln1 & puts into
                                          %Row1,Coln2 then
                                          %reads Row3,Coln1 & puts
                                          %into Row2, Coln 1
                                          %i.e. transposing pdat.
 status=fclose(fid);
 end
%
end

%This section reads all the mode files saved and plots them in one
figure.
figure;
for I=1:index                             %The no. of mode files
                                          %saved.
    point=[fout int2str(I)];              %Assemble the file name.
    fin=[point '.mat'];                   %Add stem to file name.
    eval(['load ' fin ' -ASCII']);        %Load the file to be
                                          %plotted.
    pt=eval(point);                       %execute the string as
                                          %expression
                                          %or statement.
                                          %i.e. assign data in
                                          %ModeX to pt.
    plot(pt(:,1),pt(:,2));                %Plot the data.
    axis tight;
    xlabel('Freq Thick (MHzmm)');
    ylabel('Vphase (m/s)');
    hold on;
end
%
temp=input('Are you sure?: ','s');
if temp == '1' | temp == 'y' | temp == 'Y'
disp(' ')
```

```
disp('All variables cleared!!')
disp(' ')
clear all
return
else
disp(' ')
disp('Variables still active!!')
return
disp(' ')
end
```

References

---

1 National Insituite for Occupational Safety and Health, http://www.cdc.gov/NIOSH

2 The National Aeronautics and Space Administration (NASA) , Derailed, Eschede Train Disaster, http://nsc.nasa.gov/SFCS/SystemFailureCaseStudy/Details/24

3 Boller, C., 'Structural Health Monitoring in Aerospace', Advanced Course on Structural health Monitoring, Hamburg, November 25-26, 2010.

4 MACOM, 'condition Monitoring', http://www.macom.co.uk/index.php?option=com_content&task=view&id=79&Itemid=111

5 MACOM, 'condition Monitoring', http://www.macom.co.uk/index.php?option=com_content&task=view&id=80&Itemid=112

6 MOOG, 'Blade Sensing Systems', 2010, http://www.moog.co.uk/PDF/Blade_Sensing_System.pdf

7 Clarke, T., 'Guided Wave Health Monitoring of Complex Structures', PhD, Imperial College London, 2009.

8 Muravin, B., Muravin, G., Lezvinsky, L., 'The Fundamentals of Structural Health Monitoring by the Acoustic Emission Method', Proceedings of the 20th International Acoustic Emissiob Symposium, November 17-19, Kumamoto, Japan, pp.253-258.

9 Worden K. and Dulieu-Barton J. M. 'An overview of intelligent fault detection in systems and structures', Structural Health Monitoring, vol. 3(1), pp. 85-98, 2004.

10 Borum, K.K., 'Structural Health Monitoring in Action', Advanced Course on Structural Health Monitoring, Hamburg 2010

11 Suleman, A., 'Composites manufacturing and EU Projects', Advanced Course on Structural Health Monitoring, November 25-26, 2010, Hamburg

12 Freris, L., 'Inherit The Wind', Vol. 38, Iss. 4, pp155-159, 1992.

13 http://www.bindt.org/About_us/About_NDT

14 Suleman, A., 'SHM Lecture', SHM-in-Action Lecture Series, November 25-26, 2010, Hamburg

15 Aviation Today, 'Understanding MSG-3', http://www.aviationtoday.com/am/repairstations/Understanding-MSG-3_33062.html#.UYzHVcoa47s

16 Could fibre optic sensing be a perfect match for wind energy's monitoring requirements? 25th February 2013 http://social.windenergyupdate.com/operations-maintenance/could-fibre-optic-sensing-be-perfect-match-wind-energys-monitoring-requiremen

17 Rhead,P., 'Fibre Optic Based Sensing Systems For Multi-Variable Turbine Control and Structural Condition Monitoring Applications', Insenys, 2006, http://proceedings.ewea.org/ewec2006/allfiles2/535_Ewec2006fullpaper.pdf

18 Tongue, B.H., 'Principles of Vibration', pp481-482, Second Edition, Oxford University Press, 2002

19 Cole, P.T., 'Acoustic Emission', p7, Part7, The Capabilities and Limitations of NDT, British Institute of Non-Destructive Testing Publication, 1988

20 Su, Z., Ye, L., 'Identification of Damage Using Lamb Waves', p4, Lecture Notes in Applied and Computational Mechanics Vol.48, Springer, 2009

21 Boller, C., Chang, F.K., Fujino, Y., 'Encyclopedia of Structural Health Monitoring', 2009 John Wiley & Sons, Ltd. ISBN: 978-0-470-05822-0.

22 Lei, J.F., 'High temperature thin film strain gages', HITEMP Review 1994 I:25.1–25.13, NASA CP-10146.

23 Stasiek, J., 'Thermochromic liquid crystals and true colour image processing in heat transfer and fluid flow research', Heat and Mass Transfer 1997 33:27–29.

24 Ireland, P.T., 'The response time of a surface thermometer employing encapsulated thermochromic liquid crystals', Journal of Physics E: Scientific Instruments 1987 20:1195–1199.

25 Hobbs, R.J., Currall, J.E.P., Gimingham, C.H., 'The use of thermocolor pyrometers in the study of heath fire behaviour', Journal of Ecology 1984 72:241–250.

26 Allison, S.W., Gillies, G.T., 'Remote thermometry with thermographic phosphors: instrumentation and applications', Review of Scientific Instruments 1997 68(7):2615–2650.

28 An International Comparison of Energy and Climate Change Policies Impacting Energy Intensive Industries in Selected Countries , ICF International https://www.gov.uk/government/uploads/system/uploads/attachment_data/file/31768/12-527-international-policies-impacting-energy-intensive-industries.pdf

29 UK Renewable Energy Roadmap Update 2012, page 9, DECC, http://www.decc.gov.uk/assets/decc/11/meeting-energy-demand/renewable-energy/7382-uk-renewable-energy-roadmap-update.pdf

30 Digest of United Kingdom Energy Statistics 2012, National Statistics https://www.gov.uk/government/uploads/system/uploads/attachment_data/file/279523/DUKES_2013_published_version.pdf

31 Global Wind Report – Annual Market Update 2011, Global Wind Energy Council (GWEC), http://gwec.net/wp-content/uploads/2012/06/Annual_report_2011_lowres.pdf

32 Executive Committee for the implementing agreement for co-operation in the Research, Development, and Deployment of Wind Energy Systems of the International Energy Agency, 'IEA Wind Energy Annual Report 2012', IEA 2013

33 Offshore Wind: Decision Time, November 2013, renewableUK http://www.renewableuk.com/en/publications/reports.cfm/offshore-wind-report

34 'Management of Meteorological Variables and Wind Mapping' http://www.wwindea.org/technology/ch02/en/2_2_2.html

35 'UK Electricity Generation Costs Update', June 2010, Mott MacDonald https://www.gov.uk/government/uploads/system/uploads/attachment_data/file/65715/71-uk-

electricity-generation-costs-update-.pdf

36 Lemming, J.; Morthorst, P.E.; Clausen, Niels-Erik ‘Offshore wind power experiences, potential and key issues for deployment’, ETDEWEB, Word Energy Base, 2009, https://www.etde.org/etdeweb/details_open.jsp?osti_id=948611

37 Mott MacDonald, http://www.bbc.co.uk/news/science-environment-14412189

38 L.W.M.M. Rademakers et al., ‘Assessment and Optimisation of Operation and Maintenance of Offshore Wind Turbines’, ECN Wind Energy, https://www.ecn.nl/fileadmin/ecn/units/wind/docs/dowec/2003-EWEC-O_M.pdf

39 The Betz limit – and the maximum efficiency for horizontal axis wind turbines, WindPower Program, http://www.wind-power-program.com/betz.htm

40 ‘All About Wind Turbines’, http://wind-turbine.tripod.com/id13.html

41 Nordex Wind turbine, http://web.inge.unige.it/SCL/images/Spaccato%20WT.jpg

42 International Renewable Energy Agency, ‘Wind Power’, Renewable Energy Technologies: Cost Analysis Series, Volume 1: Power Sector Issue 5/5, June 2012, https://www.irena.org/DocumentDownloads/Publications/RE_Technologies_Cost_Analysis-WIND_POWER.pdf

43 www.hie.co.uk/crest-david-infield.pdf

44 Hahn, B., Jung, H., ‘Improving Wind Turbine Availability by Reliability Based Maintenance’, Institüt für Solare Energieversorggungstechnik (ISET)

45 CP-Max Rotortechnik, Wind Turbine Blade Manufacture conference, Düsseldorf, 7-9 December 2010

46 Specialist Committee V.4, ‘Ocean Wind and Wave Energy Utilzation’, 16th International Ship and Offshore Structures Congress 20-25 August 2006, Volume 2.

47 NTN Corporation (CAT. No. 30117/E), ‘Care and Maintenance of Bearings’ http://www.ntn.co.jp/english/products/pdf/care/pdf/CareAndMaintenance_en.pdf

48 White, D., Musial, W., ‘The Effect Of Load Phase Angle On Wind Turbine Blade Fatigue Danage’, National Renewable Energy Laboratory (NREL), 42nd AIAA Aerospace Sciences Meeting and Exhibit, Reno, Nevada, January 5-8, 2004

49 ‘Assessing The Future Of Conditioning Monitoring’, Wind Power Monthly, October 2011

50 ‘Composites 101’,Quartis Engineering, http://www.quartus.com/resources/white-papers/composites-101/

51 Mendler, J., Wolfgang, K., Katzenschwanz, C., ‘Structural Design Optimisation of Wind Turbine Rotor Blades considering Manufacturing Costs’, Wind Turbine Blade Manufacture 2010 conference, Hamburg

52 Ravi, G., ‘Stage-Wise Manufacturing of Wind Turbine Rotor Blade’, Wind Turbine Blade Manufacture 2010 conference, Hamburg

53 Gurit Materials for Wind Turbine Blades,
http://www.gurit.com/files/documents/5_gurit_materials.pdf

54 SGL Group 'Benefits of using Carbon Fibres in Rotor Blades', Wind Turbine Blade Manufacture 2010, Hamburg.

54 Thomassin, R., 'Options To Increase Annual Energy Production', Wind Turbine Blade Manufacturer 2010 Conference, Hamburg

55 Stone, D.E.W., Clarke, B., 'Nondestructive Determination of the Void Content in Carbon Fibre Reinforced Plastics by Measurement of Ultrasonic Attenuation', RAE Tech. Report 74162, 1974.

56 Stone, D.E.W., 'Problems in the Nondestructive Testing of Carbon-Fibre Reinforced Plastics', RAE Tech. Report 74080, 1974.

57 Stone, D.E.W., Clarke, B., 'Ultrasonic Attenuation as a Measure of Void Content in Carbon-Fibre Reinforced Plastics', Non-Destructive Testing, 8 (3) 137-145, June 1975.

58 'Characterization, Analysis and Significance of Defects in Composite Materials', AGARD Conference Proceedings No. 355, 1983.

59 McGugan, M., Sørensen, B.F., Østergaard, R., 'Estimating damage criticality in sandwich composite material using acoustic emission signal', 2nd European Workshop on Structural Health Monitoring, July 7-9, 2004.

60 Jones, L.D., Smith, A. Robert, Weise, V.L., 'Ultrasonic NDE for Production Inspection of Composites', NDE Group, Qinetiq Ltd.

61 Potter, R.T., 'The Significance of Defects and Damage in Composite Structures', AGARD Conference Proceedings No. 355, Paper 17, 1983.

62 Lorenzo, L., Hahn, H.T., 'Detection of Ply Cracking Through Wave Attenuation', 29th National SAMPE Symposium, 1022-1033, April 3-5 1984.

63 Moyo, P., Brownjohn, JM.W., 'Detection of anomalous structural behaviour using wavelet analysis', Mechanical Systems and Signal Processing 16, pp429-445, 2002.

64 Inman, D.J., Farrar, C.R., Lopes, V.(Jnr), Steffen, V.(Jnr), 'Damage Prognosis: For Aerospace,Civil and Mechanical Systems', Ch. 1, pp 1-12, John Wiley & Sons, 2005.

65 Boller, C., 'Predictive Maintenance', Advanced Course on Structural health Monitoring, Hamburg, November 25-26, 2010.

66 Worden, K., Friswell, M.I., 'Modal–Vibration-based Damage Identification', Encyclopedia of Structural Health Monitoring, Chapter 11, 2009, John Wiley & Sons, Ltd.

67 Zagrai, A.N., Giurgiutiu, V., 'Electromechanical Impedance Modeling', Encyclopedia of Structural Health Monitoring, Chapter 5, 2009, John Wiley & Sons, Ltd.

68 Giuergiutiu, V., Rogers, C.A., 'Recent advancements in the electromechanical (E/M) impedance method for structural health monitoring and NDE', SPIE proceedings, vol. 3329, pp 536-547, 1998

69 Sundararaman, S., 'Static Damage Phenomena and Models', Encyclopedia of Structural Health Monitoring, Chapter 8, 2009, John Wiley & Sons, Ltd.

70 Haksoo, C., 'Structural Health Monitoring system based on strain gauge enabled wireless sensor nodes', Networked Sensing Systems, INSS 2008, 5th International Conference

71 Affrossman, S., Banks, W.M., Hayward, D., Pethrick, R.A.,'Non-Destructive Examination of Adhesively Bonded Structures Using Dielectric Techniques: Review and Some Results', Proc Instn Mech Engrs Vol 214 Part C.

72 Luong, M.P., 'Thermomechanical Models', Encyclopedia of Structural Health Monitoring, Chapter 6, 2009, John Wiley & Sons, Ltd.

73 Continuous health monitoring and non-destructive assessment of composites and composite repairs on surface transport applications http://www.compairproject.com/home/index.jsp

74 Wevers, M., Lambrighs, K., 'Applications of Acoustic Emission for SHM: A Review', Encyclopedia of Structural Health Monitoring, Chapter 13, 2009, John Wiley & Sons, Ltd.

75 Holroyd, T.J., 'The Acoustic Emission & Ultrasonics Monitoring Handbook', First Edition, Coxmoor Publishing Company

76 Pearson, M.R., Eaton, M.J., Szigeti, E., Pullin, R., Clarke, A., Burguete, R., Featherston, C.A., 'Damage Detection in Composite Material using Airborne Acoustics', Key Engineering Material Vols, 569-570, pp72-79, 2013

77 Pullin, R., Pearson, M.R., Eaton, M.J., Featherston, C.A., Holford, K.M., Clarke, A., 'Automated Damage Detection in Composite Components Using Acoustic Emission', Key Engineering Material Vols, 569-570, pp80-87, 2013

78 Zaitsev, V.Y., 'Acoustic Wave-Crack Interaction Mechanisms of Nonlinear Elastic and Inelastic Dynamics at Different Time-Scales', WCU 2003, Paris, September 7-10, 2003.

79 Johnson, P.A., 'NonDestructive Testing of Materials By Nonlinear Elastic Wave Spectroscopy (NEWS)', Materials World, Journal of the Institute of Materials, September 1999.

80 Donskoy, D., Sutin, A., Ekimov, A., 'Nonlinear Acoustic Interaction on Contact Interfaces and its use for Nondestructive Testing', NDT&E International 00 (2000) 000-000

81 Muller, M., Sutin, A., Guyer, R., Talmant, M., Laugier, P., Johnson, P.A., 'Nonlinar Resonant Ultrasound Spectroscopy (NRUS) Applied to Damage Assessment in Bone', J. Acoust. Soc. Am. 118(6), December 2005 pp3946-3952.

82 Johnson, P.A., Sutin, A., and TenCate, J., 'Development of Nonlinear Slow Dynamical Damage Diagnostics (S3D) for Application to Nondestructive Evaluation', WCU 2003, Paris, September 7-10.

83 Klepka, A., Pieczonka, L., Staszewski, W.J., Aymerich, F., 'Impact Damage Detection in Laminated Composites by non-linear vibor-acoustic wave modulations', Composites Part B: Engineering, 2013.

84 Smith, R.A., Dalton, R.P.,Advanced Ultrasonic methods for Composite Inspection, NDE of Composites Lecture 4, NDE Group, Qinetiq

85 Joseph L. Rose, 'Ultrasonic Waves in Solid Media', Appendix A: A.1, p113, Cambridge, 2004

86 Viktorov,I.A., 'Rayleigh and Lamb Waves – Physical Theory and Applications', Chapter II, Plenum Press, 1967

87 Prasad, S.M., Balassubramaniam, K., Krishnamurthy, C.V., "Structural health monitoring of composite structures using Lamb wave tomography", Smart Materials and Structures 16, 2375-2387, 2007

88 Alleyne, D.N., Cawley,P., 'The Interaction of Lamb Waves with Defects', IEEE Transactions On Ultrasonics, Ferroelectrics, And Frequency Control, Vol.39, No.3, May 1992

89 Choi, S.W., Farinholt, K.M., Taylor, S.G., Marquez, A.L., Park, G., 'Damage Identification of Wind Turbine Blades Using Piezoelectric Transducers', Hindawi Publishing Corporation, Shock and Vibration, Volume 2014.

90 Kaw, A.,K., 'Mechanics of Composite Materials', pp2-3, 2nd Edition, CRC

91 Lowe, M.J.S., Neau,G., Deschamps,M., 'Properties of Guided Waves in Composite Plates, And Implications For NDE', CP700, Review of Quantitative Nondestructive Evaluation vol.23.

92 Pierce, S.G., Culshaw, B., Philp, W.R., Lecuyer, F., Farlow, R. 'Broadband Lamb Wave Measurements in Aluminium and Carbon/Glass Fibre Reinforced Composite Materials Using Non-Contacting Laser Generation and Detection', Ultrasonics 35 (1997) 105-114

93 Jeong, H., Jang, Y., 'Wavelet Analysis of Plate Wave Propagation in Composite Laminates', Composite Structures 49 (2000) 443-450

94 Zak, A., Krawczuk, M., Ostachowicz, W., 'Propagation of In-plane Elastic waves in a Composite Panel', Finite Elements in Analysis and Design 43 (2006) 145-154

95 Raghavan, A., Cesnik, E.S., 'Review of Guided-wave Structural Health Monitoring', The Shock and Vibration Digest 39(2), 91-114, 2007

96 Kessler, S.S., 'Piezoelectric-Based In-Situ Damage Detection of Composite Materials for Structural Health Monitoring Systems', PhD., Dept of Aeronautics and Astronautics, MIT, Cambridge, MA, USA, 2002

97 Gachagan, A., Reynolds, P., Hayward, G., Monkhouse, R., Cawley, P., 'Piezoelectric Materials for Application in Low Profile Interdigital Transducer Designs', Proceedings of the IEEE Ultrasonics Symposium, 1996, pp853-856.

98 Guo, Z., Achenbach, J.,D., Krishnaswamy, S., 'EMAT generation and laser detection of single lamb wave modes' Ultrasonics 35, 423-429, 1997

99 Hutchins, D.A., Jansen, D.P., Edwards, C., 'Non-Contact Lamb Wave Tomography using Laser Generated Ultrasound', Proceedings of the IEEE 1992 Ultrasonics Symposium, Vol.2, pp 883-886.

100 Thompson, R.B., 'Physical Principals of Measurement with EMAT transducers', Physical Acoustic, Mason, W.P. and Thurston, R.N., (Academic Press, New York, 1990), Vol. XIX, pp179-275.

101 Atkinson, D., 'Evaluation of An Active Acoustic Waveguide Sensor for Embedded Structural Monitoring', Thesis, January 2000, Centre for Ultrasonic Engineering, University of Strathclyde.

102 Whiteley,S.,

http://www.strath.ac.uk/eee/research/cue/research/bioacoustics/batultrasound/electrostatictransducersforreplicationofwidebandbatcallsinair/

103 Castaings, M., Hosten, B., 'Lamb and SH Waves Generated and Detected by Air-Coupled Ultrasonic Transducers in Composite Material Plates', NDT&E International 34 (2001) 249-258

104 Sherman, C.H., Butler, J.L., 'Transducers and Arrays for Underwater Sound', p48, Springer, 2007

105 'Types of Earthquake Waves', http://allshookup.org/quakes/wavetype.htm

106 Viktorov,I.A., 'Rayleigh and Lamb Waves – Physical Theory and Applications', Chapter II, Plenum Press, 1967

107 Auld, B.A., 'Acoustic Fields And Waves In Solids', Volume I, 1973, John Wiley & Sons.

108 Kolsky, H., 'Stress Waves in Solids, New York, Dover Publications inc., 1963.

109 Datta, S.K., Arvind, S.H., 'Elastic Waves in Composite Media and Structures', CRC Press, 2009.

110 Lempriere, B.M., "Ultrasound And Elastic Waves, Frequently Asked Questions", Academic Press 2002.

111 Love, A.E.H., 'A Treatise on the Mathematical Theory of Elasticity', Dover Publications, New York, 1944.

112 Kino, G., S., 'Acoustic Waves: Devices, Imaging And Analog Signal Processing', pp120-122, Prentice Hall, 2000.

113 Raghavan, A., Cesnik, C.E.S., '3-D Elasticity-based Modelling of Anisotropic Piezocomposite Transducers for Guided Wave Structural Health Monitoring', Journal of Vibration and Acoustics, 129(6), pp739-751, 2007

114 Haig, A.H, Sanderson, R.M, Mudge, P.J., Balachandran, W., 'Experimental Validation of a Point Source Superposition Model for the Analysis of Transducer Directionality', 2011.

115 WAI, 'PZFlex Starter Manual', PZFLEX Training Exercises, Version 1.0, 2005

116 Hill, R., Forsyth, S.A., Macey, P., 'Finite Element Modelling of Ultrasound, with Reference to Transducers and AE Waves', Ultrasonics 42 (2004) 253-258

117 Hayward, G., Hyslop, J., 'Determination of Lamb Wave Dispersion Data in Lossy Anisotrpic Plates Using Time Domain Finite Element Analysis. Part I: Theory and Experimental Verification', IEEE Transactions on Ultrasonics, Ferroelectrics, And Frequency Control, Vol. 53, No. 2, February 2006

118 Hayward, G., Hyslop, J., 'Determination of Lamb Wave Dispersion Data in Lossy Anisotrpic Plates Using Time Domain Finite Element Analysis. Part II: Application to 2-2 and 1-3 Piezoelectric Composite Transducer Arrays', IEEE Transactions on Ultrasonics, Ferroelectrics, And Frequency Control, Vol. 53, No. 2, February 2006

119 Lee, B.C., Staszewski, W.J., 'Modelling of Lamb Waves for Damage Detection in Metallic Structures: Part I. Wave Propagation', Smart Mater. Struct. 12 (2003) 804-814

---

120 Zak, A., Krawczuk, M., Ostachowicz, W., ‘Propagation of in-plane waves in an isotropic panel with a crack’, Finite Elements in Analysis and Design 42 (2006) 929-941

121 Hancock, M., ‘Development of Tooling Suitable for Stall Regulated Blades’, Prepared for Aerolaminates, 2001.

122 Hull, D., ‘An Introduction to composite materials’, p16, Chapter 2, Cambridge University Press, 6th Edition

123 ‘Micromechanics of Failure’, http://en.wikipedia.org/wiki/Micro-mechanics_of_failure

124 Cripps, D., ‘Fibre Properties’, Netcomposites, Gurit http://www.netcomposites.com/guide/fibreproperties/27

125 C.B. SCruby, L.E.Drain, ‘Laser Ultrasonics – Techniques and Applications’, Adam Hilger, 1990, pp23

126 Lucio, B.S., ‘Optical Techniques For Examining Mechanical Materials’, Thesis, CMP, University of Strathclyde, Nov 2006

127 E.O.Brigham, ‘The Fast Fourier Transform And Its Applications’, Prentice Hall Signal Processing Series, 1988, Chapter 2, pp233

128 Loyd, J.M., ‘Electrical Properties of Macro-Fiber Composite Actuators and Sensors’, MSc., Virginia Polytechnic Institute, 2004.

129 Haig, A., ‘Ultrasonic Guided Wave Inspection with Macro Fiber Composite Actuators’, Brunel University, Uxbridge, UK TWI Ltd., Cambridge, UK, 2009.

130 Wilkie, W., Bryant, R., Fox, R., Hellbaum, R., High, J., Jalink, A., Little, B., Mirick, P., U.S. patent 6,629,341 b2, Method of fabricating a piezoelectric apparatus, 2003.

131 Daue, T.P., Kunzmann, J., Schönecker, A., ‘Energy Harvesting Systems Using Piezo-Electric Macro Fiber Composites, Smart Materila Corp.

132 Matt, H.M, Lanza di Scalea, F., ‘Macro-fiber composite piezoelectric rosettes for acoustic source location in complex structures’, NDE & Structural Health Monitoring Laboratory, Department of Structural Engineering, University of California, July 2007.

133 Blade Loss of Failure, http://www.docstoc.com/docs/71436291/Safety-Issues